Laser Induced Modification and Integration of Glasses

Panjawat Kongsuwan

Submitted in partial fulfillment of the
requirement for the degree
of Doctor of Philosophy
in the Graduate School of Arts and Sciences

COLUMBIA UNIVERSITY

2014

ABSTRACT

Laser Induced Modification and Integration of Glasses

Panjawat Kongsuwan

Glasses have been widely used as substrates in new technologies especially flat panel displays (FPD), organic light-emitting diode (OLED) lighting, and lab-on-a-chip (LOC) applications. They are inexpensive, chemically inert with excellent optical, mechanical and thermal properties. In addition, they are biocompatible, and some compositions possess bioactive properties which are highly desirable in biomedical applications. This dissertation seeks to develop fundamental understanding of feature formation mechanisms and changes in morphology, structural, and mechanical properties of glasses induced by lasers in both high (a femtosecond laser) and low (a continuous wave laser) intensity regimes, and to investigate novel processes for modification and integration of glasses.

Due to its nonlinear absorption capability in glasses, a femtosecond laser is used to generate internal features inside glass. Their morphology, structure, and mechanical properties such as modulus, hardness, ductility, and fracture toughness are experimentally characterized. Fundamental understanding of the feature formation and these property changes is developed through differential interference contrast (DIC) microscopy, spatially resolved Raman spectroscopy, spatially resolved nanoindentation, and predictive numerical simulations. The improved understanding lays ground work to investigate novel processes of transmission welding (TW) and single step channeling (SSC) in glasses. Joining or sealing of glasses in FPD, OLED, and LOC applications are currently based on adhesives. They are susceptible to moisture permeability and require high curing temperatures of entire parts for a long period of time. TW is

investigated and the mechanism of joint formation is analyzed. A numerical model, developed to predict the welding widths, demonstrates the inverse teardrop-shaped absorption volume like the experimental weld seam geometry. Using indentation fracture analysis, the joint is determined to have better mechanical properties than the base material. Fabrication of microfluidic networks in LOC using traditional lithographic processes, or other hybrid processes is cumbersome because they involve multiple steps. SSC is investigated, and numerical models are also developed and experimentally validated to predict the channel lengths resulting from different laser and focusing parameters. The understanding of the channel formation mechanism, and the channel length variation corresponding to the working parameters is developed. TW has the potential to achieve a reliable, highly localized sealing process while SSC has the potential to simplify LOC designs requiring no adhesive for FPD and biomedical industry, respectively.

Reduction of the risk of early failure for load-bearing biomedical implants could be achieved by coating bioactive glass onto bioinert metallic substrates. High bioactivity of bioactive glass accelerates the bone-bonding time. Coatings of 45S5 Bioglass, which has the highest rate of bioactivity by plasma spraying and enameling usually fail due to its significant crystallization and weak adhesion to the substrates. Double layer coating by a continuous wave (CW) laser is investigated to produce a dense bond coat having a strong adhesion and a porous top coat having high bioactivity. The morphology and microstructure of the resultant laser coatings are experimentally characterized. A mixed interfacial layer is found at the glass-titanium interface indicating a relatively strong chemical bonding. The top coat is examined revealing a porous structure with low crystallinity. A numerical model is developed to aid in understanding laser sintering mechanisms and is validated experimentally to predict the overall porosity and crystallinity of laser coating.

Table of Contents

Chapter 1: Introduction

Chapter 2: Characterization of Morphology and Mechanical Properties of Glass Interior Irradiated by Femtosecond Laser

Chapter 3: Transmission Welding of Glass by Femtosecond Laser: Mechanism and Fracture Strength

Chapter 4: Single Step Channeling in Glass Interior by Femtosecond Laser

Chapter 5: Laser Induced Porosity and Crystallinity Modification of a Bioactive Glass Coating on Titanium Substrates

Chapter 6: Conclusion

List of Figures

Chapter 1

Chapter 2

Chapter 3

Chapter 4

Chapter 5

List of Tables

Chapter 3

Acknowledgements

The completion of this thesis would not have been possible without help and support of a number of groups and individuals. I must of course acknowledge my advisor, Professor Y. Lawrence Yao, for his invaluable advice, guidance, and counsel throughout the pursuit of my doctoral studies. I would also like to thank my thesis committee members, Professor Jeffrey W. Kysar, Professor Chee Wei Wong, Professor James Im, and Dr. Sinisa Vukelic, for their valuable suggestions and comments. I would also like to thank Kim Kisslinger at Brookhaven National Laboratory for his guidance with sample preparation. Financial supports from the Royal Thai government and National Science Foundation are also gratefully acknowledged.

Support and friendship from both past and present colleagues in the Advanced Manufacturing Laboratory (AML), particularly Dr. Gen Satoh, Dr. Hongliang Wang, Dr. Shan-Ting Hsu, Grant Brandal, and Huade Tan are gratefully appreciated. Of course, my accomplishments would not have been possible without the love, support, and encouragement provided by my wife, mother, parents-in-law, sister-in-law, and siblings. I must express the deepest gratitude to them for standing by my side and pushing me forward while ensuring I had the freedom to make my own decisions.

This dissertation is dedicated to
my wife and our families

Chapter 1: Introduction

1.1 Introduction to Glasses

Glasses are amorphous or non-crystalline solids that possess no long-range atomic order and exhibit glass transformation behavior which gradually softens to the molten state upon heating, and solidifies to a rigid condition without crystallizing upon cooling from the liquid state. Glasses are essentially artificial or inorganic products which are traditionally formed by cooling from a melt. There are numerous glass systems which can be classified as oxide glasses, halide glasses, chalcogenide glasses, and metallic glasses. Oxide glasses are based on one or a combination of oxides (e.g. SiO_2, B_2O_3, SiO_2-Na_2O-CaO) in their compositions. Halide glasses comprise of halogen elements in combination with metal elements (e.g. BeF_2, $ZnCl_2$, ZrF_4-BaF_2-LaF_3) [1]. Chalcogenide glasses consist of chalcogen elements except oxygen combined with one or more elements from group IV and group V (e.g. As_2S_3, Ge-As-Se, Ge-Sb-Te). For metallic glasses, they are obtained by ultrafast quenching of liquid metal alloys and can be classified into metal-metalloid alloys (e.g. Pd-Si, Fe-B, Fe-Ni-P-B) and metal-metal alloys (e.g. Ni-Nb, Cu-Zn). Among inorganic glasses, more than 99% of the commercial tonnage consist of glass compositions which are oxides, and the silicate glasses are the most important ones which represent more than 95% of the tonnage of industrial glass products [2,3].

Silicate glasses are oxide glasses which have silica as a common fundamental constituent. They possess continuous random network structure. There are three classes of different oxides in silicate glass compositions such as network-forming oxides, network-modifying oxides, and intermediate oxides. The network-forming oxides (e.g. SiO_2, B_2O_3, P_2O_5), the most essential components of any glass, form highly cross-linked networks of chemical bonds. These networks are composed of oxygen polyhedra either the triangles (B_2O_3) or tetrahedral (SiO_2, P_2O_5) and the corners of each polyhedron are shared with other polyhedral. The network-modifying oxides (e.g. Na_2O, CaO, Li_2O, MgO, K_2O, BaO) alter the network structure by depolymerizing the network-forming oxides. They are usually presented as ions which are supposed to occupy random positions distributed through the structure, and located nearby non-bridging oxygen atoms (NBOs) to provide local charge neutrality [4]. The intermediate oxides (e.g. Al_2O_3, ZnO, PbO, TiO_2, ZrO_2) can act as both network formers and modifiers, depending upon the glass compositions involved. The schematic drawings of a two-dimensional structure for the representative one-component glass (vitreous silica) and the representative multicomponent glass (sodium-calcium-silicate glass) are shown in Fig. 1.1. [5]

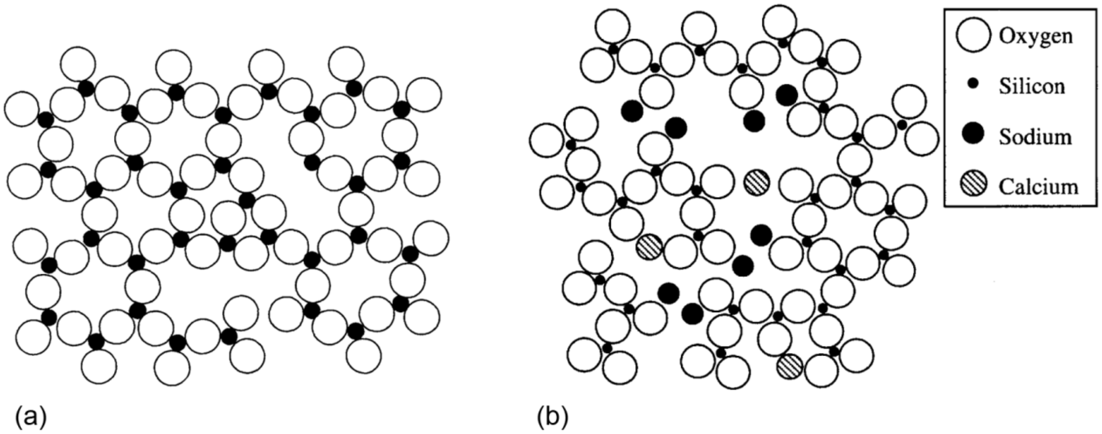

Figure 1.1: Schematic drawing of a 2D structure for (a) vitreous silica glass, and (b) sodium-calcium-silicate glass. [5]

Different oxides in glass compositions influence the properties of the silicate glasses. Silica (SiO_2), the primary network-forming oxide, improves mechanical strength, raises working temperature, and reduces the thermal expansion coefficient resulting in improving thermal shock resistance. Boric oxide (B_2O_3) enhances resistance to mechanical abrasion, adjusts the viscosity, and reduces the expansion coefficient. Phosphoric oxide (P_2O_5) lowers the chemical resistance, increases the UV and diminishes the IR transmissions. Sodium oxide (Na_2O), the most used network-modifying oxide, decreases the viscosity and chemical resistance, and increases the expansion coefficient and electrical conductivity. Calcium oxide (CaO), an essential ingredient in industrial glasses, improves the chemical resistance of sodium silicate glasses (SiO_2-Na_2O) by greatly reducing their solubility. Lithium oxide (Li_2O) increases the tendency for devitrification by reducing viscosity. Potassium oxide (K_2O) and magnesium oxide (MgO) alter the viscosity. Barium oxide (BaO) raises the refractive index. Aluminium oxide (Al_2O_3) increases its working range, improves the mechanical and chemical resistance, increases the diffusion coefficient of alkali metal ions, and decreases the tendency of unmixing. Zinc oxide (ZnO) increases the hardness of silicate glasses. Lead oxide (PbO) increases the index of refraction and increases electrical resistivity. Titanium oxide (TiO2) increases the index of refraction, enhances phase separation, and improves acid resistance. Zirconium oxide (ZrO_2) increases the tendency for devitrification, and enhances phase separation [3]. Hence, properties of silicate glasses are mainly determined by the chemical composition and, to a lesser degree, by the melting process and the subsequent thermal treatment. Silicate glasses are the most important and constitute most of the glass produced for usual applications such as construction, transportation, and lighting. There seem to be no limit in sight to what glass can offer civilization, and the silicate glasses will continue to be the material of choice for new technologies especially in optical and biomedical applications.

1.1.1 Optical Glasses

The optical properties of glasses are based on the interaction of the materials with the energy of electromagnetic waves. The components which utilize in imaging systems are mostly manufactured from glasses due to their qualified optical properties such as transmission, dispersion, and refractive index. Optical glasses have been historically developed to provide the optical engineers and scientists with a variety of materials for using in the visible portion (380 to 780 nm) of the electromagnetic spectrum. Furthermore, they have been later expanded to include new glasses for application in the ultraviolet (UV) and infrared (IR) spectral regions due to the development of intense, narrow bandwidth sources in the form of lasers and better detectors [6]. The refractive index is equal to the ratio of the speed of light in vacuum *c* to that in the material *v*, and it depends on the wavelength and normally decreases with increasing wavelength. This variation is called dispersion *D* and can be defined by the relation:

$$D = \frac{dn}{d\lambda} \tag{1.1}$$

where *n* is the refractive index and λ is the wavelength. The optical glasses must have low index variation, and are distinguished from ordinary industrial glasses where larger variations are tolerated. For many optical applications which utilize optical glasses for the formation or transmission of images, these optical glasses must have good homogeneity and a constant and well defined index. The index variation must not exceed 10^{-4} in ordinary applications, 10^{-5} in ordinary optics and 10^{-6} in glasses destined for certain scientific applications or for astronomy [3]. In imaging systems the refractive index and dispersion are the major parameters. Optical glass is classified according to its refractive index for the helium-*d* line (587.6 nm), n_d, and the Abbe number, v_d, which characterizes the dispersion. The Abbe number is given by:

$$v_d = \frac{n_d - 1}{n_F - n_C} \tag{1.2}$$

where $n_F - n_C$ is the principal dispersion. The refractive indices n_F and n_C are measured at the hydrogen *F* line (486.1 nm) and the hydrogen *D* line (656.3 nm), respectively. The refractive indices n_d and the Abbe number of optical glasses vary from approximately 1.4 to 2.4 and from

15 to 100, respectively [6]. An Abbe diagram is created by plotting the Abbe number of the material versus it refractive index. The optical glass companies usually use the Abbe diagram to illustrate these important parameters of their optical glasses as shown in Fig. 1.2. The fused silica (FS) and the borosilicate crown glass (BK-7) are widely used optical glasses that are easily observed in this diagram. Due to the fact that silica-based optical glasses are engineered materials, they can be developed to simultaneously optimize critical secondary properties (optical homogeneity, low volume light scattering, absence of striae, bubbles and particles, workability, chemical resistance, coefficient of thermal expansion, and birefringence) as well as the primary properties of refractive index and dispersion.

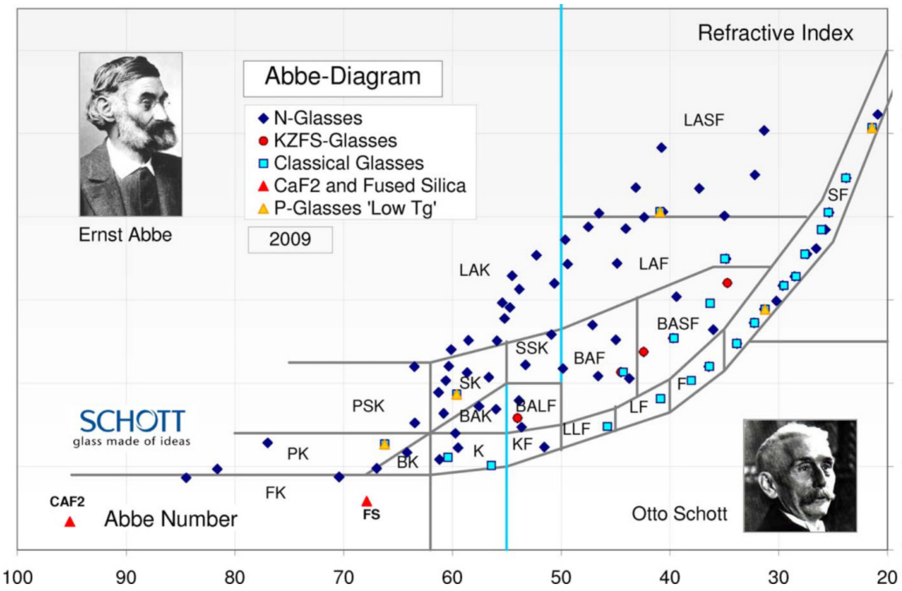

Figure 1.2: Abbe diagram of Schott's glass portfolio. [7]

1.1.2 Bioactive Glasses

Bioactive glasses are surface reactive materials that evoke a specific biological response at the interface to form a firm bond with the living tissues such as bone. Bioactive glasses have osteoiductive and osteoconductive properties that can be used for either tissue replacement or tissue regeneration of damaged bone tissues. The first bioactive glass, the 45S5 Bioglass®, was discovered by Hench in 1969. He used the Na_2O-CaO-SiO_2 diagram in phase diagram for ceramics to design the first three compositions as shown in Fig. 1.3. With a composition close to a ternary eutectic in the Na_2O-CaO-SiO_2 diagram, the 45S5 Bioglass® which contains 45% SiO_2, 24.5% Na_2O, 24.5% CaO and 6% P_2O_5 in weight percent was selected as the implanted material [8]. He found out that the implants formed a bond with bone so strong that it could not be removed without breaking the bone [9]. Its low SiO_2 content (compared to more chemically durable silicate glasses), high Na_2O and CaO content (which function as network-modifying oxides), and high CaO/P_2O_5 ratio are key compositional features that are responsible for the bioactivity of the 45S5 Bioglass [10]. There are now several types of bioactive glasses: the silicate-based bioactive glasses, borate-based bioactive glasses, and phosphate-based bioactive glasses; however, the silicate bioactive glasses tend to attract more attentions from the researchers and more widely uses as bioactive glass products and clinical trials. Bioactive glasses based on silicate compositions have been used for medical applications as synthetic bone grafts for general orthopedic, craniofacial, maxillofacial, and tissue engineering scaffolds for bone [11]. Silicate bioactive glasses could be made by both the conventional melt-quenching technique, and the low-temperature chemistry-based sol-gel processing. They mostly contain SiO_2, Na_2O, CaO, and P_2O_5. In addition to these contents, some oxides such as MgO, K_2O, or B_2O_3 could be mixed into their compositions to induce certain required properties as mentioned in section 1.1.1. Forty years of research of bioactive glasses by numerous research group surprisingly indicate that no other bioactive glass composition has been found to have better biological properties than the original 45S5 Bioglass [12].

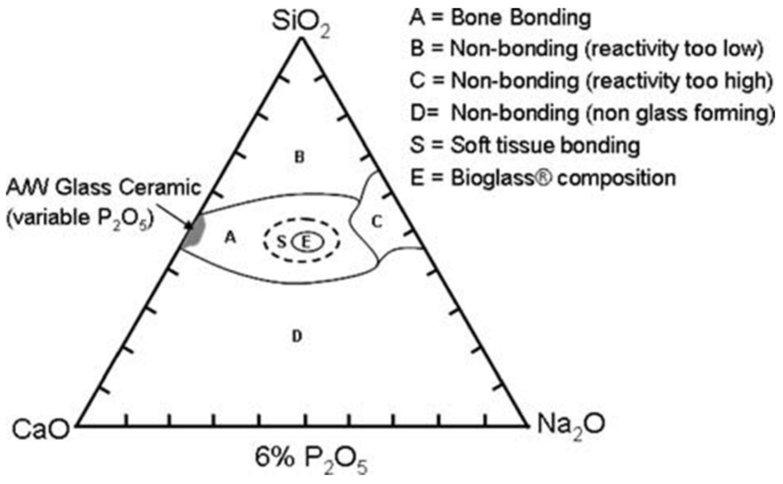

Figure 1.3: Compositional diagram of silicate-based bioactive glasses for bone bonding. [8]

1.2 Applications of Glasses

Glasses are traditionally used as windows, containers, lighting, insulation, fiber, stemware, and other hand-crafted art objects due to their transparency, luster, and durability properties. However, glasses contribute significantly in many applications of new technologies and industries. Glass is the substrate material for chemical and biological analysis, and it is an ideal for DNA and protein separation by capillary electrophoresis due to its low electrical conductivity and chemical resistance. Glass is the material of choice for use in optical detection systems because it is transparent and has low native fluorescence. It is also the material for photonic substrates in which waveguides, optical logic circuits, lasers, amplifiers, and storage devices will most certainly be integrated for enhanced function [13]. Glass is also used as sealing material for the secure and stable combination of multiple cells into a high-performance cell stack of Solid Oxide Fuel Cells (SOFC) that require hermetic sealing. According to its high transparency, glass is the main substrate used in flat panel displays (FPD) and lab-on-a-chips (LOC). Bioactive glass could be coating for prosthetic metallic implants for the repair and reconstruction of damaged bone tissues. Among the applications of glass mentioned above, three main applications which are Flat Panel Displays (FPD), Lab-on-a-Chip (LOC), and biomedical implants will be addressed here about the potential improvement if lasers are incorporated into their manufacturing processes.

1.2.1 Flat Panel Displays

In the past, display technology for televisions (TVs) and desktop computer monitors is the cathode ray tube (CRT). However, its bulky size and heavy weight are disadvantages, and CRT technology has limited applications. Nowadays, innovations for display technologies are not only making possible smaller and lighter electronic devices, bigger screens, richer colors, and remarkably high-resolution image, but also changing the way we connect with the world by making multifunctional handheld products with higher-resolution displays and lower power consumption. Flat panel displays (FDPs) have much thinner profile compared to the CRT display, and they can be used in various types of electronic systems such as cell phones, notebook computer, computer monitor, and large screen high-definition televisions (HDTVs). Flat panel display technologies can be generally classified as emissive and non-emissive [14]. Emissive displays such as plasma display panels (PDPs), organic light emitting diodes (OLEDs), and field emission displays (FEDs) emit light from each pixel with different intensities and colors to form images. Non-emissive displays such as liquid crystal displays (LCDs) and electronic paper displays (EPDs) do not emit light themselves, but modulate light in each pixel to display images. Therefore, a light source is needed for a non-emissive display such as the ambient light in a reflective display, and backlighting positioned behind the panel in a transmissive display. For example, LED TVs use light emitting diode (LED) backlighting, and LCD TVs and most other LCDs use cathode fluorescent lamp (CCFL) backlighting. The LCD is currently the dominant flat panel display technology due to the improvement of thin-film transistor (TFT) large-area fabrication technologies, liquid crystal (LC) modes, color filters (CF) and backlights, the larger size, lower weight, cheaper prices, and often lower power consumption. The OLED is regarded as the most promising technology to be able to compete with the LCD in the future according to the slimmer, lighter form and energy-efficient adjustability [15,16]. These flat panel display technologies share a common structure. They have a sandwich-like structure with light-emitting or light-modulating cells. The representative sandwich-like structure of a TFT-LCD is shown in Fig. 1.4. The two pieces of glass in the LCD are the substrates of TFT panel and CF panel. The first panel is for the vapor-deposited silicon that forms the basis for the transistor array. The second panel is for the CF materials that enable the RGB displays. A very thin layer of liquid crystal (LC) is located between these two sheets.

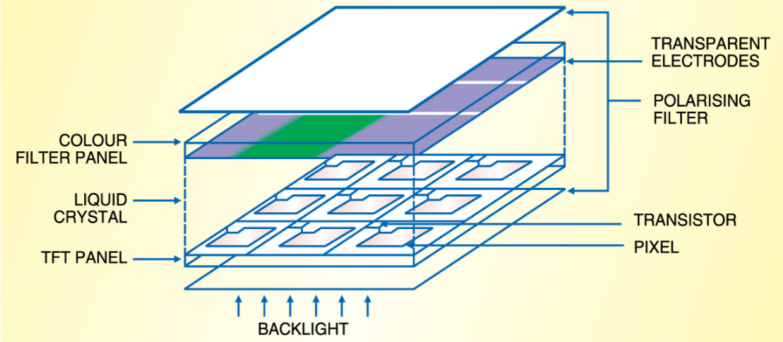

Figure 1.4: A thin-film transistor liquid-crystal display (TFT-LCD) structure. [17]

The geometry requirements for both TFT and CF substrates are essentially the same, but the chemical requirements for the TFT substrate are more rigorous, and thus LCD panel manufacturers generally require the same specifications for both products [18]. The criteria for the glass substrates are both low density and thermal expansion, and have thermo-mechanical reliability. Low density glass contributed to achieving low device weight for portable applications as well as more facile robotic handling during high-speed automation. Low coefficient of thermal expansion (CTE) brought several benefits, including the reduction of breakage due to thermal shock or gradients and minimizing dimensional distortion during transient thermal steps. With high temperature attributes and mechanical reliability throughout all the stresses of display manufacture and device lifetime, the silica-rich compositions of the substrates are required to withstand extremes of chemical processing during panel manufacturing, as well as mechanical pressures generated by customers [19].

The first glass employed in early trials for LCD applications was Pyrex®, which is low thermal expansion borosilicate glass generally used for laboratory glassware and kitchenware. However, even a small amount of sodium in its composition resulted in degrading the electronic performance of thin devices. Introduced in the early 1990s, Corning 7059, the barium borosilicate glass, was the first alkali-free glass used on a commercial scale for TFT applications. To increase chemical and thermal durability with lower density and CTE, the alkaline earth boro-aluminosilicate glasses code Corning 1737, Eagle$^{2000®}$, Eagle XG® were developed, respectively. The CTE and density desired for future substrates are quite likely to be as current substrate glasses; therefore, there are many compelling reasons to stick with alkaline earth borosilicate and aluminosilicate glasses [18,20]. The two glass substrates are assembled with different types of sealants in flat panel displays. For LCD, the main sealant is epoxy resin, and there are problems with the present manufacturing process such as viscosity increases as the solvent vaporizes, batch processes are needed for thermal curing, adherent of a jig requires a supply of consumables, and the thermocuring process causes mislocation and distortion of the glass substrates [21]. For OLED, the sealant is also epoxy, however, it does not have high reliability against moisture and oxygen permeability resulting in limited life, and the seal is quite thick [22]. Therefore, the novel process, transmission welding (TW) by ultrashort laser pulses will eliminate the need for sealant, and would offer the weld integrity leading to better lifetime of the products.

1.2.2 Lab-on-a-Chip

A lab-on-a-chip (LOC) is a device that integrates one or several laboratory functions of a single chip of only millimeters to a few square centimeters in size. LOC is sometimes called micro total analysis system (μ-TAS). When fully developed, it will contain elements for the acquisition, pretreatment, separation, post-treatment and detection of a variety of samples in a wide range of its applications in genomics, proteomics, clinical diagnostic, drug discovery, and biosensors [23]. A glass substrate has been widely used for the fabrication of lab-on-a-chip and microfluidic systems due to its excellent optical transparency and ease of electro-ormotic flow (EOF) [24]. In addition, its biocompatibility is highly desirable in the biomedical applications such as encapsulation of implantable microsystems and LOC applications. One of the most successful examples of using glass as a substrate material in lab-on-a-chip applications is the capillary electrophoresis (CE) chip, which is fabricated using the glass etching and fusion bonding techniques. Multiple sequences need to fabricate the glass microfluidic chip similar to the procedure for Si micromachining by starting from thin-film deposition, photolithography, etching, and bonding. In photolithographic process, a photomask is needed, and it is usually generated by photoablation or e-beam ablation. Etching of glass is commonly achieved by isotropic wet etch, and a one- or two-mask processes were employed for glass etching to create a channel. Two channels on the top and the bottom glass plates were etched separately using two masks. Finally, the two glass plates were aligned and bonded majorly using the thermal bonding method [25]. Beside multi-step processes for fabricating the microfluidic network, one of the major disadvantages of the techniques described up to now is the bonding step that is expensive and can introduce alignment errors [26]. Systems including photodiodes couples with a microfluidic network made of glass have been produced as shown in Fig. 1.5.

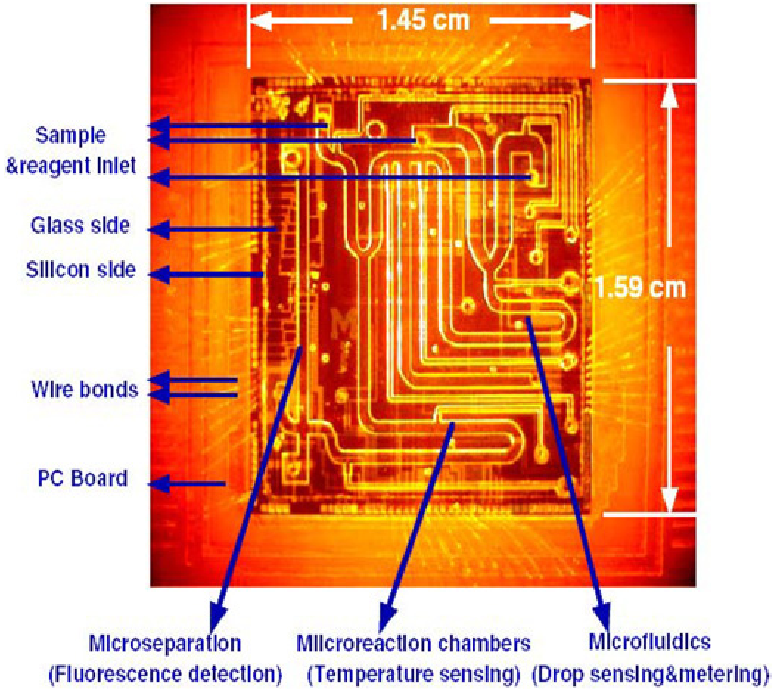

Figure 1.5: Integrated circuit including photodiodes with a microfluidic network etched in a glass substrate. [26]

Joining in some LOC applications presents a particular challenge due to requirement of maintaining precise channel alignment. Therefore, channel fabrication in the single glass piece is preferable in such cases. Currently under investigation is the use of hybrid processes. Two processes are proposed: liquid assisted femtosecond laser processing [27] and etching of material irradiated via femtosecond laser [28]. In the first process, material in the focal volume is melted via femtosecond laser and removed by liquid. The second process consists of etching previously laser treated material. Both methods are based on thermal accumulation and involve several steps which make fabrication cumbersome. Based on an explosive plasma expansion mechanisam, when a femtosecond laser pulse is deposited into the glass, microexplosion in the focal volume will create a void [29], and there is potential for channel fabrication through applying a train of connected voids generated from single femtosecond laser pulses.

1.2.3 Biomedical Implants

Implants are biomedical devices which are used for replacing missing biological hard tissues, supporting damaged biological hard tissues, or enhancing existing biological hard tissues. Biomedical Implants are artificial devices, and are usually called “prostheses”. The first basic requirement for any materials to be selected as prostheses for placing in the living body is that it should be biocompatible and not cause any adverse reaction in the body. The damaged hard tissue is often a joint which is formed by the ends of two or more bones that are connected by thick tissues. The bone ends of a joint are covered with a smooth layer called cartilage, and normal cartilage allows nearly frictionless and pain-free movement. When the cartilage is damaged or diseased by arthritis, joints become stiff and painful. If the extent of damage to the joint is severed, and other treatment options do not relieve the pain and disability, the damaged joint or the arthritic will need to be removed and replaced by the artificial joint or the prosthesis. The prosthesis is generally composed of two parts: a metal piece that fits closely into a matching sturdy plastic piece. The plastic material is durable, wear resistant (polyethylene). For metal piece, titanium (Ti), its alloys (Ti-6Al-4V), alloys of cobalt and chrome (Co-Cr-Mo), and stainless steel (316L) which have excellent hard tissue biocompatibilities are used. Joint replacements can be implanted without cement when the prosthesis and the bone are designed to fit and lock together directly. On one hand, bonding between bone and biocompatible metals is biomechanical binding or biomechanical interlocking, which bone ingrowth occurs into micrometer-sized surface irregularities of the implants; however, its bonding to bone does not meet the clinical expectation. Biomechanical anchorage takes weeks to develop. On the other hand, bonding between bioactive glass and bone is biochemical bonding, which is strong, and the anchorage is accomplished within a relatively short period of time. However, the limited mechanical strength and low toughness of bioactive glasses have prevented their use as load bearing devices [30]. Therefore, to apply the bioactive glass as a coating on a mechanically tough substrate can solve the problem mentioned above. Biocompatible metal implants coated with bioactive glass thus possess both anchorage mechanisms because coated surfaces are normally rough which can facilitate the biomechanical anchorage, and coated materials accommodate biochemical bonding. The schematic diagram of artificial hip joints that consist of an articulating bearing (femoral head and cup) and stem, and the porous coating on the proximal portion of the femoral and hip stem are depicted in Fig. 1.6.

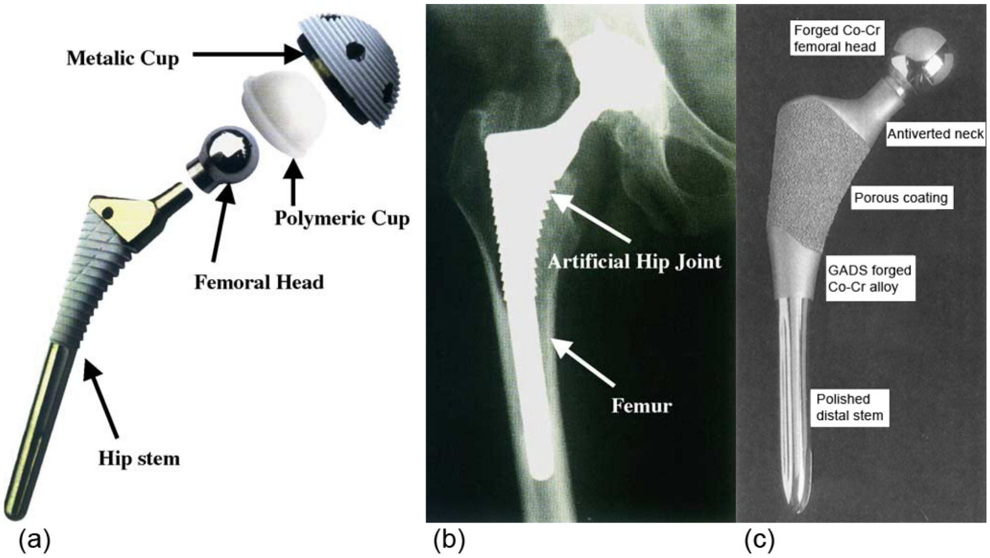

Figure 1.6: (a)(b) Schematic diagram of artificial hip joint and its position after surgery [31]**, and (c) porous coated cobalt alloy total hip replacement implant.** [32]

The bioactive glass coating has increased bone-implant contact in the early growth period according to the rates of bioactivity of bioactive glasses, and the early bone ongrowth is known to increase primary implant fixation and reduce the risk of early implant failure [33]. However, after the first discovery of bioactive glass, there is no other bioactive glass composition that has higher rate of bioactivity than 45S5 Bioglass®, and there is also no report of successful coating of this material either. Therefore, the potential of laser induced functionally graded coating of 45S5 Bioglass would be crucial to explore.

1.3 Laser Processing of Glasses

1.3.1 Laser Absorption in Glass Materials

The propagation of an electromagnetic wave in a material produces a displacement of electric charge. For a sinusoidal wave, the change of speed and intensity are contained in the complex index of refraction n^* which is given by $n^* = n - ik$; where n is the refractive index and k is the absorption index. From the absorption index, a function of the wavelength λ, and the absorption coefficient α is defined as:

$$\alpha = \frac{4\pi k}{\lambda} \tag{1.3}$$

For a homogeneous material, the relative fraction of the light intensity absorbed in traversing thickness dx depends on α. Thus, the attenuation of the light traversing a material of thickness x is given by the Beer-Lambert law: $I = I_0 \exp(-\alpha x)$. Since at the entrance surface a part of the beam is reflected, and at the exit surface another reflection also occurs, the transmitted beam through the glass plate has the intensity:

$$I_t = I_0 (1 - r)^2 exp(-\alpha x) \tag{1.4}$$

where I_t is the transmitted intensity, I_0 is the incident intensity, and r is the reflectivity. Derived from Fresnel's formula which describes the relation between the reflectivity r and the refractive index *n*, the reflected intensity of the beam incident perpendicularly upon a dielectric material like glass plate with the refractive index *n* is:

$$r = \left[\frac{n-1}{n+1}\right]^2 \tag{1.5}$$

The change in the intensity of a light beam passing through a glass plate is illustrated in Fig. 1.7. From Eq. (1.5), the reflectivity of a light beam on the ordinary glass surface is about 4% per surface.

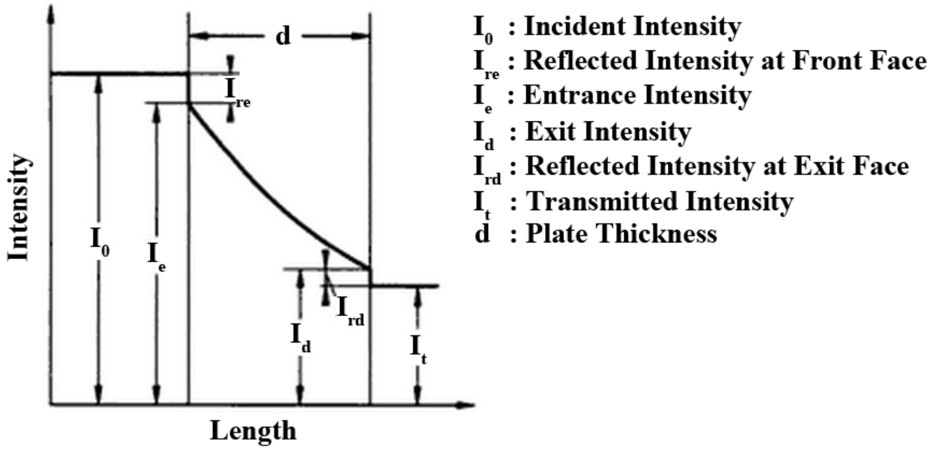

Figure 1.7: Change in the intensity of a light beam passing through a glass plate [6]

When the laser radiation hits a material, the processes taking place depend on the amount of deposited laser energy. This energy and its spatial and temporal distribution determine what kind of material modification will occur, and the main laser-solid interaction process is the excitation of electrons from their equilibrium states to some excited states by absorption of photons [34]. The typical single photon absorption process is the linear photon absorption mechanism that obeys the Beer-Lambert Law. The capacity of a material to absorb laser radiation depends mainly on the electronic structure of the material and the wavelength of radiation. Glass materials usually offer high transmission throughout the entire visible spectrum and beyond in the near ultraviolet and near infrared ranges as shown in Fig. 1.8.

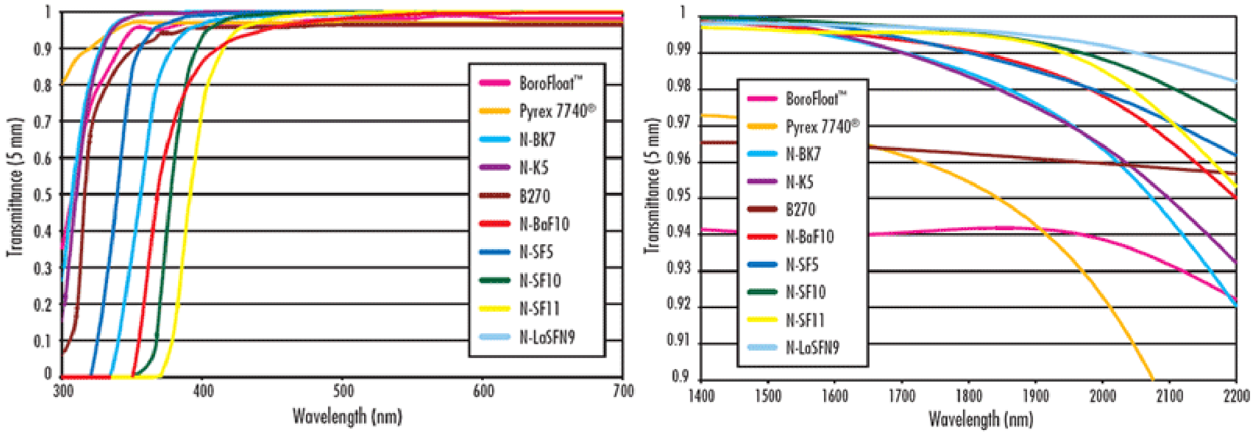

Figure 1.8: Transmittance curves of sample optical glasses. [35]

Refer to the transmission curves in Fig. 1.8, and the reflectivity from Eq. (1.5), most of the silicate glasses exhibit high transmission resulting in very low absorption over almost all conventional laser wavelengths. Unless radiation by extremely high power laser, there will be nothing happen or it would be too difficult to induce any modification or integration of silicate glasses by conventional lasers based on a linear absorption mechanism.

1.3.2 Introduction to Femtosecond Laser

A femtosecond laser is a laser which emits optical pulses with durations between a few femtoseconds and hundreds of femtoseconds, and it essentially belongs to the category of ultrashort pulse or ultrafast lasers. Femtosecond laser pulses can be generated directly from a wide variety of lasers with wavelengths ranging from the ultraviolet to the infrared. With very few exceptions, the generation of ultrashort laser pulses relies on a mode locking technique. A laser is typically constructed with a pair of mirrors separated by a distance *L* which enclose a gain medium and other components. The generation of ultrashort laser pulses is based on the confinement of the energy in the cavity into a small spatial region [36]. A single pulse bounces back and forth between the mirrors at the velocity of light, *c*, and the output beam arises from partial transmission of the intracavity pulse through the output coupler. Thus, the output beam consists of a train of replicas of the cavity pulse separated by *2L* in space or *2L/c* in time. Two conditions generally govern the frequency spectrum of a laser. First, the overall envelope of the spectrum is determined by the emission profile of the laser medium and by the characteristics of any wavelength selective element within the cavity. Second, for each transverse mode the cavity allows oscillations only at discrete set of frequencies, known as the longitudinal modes of the cavity as shown in Fig. 1.9 (a). In general, the longitudinal mode in the laser cavity will oscillate independently, and the phases of these modes are different from each other. Consequently, the output from a laser is temporally fluctuated to a random intensity (in case that there are only a few oscillating modes) or the output is averaged to a near-constant intensity: CW (incase that there are many thousands of modes). The total electric field *E(t)* resulting from such a multimode oscillation at a fixed point in space is given by:

$$E(t) = \sum_{n=0}^{N-1} E_n \, sin[2\pi(v_0 + n\delta v)t + \varphi_n(t)] \tag{1.6}$$

where *N* is the number of oscillating modes, $\varphi_n(t)$ is the phase of the nth mode and v_0 is the lowest-frequency mode above the lasing threshold. The average laser power output *P(t)* is proportional to the square of the total electric field. Mode locking refers to the use of a modulating optical element to lock together the phases of *N* longitudinal modes existing in a cavity and therefore to produce a train of pulses with increasing peak power and shorter pulses on the order of picoseconds or femtoseconds. To simplify the analysis in mode-locking condition, the identical amplitudes $E_n = E_0$ for all modes are assume, and the phases of all modes are set to zero; therefore, the summation of Eq. (1.6) then yields:

$$E(t) = E_0 sin\left[2\pi\left(\nu_0 + \frac{N-1}{2}\delta\nu\right)t\right]\frac{sin(N\pi\delta\nu t)}{sin(\pi\delta\nu t)} \tag{1.7}$$

The resulting electric field consists of a rapid oscillating part at the light central frequency $\nu_0 + \frac{N-1}{2}\delta\nu$ with the envelope $\left|\frac{\sin(N\pi\delta\nu t)}{\sin(\pi\delta\nu t)}\right|$ oscillating with $\delta\nu = c/2L$. The example of four oscillating modes in mode-locking condition is illustrated in Fig. 1.9 (c).

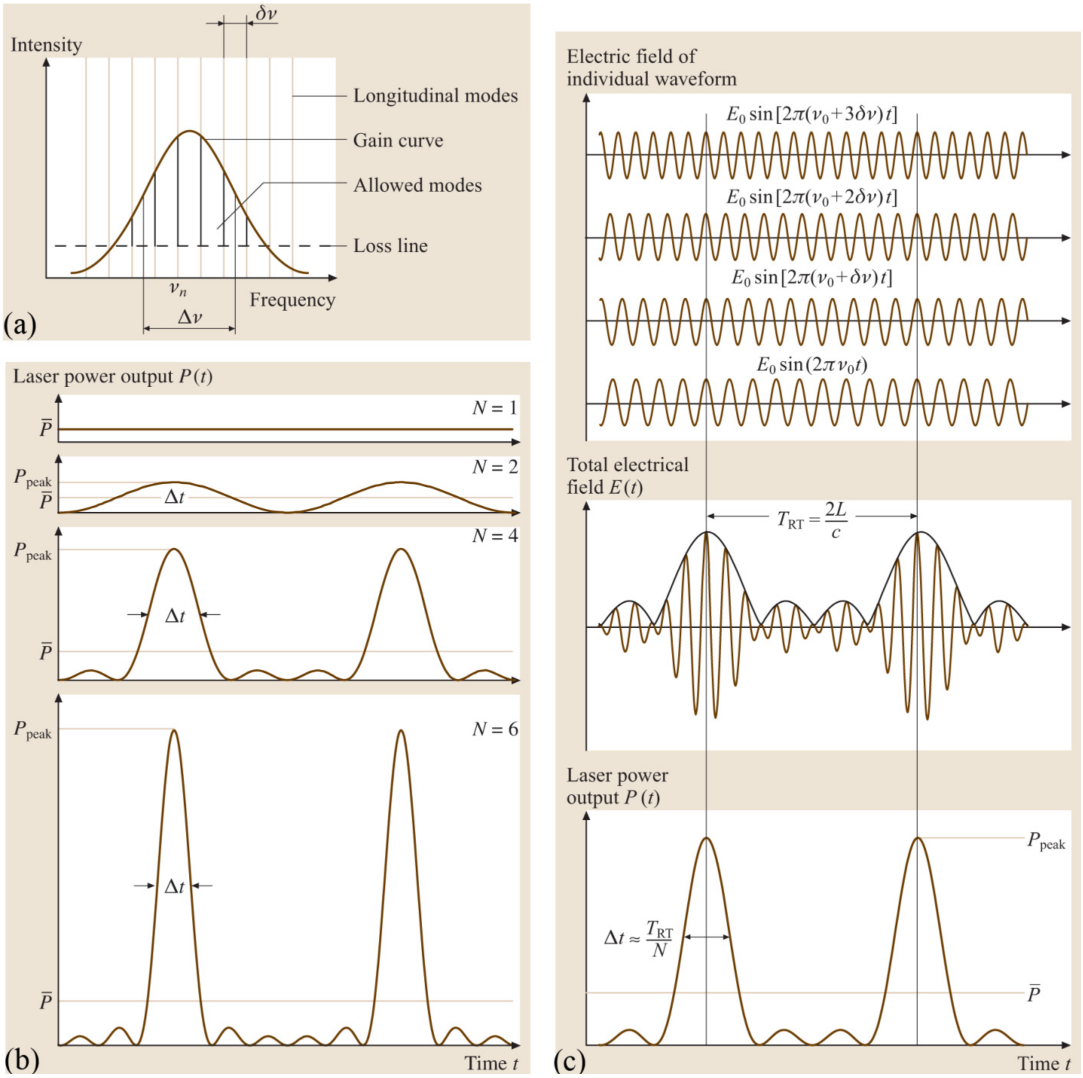

Figure 1.9: (a) Longitudinal modes in a laser cavity, (b) comparison of one, two-, four- and six-mode cases, and (c) superposition of four sine wave with equal amplitude E_0, differing in frequency by $\delta\nu$. The electric field of individual waveforms, the total electric field *E(t)*, its envelope and the output power *P(t)* are shown.
[36]

Averaging the fast oscillation ν_c the output power $P(t)$ is proportional to the average power of one wave P_0 and is expressed by:

$$P(t) = P_0 \left[\frac{sin(N\pi\delta v t)}{sin(\pi\delta v t)}\right]^2 \tag{1.8}$$

In conclusion, the properties of laser pulses generated by mode locking technique are the power is emitted in the form of a train of pulses with a period corresponding to the cavity round-trip time $T_{RT} = 1/\delta v$, the peak power P_{Peak} increases quadratically with the number N of modes locked together: $P_{Peak} = N^2 P_0$, and the FWHM pulse duration Δt decreases linearly with the number N of mode locked together or equivalent is approximately the inverse of the gain bandwidth Δv: $\Delta t \approx \frac{T_{RT}}{N} = \frac{1}{N\delta v} = \frac{1}{\Delta v}$. The increase in the number of modes leads to an increase in the peak power and a decrease in pulse duration as shown in Fig. 1.9 (b). There are a number of methods for generating a mode-locked ultrashort pulsed beam such as electro-optical, acoustic-optical, and saturable absorber mode-locking. To achieve ultrashort pulse, the laser medium is required to have high bandwidth. Due to its high bandwidth of about 128 THz in Ti:sapphire laser medium, the common ultrashort pulse laser technology is Ti-sapphire lasers with the central wavelength about 800 nm. A mode-locked Ti:sapphire pulsed laser oscillator usually outputs low power ultrashort pulses. To generate the high power ultrashort pulses, the integrated Ti:sapphire Regenerative Amplifier system is needed. In this system, the lower power ultrashort pulse from the oscillator is delivered to the pulse stretcher, regenerative amplifier, and pulse compressor, respectively to produce the high power compressed pulse through Chirped Pulse Amplification process as illustrated in Fig. 1.10.

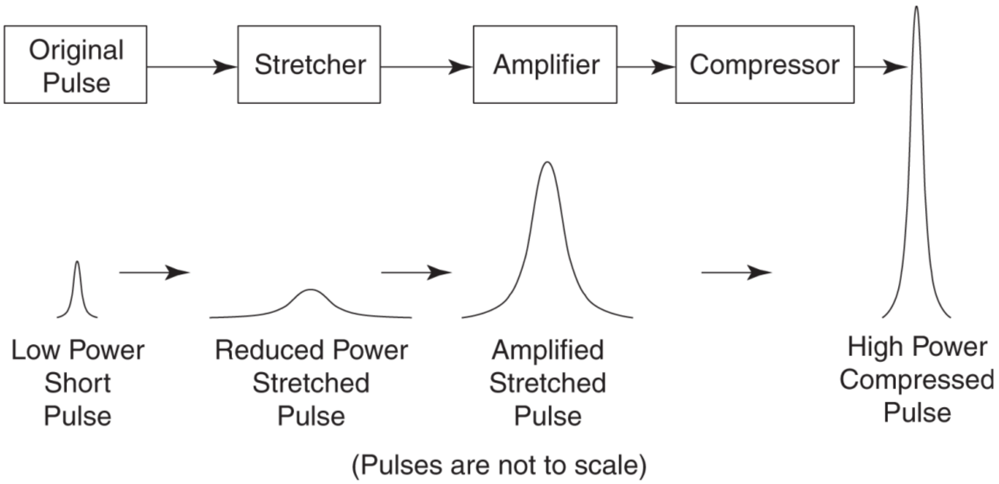

Figure 1.10: Principle of Chirped Pulse Amplification

1.3.3 Nonlinear Absorption Mechanisms

Light or photon absorptions can be categorized into linear process and nonlinear process. Linear photon absorption obeys the Beer-Lambert Law, which states, "The absorption of a specific wavelength transmitted through a material is a function of material path length and is independent of incident intensity." For femtosecond laser pulse width, which is extremely short, the laser power in the pulse duration is significantly higher, or several orders of magnitude larger than that of conventional nanosecond laser pulses; therefore, nonlinear absorption becomes significant for all materials, no mattering it is opaque or transparent to its wavelength [37]. For the interaction between visible or near-infrared light with glasses, under normal conditions (e.g. continuous low power illuminations), glasses will transmit almost all of the light through as shown in Fig. 1.8. Therefore, in a transparent material like glass, there is no linear absorption of the incident laser light. For any modification of glass to occur, a nonlinear absorption mechanism must deposit laser energy into the material by promoting electrons from the valence band to the conduction band. Photoionization and avalanche ionization are two classes of nonlinear excitation mechanisms. Because the probability of nonlinear absorption increases strongly with growing laser intensity, photoionization and avalanche ionization occur in femtosecond laser irradiation. Photoionization excites the electron from the valence to the conduction band; seed electrons are thus generated. There are two regimes of photoionization: the multiphoton ionization (MPI) regime and tunnel ionization (TI) regime [38]. In multiphoton ionization, a bound electron in valence band absorbs enough photons so that the number of photons, *N*, times the photon energy, *hv*, is greater than ionization potential (band-gap), E_g, of material, then it is promoted to be a free electron in conduction band as shown in Fig. 1.11 (a). In tunneling ionization, a strong electric field distorts the Coulomb well so that a bound electron would escape through the short barrier as shown in Fig. 1.11 (b).

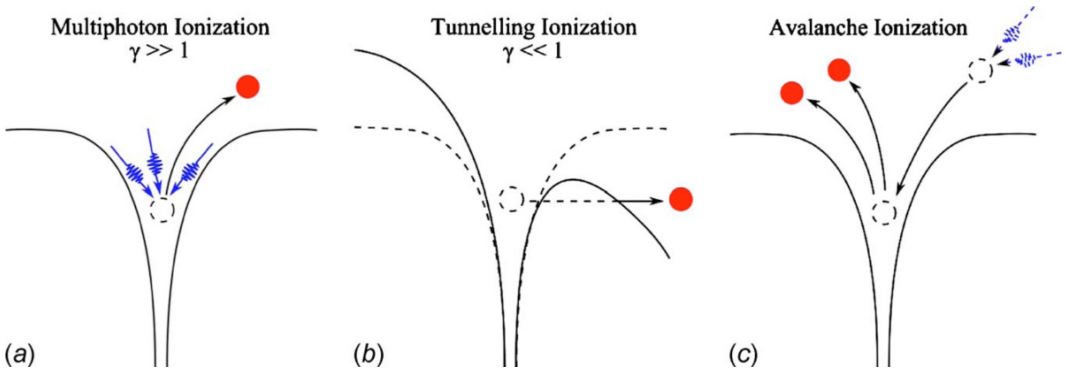

Figure 1.11: Schematic diagram of ionization induced by femtosecond-laser irradiation: photoionization as function of Keldysh adiabatic parameter : (a) multiphoton ionization, (b) tunneling ionization, and (c) avalanche ionization. [39]

Keldysh [40] showed that the two regimes could be described within the same framework. He introduced the adiabatic parameter called Keldysh parameter, γ, that determines which of two regimes will take place. He derived this parameter from the consideration that the ease or difficulty of tunneling can be expressed as the ratio of “the time it takes for the electron to tunnel out the potential barrier while the potential is bent down” to “half of the laser cycle time”.

Therefore, the Keldysh parameter represents the ratio between the frequency of the laser light, ω, and the frequency of an electron tunneling through a potential barrier, ω_t, and is expressed as:

$$\gamma = \frac{\omega}{\omega_t} = \frac{\omega}{e}\sqrt{\frac{mcn\varepsilon_0 E_g}{I}} = \frac{1}{2K_0 F} \tag{1.9}$$

where m and e are the mass and charge of an electron, c is the speed of light, n is the refractive index of the material, E_g is the band-gap of the material, ε_0 is the permittivity of free space, I is the laser intensity, F represents the reduced electric wave field, and K_0 is a process parameter. When $\gamma >> 1$, or the laser intensity (photon flux) is above 10^{13} W/cm^2 [37], the multiphoton ionization dominates, while $\gamma << 1$, or the intensity is higher than 10^{15} W/cm^2 [37], the tunneling ionization dominates. For a general multiphoton ionization process in which N photons are absorbed, the ionization rate can be expressed as [41]:

$$P(I) = \delta_N \left(\frac{I}{\hbar\omega}\right)^N N_S \tag{1.10}$$

where δ_N is the cross section of N-photon ionization with a unit of $cm^{2N}s^{N-1}$, which refers to the probability of a particle (here an electron) being emitted, $\hbar$ is the reduced Planck constant defined as $\hbar = h/2\pi$, ω is the laser frequency given by $\omega = 2\pi c/\lambda$, and N_S is the solid atom density. For transparent dielectric materials such as glasses, multiphoton ionization is an important mechanism to produce initial seed electrons (free electrons) for avalanche ionization.

In avalanche ionization, two sequences, started with free carrier absorption of a seed electron and followed by impact ionization to produce two free electrons as shown in Fig. 1.11 (c). Free carrier absorption is a phenomenon that a free electron in conduction band absorbs photons sequentially and moves to higher energy states. When a free electron at higher energy states (conduction band minimum + band-gap) collides with a bound electron in valence band, it results in two free electrons with band energy near the conduction band minimum. This process is called impact ionization. In femtosecond laser micromachining inside glass, the photoionization (either multiphoton or tunneling ionization) and the avalanche ionization work together and can be called as avalanche photoionization. The process iterates and produces a critical density of free electrons in the cloud necessary for plasma formation and the ablation process. The electron density distribution is governed by the Fokker-Planck equation [42]:

$$\frac{\partial N(E_k,t)}{\partial t}+\frac{\partial}{\partial E_k}\left[R_J(E_k,t)N(\varepsilon,t)-\alpha(E_k)E_pN(E_k,t)-D(E_k,t)\frac{\partial N(E_k,t)}{\partial E_k}\right]=S(E_k,t) \quad (1.11)$$

where N is the free electron density distribution, E_k is the kinetic energy of an electron, E_p is the phonon energy, t is the time, R_J is the electron heating rate, α is the rate of electron-photon energy transfer to the lattice, D is the diffusion coefficient, and S represents sources and sinks of electrons. The term $R_J(E_k,t)N(\varepsilon,t)$ describes the Joule heating, which causes electron-electron collisional ionization (avalanche); $\alpha(E_k)E_pN(E_k,t)$ is the energy transferred to the lattice; $D(E_k,t)\frac{\partial N(E_k,t)}{\partial E_k}$ accounts for the electron energy diffusion. The nonlinear absorption nature of femtosecond laser pulses, thus enables the modification and integration of glass materials.

1.3.4 Femtosecond Laser Matter Interaction

For conventional laser processing (from near infrared to near ultraviolet), photons are absorbed by electrons through inter- and intra-band electronic transitions. Therefore, the laser beam induces a non-equilibrium electronic distribution that thermalizes via electron–electron and electron–phonon interactions [43]. In general, the excitation energy is dissipated into heat within a time which is short compared to any other time involved in the process. As a consequence, with low to medium intensity of conventional lasers (either continuous wave or nanosecond pulses), the laser beam can just be considered as a heat source which induces a temperature rise on the surface and within the bulk of the material. The temperature distribution is determined by optical and thermal properties of the material and, near phase transitions, by transformation energies for crystallization, melting, boiling, etc. When the laser-light intensity is increased, material vaporization (vapor plume) or plasma plume would take place resulting in removing of the material from the surface [44]. An overview of the various applications and parameter regimes employed in laser processing is illustrated in Fig. 1.12.

For material processing with femtosecond laser pulses, the dominant absorption is nonlinear process, and when a significant number of valence band electrons are ionized through avalanche photoionization, or when free electron density reaches the critical density (plasma critical density), plasma is then formed in the material. Critical density is the free electron density at which the plasma frequency equals to the laser frequency. The plasma frequency, ω_p, is given by [45]:

$$\omega_p = \sqrt{\frac{4\pi N_e e^2}{m_e}} \tag{1.12}$$

where N_e is the electron density, e is the electron charge, and m_e is the electron mass. The laser frequency, $\omega = 2\pi c/\lambda$, where c is the speed of light and λ is the laser wavelength. Therefore, the critical density, N_{cr}, can be expressed by:

$$N_{cr} = \frac{m_e \omega^2}{4\pi e^2} = \frac{\pi m_e c^2}{e^2 \lambda^2} \tag{1.13}$$

The number of the critical density is on the order of 10^{21} cm^{-3} [38,45]. Plasma becomes strongly

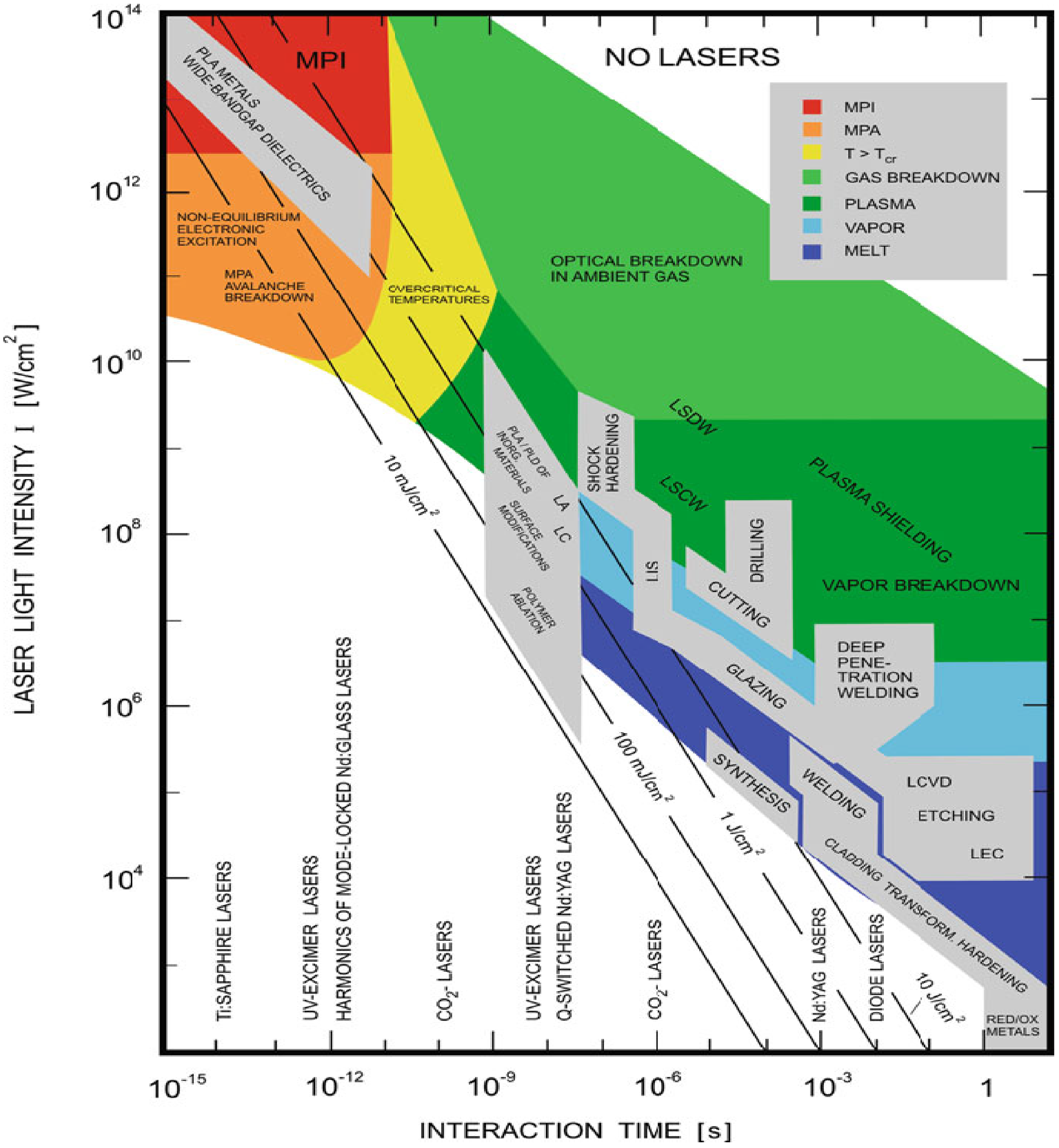

Figure 1.12: Applications of lasers in materials processing. [44]

absorbing the laser pulse energy leading to the transfer of the energy from hot plasma to the lattice. The timescale of the physical phenomena associated with the interaction of a femtosecond laser pulse with transparent materials is shown in Fig. 1.13. The dissipation mechanisms are the combination of thermal diffusion and shockwave emission. It is widely assumed that the ablation starts when the free electron density reaches the critical density. With

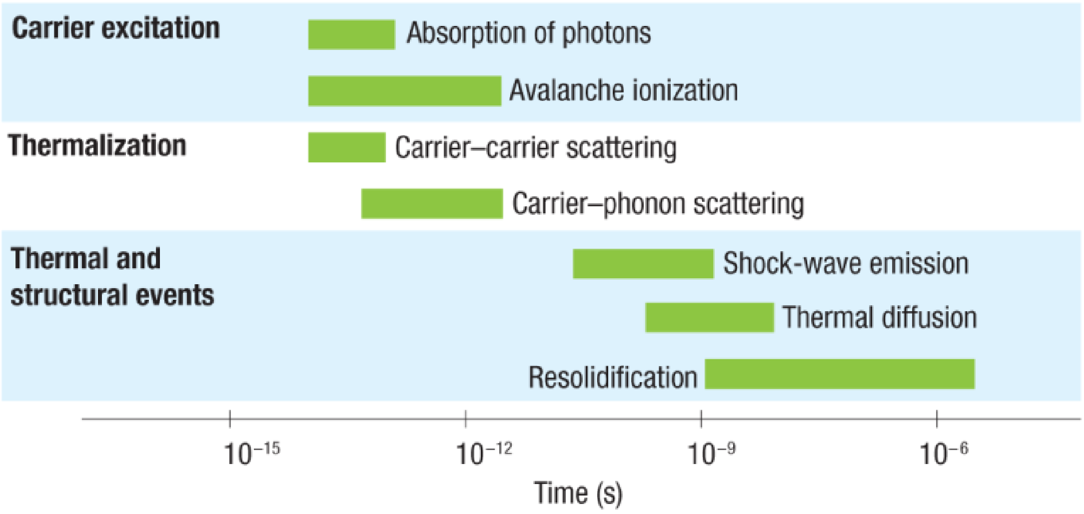

Figure 1.13: Timescale of the physical phenomena associated with the interaction of a femtosecond laser pulse with transparent materials. [46]

all types of materials, ablation is strongly non-stationary and starts only after approximately one to several ten picoseconds. In metals, femtosecond laser pulses generate a hot electron gas in a ‘cold’ lattice. This transient nonequilibrium is described by the two-temperature model (TTM). In semiconductors, hot electron-hole pairs are generated by single-photon and/or avalanche photoionization. In dielectrics, avalanche photoionization results in the formation of plasma within a thin surface layer. At very high intensities, Coulomb explosion is observed [44]. Since the energy input is terminated before the modification or the removal of material occurs, the femtosecond laser results appear, in most cases, much cleaner, better defined, and less heat affected zone (HAZ) than those obtained with the conventional laser pulses [43]. For metals and semiconductors, the laser-matter interaction, the modification, and the removal of materials could only take place at the surface. For the transparent dielectrics such as glasses, it is desirable to induce modification either at the surface or inside the bulk depending on the focusing parameters.

1.3.5 Effects of Focusing Parameters

As mentioned earlier, there is no linear absorption of the incident laser light in a transparent material like glass. Using femtosecond laser pulses, the photon absorption in glass is a nonlinear process. Nonlinear absorption take places spatially in the region in which there are extremely high laser intensities, and that region has to be in the vicinity of the focusing plane by an optic lens. Therefore, this nonlinear absorption mechanism enables the structural modification in the interior of transparent bulk glasses. In general case of laser processing by linear absorption mechanism, the laser beam is focused on the surface of a material, and the calculation and adjustment of the focal area or focal spot size are done before actual processing. The absorption will be occurred mainly inside the focal area and over the penetration depth of the laser beam. However, in case of nonlinear absorption of a femtosecond laser pulse inside a transparent material like glass, the absorption could be estimated as the focal volume. Quantification of the focal volume is done primarily in the field of fluorescence correlation spectroscopy (FCS), where nonlinear absorption properties of femtosecond laser pulses are utilized for imaging the interior of biological systems. The theoretical basis comes from the theory of electromagnetic diffraction in optical systems [47]. The illumination point spread function, IPSF(x,y,z), describes intensity everywhere in space near the focus. IPSF can be calculated based on the work of Richards and Wolf [48], and fits of the lateral and axial intensity squared profiles to a Gaussian function. By approximating the IPSF as a three-dimensional Gaussian volume, analytical integration over all space yields the focal volume of Gaussian ellipsoid shape with the estimated diffraction-limited lateral (ω_{xy}) and axial (ω_z) *1/e* radii of IPSF [49]. This Gaussian ellipsoid focal volume provides a quite good start to predict the ratios of longitudinal and lateral radii of the affected region of glass irradiated by femtosecond laser pulses [50]. Although the theoretically predicted major and minor radii of the focal volume ellipsoid are multiple times smaller than the radii of the affected volume observed experimentally, the ratios are relatively close and it indicates that the focal and affected volumes are indeed in proportion. Tight focusing is related to the high numerical aperture (NA) of focusing lens and in correlation with amount of laser energy deposited into the focal volume. Morphology is a function of focusing parameters, NA of the objective lens in particular. NA governs the shape of the affected region, and is inversely proportional to the feature aspect ratio [51]. The role of NA on the nature of structural changes is quite significant, and it depends on the shape and size of features required in each application, the focusing lens with appropriate NA would be selected accordingly. The focal distance of each focusing lens is fixed; however, by adjusting the position of the material with respect to the lens, the location of the feature in the interior of glass sample can be controlled. Since the laser beam that is focused inside the glass plate propagates through both air and glass, the effect of the longitudinal aberration due to the refractive mismatch of two different mediums would be unavoidable [52]. This aberration affects both shape and size of the feature inside glass, and the deeper the focusing depth from an air-glass interface resulting in the larger longitudinal aberration range. Therefore, understanding the effects of focusing parameters on the results of femtosecond laser induced modification of glasses would be crucial to predict and get the desirable finished products.

1.4 Glass Powder Sintering

Sintering is a thermal treatment for bonding particles into a coherent, predominantly solid structure via mass transport events that often occur on the atomic scale. The bonding leads to improved strength and lower system energy [53]. A sintering process is traditionally viewed as occurring in three stages. The initial stage of sintering begins with the formation of contacts in a loose powder stack. It becomes interparticle welds or neck growth between contacting particles that grow with time at the sintering temperature. In the intermediate state, the pore network gradually disconnects itself as channels achieve unstable shapes and close. At the onset of the final stage the pore network has completed its disconnection and the pores collapse into isolated spherical pores. In this final stage, these isolated pores shrink and mostly disappear. All three stages are accompanied by densification such as the macroscopic shrinkage of the body [54]. The reduction in surface energy is the thermodynamic driving force for sintering. The total interfacial energy of a powder compact is expressed as γA, where γ is the specific surface (interface) energy and A is the total surface (interface) area of the compact. The reduction of the total energy can be expressed as [55]:

$$\mathit{\Delta}(\gamma A) = \mathit{\Delta}\gamma A + \gamma \mathit{\Delta} A \tag{1.14}$$

The change in interfacial energy ($\mathit{\Delta}\gamma$) is due to densification and the change in interfacial area is because of grain coarsening. However, the actual occurrence of sinter binding requires transport of matter. In crystalline solids, matter transport occurs by diffusion of atoms, ions, or molecules along definite mechanisms or paths such as surface diffusion, lattice diffusion, vapor transport, grain boundary diffusion, and plastic flow. In glass (or amorphous materials), viscous flow is the dominant sintering mechanism due to densification of glass proceeds more rapidly by viscous flow than by diffusion [56]. A viscous material like glass follows the behavior of a Newtonian fluid. Viscous flow, where the particles coalesce at a rate that depends on the particle size and material viscosity, η, is a thermally activated process, and is characterized by a deviation from the Arrhenius-type behavior:

$$\eta(T) = \eta_0 exp(\frac{Q}{RT}) \tag{1.15}$$

where Q is activation energy, T is temperature, R is the molar gas constant, and η_0 is approximately a constant. The activation energy of viscosity Q changes from a high value at low temperatures in the glassy state to a low value at high temperatures in the super cooled liquid state. When the temperature is higher than the glass transition temperature, $T > T_g$, the activation energy of viscosity is low because most of its joining bonds in glass has broken, which facilitates flow [57]. Viscous sintering models based on an energy balance concept have been developed to account for the kinetics of sintering. The energy released by the decrease of surface area is used for viscous flow, which is responsible for the mass transport that produces densification. Frenkel [58] first developed the viscous sintering model for the initial stage to calculate the shrinkage rate of two equal particles. Mackenzie and Shuttleworth [59] developed the model for the final stage by considering a matrix with spherical monodispersed pores. Scherer [60] developed the viscous sintering model for the intermediate stage by considering a geometric array of sintering particles that mimicked the structure of dry gels. These viscous sintering models provide an excellent description of the sintering of glass. The major variables which determine sinterability and the sintered microstructure of a powder compact can be divided into two categories: material variables and process variables. Material variables relate to raw materials including chemical composition of powder compact, powder size, powder shape, powder size distribution, degree of powder agglomeration, and etc. The process variables are mostly thermodynamic variables such as temperature, time, atmosphere, pressure, heating and cooling rate [55]. In case of laser induced sintering, the effects of process variables that involve the temperature, time, heating and cooling rate on sinterability, morphology, and microstructure of glass powder would be interesting to examine.

1.5 Crystallization in Glasses

Glasses are amorphous solids that are typically obtained upon rapid cooling or quenching from the melt to the temperatures below the glass transition to prevent crystallization or to avoid significant nucleation and growth of the more stable ordered phases. Typical glass-forming liquids such as silicate melts are commonly characterized by their relatively high viscosities ($\eta >$ 100 Pa·s) at the apparent melting point or liquidus temperature, and by a steep increase of viscosity with decreasing temperature. These properties favor the process of transformation of a liquid into a glass [61]. The cooling rate that produces the lowest detectable degree of crystallization is called the critical cooling rate for glass formation. It represents the least time required to form a given degree of crystallinity. For two melts of identical size, the melt with the smaller critical cooling rate has better glass forming ability. Currently, the quenching rate up to $10^4 – 10^6$ Ks^{-1} is possible to achieve for silicate glasses [62]. On one hand, any melt forms a glass if rapidly cooled so that insufficient time is provided to allow reorganization of the structure into crystalline arrangements. On the other hand, most glass-forming melts can be crystallized if holding at the temperature just below its liquidus point long enough for structural arrangements to occur. Crystallization, which actually refers to a combination of two individual kinetic processes: nucleation and crystal growth respectively, can occur either on cooling or reheating. When a glass is heated for sufficiently large time intervals to temperatures within or above the glass transition range, crystallization or "devitrification" readily starts either from the surface (heterogeneous) or bulk (homogeneous) nucleation. Heterogeneous nucleation starts at the interface boundaries and surfaces and is catalyzed by the presence of foreign impurities and nucleating agents. Homogeneous nucleation is a stochastic process occurring with the same probability in any given volume, and nucleus forms in the absence of any phase inhomogeneity, surface borders, or interfacial boundaries. The general expression of the nucleation rate is an exponential function of the thermodynamic and kinetic barriers. The thermodynamic barrier involves the net free energy change in the system when a nucleus is formed. The kinetic barrier is the activation energy required for an atom to cross the liquid-nucleus interface. It involves the breaking of bonds with its nearest neighbors and certainly some realignment into the more ordered structure within the surface of the nucleus. The nucleation rate either the steady-state or time-dependent, I, can be expressed as [5,62]:

$$I = I_0 exp\left(-\frac{W^* + \mathit{\Delta} G_D}{k_B T}\right) \tag{1.16}$$

where I_0 is a constant, W^* and $\mathit{\Delta} G_D$ are the thermodynamic and kinetic free energy barriers to nucleation, respectively, k_B is the Boltzmann constant, and T is the absolute temperature. For the crystal growth rate, U, it general equation is given by the expression [5]:

$$U = a_0 v \; exp\left(-\frac{\mathit{\Delta} E}{k_B T}\right)\left[1 - exp\left(\frac{\mathit{\Delta} G}{k_B T}\right)\right] \tag{1.17}$$

where a_0 is the interatomic separation distance, v is the vibrational frequency, and $\mathit{\Delta} E$ and $\mathit{\Delta} G$ are the kinetic and thermodynamic barriers to crystal growth. Since crystallization occurs between the glass transition and melting temperatures, and both the nucleation and crystal growth rate are temperature dependent functions, the effects of temperatures on these rates for a glass forming melt are traditionally shown as in Fig. 1.14. In silicate glasses, two classic glass systems: the lithium disilicate and calcium sodium silicate glasses, have received substantial attention concerning their nucleation and crystallization kinetics over a number of decades [61,63]. These glass systems have had considerable commercial application especially in the area of optical and dental glass-ceramics (GCs), however, it depends on applications whether crystallization of glasses is desirable. Crystallization and glass formation are essentially competitive kinetic processes, and in order to avoid uncontrolled crystallization of glass products one needs to know the main factors governing nucleation and crystal growth.

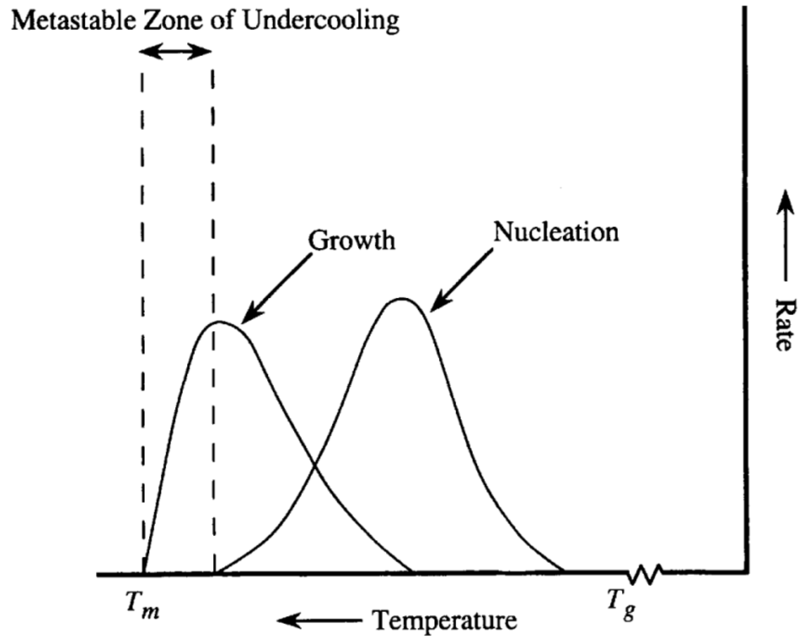

Figure 1.14: Effect of temperature on the rates of nucleation and crystal growth for a glass forming melt. [5]

1.6 Nanoindentation

The application of traditional testing procedures such as uniaxial tensile test, three-point bending test, double torsion test, etc. to micro-scale geometries, become difficult due to challenges in setting up fixtures, applying controlled loads, and handling the specimen. In addition, these methods cannot measure the spatially resolved material properties in micro-scale areas.

Nanoindentation is favorable in this characterization due to the small indentation size. The nanoindentation, depth-sensing indentation testing, is a modern technique which can be used to characterize the mechanical properties of materials. A small diamond-tip indenter in one of different geometries such as Conical, Berkovic, Cube-corner, and Vickers, is pressed into the sample to a prescribed displacement or load. From the basic principle of Oliver and Pharr method [65], experimental readings of indenter load and depth of penetration with the known geometry of the indenter provide an indirect measure of the area of contact at full load, thus the indentation hardness or the mean contact pressure of the specimen material can be estimated. Schematic diagram of load-displacement curve from indentation of a conical indenter tip is shown in Fig. 1.15. Indentation hardness indicated a resistance to penetration or permanent deformation. Indentation hardness, H_{IT}, is the mean contact pressure of the contact, and is found by dividing the indenter load by the projected area of the contact, and it can be expressed as:

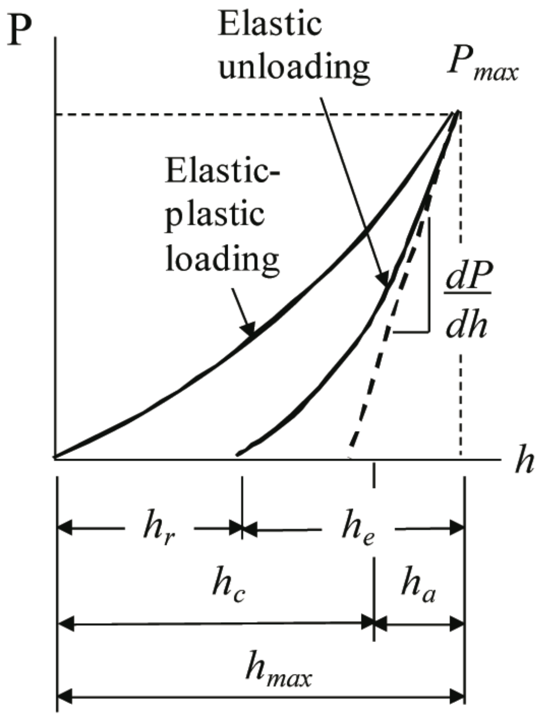

Figure 1.15: Load versus displacement for elastic-plastic loading followed by elastic unloading. [64]

$$H_{IT} = \frac{P}{A} = \frac{P}{\pi {h_p}^2 tan^2\alpha} \tag{1.18}$$

where P is the indenter maximum load, A is the projected area of the contact, h_p is the depth penetration measured from the edge of the circle or area of contact, and α is the semi-angle for an equivalent conical indenter. When the load is removed from the indenter, there is some degree of recovery due to the relaxation of elastic strains within the material. Thus an analysis of the initial portion of the elastic unloading response gives an estimate of the elastic modulus of the indented material. The elastic modulus, E_{IT}, of the specimen can be determined from the slope of the unloading of the load-displacement response, and it can be expressed as:

$$E_{IT} = \frac{1}{2}\frac{\sqrt{\pi}}{\sqrt{A}}\frac{dP}{dh} \tag{1.19}$$

where *dP/dh* is the slope of the elastic unloading. The area enclosed by the load-displacement curve represents the energy lost through plastic deformation. The energy recovered elastically is the area underneath the elastic unloading curve [64]. Due to the small indentation size and by the arrangement of indentations in spatial arrays at close spacing practically three-times the depth of the indents, nanoindentation can be highly spatially-resolved in the sub-micron scale. Since nanoindentation is a non-destructive test at microscopic dimensions, spatially resolved indents can be conducted covering the micro-scale area of interest to study the change in mechanical properties.

1.7 Objectives and Organization of Dissertation

In Chapter 2, femtosecond laser pulses were focused in the interior of a single fused silica piece. Proper use of optical and laser processing parameters generated structural rearrangement of the material through a thermal accumulation mechanism, which could be potentially used for the transmission welding process. The morphology of generated features was studied using differential interference contrast optical microscopy. In addition, the predictive capability of the morphology is developed via a finite element analysis. The change in mechanical properties was studied through employment of spatially resolved nanoindentation. The specimen was sectioned and nanoindents were applied at the cross-section to examine mechanical responses of the laser modified region. Fracture toughness measurements are carried out to investigate the effects of the laser treatment on strength of the glass.

In Chapter 3, femtosecond laser pulses were focused on the interface of two glass specimens. Proper use of optical and laser processing parameters enables transmission welding. The morphology of the weld cross section was studied using differential interference contrast optical microscopy. In addition, a numerical model was developed to predict the absorption volumes of femtosecond laser pulses inside a transparent material. The model takes into account the temporal and spatial characteristics and propagation properties of the laser beam, and the transmission welding widths were subsequently compared with the absorption widths predicted by the model. The model can lead to the achievement of a desirable weld shape through understanding the effects of laser pulse energy and numerical aperture on the shape of the absorption volume. The changes in mechanical properties of the weld seams were studied through spatially resolved nanoindentation, and indentation fracture analysis was used to investigate the strength of the weld seams.

In Chapter 4, channeling inside a transparent material, glass, by femtosecond laser was performed by using a single step process rather than hybrid processes that combine the laser irradiation with an additional tool or step to remove the material. Tightly focusing of a single femtosecond laser pulse using proper optical and laser processing parameters could induce the micro-explosion and could create voids inside transparent materials, and the effects of these parameters on the resultant feature geometry and channel length were studied. Understanding of the channel length variation at different locations from the specimen surface could enhance prediction capability. Taking into account of the laser, material, and lens properties, numerical models were developed to predict the absorption volume shape and size at different focusing depths below the surface of a specimen. These models will also be validated with the variation in feature and channel lengths inside the specimen obtained from the experiments. Spacing between adjacent laser pulses and laser parameters were varied to investigate effects of channel overlapping and its influence on long channel formation.

In chapter 5, functionally graded bioactive glass coatings on bioinert metallic substrates were produced by using continuous-wave (CW) laser irradiation. The aim is to achieve strong adhesion on the substrates and high bioactivity on the top surface of a coating material for load-bearing implants in biomedical applications. The morphology and microstructure of the bioactive glass from the laser coating process were investigated as functions of processing parameters. Laser sintering mechanisms were discussed with respect to the resulting morphology and microstructure. A numerical model was developed to aid in understanding the laser sintering mechanisms by capturing the combined effects of laser heating, densification, pore coalescence, and crystallization on the sintering behavior of bioactive glass. The numerical model was validated using experimental results and could be used to predict the porosity and crystallinity of sintered bioactive glass.

Chapter 2: Characterization of Morphology and Mechanical Properties of Glass Interior Irradiated by Femtosecond Laser

2.1 Introduction

Glasses are widely used in optical, electronic, and biomedical applications because of their excellent mechanical, thermal, and optical properties. For applications such as microfluidics, lab-on-a-chip, and flat panel displays, there is a need to join glasses. Glass joining techniques based on adhesive agents are unreliable and have poor mechanical, thermal and chemical durability [1]. Further, anodic bonding, another glass joining technique, requires heating of the entire device by applying a large electrical field for an extended period of time [2]. This is undesirable as the entire device is subject to thermally induced changes due to elevated temperatures. Therefore, localized melting and joining only at the interface by transmission welding using a femtosecond pulse laser has the potential to improve reliability and durability.

Over the last decade, several research groups have studied the use of femtosecond lasers to process transparent materials. Davis et al. [3] and Glezer et al. [4] reported on the femtosecond laser induced changes in the interior of transparent materials, and discussed the potential for fabrication of photonic devices for telecommunication applications and three-dimensional optical data storages. These early reports prompted further investigation into the laser-matter interactions and the mechanisms for feature formation in transparent materials. Due to the physics of laser-matter interactions, femtosecond lasers are specifically suitable for processing dielectric materials. When a femtosecond laser pulse is focused into the interior of the material, the laser intensity around the focal volume is extremely high and causes nonlinear absorption. Consequently, permanent structural modification occurs locally at the location of the laser focus. A study of the morphology of these structural changes showed that laser energy governs the size and the numerical aperture (*NA*) of the objective lens governs the shape of the affected region [5]. It was also shown that the features can be induced through mechanisms dominated by localized melting or explosive plasma expansion, depending on the laser and focusing parameters [6,7].

More recently, there has been interest in joining transparent materials by utilizing the thermal accumulation mechanism. Tamaki et al. [8] first reported welding between two pieces of silica glass by femtosecond laser pulses without the insertion of an intermediate layer. The mechanical properties of the weld and treated bulk samples were then characterized by various methods. Tamaki et al. [9] conducted tensile tests to determine the joint strength; however, the testing procedure was not precise because of inability to continuously increase the applied load. Another early attempt to characterize mechanical properties of femtosecond laser-irradiated glass was done by Miyamoto et al. [10]. They performed three-point bending test, and showed that the mechanical strength of the laser-melt zone was higher than that of base material; however, the sample had to be polished to unveil the laser induced feature at the bottom surface in order to experience the maximum tensile stress. Borrelli et al. [11] used a double torsion test to measure fracture toughness and investigate the strengthening effect and revealed that the fracture toughness is increased within the laser-treated area. Bellouard et al. [12] performed nanoindentation tests on treated regions of fused silica and showed an increase in Young modulus within the laser irradiated zones. However, these measurements were not spatially resolved, and were not constrained to within the treated regions.

Studies referenced above demonstrated the feasibility of transmission welding using femtosecond lasers. However, the understanding of the changes in mechanical properties within the affected area is limited, while the changes in optical properties were well described by Schaffer et. al. [13,14]. In the study presented here, two aspects are studied, the feature morphology and its mechanical properties. In order to simplify characterizations, experiments were conducted using single-piece specimens. Diffraction interference microscopy is employed to study morphology, and spatially resolved nanoindentation is used to develop a further understanding of the change in mechanical properties such as modulus, hardness, ductility, and fracture toughness upon femtosecond laser irradiation of bulk transparent materials. The effects of laser processing parameters such as pulse energy and scanning speed on those mechanical properties are also reported.

2.2 Background

2.2.1 FS Laser Interaction and Feature Formation Mechanisms in the Interior of Glasses

When femtosecond laser pulses are focused in the interior of a transparent material, the laser intensity within the focal volume becomes extremely high resulting in nonlinear absorption. Due to the high intensity (> 10^{13} W/cm^2), free electrons are initially produced by multiphoton ionization. These electrons serve as seeds for subsequent avalanche ionization, through which a substantial number of free electrons will be produced. The probability of multiphoton ionization per atom per second, w_{mpi}, and that of avalanche ionization per unit time w_{avi}, are written as [15]:

$$w_{mpi} \approx \omega n_{ph}^{\frac{3}{2}} \left(\frac{\varepsilon_{osc}}{2E_I} \right)^{n_{ph}} \qquad and \qquad w_{avi} \approx \frac{\varepsilon_{osc}}{E_I} \left(\frac{2\omega^2 v_{eff}}{\omega^2 + v_{eff}^2} \right) \tag{2.1}$$

where ω is the laser frequency, v_{eff} is the electron-phonon collision frequency, n_{ph} is the number of photons necessary for the electron to be transferred from the valence to the conduction band, E_I is the ionization energy, and ε_{osc} is the electron quiver energy in the laser field. ε_{osc} has units of eV and is expressed in a scaling form [15], $\varepsilon_{osc} = 9.3(1+\alpha^2)I\lambda^2/10^{14}$, where α is the coefficient for beam polarization, I is the laser intensity in units of W/cm^2, and λ is the laser wavelength in units of μm. The density of free electrons, n_e, from the two major mechanisms, multiphoton and avalanche ionization is [15]:

$$n_e(I,\lambda,t) = \left(n_0 + \frac{n_a w_{mpi}}{w_{avi}} [1 - exp(-w_{avi}t)] \right) exp(w_{avi}t) \tag{2.2}$$

where n_0 is the density of initial seed electrons, n_a is the density of neutral atoms, and t is time. When the free electron density reaches the critical value, n_{cr}, the ionization threshold is achieved, and plasma is created in the material. This critical free electron density is described as [16]:

$$n_{cr} = \frac{\pi m_e c^2}{e^2 \lambda^2} = \frac{m_e \omega^2}{4\pi e^2} \tag{2.3}$$

where m_e is the electron mass, c is the speed of light, e is the electron charge, and λ is the laser wavelength. The free electron density is saturated in a few femtoseconds at the beginning of the laser pulse. During the remaining part of the pulse, plasma strongly absorbs the laser pulse energy, which creates a region of high energy density. Subsequently after the end of laser pulse, the transfer of the energy from the hot plasma to the lattice results in structural changes in the bulk transparent material [16].

Depending on the optical and laser processing parameters, the bulk transparent material can be modified through the micro-explosions or thermal accumulation mechanisms [17]. For the micro-explosion mechanism when a single laser pulse is deposited into the target material, high laser intensity created by either tight focusing of low energy pulse or loose focusing of high energy pulse cause shock wave generation. The shock wave carries matter and energy away from the focal volume, compressing the surrounding material while a rarefaction wave behind the shock front propagates into the opposite direction, creating a rarified central region or void [18]. As a result a void surrounded by densified shell is generated. The thermal accumulation mechanism occurs, when multiple pulses either with low energy and high repetition rate or with high energy and low repetition rate are irradiated at same location or at low scanning speed. Heat accumulates inside the focal volume causing the localized melting which is followed by heat conduction into the surrounding material. Due to rapid resolidification the melted region subsequently solidifies into a higher density phase [13]. In the latter mechanism, the feature size is determined by a combination of pulse energy and repetition rate, the stage translation speed, and the NA of the objective lens.

2.2.2 Characterization of Mechanical Properties by Nanoindentation

Nanoindentation or depth-sensing indentation testing is a modern technique which can be used to characterize the mechanical properties of materials at small length scales. An analysis of a load-displacement curve gives hardness and the elastic modulus of the indented material, which are expressed as [19]:

$$H_{IT} = \frac{P}{A} = \frac{P}{\pi z_p^2 tan^2 \alpha} \qquad and \qquad E_{IT} = \frac{1}{2}\frac{\sqrt{\pi}}{\sqrt{A}}\frac{dP}{dz} \tag{2.4}$$

where H_{IT} is the indentation hardness, E_{IT} is the indentation modulus representing the combined modulus of the indenter tip and the specimen, P is the indenter maximum load, z_p is the penetration depth, *dP/dz* is the slope of the elastic unloading curve, and α is the semi-angle for an equivalent conical indenter.

Lawn et al. [20] studied the deformation properties of materials using indentation tests. Their primary interest is in the brittle materials especially glasses. Using the condition for compatibility of the two half-cycles at the maximum load, the elastic recovery is:

$$\left(\frac{z_r}{z_m}\right)^2 = 1 - \eta\frac{H}{E} \tag{2.5}$$

where z_r is the residual impression depth, z_m is the maximum depth of penetration, η is the numerical constant related to the Poisson's ratio and indenter's geometrical factor. From Eq. (2.5) the extent of recovery depends on the *H/E* ratio. Thus, the ratio of *H/E* plays an important role in identifying the elastic/plastic behavior of materials.

When dealing with an elastic/plastic field in large scale events, where cracking occurs, *H/E* can be related to toughness. Lawn et al. [21] have shown that the quantity *E/H* emerges as the primary manifestation of the elastic/plastic far-field driving force for fracture. The crack opening force, P_r, produced by the residual stress field, can be expressed as $P_r \sim (E/H)^{1/2} \cot\alpha^{2/3} P$, where P is the peak indentation load, and α is the semi- angle for an equivalent conical indenter. Assuming half-penny crack geometry, the stress intensity factor due to residual far-field force is written as $K \sim f(\phi) P_r / c^{3/2}$ [22], where $f(\phi)$ is an angular function introduced to allow for the effects of the free surface, and c is the crack length. Assuming that the crack arrests when it grows to a length at which the stress intensity factor is just equal to the fracture toughness [23]. An appropriate expression of fracture toughness, K_C, evaluated by indentation testing can be written as:

$$K_C = k\left(\frac{E}{H}\right)^{1/2} \frac{P}{c^{3/2}} \tag{2.6}$$

where k is an empirical constant which depends on the geometry of the indenter.

Because brittleness measures the relative susceptibility of a material to two competing mechanical responses, deformation and fracture, H/K_C has been proposed as the quantification of the brittleness [24] based on the critical flaw condition, $C^* = \mu_0 (K_C / H)^2$, where μ_0 is geometrical constant. The inversion of brittleness is the ductility; therefore, K_C/H, which is related to the allowable critical flaw size represents the ductility index of materials in indentation testing.

In addition to the fracture mechanics analysis, an energy-based analysis is another approach that is used to determine elastic recovery, densification energy [25], and ductility [26] from load versus displacement curves obtained through indentation testing. Ductility is typically defined as the degree of plastic strain at fracture. The ductility index, *D*, is defined in terms of the indentation energy ratio as the following [26]:

$$D = \frac{U_r}{U_t} = \frac{U_t - U_e}{U_t} = 1 - \left(\int_{z_r}^{z_m} P_{ld} dz \Big/ \int_{0}^{z_m} P_{ud} dz \right) \tag{2.7}$$

Where U_r is the irreversible hysteresis energy, U_t is the total applied energy, U_e is the elastically-recovered energy, z_r is the residual indentation depth, z_m is the maximum indentation depth, P_{ld} is the indentation load during loading, and P_{ud} is the indentation load during unloading.

2.3 Experimental Setup and Characterization

Experiments have been conducted utilizing a chirped amplified Ti:Sapphire laser system which outputs high energy ultrashort pulses with 800 nm wavelength and 130 fs pulse duration at a 1 kHz repetition rate. S1-UV grade fused silica was used as the base material for these experiments. The laser beam was focused by 40x objective lens with *NA* 0.60 into the interior of 1.0 mm thick, 10 mm square fused silica specimen mounted on a motorized linear stage. A schematic diagram of the experimental setup is illustrated in Fig. 2.1. Different conditions of laser processing parameters were applied by varying the feed rate of the stage and the energy of the laser pulses. Pulses were applied at energies ranging from 12 μJ to 30 μJ at stage velocities between 0.04 mm/s and 0.2 mm/s. After the femtosecond laser treatment, the samples were then sectioned, ground and polished with cerium-oxide and a leather polishing pad. Due to the transparency of the sample, transmitted-light differential interference contrast (DIC) optical microscopy, which can reveal more contrast and detail in the feature morphology was used to obtain the side view optical micrographs.

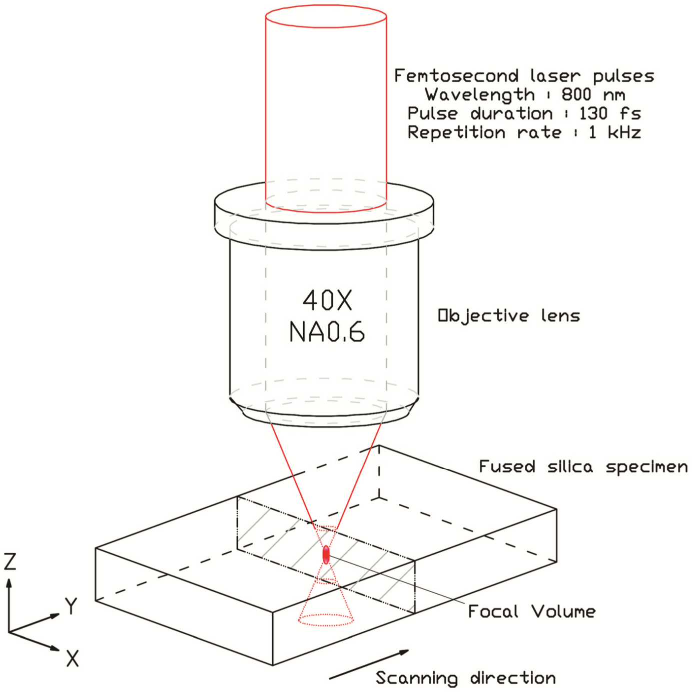

Figure 2.1: Schematic illustration of experimental setup. The laser beam is focused into the interior of the fused silica sample, and the scanning direction is along y-axis.

After the femtosecond laser treatment, the affected region was examined via nanoindentation using a three-sided Berkovich indenter tip to characterize the mechanical properties. The Berkovich geometry has the advantage that the edges of the pyramid are more easily constructed to a sharper point than the four-sided Vickers geometry, and is generally used in small-scale indentation [19]. 200 nm depth spatially resolved nanoindents with 5 μm spacing in the x and z directions were conducted to cover both the affected and unaffected regions of the cross-section. 2 μm deep and 440 mN load nanoindents were also performed on the features to induce cracks, which were then scanned by atomic force microscopy (AFM) to measure the crack length and investigate the change in fracture toughness of the laser-irradiated zones. Five feed rate conditions at the same energy level, 30 μJ, and another five laser pulse energy conditions at the same feed rate, 0.04 mm/s, were used to investigate the effects of laser pulse energy and laser scanning speed on feature morphology and mechanical properties due to structural modifications.

2.4 Results and Discussion

2.4.1 Experimental Morphology by Transmission DIC

As mentioned previously, when femtosecond laser pulses are focused through an objective lens to a spot inside bulk glasses, if proper conditions are met, the material confined within the focal volume experience structural modification. Usage of objectives with high *NA*s (*NA*>0.4), feature morphologies appear to have shapes with smaller ratios of longitudinal to lateral radii [5]. This agrees well with the ratios of major to minor radii of an ellipsoidal focal volume as described by Zipfel et al. [27]. Using a three-dimensional Gaussian ellipsoid to approximate focal volume, the radii of focal volume at $1/e^2$ intensity are *NA* dependent and written as [27]:

$$\omega_{xy} = \frac{0.32\lambda}{NA}, \quad NA \le 0.7 \qquad or \qquad \omega_{xy} = \frac{0.325\lambda}{NA^{0.91}}, \quad NA > 0.7$$

$$\omega_{xy} = \frac{0.532\lambda}{\left[n_i - \sqrt{n_i^2 - NA^2}\right]} \tag{2.8}$$

where ω_{xy} and ω_z represent the lateral and longitudinal radii of the Gaussian elliopsoid at $1/e^2$ position in their corresponding direction, respectively, λ is the laser wavelength and n_i is the refractive index of the transparent material.

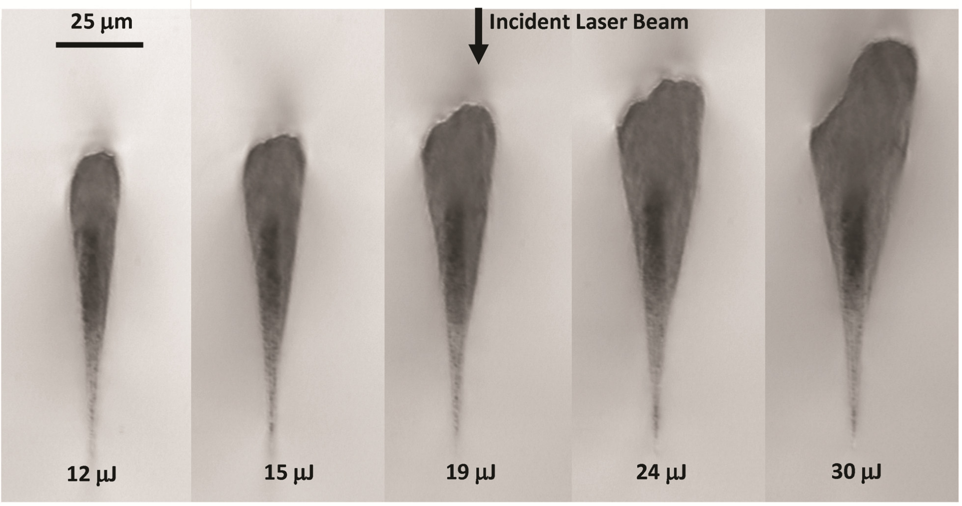

Figure 2.2: Transmission DIC optical microscopy of cross section view (x-z plane) of femtosecond laser-irradiated fused silica (beam diameter of 1.5 µm, scanning speed of 0.04 mm/s, and rep rate of 1 kHz).

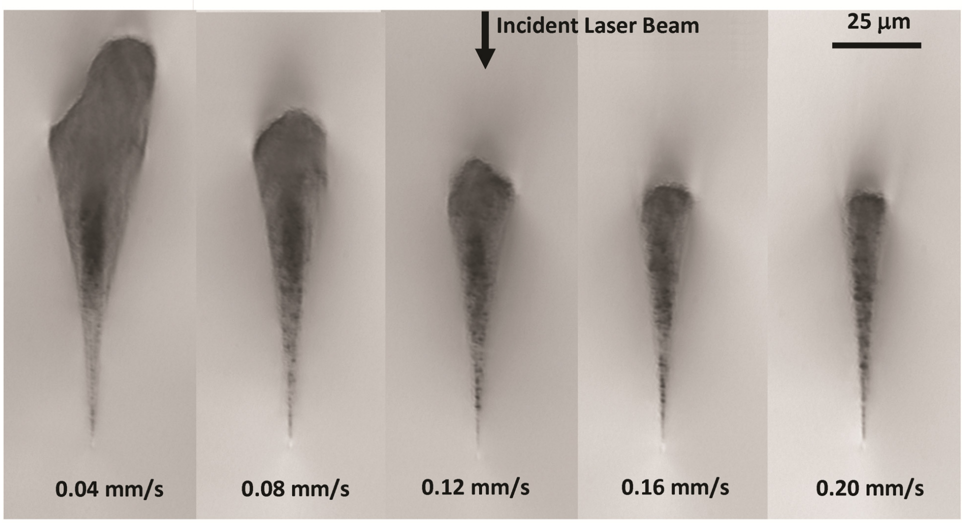

Figure 2.3: Transmission DIC optical microscopy of cross section view (x-z plane) of femtosecond laser-irradiated fused silica (beam diameter of 1.5 µm, pulse energy of 30 µJ, and rep rate of 1 kHz).

The cross sections of features created by different laser pulse energies with a scanning speed of 0.04 mm/s and by 30 μJ laser pulses at various feed rates are seen clearly with the use of DIC optical microscopy as shown in Fig. 2.2 and Fig. 2.3 respectively. These features have a long and narrow teardrop shape with an ellipsoidal dark core in the center. The shape and size of the core relates to the focal volume as described by Eq.(2.8), and the distinctive color of this region could be a consequence of the high level of interaction of a material with laser pulses, which repeatedly deposit energy into this region with large overlap. The outer regions show some discoloration and are expected to have experienced a temperature equal or greater than the softening point of fused silica. The asymmetric shape of outer regions is considered to be the result of focusing effects [16] and different temporal slices of the energy above the threshold [1,5]. The irregular profile near the top area of the features is probably caused by the inhomogeneous distribution of the laser intensity rather than material properties. Due to the nature of the process, the focal volume can be seen as heat source. This inner darker region can be associated with focal volume where laser energy is directly deposited and the presence of the outer region is due to heat conduction between the focal volume and surrounding material [10,13,17]. From Fig. 2.2 and Fig. 2.3, it can be seen that the feature size is strongly dependent on the scanning speed and laser pulse energy. The higher the laser pulse energies and lower feed rates correspond to formation of larger features. This is particularly important for transmission welding of the glasses in flat display industry where components inside of the enclosure can be thermally sensitive and highly localized weld is desired.

Figures 2.4 and 2.5 show the feature heights, widths, and aspect ratios (height/width) as a function of laser pulse energy and laser scanning speed respectively. The feature heights and widths are respectively defined from the longest and the widest portions of both regular and irregular features. For higher laser pulse energies, the temperature in the focal volume is higher, and when it is conducted to the surrounding area, the affected region which experiences the temperature above the softening point is bigger in both directions as shown in Fig. 2.4. On the other hand, the higher the speed, the less time there is for heat to accumulate inside the focal volume. As a result, the temperature is lower, and the affected region is smaller both in height and width as shown in Fig. 2.5. At same laser scanning speed, 0.04 mm/s, the aspect ratios are more-or-less constant with the laser pulse energy in the range of this study as shown in Fig. 2.4. This suggests that since each area of the material is processed for the same amount of time and there is no change in the focal volume ratio, the percentage of increasing in size each direction due to different pulse energies is about the same. However, from Fig. 2.5 the aspect ratios are decreased when the laser scanning speed is decreased as similarly observed by Vukelic et. al. [17]. Since the temperature gradients between the focal volume and the surrounding material in the axial and lateral directions are different due to the Gaussian ellipsoidal shape of the focal volume, Heat flux will be greater and strongly conducts in the lateral direction. Thus, the percentage of increasing size in this direction is higher than another direction as a function of time, resulting in the decreased aspect ratios.

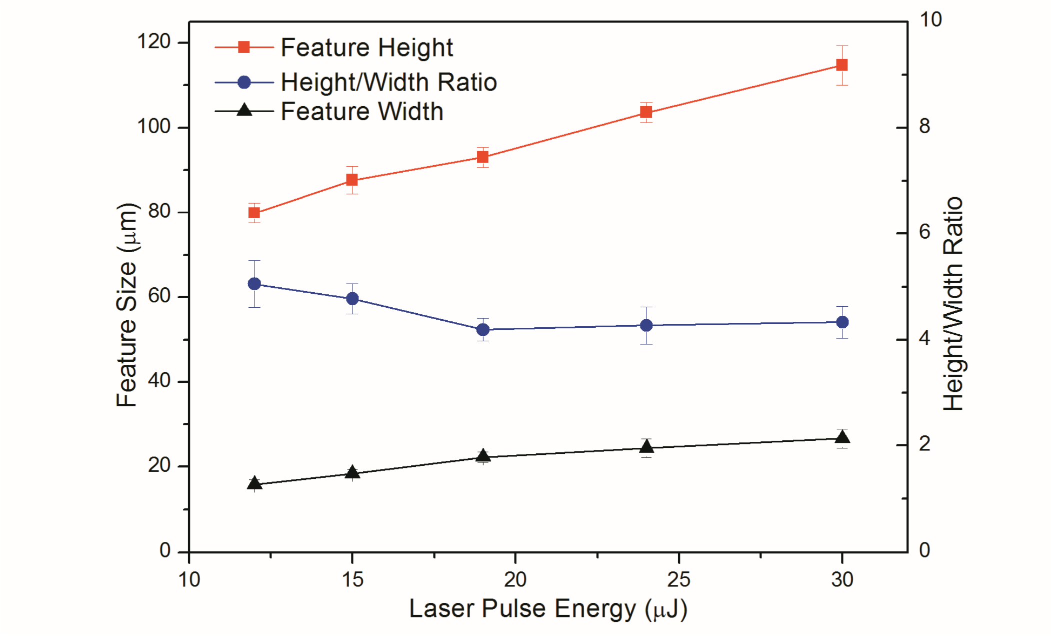

Figure 2.4: Height, width, and height/width ratio of the feature (affected area as shown in Fig. 2.2) in femtosecond laser-irradiated fused silica at different pulse energy levels but same scanning speed of 0.04 mm/s. Error bars denote standard deviation.

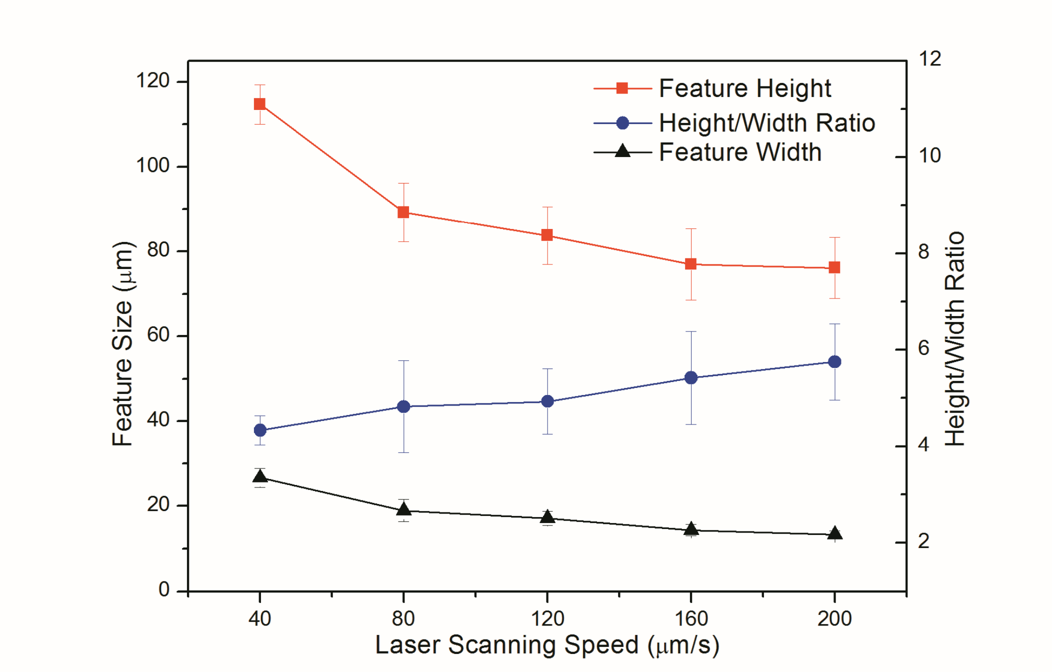

Figure 2.5: Height, width, and height/width ratio of the feature (affected area as shown in Fig. 2.3) in femtosecond laser-irradiated fused silica at pulse energy level of 30 μJ with various scanning speeds. Error bars denote standard deviation.

2.4.2 Morphology from Isotherm Modeling

As described in the previous section, heat accumulation and diffusion play an important role in feature formation. A simplified heat conduction model was used in order to capture the basic mechanisms of structure changes and to predict the size of the softening/melting region induced by femtosecond laser processing of transparent materials. The work piece material is assumed to be isotropic, and the temperature dependence of thermal conductivity and specific heat is taken into account. Modeling includes deposition of the femtosecond laser pulses at a 1 kHz repetition rate into the interior of a finite three-dimensional plate of fused silica. One-temperature heat conduction equation has been solved since the two-temperature model is suitable only for low fluences and widely used for metals [28]. The governing equation is therefore the temperature dependent classical heat equation with a laser source:

$$\rho C_p(T)\frac{\partial T}{\partial t} = \nabla(k(T)\nabla T) + I(x,y,z,t) \tag{2.9}$$

where ρ is density, Cp is specific heat, k is conductivity, x, y, and z are the Cartesian coordinates, t is time, and I is the laser intensity or the energy rate supplied externally into the body. Laser energy is assumed to be absorbed only inside a focal volume. Based on Eq. (2.8), the focal volume is modified to use a double ellipsoidal shape in order to compensate for a teardrop shape of features caused by focusing effects [16]. Therefore, the intensity profile of a moving laser beam is a 3D spatial Gaussian ellipsoid and a 1D Gaussian in time, which can be written as:

$$I(x,y,z,t) = I_0 exp\left(\frac{-2((\Delta x)^2 + (\Delta y)^2)}{\omega_{xy}^2}\right) exp\left(\frac{-2(\Delta z)^2}{\omega_z^2}\right) exp\left(-4ln2\frac{\left(t - 2t_p\right)^2}{t_p^2}\right) \quad (2.10)$$

where I_0 is the peak intensity, Δx, Δy, and Δz are distances measured in Cartesian coordinate system from the center of the laser beam, and t_p is a full-width-at-half-maximum (FWHM) pulse width. The aspect ratio of the focal volume, ω_z/ω_{xy}, is kept constant as it depends on wavelength and *NA* only, which are constant. Although simplified with respect to actual process, the established numerical model allows one to estimate the size of the affected region based on the input parameters, laser pulse energy, repetition rate and feedrate. The analysis is implemented with the commercial finite element (FEM) program ABAQUS/Standard.

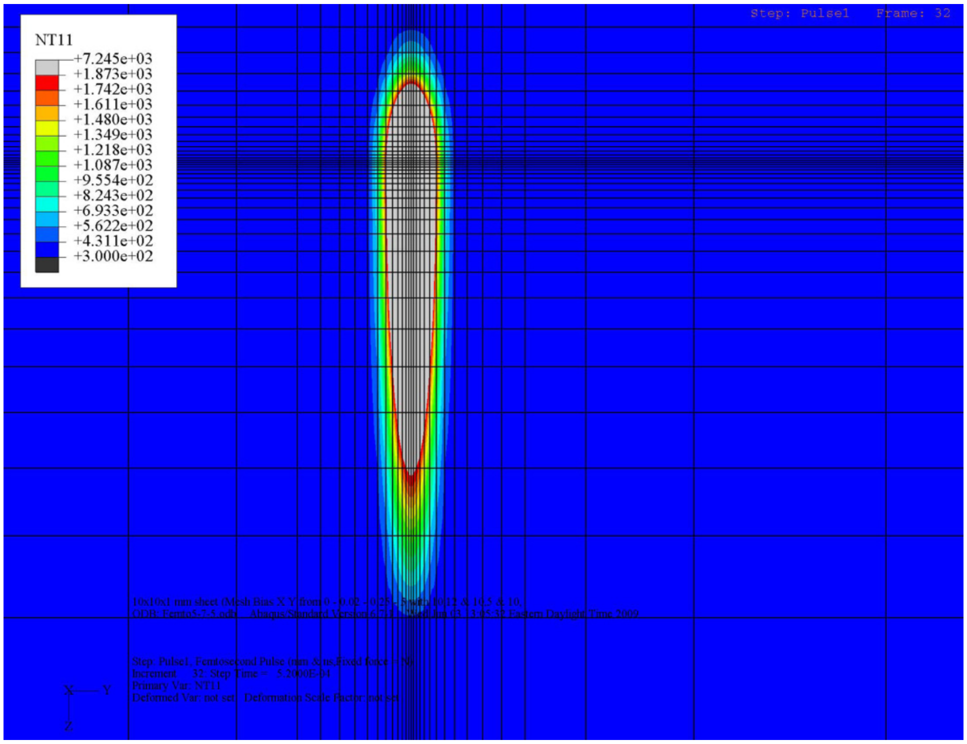

Figure 2.6: Representative temperature distribution in femtosecond laser-irradiated fused silica at pulse energy level of 30 μJ and scanning speed of 0.04 mm/s. The gray area represents the material region that experiences the temperature equal or greater than the softening point (step time of 520 fs).

The representative isothermal contours of the affected region during processing using 30 μJ laser pulse energy and 0.04 mm/s laser scanning speed is illustrated in Fig. 2.6. The gray color contour represents the material region that experiences temperatures equal or greater than the softening temperature of fused silica. This contour shape is similar to the feature morphology as shown in Fig. 2.2 and Fig. 2.3. The feature sizes and aspect ratios of these numerical results along with the experimental ones are plotted as a function of laser pulse energy in Fig. 2.7. The numerical models predict the same increasing trend of feature size as the experimental results both in height and width as shown in Fig. 2.7 (a), and also the same more-or-less constant trend of the aspect ratios as the experimental ones as shown in Fig. 2.7 (b). However, there is some discrepancy between the numerical and experimental sizes. This is due the fact that the numerical model does not take into account hydrodynamic motion and shock wave that comes as its consequence as well as pressure effect. As a result the size of the feature is underestimated. From Fig. 2.7 (a), it is clearly seen that there is higher discrepancy in the prediction of the feature widths. Thus, it could be thought that the effects of shock wave and pressure are more dominant in determining the feature size in the lateral direction than in the axial direction. Subsequently, the aspect ratios are overestimated, as seen in Fig. 2.7 (b). Therefore, the thermal model suggests that the mechanisms responsible for feature formation of femtosecond laser-irradiated fused silica using low repetition rate, high energy regime, and low scanning speed are more complex and could be the combinations of high pressure explosive plasma expansion and high temperature thermal diffusion. Future studies will concentrate on further improvement of the established numerical model.

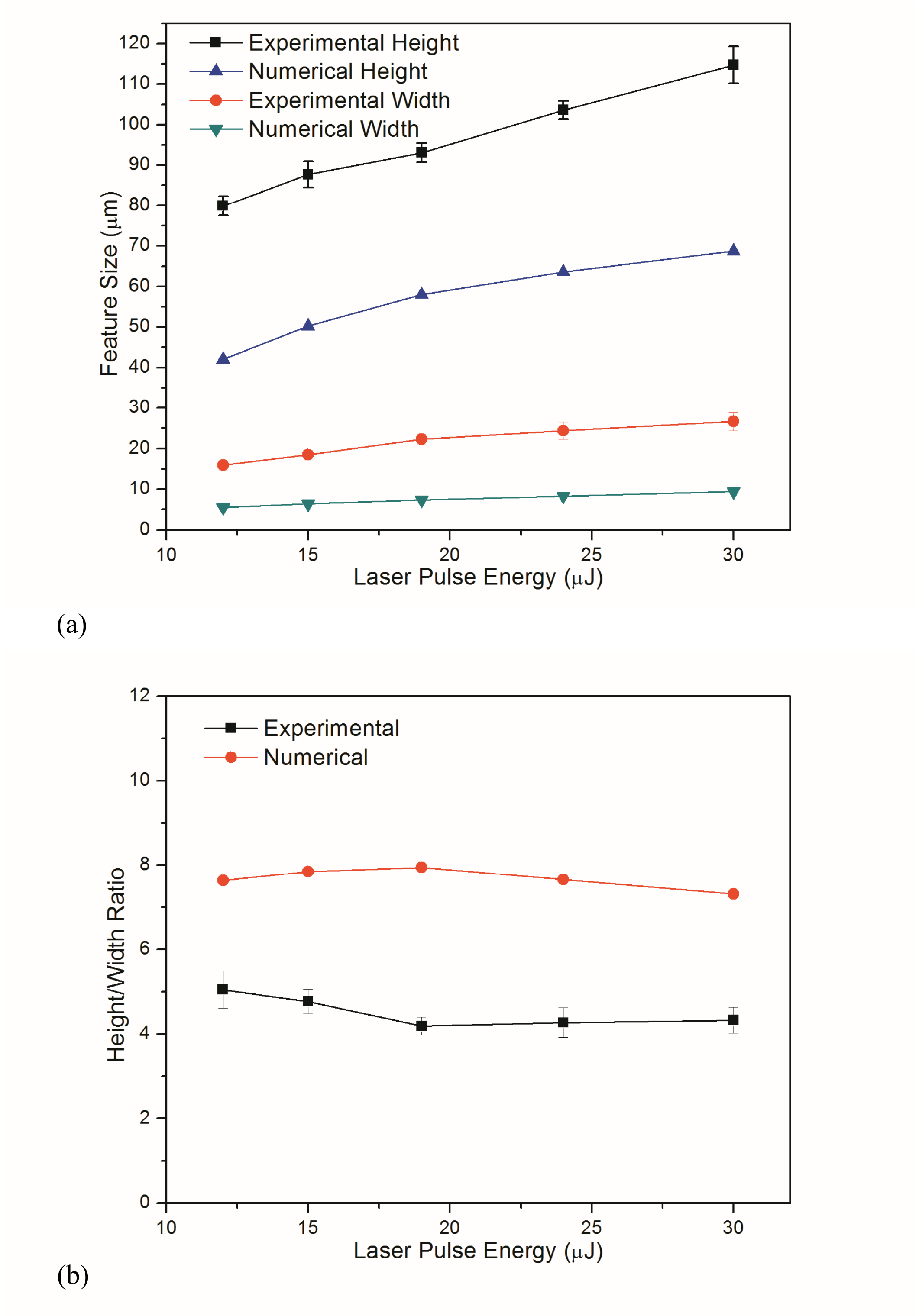

Figure 2.7: Experimental and numerical feature morphology comparison (a) feature size (b) height/width ratio of femtosecond laser-irradiated fused silica at different pulse energy levels with same scanning speed of 0.04 mm/s. Error bars denote standard deviation.

2.4.3 Spatially Resolved Nanoindentation

An array of 200nm depth nanoindentation measurements were performed over the cross section of femtosecond laser-modified fused silica with spatial resolution of 5 μm as shown by the reflection DIC optical micrograph in Fig. 2.8. The radius of plastic zone from a cavity model of an elastic-plastic indentation by a conical indenter, which described by Johnson [29], was used as a guideline to define the spacing between each indent. The plastically deformed radius is written as:

$$r_p = \frac{d}{tan\beta}\left[\frac{Etan\beta}{6Y(1-\nu)} + \frac{2-4\nu}{3-3\nu}\right]^{1/3} \tag{2.11}$$

where r_p is the radius of plastic zone, d is the indentation depth, β is the angle between the indenter face and the surface (19.7° for the equivalent cone for a Berkovich indenter), E is Young's modulus, Y is the yield stress, and ν is Poisson's ratio. The load-displacement curves of indents on both modified and unmodified regions in Fig. 2.8 were measured, and the representative curves of these two regions were compared as illustrated in Fig. 2.9. Hardness and Young's modulus are extracted from the loading and unloading curves respectively.

The contour maps of two basic material properties, Young's modulus and hardness, correspond to the array of nanoindents in the optical micrograph were plotted as shown in Fig. 2.10. It is observed that the Young's modulus and hardness in the femtosecond laser-irradiated region are reduced, and that the size and shape of these contours look similar to the morphology of the affected region in Fig. 2.8. The reduction in modulus and hardness confirms presence of structural

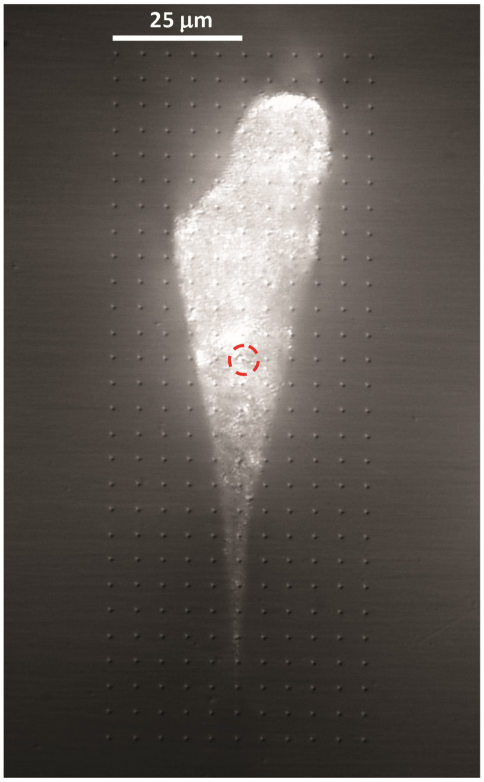

Figure 2.8: Representative reflection DIC optical microscopy of spatially resolved nanoindentation array (200nm depth and 5 µm spacing) on the cross section (x-z plane) of fused silica irradiated by femtosecond laser. The circle locates the weakest point in Young's modulus and hardness corresponds to Fig. 2.10.

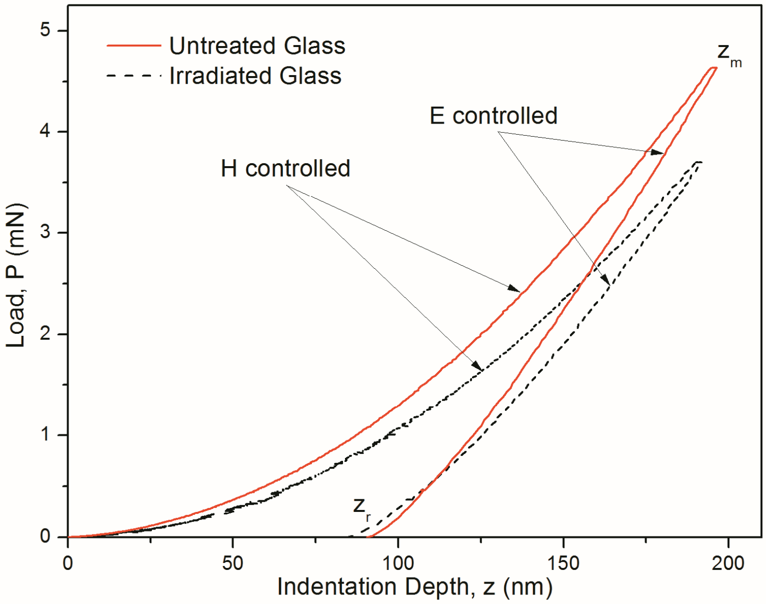

Figure 2.9: Representative load-displacement curves for 200nm indentation in untreated and irradiated regions of fused silica sample.

modifications inside the affected region. The region undergoes irreversible densification which is a consequence of high pressures created by the plasma expansion. At the same time the presence of breaks in the linkage within a structure due to the nature of the process also allows easier displacement of the atoms and reduces the elastic modulus [30]. Young's modulus should be proportional to the number of bridging bonds per unit volume of glass [31], and the hardness relates to the connectivity of the structure [32]. From fluorescence microscopy it was shown that in fused silica nonbridging oxygen hole centers (NBOHC) are formed in the regions exposed to femtosecond laser irradiation especially in high pulse energy regime [14]. NBOHC are considered as defects, and cause the connectivity of glass network structure to be decreased.

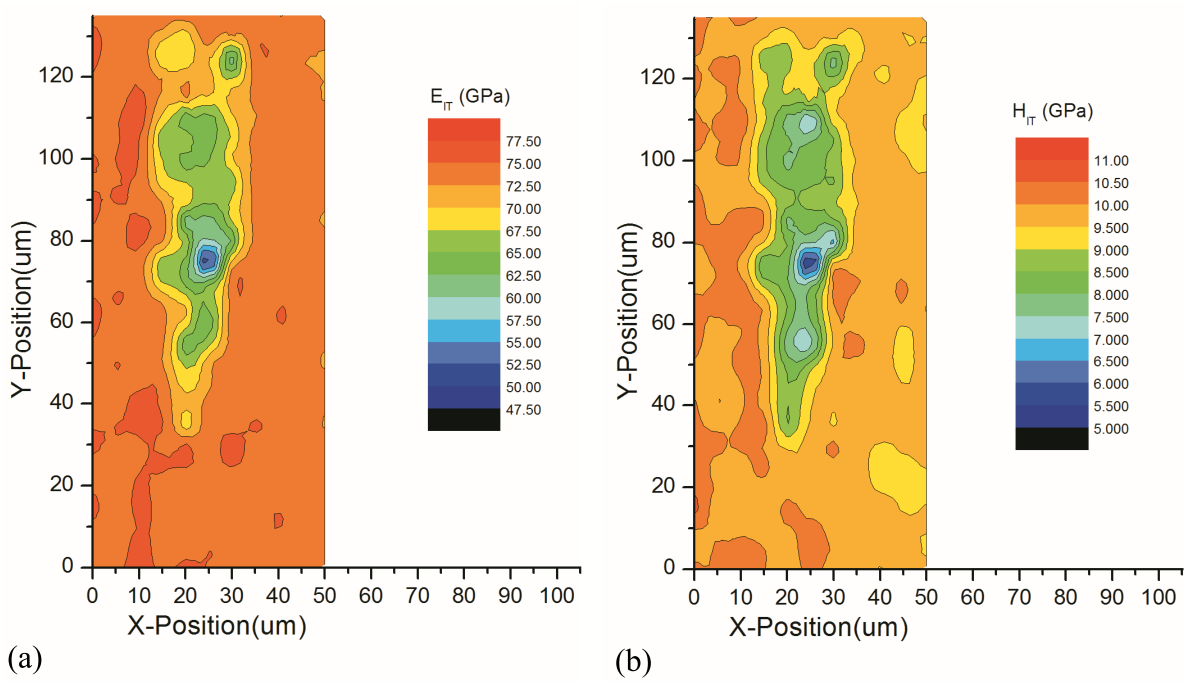

Figure 2.10: Spatially resolved determination of (a) Young's modulus (b) hardness on the cross section of laser-irradiated region (30 μJ pulse energy and 0.04 mm/s scanning speed). The maps correspond to the array of 200nm depth nanoindents with 5 μm spacing shown in Fig. 2.8 and are constructed based on the load-displacement measurement results shown in Fig. 2.9.

Therefore, the combination of high pressure and high temperature generated by femtosecond laser pulse trains cause the material in the affected region to become more flexible (lower *E*) and softer (lower *H*). As the point which has the lowest value of Young's modulus and hardness shown in Fig. 2.10 is aligned with the optical axis of laser pulses and is almost in the middle of the feature, it could be the center of the intensive interaction region as discussed in the experimental morphology analysis section, and the existence of this weakest point is a consequence of that.

Figure 2.11 shows the spatially resolved mapping of *H/E* ratios over the femtosecond laser-irradiated region. It is observed that the *H/E* ratios in the femtosecond laser-irradiated region are reduced. When focusing on elastic and plastic strains and considering each of the two properties,

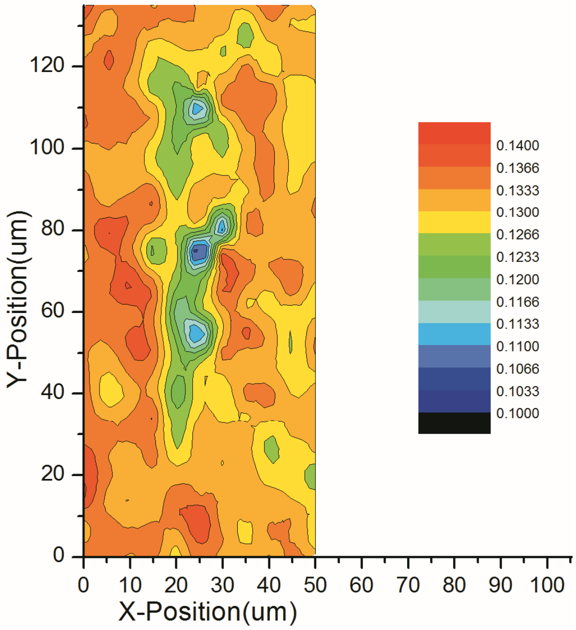

Figure 2.11: Spatially resolved determination of the ratio between hardness and Young's modulus (H/E) on the cross section of laser-irradiated region (30 μJ pulse energy and 0.04 mm/s scanning speed). The maps correspond to the array of 200nm depth nanoindents with 5 μm spacing shown in Fig. 2.8 and are constructed based on the load-displacement measurement results shown in Fig. 2.9.

Young's modulus and hardness, materials with lower values of Young's modulus exhibit lower resistance to elastic deformation or higher elastic strain, while materials with lower values of hardness exhibit lower resistance to plastic deformation or higher plastic strain. However, in displacement-controlled nanoindentation, there is the same amount of total strain, and the elastic and plastic strain portions cannot increase or decrease in the same time. Thus, the changes of these two properties will compete with each other, and the materials will show their changes in elastic/plastic behavior. Plastic behavior dominates at lower values of *H/E* while elastic behavior dominates at higher values of *H/E*. Therefore, the decrease in *H/E* ratios means the material in the modified region experiences a higher degree of plastic deformation which can be viewed as an increase in ductility.

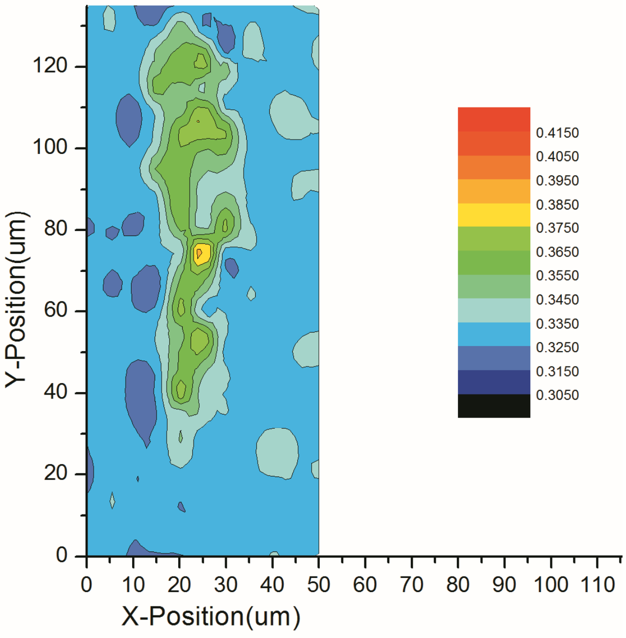

Figure 2.12: Spatially resolved determination of the normalized dissipated energy on the cross section of laser-irradiated region (30 μJ pulse energy and 0.04 mm/s scanning speed). The maps correspond to the array of 200nm depth nanoindents with 5 μm spacing shown in Fig. 2.8 and are constructed based on the load-displacement measurement results shown in Fig. 2.9. The maps represent ductility index and densification.

Further, one can determine the ductility index through employment of Eq. (2.7). The ratio of the irreversible hysteresis loop energy U_r to the total energy U_t, is defined as the degree of plastic flow [26]. The ductility index D varies from 0.0 for a purely elastic to 1.0 for a purely plastic material. A mapping of the results from this approach is illustrated in Fig. 2.12. The contour map showed that ductility index of femtosecond laser-irradiated region is increased up to 25%. The increase in ductility index corresponds well with the highly plastic behavior indicated by the decrease in *H/E* ratio.

With the "open" network structure of fused silica, it is considered that the main mechanism for plastic deformation is densification rather than plastic flow [33], and that the irreversible hysteresis loop energy U_r can also be defined as the energy consumed for densification [25]. The increase in normalized irreversible loop energy shown in Fig. 2.12 corresponds to the increase in

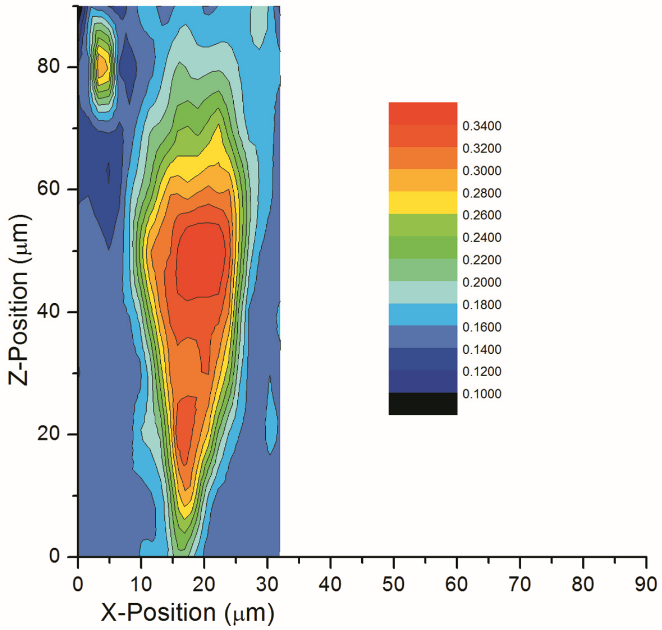

Figure 2.13: Volume fraction distribution of three- and four-fold ring structure based on the 606 cm^{-1} and 495 cm^{-1} peak in Raman spectra of cross section of femtosecond laser-irradiated region (30 μJ pulse energy and 0.04 mm/s scanning speed). [17]

refractive index of the treated glass [13]. Spatially resolved and decomposed Raman spectral analysis [17] revealed that the volume fraction of three- and four-fold rings of affected regions irradiated by 30 μJ pulse energy and 0.04 mm/s scanning speed, increases as illustrated in the contour map of Fig. 2.13. The densification has been related to the change of structure from five- and six-fold rings to become three- and four-fold rings, which have smaller intertetrahedral angles and thus are more densely packed. Therefore, in addition to the increase in refractive index [13,14], as well as the structural changes characterized by spatially resolved Raman spectroscopy [17], the increase in normalized dissipated energy by spatially resolved nanoindentation testing also suggested that fused silica irradiated by femtosecond laser pulses undergoes densification.

Toughness, a measure of the ability of a material to absorb energy up to fracture, is an integration product of strength and degree of plastic strain or ductility. Considering the conservation of the volume in the cavity model, Johnson [29] locates the elastic-plastic boundary for conical or pyramidal indenters during contact. The expression, which relates hardness, H, to yield strength, Y, and Young's modulus, E, is written as:

$$\frac{H}{Y}=\frac{2}{3}\left[1+ln\left(\frac{Etan\beta}{6(1-\nu)Y}+\frac{2(1-2\nu)}{3(1-\nu)}\right)\right] \tag{2.12}$$

where β is the angle between the indenter face and the surface, and ν is Poisson's ratio. As can be seen from this equation, when H/E is decreased, the yield strength is also decreased. Femtosecond laser-irradiated regions showed a decrease in yield strength and an increase in ductility. Thus, the changes in toughness result from the competitions between the percentage decrease in yield strength and the percentage increase in ductility. If the change in yield strength was less dominant, the affected regions of fused silica would have higher toughness.

2.4.4 Effect of Laser Processing Parameters on Mechanical Responses

As demonstrated previously, the materials in the affected region are more flexible (lower *E*), softer (lower *H*), and highly plastic (lower *H/E* ratio). Referring to the difference of each property between the untreated and the irradiated regions, Figure 2.14 and Fig. 2.15 show the maximum decrease of modulus, *E*, hardness to modulus ratio, *H/E*, and hardness, *H*, as a function of laser pulse energy and laser scanning speed, respectively. All three quantities show decreasing trends in cases of increasing pulse energy or decreasing scanning speed. The decreasing trend of the *H/E* ratios revealed more dominant plastic behavior in the new structural materials created by more energetic pulses or by slower scanning speeds. Due to higher pressures and temperatures caused by more energetic pulses, the mean separation between the atoms increases, and the structure of the irradiated glass tends to exhibit more breaks in the linkage. Thus, the more nonbridging oxygen hole centers (NBOHC) are created, and the connectivity of the structure decreases. Therefore, *E* and *H* decrease further with increase in laser pulse energy. On the other hand, the lower the speed, the more interaction time and a higher number of pulses are used to modify the network structure of the glass. As a result, there are more NBOHC, and the connectivity of the structure decreases. Therefore, there is a further decrease in *E* and *H* due to the decrease in laser scanning speed.

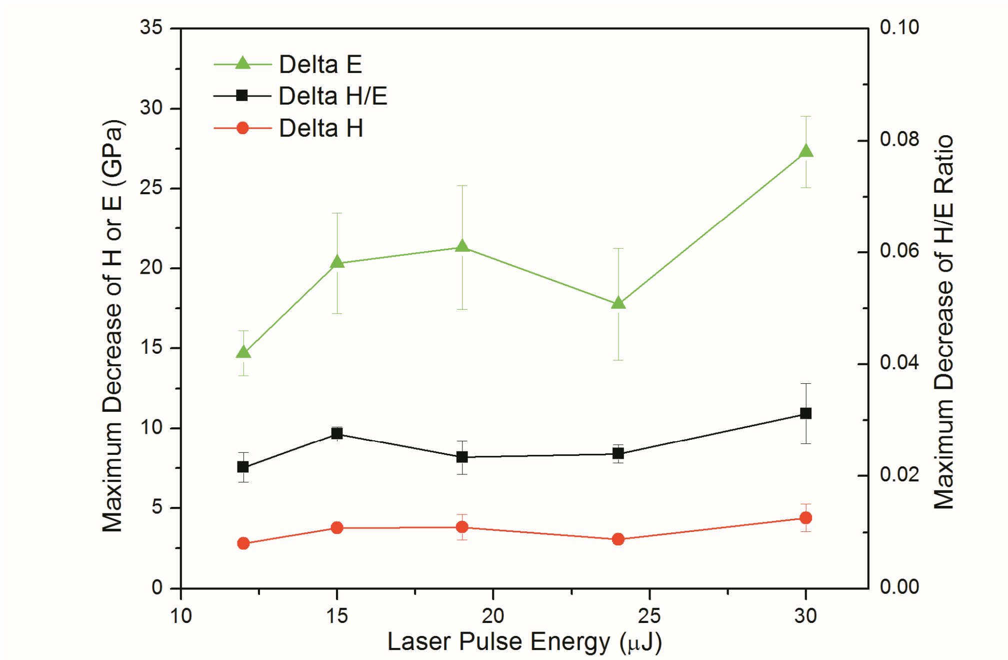

Figure 2.14: Maximum decrease of modulus (E), hardness (H), and hardness to modulus ratio (H/E) of 200nm depth nanoindents inside the femtosecond laser-irradiated regions (same scanning speed of 0.04 mm/s but different pulse energy levels.) Error bars denote standard error.

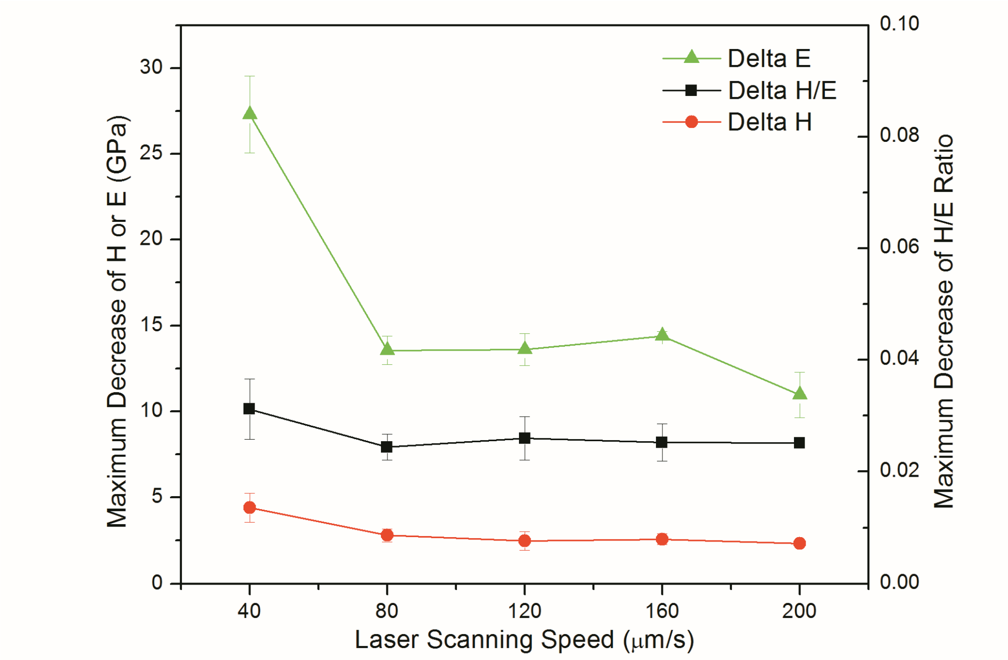

Figure 2.15: Maximum decrease of modulus (E), hardness (H), and hardness to Young's modulus ratio (H/E) of 200nm depth nanoindents inside the femtosecond laser-irradiated regions (same pulse energy level of 30 μJ with various scanning speeds.) Error bars denote standard error.

2.4.5 Fracture Toughness Comparison

Cracks were produced in the glass using 2 μm depth displacement-controlled and 440 mN load-controlled nanoindentation tests. Due to the feature size and the residual imprint size, only one or two indents could be placed on each feature as shown by the reflection DIC optical micrograph in Fig. 2.16. After indentation, the fused silica samples were scanned by AFM to investigate and measure the final crack lengths, *c*, from the center of the residual impression to the ends of cracks at specimen surface as shown in Fig. 2.17. The decrease in *H/E* ratios of the affected regions as shown in the previous section, which represents highly plastic behavior, will cause the larger impression lengths, a, measured from the center of the contact to the corners of the impression. As expected, the final crack lengths, *c*, which should have a direct relationship with the impression lengths were larger in the affected regions were created by both load- and displacement-controlled nanoindentations.

From the final crack length, *c*, max load, *P*, and the *E/H* ratio, the fracture toughness, K_{IC}, in the femtosecond laser-irradiated regions was calculated as a function of laser pulse energy and laser scanning speed and compared to the values from the untreated regions as shown in Fig. 2.18. Although the higher *E/H* ratios of the modified materials enhance the residual forces which drive the crack, the power of the *E/H* term is three times less than that of the *c* term in Eq. (2.5). Thus, the fracture toughness is decreased comparing to the untreated regions. However, the brittleness index H/K_C in the affected region is decreased as well, which corresponds to the increase in ductility index. As shown previously in Fig. 2.14 and Fig. 2.15, the *H/E* ratios were more reduced

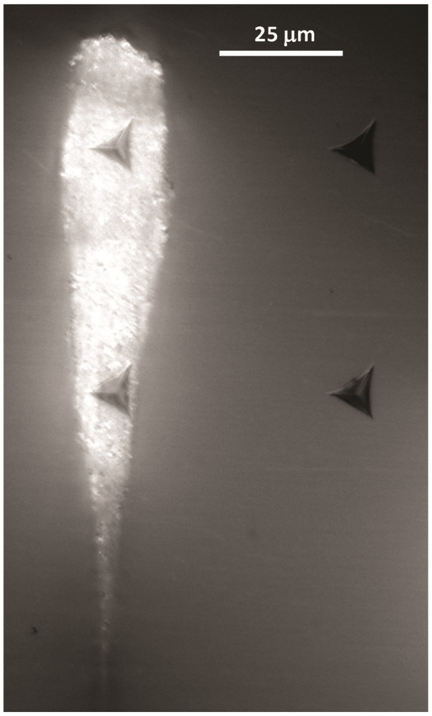

Figure 2.16: Reflection DIC optical microscopy of 2 μm depth nanoindents on and off the femtosecond laser-irradiated region for fracture toughness measurements.

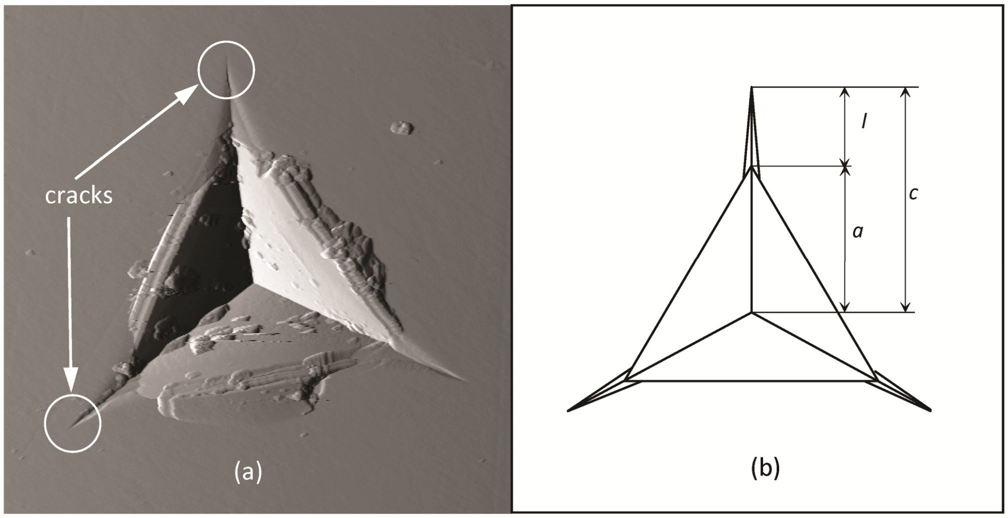

Figure 2.17: (a) AFM scan (the derivative of topography) of 2 μm depth indentation (b) Crack parameters for Berkovich indenter. Crack length c is measured form the center of the residual impression to the tip of crack at specimen surface.

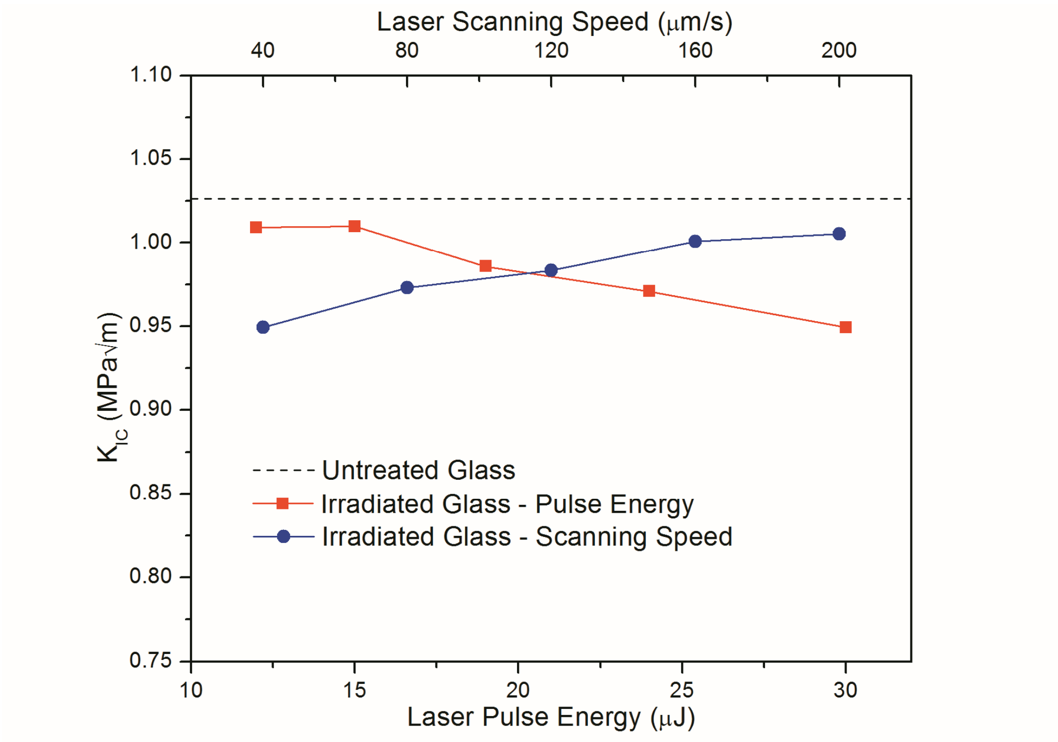

Figure 2.18: Comparison of fracture toughness measured by crack-induced indentation method between untreated and irradiated regions at 30 μJ pulse energy with various scanning speeds, and at different pulse energy levels with 0.04 mm/s scanning speed of fused silica sample.

in cases of increased laser pulse energy and decreased laser scanning speed. The increase in *E/H* ratios and the larger crack lengths, *c*, in cases of increasing pulse energy or decreasing scanning speed, cause decreasing trends of fracture toughness as shown in Fig. 2.18. It is shown that the maximum decrease is less than 10%, and the decrease in fracture toughness can be minimized if lowering the pulse energies or increasing the scanning speeds.

2.5 Conclusion

The interior of fused silica was irradiated by femtosecond laser pulses with pulse energies higher than the threshold for multiphoton and avalanche ionization. The morphology of the affected regions has been investigated, and it has been observed that the feature size increased in both height and width with an increase of the laser pulse energy or with decrease of the scanning speed. The aspect ratios remain more-or-less constant with pulse energy due to the constant size of focal volume and constant interaction time. Further, an increase with scanning speed is due to reduced interaction time and the preferable direction of heat conduction caused by the differences in temperature gradients between the radial and longitudinal directions. Spatially resolved measurements of mechanical properties, i.e. hardness, Young's modulus, *H/E* ratios, etc., on cross sections of the affected regions were performed. A decrease in the Young's modulus and hardness were observed due to higher content of the NBOHC in treated regions that cause lower connectivity of the atomic structure caused by energetic pulse interaction with the material. However, the new structural material exhibits greater plastic behavior, and the ductility increases. This study has also shown that the fracture toughness is slightly decreased (< 10%) and the processing conditions of this study could be used for transmission welding applications. Furthermore, this study has shown that the decrease in fracture toughness can be minimized by lowering the laser pulse energy or increasing the laser scanning speed.

Chapter 3: Transmission Welding of Glass by Femtosecond Laser: Mechanism and Fracture Strength

3.1 Introduction

Glasses are widely used in various flat panel displays and biomedical applications. Joining techniques of glasses are usually based on the use of an adhesive agent or interlayer. Laser beam welding is considered to be a highly flexible technique with potential for joining glasses. The main advantages of laser welding over processes such as adhesive joining and anodic bonding are that the energy is supplied without physical contact to the workpiece and can be selectively coupled to the desired joining area, respectively. Due to the high level of transmission of light through transparent materials, glass-glass joining by conventional lasers requires an interlayer or opaque material between the top and bottom pieces to absorb the laser energy. Due to the non-linear absorption characteristics of femtosecond lasers, however, transmission welding of transparent materials without an interlayer is possible when the laser beam is tightly focused on the interface.

Two different regimes of transmission welding by ultrashort pulsed lasers have been identified. Welding in the low repetition rate regime (1-200 kHz) and high repetition rate regime (>200 kHz) is dependent on whether the time interval between successive pulses is longer or shorter than the characteristic time for heat diffusion outside the focal volume [1]. Tamaki et al. [2] first demonstrated welding between two silica glass plates without a light-absorbent intermediate layer using a low repetition rate femtosecond laser. Watanabe et al. [3] then reported the welding of dissimilar transparent materials using the same femtosecond laser, and also investigated the parameters that resulted in joining by varying the laser pulse energy and the translation velocity.

To this point, however, there have been no morphological studies of the weld seam and the geometry of the weld in this low repetition rate regime is not well understood. Tamaki et al. [4] also reported on laser micro-welding of transparent materials based on a localized heat accumulation effect using high repetition rate femtosecond laser irradiation, and performed a simple tensile test after welding to estimate the joint strength. The testing procedure, however, was not precise due to its inability to continuously increase the applied load. Further studies [5–7] on the possibility of ultrashort pulsed laser welding of borosilicate glass substrates in the high repetition rate regime have been reported; however, there has been no quantitative evaluation of joint strength and no studies on the mechanical properties of the weld seam.

There are many attempts to simplify the problem by characterizing mechanical properties of the molten region irradiated by an ultrashort pulse laser inside a single piece of transparent material. Miyamoto et al. [8] evaluated the mechanical strength of the laser-melt zone using a three-point bending test, and showed that the strength in that zone was as high as in the un-irradiated base material; however, the sample had to be polished to locate the laser induced feature on the bottom surface of the test sample in order to maximize the tensile strength. Borrelli et al. [9] performed a double torsion test to measure fracture toughness, and revealed that the apparent fracture toughness is increased within the laser-treated area. Bellouard et al. [10] used nanoindentation tests to show an increase in Young's modulus within the laser treated zones of fused silica irradiated by femtosecond pulses with high repetition rate; however, these measurements were not constrained to within the treated regions. Kongsuwan et al. [11] performed spatially resolved nanoindentation tests and revealed a decrease in Young's Modulus and hardness, and an increase in ductility in regions of fused silica irradiated by femtosecond laser pulses with low repetition rate. The mechanical properties and strength of real weld seams rather than of features created inside single-piece specimen, however, still requires further investigation.

In this study, transmission welding using a femtosecond laser at a low repetition rate has been performed to investigate the morphology and mechanical properties of the weld zone. The role and effect of the gap at the interface between two transparent material plates on the welding and joining mechanisms have also been investigated. Differential interference contrast optical microscopy is employed to study the morphology of the weld cross section, and a numerical model is developed to predict the feature shape. The possibility of using the absorption volume predicted by the model as a guideline for selecting processing parameters to get a desirable weld shape is also discussed. Spatially resolved nanoindentation is used to investigate the changes in mechanical properties, and indentation fracture analysis is performed to study the strength of the material in the weld seams.

3.2 Background

3.2.1 Formation Mechanism of Transmission Welding by Femtosecond Laser

When a femtosecond laser beam is tightly focused by objective lens on the interface of two transparent material plates, the laser intensity at a focal region becomes extremely high resulting in nonlinear absorption. Due to the Gaussian temporal profile of a femtosecond laser pulse, the leading edge of the converging laser pulse starts breakdown the material at or above the focal plane when the intensity reaches the material ionization threshold, and the subsequent portions of the laser pulse with higher intensity then produce breakdown still further above the focal plane where the beam diameter is larger [12,13] leading to a teardrop-shaped absorption volume.

At the end of the femtosecond laser pulse, the laser energy absorption process is completed, and a hot-electron plasma will be almost completely confined within the absorption volume with its surface area partially exposed to the air gap inevitably existing between the two plates. When the electrons have transferred their energy to the ions of the material, hydrodynamic motion starts, and a shock wave emerges from the energy deposition zone [14]. The average pressure, P_{avg}, in the absorption volume, V_{abs}, that drives the shock wave can be calculated as [15]:

$$P_{avg} \approx Q_{dep} = \frac{AE_p}{V_{abs}} \tag{3.1}$$

where Q_{dep} is the total deposited energy density, A is the absorption coefficient and E_p is the laser pulse energy. When two parallel transparent material plates are pressed together to have a very small gap, the van der Waals force per unit area, F_{vdw}, between the two plates is given by [16]:

$$F_{vdw} = \frac{0.162hc}{d^4\pi^3}\left(\frac{n_\infty^2 - 1}{n_\infty^2 + 2}\right)^2 \tag{3.2}$$

where d is the distance between plates, h is the Planck's constant, c is the speed of light, and n_∞ is the refractive index of the plates at infinite wavelength. The shock pressure in the absorption volume due to ultrafast laser processing is considerably higher than the van der Waals force per unit area between the two plates. Considering model of a beam simply supported at both ends and subjected to a concentrated load at any point [17], the gap at the interface is increased by a deflection, δ, which can be written as:

$$\delta = \frac{2\left[\left(P_{avg} - F_{vdw}\right)\pi w_{xy}^2\right]ba\left(l^2 - a^2 - b^2\right)}{6lEI} \tag{3.3}$$

where w_{xy} is the radius of the absorption volume, l is the distance between both supported ends, a and b are the distance from the load point to each supported end, E is the Young's modulus of the material, and I is the area moment of inertia. This deflection is approximated from the average pressure in Eq. (3.1) which is a simplified model with a linear relationship to energy density. However, the pressure inside the absorption volume could be a non-linear function of energy density due to phase transition. After the femtosecond laser absorption process, the free electrons and the lattice will attain a local thermodynamic equilibrium in a time scale on the order of picoseconds [15] after which the materials will be in a superheated state [18]. In addition to shock-wave emission, the absorption volume will undergo a thermal process in which phase transitions take place. For high levels of superheating, corresponding to high excitation energy density, nucleation of gas bubbles or phase explosion can occur, and a heterogeneous phase of vapor and liquid droplets may develop [19,20]. The nucleation of gas bubbles causes an increase in the pressure within the absorption volume [20]. This could result in greater deflection of the plates and possible ejection of the material [20,21].

3.2.2 Numerical Analysis of Absorption Volume

In practical, most of the ultrashort laser pulses from mode-locked lasers are a transform-limited pulsed beam, in which case, the temporal shape of a pulse is a sech-function. However, for the sake of simple mathematical manipulations, the temporal shape can often be approximated with a Gaussian function [22]. Based on the fundamentals of laser beams and optics, in order to accurately capture the shape of the absorption volume, a numerical model should be constructed by considering the assumed Gaussian temporal distribution of laser power, $P(t)$, within the laser pulse duration as given in Eq. (3.4) as well as the Gaussian spatial distribution of the laser intensity, $I(x, y, t)$, as given in Eq. (3.5).

$$P(t) = \frac{E_p\sqrt{4ln2}}{\sqrt{\pi}t_p} exp\left(-4ln2\frac{\left(t-2t_p\right)^2}{t_p^2}\right) \tag{3.4}$$

$$I(x,y,t) = \frac{2P(t)}{\pi R_0^2} exp\left(\frac{-2r^2}{R_0^2}\right) \tag{3.5}$$

where E_p is the laser pulse energy, t_p is pulse duration, $r = \sqrt{x^2+y^2}$ is the distance from the center of laser beam, R_0 is the 1/e^2 radius of the unfocused beam, and t is time. A laser beam with an intensity profile corresponding to Eq. (3.5) will converge to a diffraction-limited spot radius, w_o, and the beam waist as a function of distance from the focal plane, $w(z)$, can be calculated as:

$$w(z) = w_0\sqrt{1+\left(\frac{\theta z}{w_0}\right)^2}; \qquad w_0 = \frac{M^2\lambda}{\pi NA} \tag{3.6}$$

where z is the distance from the laser focal plane, Θ is the half-convergence angle of laser beam coming into the focus, M^2 is the laser quality factor, λ is the laser wavelength, and NA is the numerical aperture of an objective lens. At each point in time during the pulse duration, the spatial distribution of the laser intensity is described by Eq. (3.5). As the beam propagates into the sample, the width decreases as described by Eq. (3.6), and at some point, the laser intensity is absorbed at various locations forming a plasma when it reaches the intensity threshold, I_{th}, of the material given by [23]:

$$I_{th} = \left(\frac{n_c}{n_a\tau_{rec}\beta_{mpi}}\right)^{1/n_{ph}} \tag{3.7}$$

where n_c is the electron critical density, n_a is the density of neutral atoms, β_{mpi} is the field ionization coefficient, and n_{ph} is the number of absorbed photons. The breakdown will start closest to the focal plane and move upwards along the beam axis during the first half of the pulse duration due to the Gaussian temporal distribution of the laser power. This requires a smaller beam spot to reach the threshold intensity at lower powers and a larger beam spot at higher powers. The absorption volume is determined by combining all of the points where absorption occurred during the first half of the laser pulse. The energy in the second half of pulse duration will be absorbed in this absorption volume to generate a higher-density plasma in the absorption volume.

3.2.3 Fracture Strength of the Weld Seam

The material in transmission welded region possesses properties different from that in the initial state. Nanoindentation is a non-destructive test capable of extracting elastic modulus and hardness of the specimen, and in addition to those properties, it is widely accepted that K_{IC} can also be obtained by measuring the post-indentation radial crack size emanating from the indent as a function of load as shown by Lawn : $K_{IC} = k\left(\frac{E}{H}\right)^{1/2}\frac{P}{c^{3/2}}$ [24]. For triangular pyramid indenters such as a Berkovich or cube corner, the profile of the radial crack is more likely a semi-elliptical geometry [25] rather than halfpenny shape observed for Vicker indenters. For an elliptical crack embedded in an infinite body in tension, Irwin [26] derived the stress intensity factor, K_I, using 3D potential functions as:

$$K_I = \frac{\sigma\sqrt{\pi b}}{E(k)}\left\{sin^2\theta + \frac{b^2}{a^2}cos^2\theta\right\}^{1/4} \tag{3.8}$$

where σ is the tensile stress, a and b are major and minor radii of an elliptical crack, Θ is the angle from the major axis, and $E(k)$ is a complete elliptic integral of the second kind defined as:

$$E(k) = \int_0^{\pi/2}\sqrt{1 - k^2sin^2\varphi}\, d\varphi; \qquad k = \sqrt{1 - \frac{b^2}{a^2}} \tag{3.9}$$

Although no closed-form solution is available for semi-elliptical surface cracks, proper numerical factors can be used to account for the effect of free surfaces. The free surface factor tends to 1.1215 for long surface cracks, and would tend to 1 for semicircular shapes. The free surface factor, *f*, is typically written as [27]:

$$f = 1 + 0.1215(1 - \frac{b}{a}) \tag{3.10}$$

Indentation testing at high loads will initiate radial cracks with known length, *c*, from the center of indentation point and with depth, *d*, assumed equal to the indentation depth. Therefore, assuming a semi-elliptical geometry with one free surface, the stress intensity factor at the tips of the post-indentation radial cracks under an applied tensile stress will be the following:

$$K_I = \frac{\sigma}{E(k)}\sqrt{\frac{\pi c}{2}}rf; \qquad r = \frac{b}{a} = \frac{d}{c/2} \tag{3.11}$$

where *r* is depth-to-length ratio of surface semi-elliptical cracks induced by a Berkovich indenter. Depending on the application, the weld seams may be subjected to different types of loading such as tension, shear, etc. Mode I (opening mode) fracture is the most applicable to glasses since they generally fail in tension. From the post-indentation radial crack, if the material is under a tensile load, fracture will occur when the stress intensity factor at the crack tip, K_I, reaches the critical stress intensity factor, K_{IC}, which is a physical characteristic of the material. Using a power series to express the *E(k)* function in Eq. (3.12) and accounting for only the first four terms, the tensile fracture stress, σ_f, of the materials can be obtained using Eq. (3.13).

$$E(k) = \frac{\pi}{2}\sum_{0}^{\infty}\left[\frac{(2n)!}{2^{2n}n!^2}\right]^2 \frac{k^{2n}}{1-2n} \tag{3.12}$$

$$\sigma_f = \frac{K_{IC}\sqrt{\pi}[175/256 + 103r^2/256 + 27r^4/256 + 5r^6/256]}{2\sqrt{c}r[1 + 0.1215(1 - r)]} \tag{3.13}$$

where K_{IC} is the fracture toughness from indentation. Due to the presence of the crack, the residual strength of the structure decreases progressively with increasing crack size.

3.3 Experimental Setup and Characterization

Transmission welding is performed using a chirped amplified Ti:Sapphire laser system which outputs high energy ultrashort pulses with 800 nm wavelength and 130 fs pulse duration at a 1 kHz repetition rate. Commercial grade borosilicate glass (BK7) 1.0 mm thick was sectioned into 6 mm x 12 mm samples and cleaned by RCA-cleaning [28], and were subsequently pressed together at a pressure of roughly 2 MPa for 10 min. The pressed samples were super glued on the both ends before being fixed to a motorized linear stage and processed by femtosecond laser pulses. The laser beam was focused by a 40x objective lens with a *NA* of 0.60 at the interface between the plates. A schematic diagram of the experimental setup is illustrated in Fig. 3.1.

After the femtosecond laser treatment, the samples were then ground with carbide papers and polished with cerium-oxide and a leather polishing pad to have smooth surface. Reflective light differential interference contrast (DIC) optical microscopy, which can reveal more contrast and details in the feature morphology, was used to obtain the cross section view of the weld seams. The weld zone was examined via nanoindentation using a three-sided Berkovich indenter tip to characterize the mechanical properties. Arrays of 100 nm deep nanoindents with 3 μm spacing in the x and z directions were conducted to cover the cross section of both the weld zone and a nearby unaffected regions to provide a spatially resolved measurement of material properties. 150gf to 350gf load nanoindents were also performed on the features to induce cracks in order to

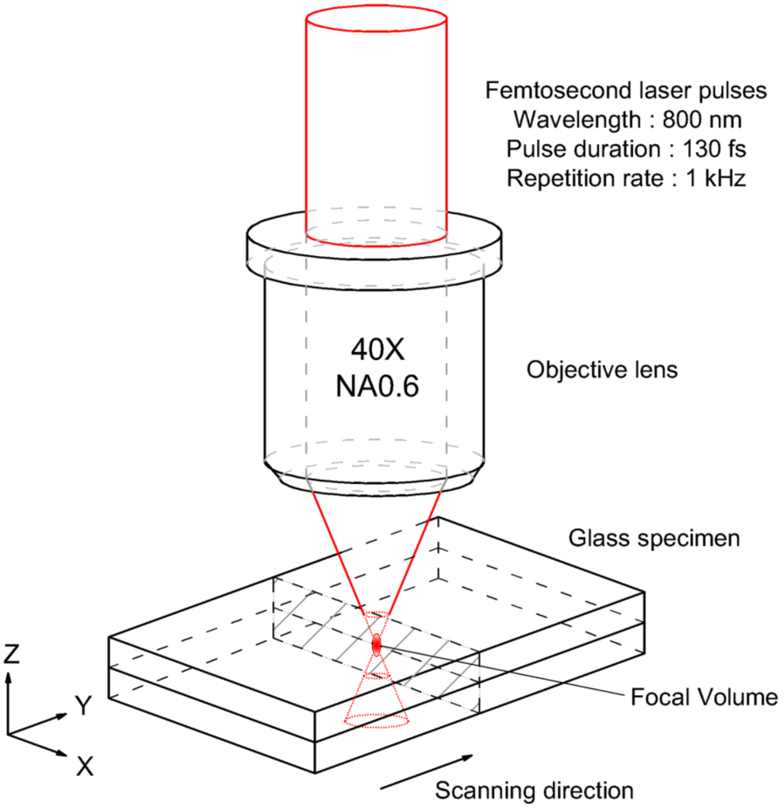

Figure 3.1: Schematic illustration of experimental setup. The laser beam is focused onto the interface of two borosilicate glass plates, and the scanning direction is along the y-axis.

investigate the fracture toughness of the weld zones. Different laser pulse energy conditions were used to investigate the effects of laser pulse energy on morphology and mechanical properties of the weld seams.

3.4 Results and discussion

3.4.1 Weld Formation and Geometry

While other studies [6–8] have used high precision flatness glass plates and required the gap between the plates to be less than λ/4 in order that the welding to succeed, BK7 glass plates with standard flatness of 3-5 waves/inch were used in this study. Figure 3.2 shows the transmission welded cross section (xz-plane) of two BK7 glass plates with the processing condition of 10 μJ

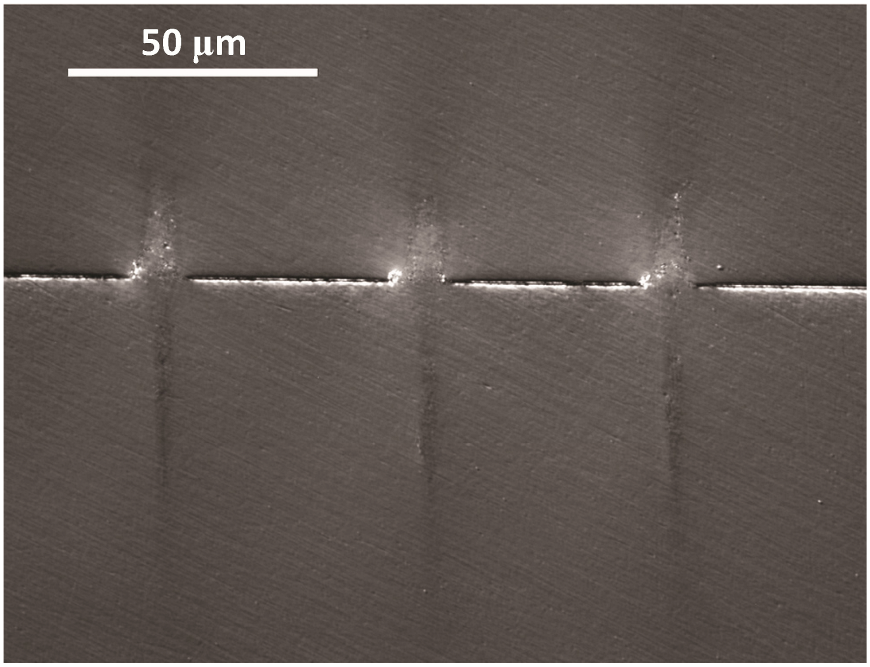

Figure 3.2: Reflective DIC optical microscopy of cross section view (xz-plane) of a weld seam (laser pulse energy of 10 µJ, scanning speed of 0.02 mm/s, and repetition rate of 1 kHz.)

laser pulse energy and 0.02 mm/s laser scanning speed from reflective DIC optical microscopy. There is continuity of the material from the top piece to the bottom piece in the processed region. From this figure, it can also be observed that the shape of the affected region is a teardrop shape and it looks similar to the morphology of femtosecond laser modified regions inside a single piece of a material [11]. AFM topography was also carried out to image cross section profiles across both welded and reference regions as shown in Fig. 3.3 (a) and Fig. 3.3 (b). Although the gap between the plates is not as low as λ/4 due to the standard flatness of the plates, it is very clear that the two borosilicate glass plates were joined. In order to investigate the possibility of connecting multiple weld lines to have a larger weld seam, transmission welding of multiple laser scanning lines with the spacing between lines less than the weld width from the single line case was performed. Figure 3.4 shows the cross section view (xz-plane) of a sample processed with five overlapping weld lines. The individual weld lines cannot be distinguished, and it can be

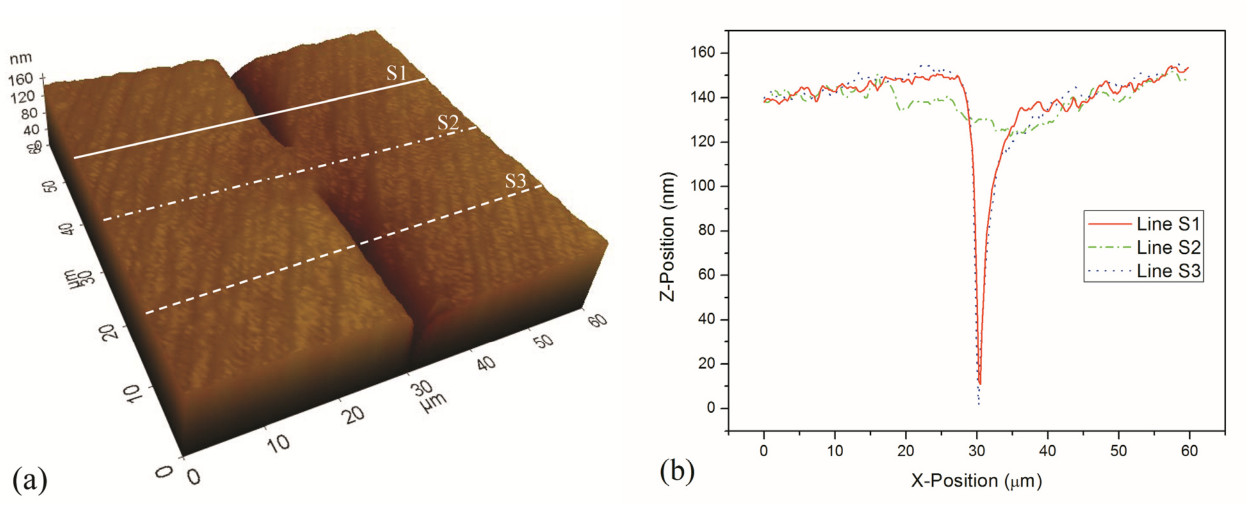

Figure 3.3: (a) 3D AFM topography on the cross section (xz-plane) of a weld seam (laser pulse energy of 10 µJ and scanning speed of 0.02 mm/s) and (b) AFM line profiles across glass interface near and on the weld seam.

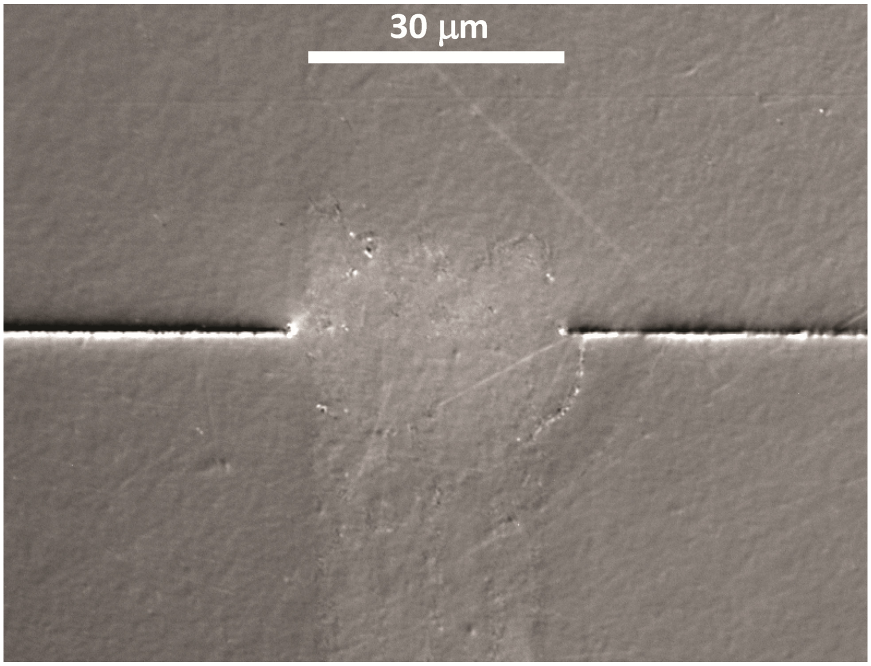

Figure 3.4: Reflective DIC optical microscopy of cross section view (xz-plane) of a multiple-line weld seam (laser pulse energy of 10 µJ, scanning speed of 0.02 mm/s, and repetition rate of 1 kHz, 5 scanning lines with 6 µm spacing between lines.)

concluded that the transmission welding of large areas may be performed by automatically controlling the movement of a positioning stage and overlapping welds with a spacing less than the width of a single-line weld seam.

Due to its low repetition rate and the presence of an air gap at the interface, the pressure evolution inside the absorption volume will play an important role in the mechanism of weld seam formation. The glass and air inside the absorption volume that are ionized and experience high temperatures and high pressures will eventually be transformed and solidified, and become the weld joint and surrounding affected regions. According to the numerical analysis of the absorption volume in section 3.2.2, when a 10 μJ pulse energy is used, the absorption volume is approximately 9.08×10^{-16} m^3, and the surface area of this absorption volume is approximately 4.80×10^{-10} m^2. An average pressure of 11.0 GPa, which calculated from Eq. (3.1), is assumed to be generated inside the absorption volume. From Eq. (3.3), this pressure causes deflection of the plates in the z-direction of roughly 44 nm if the weld line is 1 mm from a glue-supported end or 476 nm if the weld line is located at the center of the workpiece. The standard roughness of the glass plates and the images in Fig. 3.2 to Fig. 3.4 suggest that the final gap at the weld interface is approximately 2 μm. Assuming the initial gap is less than 2 μm, due to the effect of laser energy deposition, the gap will be opened wider, and the surface area of the absorption volume will be almost completely confined by the surround solid material with approximately 10% of the area exposed to the open space within the gap. Therefore, depending on the average pressure and the area which is exposed to open-space, some fraction of the post-shock state material could be driven out of the absorption volume to the surrounding area at the interface between the plates as debris.

To verify this mechanism, the top view (xy-plane) of weld lines processed with different pulse energies as shown in Fig. 3.5 (a), were analyzed. From the numerical analysis in section 3.2.2, the absorption volume and the deposited energy density increase at a higher rate than laser pulse energy; therefore, as defined by Eq. (3.1), the average pressure inside the absorption volume decreases with increasing laser pulse energy. Due to higher average pressure and higher deposited energy, debris which was driven out to the area surrounding the welding lines is clearly observed in the two conditions on the right of Fig. 3.5 (a) using lower pulse energy 10 μJ and 20 μJ, respectively. This debris is considered to be due to the occurrence of phase explosion under these conditions. However, for the 10 μJ pulse energy condition the debris was not driven far away from the welding line compared to the 20 μJ pulse energy, as seen in Fig. 3.5 (a). This

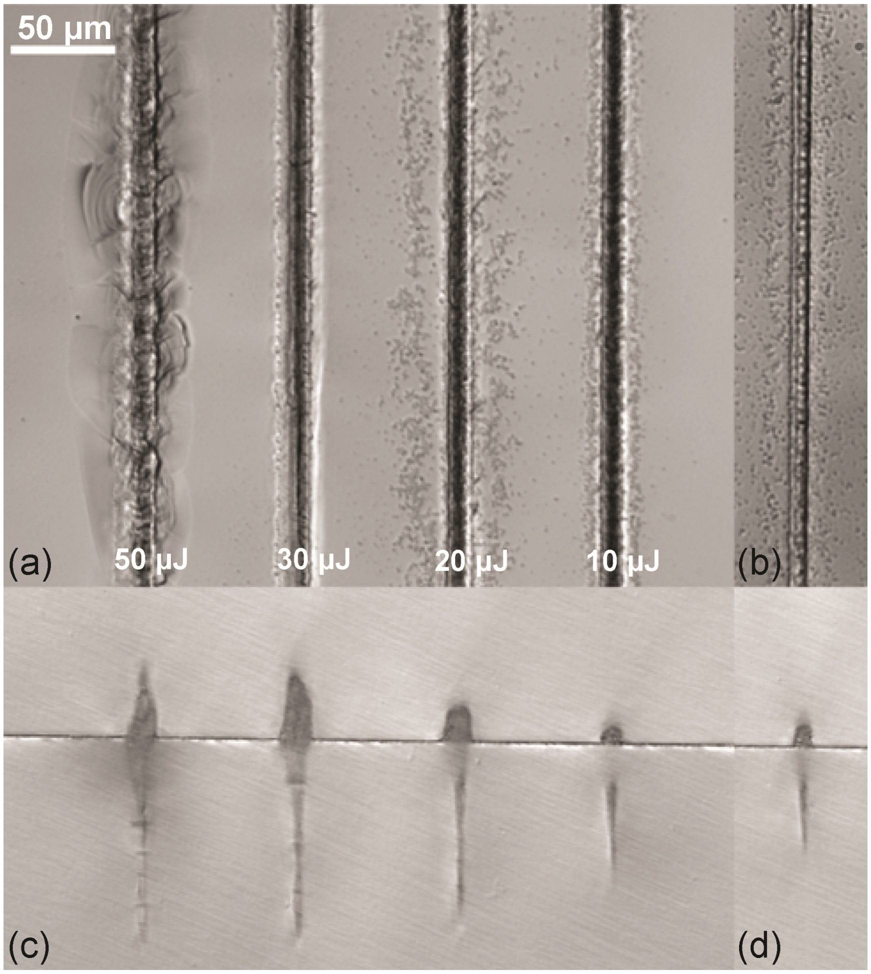

Figure 3.5: (a) Top view (xy-plane) and (c) cross section view (xz-plane) of weld seams performed at different processing conditions obtained through transmission DIC optical microscopy (laser scanning speed of 0.06 mm/s, 0.04 mm/s, 0.03 mm/s, and 0.02 mm/s respectively from the left) (b) Top view (xy-plane) and (d) cross section view (xz-plane) of a weld seam for 10 μJ and 0.02 mm/s condition.

could be due to the location of absorption volume with respect to an interface as shown in Fig. 3.5 (c). Because of its teardrop shape, the higher position of the absorption volume with respect to the interface causes the larger confined area of the absorption volume by the surrounding material, and it implies that the shockwave pressure will be greater. Therefore, if the absorption volume is moved up as shown in Fig. 3.5 (d), the debris will be driven further from the welding line as observed in its corresponding top view in Fig. 3.5 (b). On the other hand, no debris will be observed as shown in the two conditions on the left of Fig. 3.5 (a) using pulse energy of 50 μJ and 30 μJ, respectively due to their lower average pressure and lower deposited energy density, which could not induce phase explosion. While significant cracking is observed around the leftmost weld line, this cracking is considered to be due to thermal shock rather than pressure created by the expanding plasma. The higher peak power and higher scanning speed result in a

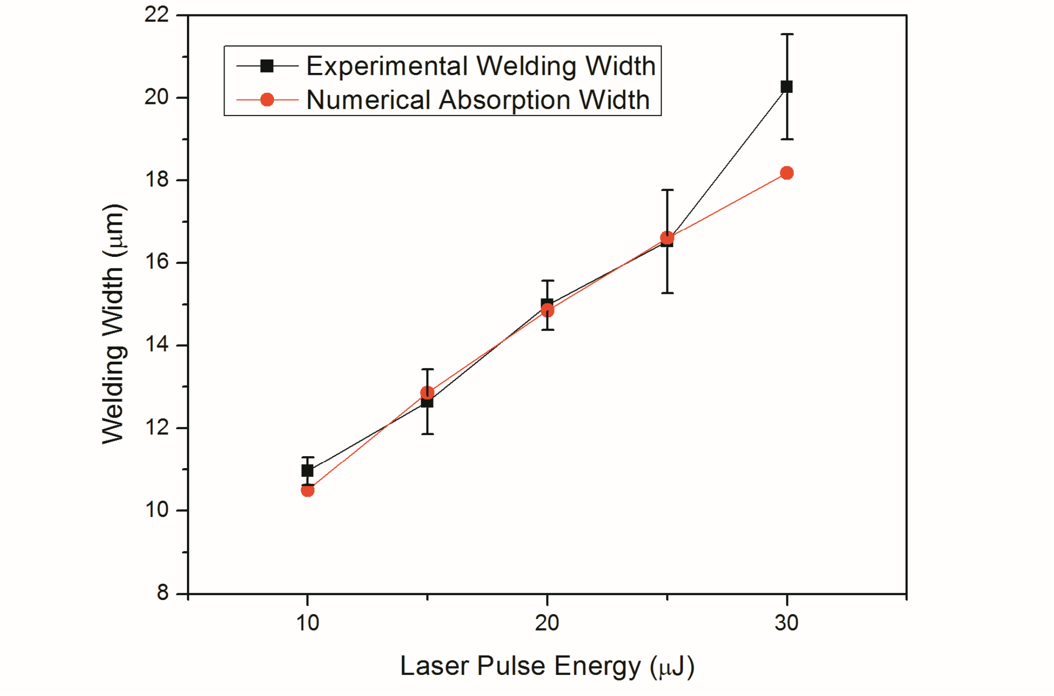

Figure 3.6: Comparison of experimental weld width and simulated absorption width at different laser pulse energies. Error bars denote standard deviation.

higher peak temperature and greater thermal gradient surrounding the absorption volume, respectively. The thermal stress overcomes the fracture stress of the material, and cracks are initiated as clearly observed in the leftmost weld line of Fig. 3.5 (a).

The effect of laser pulse energy on the weld width is shown in Fig. 3.6. The weld width should be the same order of magnitude as the width of features created inside single-piece specimen. Higher laser pulse energies have shown to result in larger widths of features in single-piece specimen [11]; therefore, it is expected that the weld width will increase in size when the laser pulse energy is increased as clearly seen in Fig. 3.6.

3.4.2 Absorption Volume Modeling

To model the absorption volume shape, one should consider both temporal and spatial distribution characteristics of femtosecond laser pulses, and also account for the focusing characteristics of a collimated laser beam through transparent materials. In a transparent material, significant absorption is not achieved below a specific intensity threshold. This model aims to determine the locations within the material that achieve this intensity as a function of time within the laser pulse duration. Fig. 3.7 illustrates the schematic flow diagram of the absorption volume modeling. From the laser pulse energy, the full-width-at-half-maximum (FWHM) pulse width, and the assumption of a Gaussian temporal profile, the distribution of power in the laser pulse duration can be determined by Eq. (3.4). Subsequently, using Eq. (3.5), the distribution of intensity in the unfocused laser spot can be calculated at each point in time during the pulse duration using the $1/e^2$ radius of the unfocused beam and the assumption of a Gaussian spatial profile. From the laser intensity at any location within the unfocused laser beam and the intensity threshold of the transparent material, the material breakdown locations in the lateral direction of

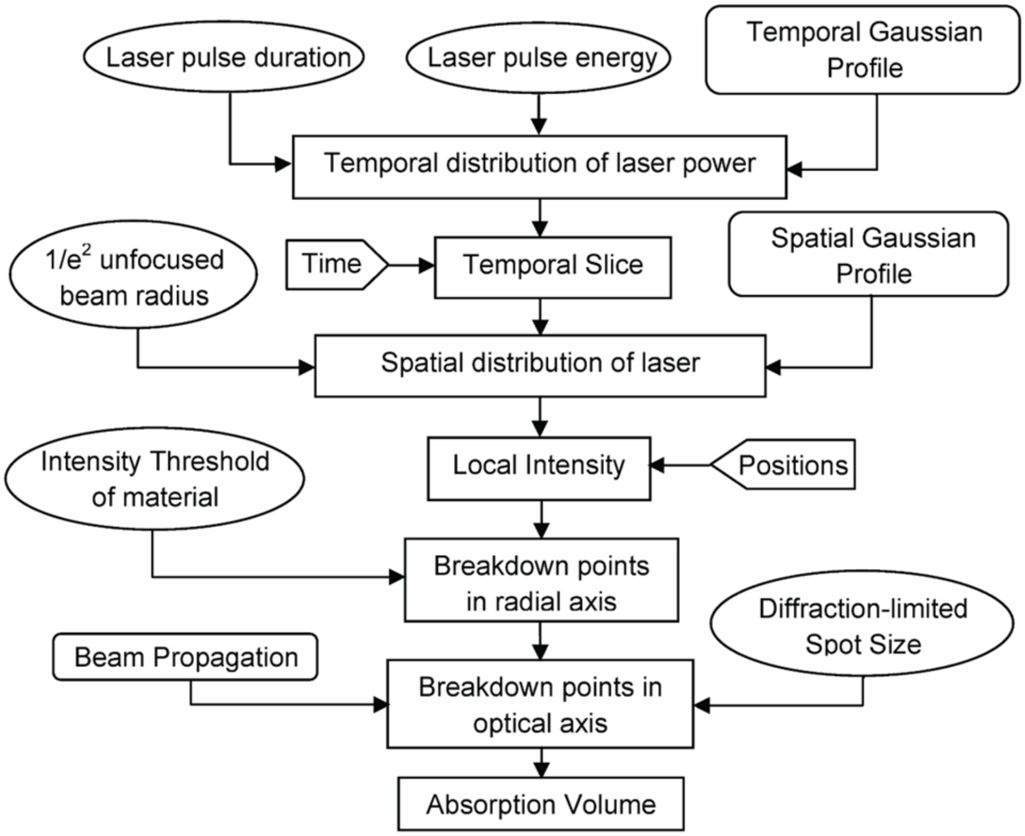

Figure 3.7: Schematic diagram of absorption volume modeling process.

the converging laser beam can be derived by considering how small the beam area should be in order that the intensity at these locations will reach the material intensity threshold. Consequently, the material breakdown locations along the optical axis can be determined using the diffraction-limited spot size and the beam propagation equation as described by Eq. (3.6). The material breakdown locations at each point in time form concave-down parabolic line which, when combined over the full temporal profile, form the absorption volume as shown in Fig. 3.8 (a) and Fig. 3.9 (a). The numerical calculations have been performed by using parameters presented in Table 3.1. Assuming a small air gap at the interface (the dielectric properties of air gap are negligible), and ignoring reflections at the interface, this model is applicable for transmission welding as well as for processing inside bulk samples.

Table 3.1: Laser, optical, and material parameters used in the absorption volume model

Parameters	Value	Unit
Laser wavelength, λ	800	nm
Laser pulse duration, t_p	130	fs
Laser quality factor, M^2	1.5	-
Laser pulse energy, E_p	10 - 30	μJ
Unfocused beam radius, R_0	6	mm
Absorption coefficient, A	0.7	-
Numerical aperture, NA	0.4 – 1.2	-
Intensity threshold of BK7, I_{th}	2.15 x 10^{13}	W/cm^2

Figure 3.8 (a) shows the simulated cross sections of the absorption volume at different laser pulse energies. The cross section shape of the absorption volume indeed looks like the teardrop shape. The width and height of cross section increase with increasing laser pulse energy corresponding to experimental results reported in other studies [11–13]. Higher laser pulse energy leads to higher peak power, which generates higher local intensities at the same spot size. Consequently, the material breakdown locations will be farther from the center in the radial axis, and will also be farther from the focal plane in the optical axis. Therefore, the height and width of the absorption volume for high laser pulse energies are greater than for low laser pulse energies as shown in Fig. 3.8 (b). The aspect ratios of the absorption volumes at different laser pulse energies are more-or-less constant; a similar trend was observed for features created in single-piece specimen in a previous study [11]. This trend agrees well with the focal volume aspect ratio calculated using the illumination point spread function, for which the ratio is constant and independent of laser pulse energy [29]. The widths of absorption volume at

different laser pulse energies were also compared to the experimental weld widths in Fig. 3.6. The simulated widths showed good agreement with the experimental ones, and followed the same trend of increasing width for higher laser pulse energy. Therefore, the absorption volume model allows for prediction of the weld width for a wide range of pulse energies.

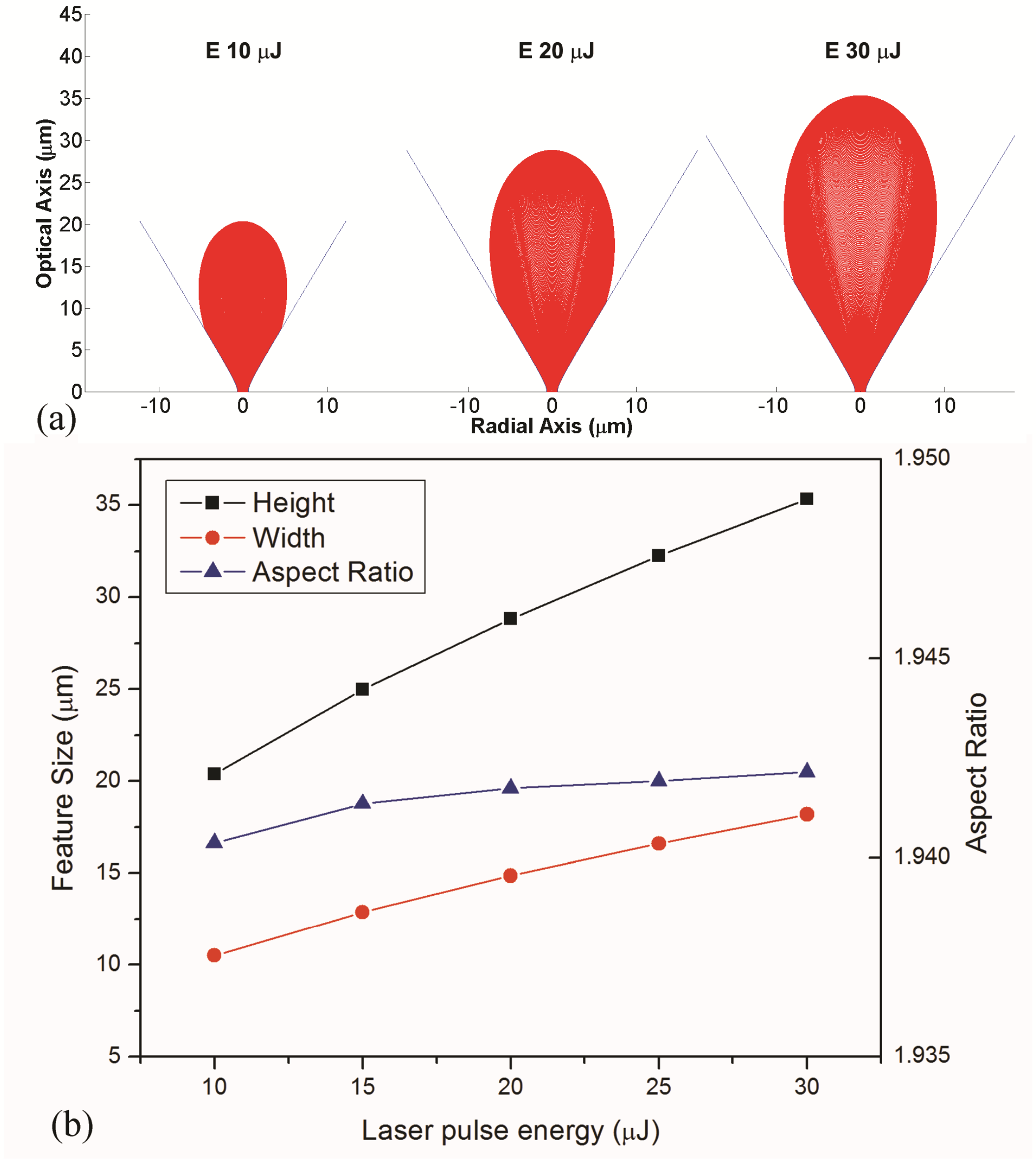

Figure 3.8: (a) Cross section view (b) height, width, and height/width ratio of modeling absorption volume at different laser pulse energies (NA 0.6)

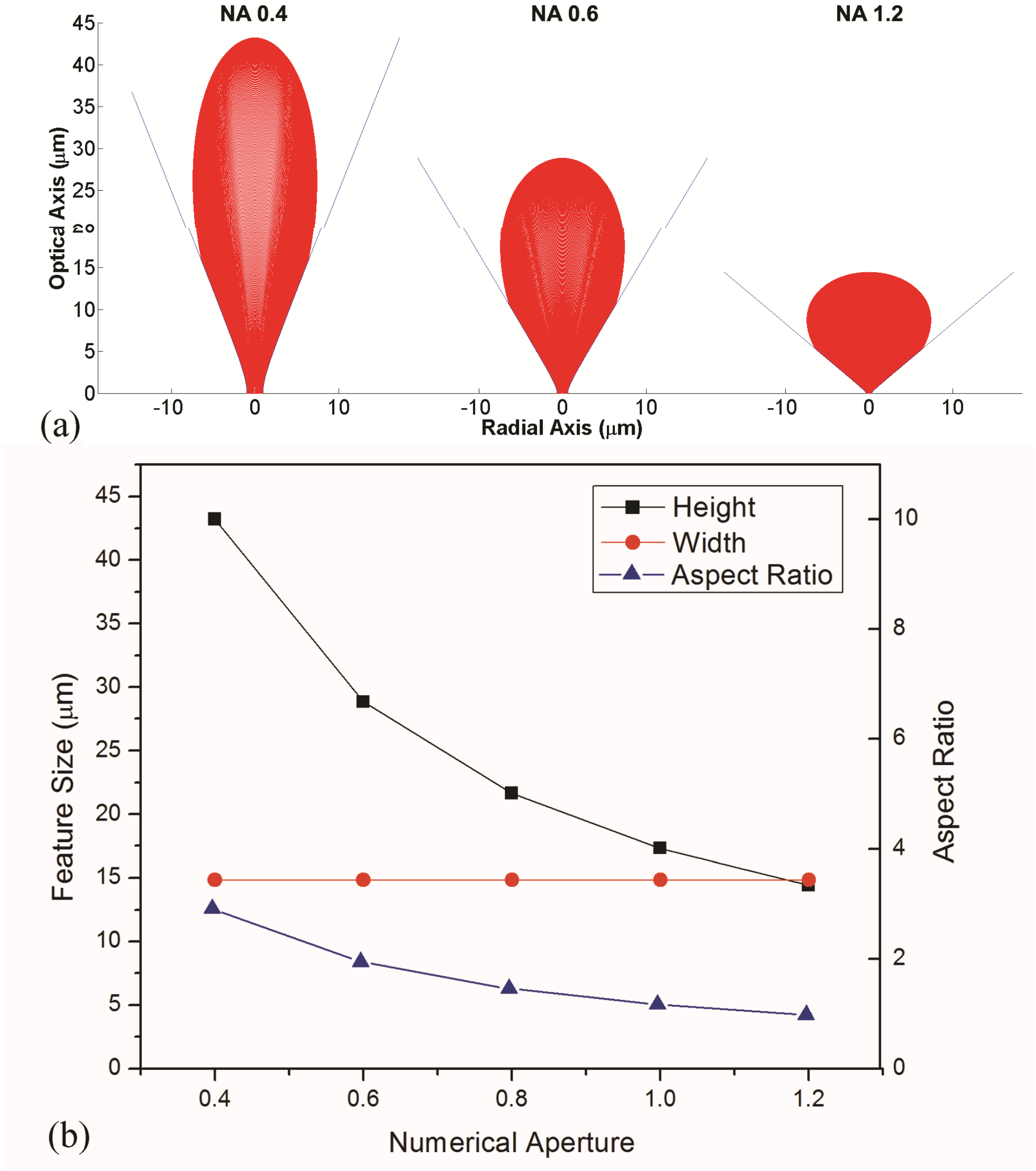

Figure 3.9: (a) Cross section view (b) height, width, and height/width ratio of modeling absorption volume at different NAs (laser pulse energy of 20 µJ)

Figure 3.9 (a) shows the simulated cross sections of the absorption volume using different numerical aperture (NA) objective lenses for a fixed laser pulse energy. For high NAs, the teardrop shape of the absorption volume tends to have more-or-less equivalent size in height and width corresponding to the experimental results of Schaffer et al. [12]. Each point within the

Gaussian intensity distribution of the unfocused laser beam requires a specific magnification to reach the intensity threshold of the material. This magnification defines the radius of the focused beam at which absorption will occur and is dependent of the NA of the objective lens. Therefore, the widths of absorption volumes are constant and independent of NA as shown in Fig. 3.9 (b). However, the corresponding breakdown locations of the material along the optical axis depend on the diffraction-limited spot size and the converging angle of the focused laser beam. For higher NAs, the unfocused laser beam is converged at a greater rate; therefore the focused beam will achieve the required magnification and radius at a location closer to the focal plane along the optical axis. The heights of the absorption volumes are thus decreased with higher NAs as shown in Fig. 3.9 (b). The aspect ratio of the absorption volume decreases with higher NAs, which corresponds well with the feature aspect ratio of the experimental results studied by Schaffer et al. [12].

As seen in section 3.4.1, the weld width depends on the laser pulse energy. The higher the energy, the wider the weld width; the height of the affected region also increases with laser pulse energy. However, minimizing the size of the region affected by transmission welding may be required for certain applications since there is less alteration of material properties. It can be seen from the numerical model that the higher the numerical aperture, the smaller the aspect ratio and height of absorption volume. Therefore, the absorption volume model could be used to choose the optimal optical and laser processing parameters that should be used in order to get a desirable weld shape. The initial results suggest that higher laser pulse energies and higher numerical apertures are more desirable for transmission welding due to their wider weld widths and smaller affected regions.

3.4.3 Mechanical Properties of the Weld

Figure 10 shows the reflective DIC optical image of a nanoindentation array on the cross section (xz-plane) of a transmission welded line of two borosilicate glass plates. The indents were performed to a depth of 100 nm with a spatial resolution of 3 μm and covered both the unaffected and welded regions. At same maximum indentation depth, the maximum load of an indent performed in the unaffected region is greater, and its residual depth is shallower than in the welded region, which implies that the mechanical properties in transmission welded region are changed through processing. In order to understand how mechanical properties change, and how they relate to the weld strength, the spatially resolved nanoindentation and indentation fracture will be drawn into consideration.

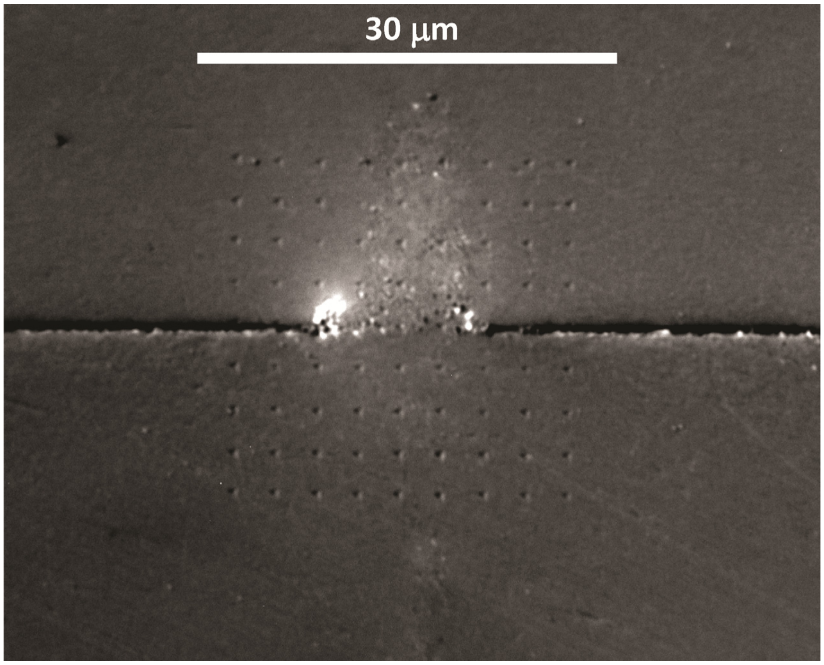

Figure 3.10: Reflective DIC optical image of spatially resolved nanoindentation array (100nm deep indents with 3 μm spacing) on the cross section (xz-plane) of a weld seam (laser pulse energy of 10 μJ and scanning speed of 0.02 mm/s).

Figure 3.11 (a) and Fig. 3.11 (b) illustrate the contour plots of Young's modulus to hardness (E/H) ratios corresponding to the array of 100 nm deep nanoindents with 3 um spacing on the cross section (xz-plane) of a transmission welded region and on the cross section of a feature inside a single-piece bulk specimen irradiated by the same laser pulse energy of 10 μJ, respectively. The thick white lines in Fig. 3.11 (a) represent the weld interface. Compared to their original values, the E/H ratios in the welded and treated regions are increased. The widths of the contours in these two cases are also similar; however, the E/H ratios in the weld seam show two separate regions with high E/H ratios. Fig. 3.12 (a) shows the variation of E/H ratios along the three horizontal lines (H_1 – H_3) across the weld seam of Fig. 3.11 (a). The vertical dash-dot line in this figure represents the optical axis, which is the line in z-direction that passes through the center of the weld seam. Due to the effect of the air gap at the interface, some fraction of laser energy may be reflected back to the top piece, and an air gap with a lower breakdown threshold may be ionized during irradiation and partially obstruct the nonlinear absorption of laser beam in the bottom piece of material. Therefore, less energy is coupled into

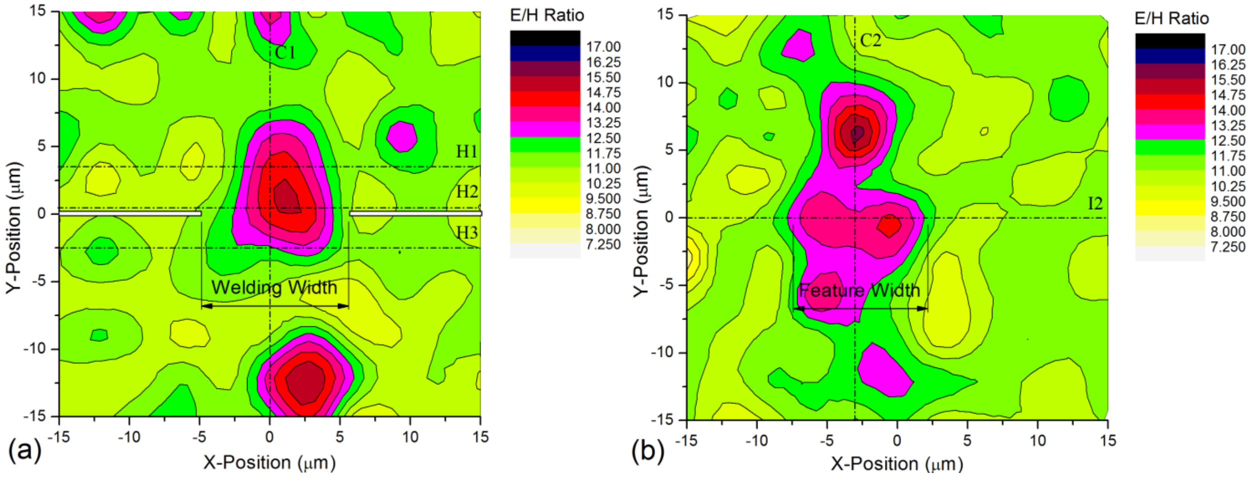

Figure 3.11: Spatially resolved determination of the ratio between Young's modulus and hardness (E/H) on the cross section of (a) a welded region of two-piece specimen (b) a feature inside one-piece specimen using the same laser pulse energy of 10 uJ and scanning speed of 0.02 mm/s. The contour maps correspond to the array of 100 nm depth nanoindents with 3 μm spacing.

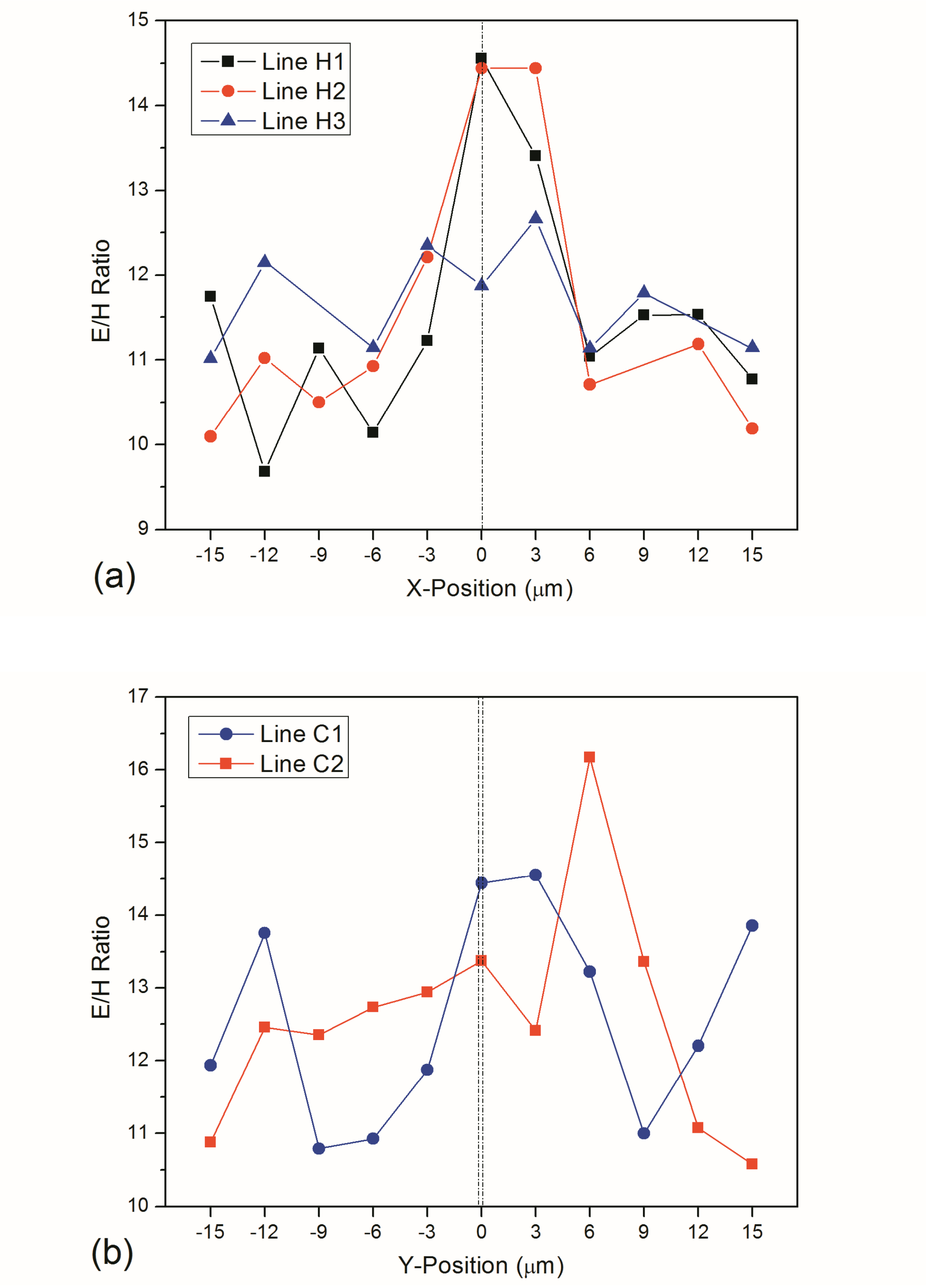

Figure 3.12: The variation of E/H ratio (a) vs. X-position along the horizontal lines (lines H1 – H3) in Fig. 3.11 (a) across the weld seam, and (b) vs. Y-position along the line C1 in Fig. 3.11 (a) across the weld seam and the line C2 in Fig. 3.11 (b) across the feature inside one-piece specimen (laser pulse energy of 10 μJ, scanning speed of 0.02 mm/s.)

the bottom portion of the absorption volume, and there is less change in mechanical properties in the region of the weld seam right below the interface as shown by the smaller increase in E/H ratios in line H_3 compared to lines H_1 and H_2 in Fig. 3.12 (a). The E/H ratios along the line C1 across the weld seam do not change gradually as in the case of the one-piece specimen shown by line C2 in Fig. 3.12 (b). Therefore, the air gap plays a significant role in the coupling of laser energy into the bottom piece during transmission welding.

From indentation analysis, higher E/H corresponds to a higher residual stress field intensity, implying a weaker elastic recovery and thus less pronounced radial crack extension during the unloading half-cycle [24]. Therefore, the E/H ratio of a material can be directly related to the fracture toughness of material, and higher E/H ratios may lead to higher fracture toughness. To confirm this effect in the transmission welded region, deeper indents were performed to induce radial cracks at the corners of the nanoindentation features. Figure 3.13 shows a DIC optical image

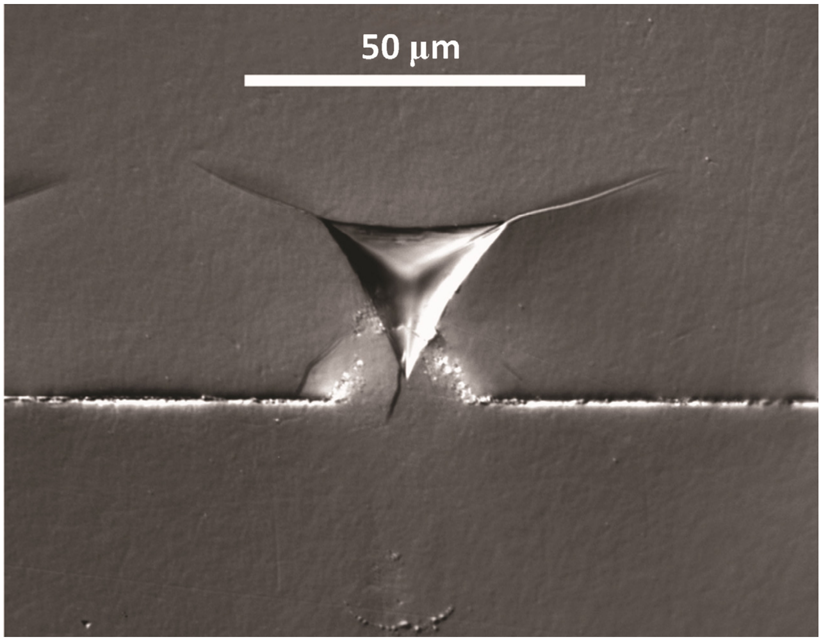

Figure 3.13: Reflective DIC optical microscopy of indentation fracture on cross section (xz-plane) of a weld seam (laser pulse energy of 30 µJ, scanning speed of 0.02 mm/s, repetition rate of 1 kHz.)

of cracks induced by a high load nanoindentation test. The bottom corner of the nanoindentation imprint is within the welded region, and the crack at the bottom corner extends across the weld at the interface between the two borosilicate glass plates. Comparing the crack lengths at the three corners of the nanoindentation imprint in Fig. 3.13, it is clear that the crack length in the welded region is shorter than those in unaffected region. Due to higher E/H ratio and shorter crack length in the transmission welded region, it can be confirmed that the fracture toughness of material inside the welded region is increased which agrees with the fracture toughness increase observed in ultrafast laser-treated areas of glasses obtained using double torsion tests by Borrelli et al. [9]. The direction of a propagating crack front can be altered by a residual stress field and since there are significant residual stresses in glasses irradiated by femtosecond lasers [30,31], the crack will be on a more tortuous path and thus more energy will be required for propagation [32].

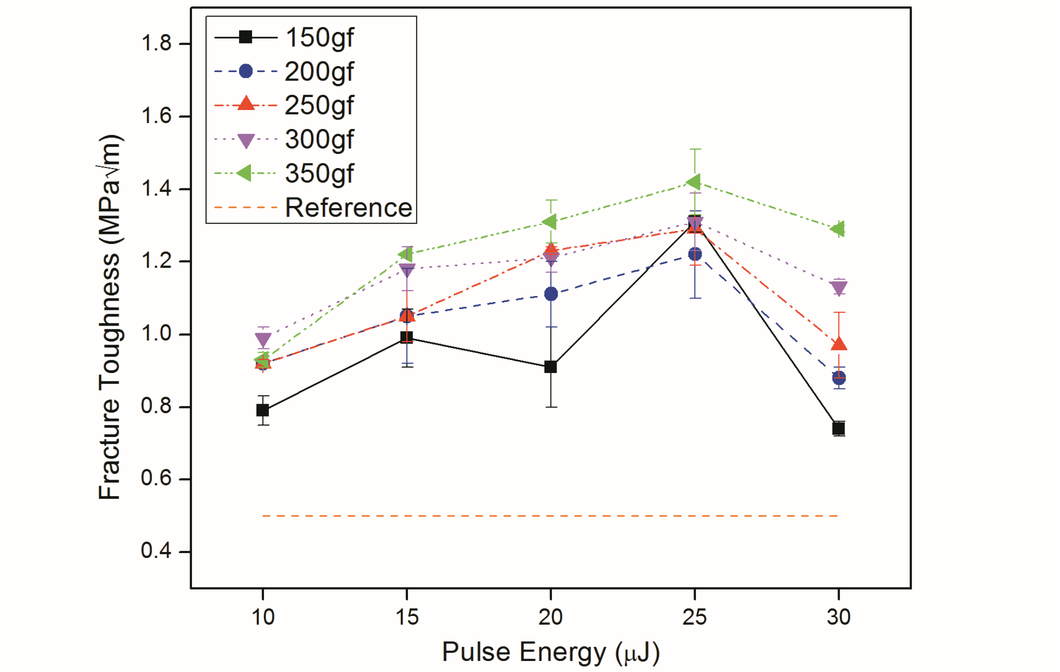

Figure 3.14: Fracture Toughness of the material in welded regions with different laser pulse energy levels (10μJ – 30μJ) at fixed laser scanning speed of 0.02 mm/s and in a reference region from indentation fracture measurements at different loads. Error bars denote standard deviation.

Figure 3.14 shows the indentation fracture toughness of material inside the weld seam compared to the reference material, and also shows the effect of laser pulse energy on the fracture toughness. In the ultrafast laser-treated region, there are more nonbridging oxygen hole centers (NBOHCs) [33] and the connectivity of the structure is decreased, and at the same time the remaining connected ring structures of material become more compact [11]. The presence of NBOHCs may help branch the main crack while a higher driving force is required to propagate the main crack through the more compact ring structure. Therefore, the fracture toughness of material in the weld seam is greater than in the reference material as shown in Fig. 3.14. The higher the laser pulse energy, the stronger the laser-matter interaction is inside the focal volume. It has been shown that there are more NBOHCs and more compact ring structures when processing is performed using higher pulse energies [33]. The presence of micro cracks, which are initially observed in the 30 uJ case and very distinctive in the 50 uJ case, has been shown in Fig. 3.5. Each of these micro cracks is a fracture surface which aids crack propagation, reducing the toughness of the material [32]. Therefore, there is an increasing trend in fracture toughness with pulse energy in the energy range of 10 – 25 μJ and the fracture toughness begins decreasing at a pulse energy of 30 μJ as shown in Fig. 3.14. It is also shown that in case of indentation field cover the area of the non-homogenous material (weld seam plus reference region), the fracture toughness calculated by nanoindentation method will be varied depending on the size of indentation filed. The higher the indentation field could affect the variation in fracture toughness as seen in Fig. 3.14.

Indentation at different levels of load will produce cracks with different lengths at the corners of indentation imprint. Assuming that these cracks have a semi-elliptical geometry, the externally applied tensile stress to fracture the material both in the weld seam and the reference regions can be calculated by Eq. (3.13). The fracture stress of a cracked plate is lower than both the strength of the uncracked material and the ultimate tensile strength. When the tensile fracture strength of materials is plotted as a function of crack length the material with higher fracture toughness will show higher residual strength [34]. Figure 3.15 shows the tensile fracture stress of material in the reference and welded regions as a function of initial crack length. Due to the higher fracture strength at the same crack length, for a given crack size, the tensile stress required to fracture the weld seam is higher than the reference material. To obtain high fracture energy, it is necessary for glass to utilize energy absorbing processes [35]. It has been shown that several processes can toughen glass resulting in an energy absorbing process around the primary crack front and non-linear behavior prior to fracture [32]. The ultrafast laser-treated region, including the weld seam, could be analogous to a toughened processed zone; therefore, a higher stress is required to fracture

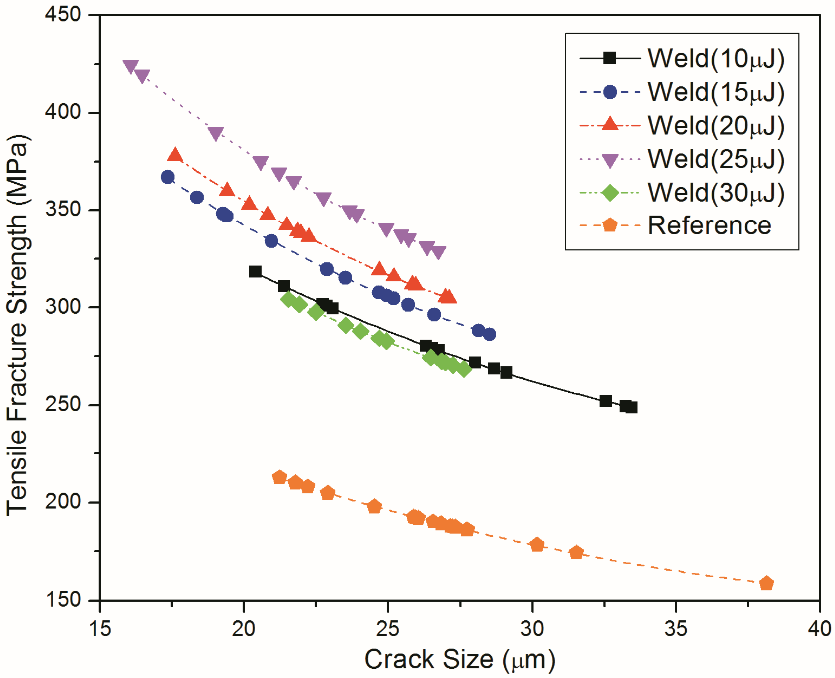

Figure 3.15: Fracture Strength as a function of crack size of the material in welded regions with different laser pulse energy levels (10μJ – 30μJ) at fixed laser scanning speed of 0.02 mm/s and in a reference region.

the weld compared to the reference regions. This is consistent with concepts that suggest that toughening (increase K_{IC}) leads to strengthening (increase σ_f) especially for brittle solids such as glass [36]. The effect of the laser pulse energy on the fracture strength is also illustrated in Fig. 3.15. Due to the presence of micro cracks at sufficiently higher laser pulse energies as mentioned earlier in this section, it can be seen that the fracture strength does not monotonically increase with laser pulse energy, rather there is an optimum pulse energy beyond which the resultant fracture strength will decrease. However, the detrimental effect of the micro cracks is smaller than the beneficial effect of the compact ring structure (3-member rings) which has the highest barrier to fracture of all ring configurations [37]; therefore, the fracture strengths in welded regions for all laser pulse energy conditions in this study are still higher than the reference region.

3.5 Conclusion

Transmission welding of two borosilicate glass plates with standard flatness was performed by using low repetition rate femtosecond laser irradiation. The weld cross section (xz-plane) revealed that the transmission welding of standard flatness glass plates was successful. The weld morphology was investigated, and it was observed that the affected region is a teardrop shape similar to the features created by femtosecond laser irradiation of the interior of single piece transparent samples. Large area transmission welding seams can also be formed by applying a multiple-line overlap welding process. A numerical model was developed to investigate the size and shape of the absorption volume as a function of laser pulse energy and numerical aperture of the objective lens. The model was able to predict the teardrop shape of the absorption volume, and the width of the absorption volume agreed well with the weld widths obtained through experiments for a wide range of pulse energies. The E/H ratios in the weld seam showed two separate regions with high E/H ratios implying that air gap plays a significant role in the coupling of laser energy into the bottom piece during transmission welding. The material inside the welded region revealed an increase in fracture toughness; therefore, a higher stress may be required to fracture the weld compared to the reference region. The geometry and mechanical properties of the weld seam obtained in this study suggest that transmission welding using low repetition rate femtosecond laser irradiation is a promising technique for spatially selective joining of glasses.

Chapter 4: Single Step Channeling in Glass Interior by Femtosecond Laser

4.1 Introduction

Microchannels are the essential features in micro-fluidic devices, micro-total analysis systems (μ-TAS), and lab-on-a-chip (LOC) devices for biomedical applications. Lab-on-a-chip devices are microsystems integrated with functional components such as micro-optics, waveguides and micro-fluidics aiming at the miniaturization onto a single substrate of several functionalities. LOCs use networks of microfluidic channels to transport, mix, separate, react and analyze very small volumes of biological samples. Several substrate materials are used for LOC fabrication including silicon, glass and polymers. However, glass is still the material of choice for many applications due to its chemical inert, stable in time, hydrophilic, nonporous, optically clear, and easily supports electro-osmotic flow [1]. Currently, fabrication of microfluidic devices still heavily relies on photolithographic techniques, which require multilayer and multistep processing procedures to form 3D microstructures [2].

Femtosecond laser micromachining has emerged as a revolutionary technique for creating 3D microfluidic structures inside transparent substrates [2]. Laser irradiation inside transparent materials using the fluence equal or above the material damage threshold can alter the material structure and resulting mainly in positive/negative refractive index change. For higher fluence, a strong laser-matter interaction is occurred, and micro-explosion confined in the focal volume takes place with creation of voids. Glezer et al. [3] tightly focused femtosecond laser pulses to initiate micro-explosions inside transparent materials and found that submicrometer structures or voxels can be produced inside the materials. Juodkazis et al. [4] showed that the nanovoid in glass is formed as a result of shock and rarefaction waves at pulse power much lower than the threshold of self-focusing. Gamaly et al. [5] determined the mechanism of void formation as a result of micro-explosion and analyzed the size of the void as a function of the deposited energy. Using this mechanism, there is potential to form 3D patterns of voids inside glass.

Currently, there are mainly two strategies for fabricating 3D microchannels embedded in glass using femtosecond laser. The first strategy employs femtosecond laser direct writing followed by chemical etching in either silica glass or photosensitive glass. Marcinkevicius et al. [6] first demonstrated the possibility of 3D microchannel fabrication in fused silica using the combination of femtosecond laser dielectric modification and subsequent etching in an aqueous solution of hydrofluoric (HF) acid. Hnatovsky et al. [7] fabricated microchannels in fused silica and BK7 borosilicate glass by this two-step hybrid process, and also investigated the optimum irradiation conditions needed to produce high-aspect ratio microchannels with small symmetric cross-sections and smooth walls. Sun et al. [8] demonstrated the dependence of the microchannels fabricated in fused silica glass using chemical etching on the femtosecond laser pulses with different central wavelengths. Kiyama et al. [9] compared two different etching agents and demonstrated that a concentrated aqueous solution of potassium hydroxide (KOH) allowed higher etching selectivity than commonly used aqueous HF solution. Some researchers [10,11] also performed a three-step hybrid process to fabricate the 3D microfluidic structures by irradiating femtosecond laser into a photosensitive Foturan glass, thermal annealing to produce crystallites of lithium metasilicates in the laser-irradiated regions, and selectively chemical etching those regions in aqueous HF solution. Another strategy is to perform femtosecond laser drilling from the rear surface of the glass in contact with distilled water, by which the water introduced into the microchannel can help remove the ablated material. Li et al. [12] first demonstrated the possibility of 3D microhole fabrication inside silica glass by water-assisted femtosecond laser drilling. Hwang et al. [13] fabricated straight, bent, and curved microfluidic channels in fused silica by this method, and clarified that the debris is removed with the help of bubbles generated in the channel. Iga et al. [14] investigated how the diameters of the channels drilled from the rear surface of silica glass by a femtosecond laser depend on the incident energy and the number of laser pulses. An et al. [15] machined combined structures consisting of cascaded microchambers and microtrenches inside silica glass by water-assisted ablation with femtosecond laser pulses. The first process is limited by the etching selectivity as a function of etching period, and by the amount of fresh aqueous solution to reach the inward part of a microchannel. It thus usually gets a taper channel. For the second process, the ablated debris can no longer be ejected from the microchannel when the length of the channel increases. This clogging issue may be resolved by using a porous glass of which its porous network allows continuous infiltration of water into the ablation zone; however, the whole channel needs to be repeatedly scanned multiple times to completely remove all the debris, and subsequently post-annealing process is required to consolidate the porous glass into a compact glass resulting in shrinking of the channel dimensions in all directions [2,16].

In this study, rather than using hybrid processes such as liquid assisted femtosecond laser processing or femtosecond laser irradiation combined with subsequently chemical etching the treated region, single-step channeling is investigated by attempting to connect the voids created from each single femtosecond laser pulse irradiation. This novel process uses single femtosecond laser pulses instead of pulse trains at a specific repetition rate, and does not require an additional process to remove material from the channel. In order to understand the channel formation mechanism, to get the acceptable channel geometry, and to develop prediction capability, the effects of optical and laser parameters on the resultant morphology by single femtosecond laser pulse are studied. Numerical models are developed to predict the feature shape and lengths which also correspond to the channel lengths. The possibility of using the numerical features length simulated by absorption volume modeling and electromagnetic diffraction modeling as a guideline to estimate the experimental results is also discussed.

4.2 Background

4.2.1 Channel Formation and Focusing Effect

When a femtosecond laser pulse with high energy in the order of microjules is tightly focused into fused silica, non-linear absorption will occur, a high number density of free electrons will be generated inside the absorption volume due to multi-photon and avalanche ionization. These hot free electrons will transfer their energy to ions, and thermal equilibrium of free electrons and lattice will be attained in picoseconds. In addition to a thermal process in which phase transitions take place, high pressure within the absorption volume builds up. When a high pressure and temperature volume is created inside this restricted volume, there is hydrodynamic expansion which proceeds as a micro-explosion. Shock wave emerges from this volume, compressing the surrounding material, and simultaneously rarefaction wave behind the shock front propagates in the opposite direction creating a void [17,18].

Spherical aberration caused by focusing through the air-sample refractive index mismatched interface determined the variation of the threshold pulse energy as a function of the focusing depth and the size of the modified zones in fused silica [19]. Marcinkevicius et al. [20] reported that the spherical aberrations increased the size and distorted the shape of the photo-damaged region. Liu et al. [21] experimentally studied the influence of the focusing depth on both the index change threshold and damage threshold as well as on the cross section of the fabricated waveguides under irradiation of 1-kHz femtosecond laser pulses.

When the laser beam is focused through the air-glass interface, the paraxial focus or the focus produced by the central area of a focusing lens is located at the distance which is the product of the refractive index of glass and the focusing depth ($n_2 d$). By paraxial approximation and using the Snell's law on the interface, $n_2 sin\theta_2 = n_1 sin\theta_1 = NA$ is satisfied, and the longitudinal aberration range, l_{pa}, due to spherical aberration, which is the distance from the paraxial-ray focal plane to the peripheral-ray focal plane can be written as [21,22]:

$$l_{pa} = \frac{tan\theta_1}{tan\theta_2} d - n_2 d = \left[\sqrt{\frac{n_2^2 - NA^2}{1 - NA^2}} - n_2 \right] d \tag{4.1}$$

where θ_1 is incident angle of focusing beam, θ_2 is the refracted angle of the focusing beam, n_2 is the refractive index of glass, d is the focusing depth from the interface , and NA is the numerical aperture of an objective lens. On the other hand, by using diffraction theory and taking into account the variation in size of the converging Gaussian beam, $w(z) = w_0 \sqrt{1 + \left(\frac{\theta z}{w_0}\right)^2}$ is satisfied. The diffraction limited spot size location, f, will be related to the focusing depth, the converging incident angle, and the converging refracted angle as : $f = \frac{\theta_1 d}{\theta_2}$, and longitudinal aberration range, l_{df}, due to spherical aberration, which is the distance from the diffraction limited focal plane to the peripheral-ray focal plane can be written as:

$$l_{df} = \frac{tan\theta_1}{tan\theta_2} d - \frac{\theta_1 d}{sin^{-1}\left(\frac{NA}{n_2}\right)} = \left[\sqrt{\frac{n_2^2 - NA^2}{1 - NA^2}} - \frac{sin^{-1}(NA)}{sin^{-1}(NA/n_2)} \right] d \tag{4.2}$$

Either the longitudinal aberration range in Eq. (4.1) or that in Eq. (4.2) will have an influence on the nonlinear energy deposition by spreading the intensity distribution along its range. Therefore, the feature or the channel resulting from the laser-matter interaction region due to nonlinear absorption inside transparent materials will be proportional to the focusing depth.

4.2.2 Numerical Analysis

By taking into account the effect of the longitudinal aberration range, the numerical model based on the electromagnetic diffraction of a laser beam focused through an air-glass interface could be constructed to predict the absorption volume shape and size at different focusing depths below the surface of a specimen. A laser beam of known power arrives at the interface through the first medium of refractive index n_1, and the interface at the surface of a specimen separates the medium of refractive index n_1 from the second medium of refractive index n_2. The electromagnetic field before the interface can be expressed as a superposition integral that sums up all possible plane waves propagating within the convergence angle of the high-aperture lens. Each plane wave is transmitted through the interface obeying the Fresnel refraction law. Using the fields calculated in the first medium as boundary conditions to obtain solution for the diffraction problem using a second integral representation of the electromagnetic field in the second medium. The resulting electric field distribution in the second medium is then a solution of the time-independent wave equation and Maxwell's equations and can be written as [23,24]:

$$E_{2x}(x,y,z) = \frac{-ik_1 f l_0}{2}\left[I_0 + I_2 \cos\left(2\theta_p\right)\right] \tag{4.3}$$

$$E_{2y}(x,y,z) = \frac{-ik_1 f l_0}{2} I_2 \sin\left(2\theta_p\right) \tag{4.4}$$

$$E_{2z}(x,y,z) = \frac{-ik_1 f l_0}{2} I_1 \cos\theta_p \tag{4.5}$$

where k_1 is wave number in the first medium, f is the focusing distance, l_0 is the field amplitude factor, x and y are the positions in lateral directions, z is the position in axial direction, and $\theta_p =$

$tan^{-1}(y/x)$ is the inclination angle. The integrals I_0, I_1, and I_2 are given by [23]:

$$I_0 = \int_0^{\alpha} \sqrt{cos\phi_1} sin\phi_1 exp[-id(k_1 cos\phi_1 - k_2 cos\phi_2)] \times (\tau_s + \tau_p cos\phi_2) J_0\left(k_1\sqrt{x^2+y^2} sin\phi_1\right) exp(ik_2 z cos\phi_2)\, d\phi_1 \tag{4.6}$$

$$I_1 = \int_0^{\alpha} \sqrt{cos\phi_1} sin\phi_1 exp[-id(k_1 cos\phi_1 - k_2 cos\phi_2)] \times \tau_p sin\phi_2 J_1\left(k_1\sqrt{x^2+y^2} sin\phi_1\right) exp(ik_2 z cos\phi_2)\, d\phi_1 \tag{4.7}$$

$$I_2 = \int_0^{\alpha} \sqrt{cos\phi_1} sin\phi_1 exp[-id(k_1 cos\phi_1 - k_2 cos\phi_2)] \times (\tau_s - \tau_p cos\phi_2) J_2\left(k_1\sqrt{x^2+y^2} sin\phi_1\right) exp(ik_2 z cos\phi_2)\, d\phi_1 \tag{4.8}$$

where α is the angular semi-aperture of the lens, k_2 is wave number in the second medium, ϕ_1 is the incident angle on the interface, ϕ_2 is the refracted angle from the interface, τ_s and τ_p are the Fresnel coefficients, and J_0, J_1, and J_2 are the Bessel function of the first kind and order zero, one, and two, respectively. Hence the distribution of the time-averaged electric energy density, w_e , and the total energy density, w , inside the specimen near the focal plane is the following [24]:

$$\langle w_e(x,y,z)\rangle = \frac{k_1^2 f^2 l_0^2}{64\pi}\{|I_0|^2 + 4|I_1|^2 cos^2\theta_p + |I_2|^2 + 2\cos(2\theta_p) Re(I_0 I_2^*)\} \tag{4.9}$$

$$\langle w(x,y,z)\rangle = \frac{k_1^2 f^2 l_0^2}{32\pi}\{|I_0|^2 + 2|I_1|^2 + |I_2|^2\} \tag{4.10}$$

where * is the conjugate of an complex number. The electric energy density and total energy density of points in the vicinity of a focal plane will be significantly high, and when compared to the material damage threshold, the absorption volume could be identify to predict the size of features and channels at different focusing depths below the top surface of transparent materials.

4.3 Experimental Setup and Characterization

Single step channeling is achieved by using a chirped amplified Ti:Sapphire laser system which outputs high energy ultrashort pulses with 800 nm wavelength and 130 fs pulse duration at a 1 kHz repetition rate. The commercial grade S1-UV fused silica of 3.0 mm thick was cut to approximately 6 mm x 12 mm size. The laser beam was focused by 40x objective lens with *NA* 0.6 inside the specimen. A schematic diagram of the experimental setup is illustrated in Fig. 4.1. Different conditions of laser processing and optical parameters were applied by varying the energy of the laser pulses and focusing depth with respect to the top surface of the material. Long channels were obtained by cascading each channel generated by single laser pulses along an optical axis. Different laser pulse energy and focusing depth conditions were used to investigate the size of features and channels and to investigate the effects of channel overlapping and its influence on long channel formation.

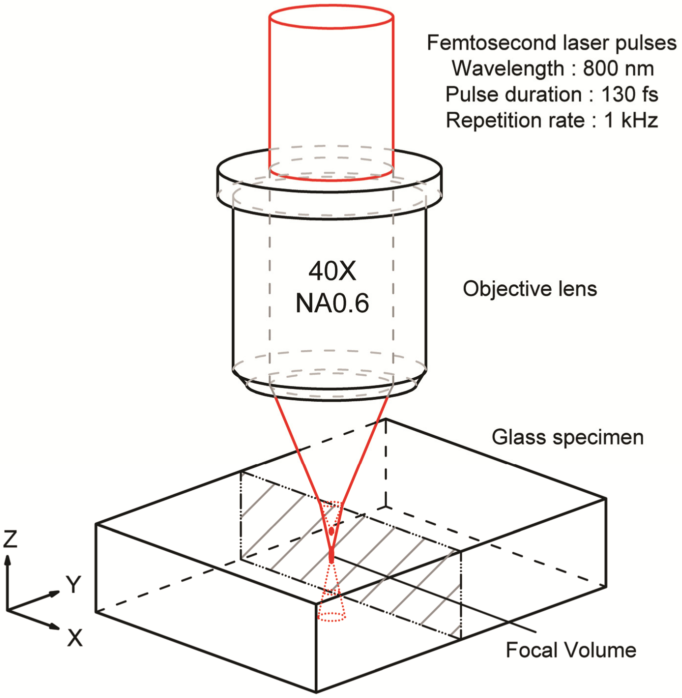

Figure 4.1: Schematic illustration of experimental setup. The laser beam is focused through the air-glass interface into the interior of fused silica sample.

After the femtosecond laser irradiation, transmission light differential interference contrast (DIC) optical microscopy was used to obtain the axial cross section (xz-plane) of the features and channels. The samples were ground and polished with lapping films to the line across channels. Reflection DIC optical microscopy and AFM topography were used to verify the existence of cavities on the polished surface. Raman spectroscopy was also carried out to further support whether the channels are real cavities.

4.4 Results and Discussion

4.4.1 Channel Geometry

In order to achieve long micro-scale channels in glass materials, other studies have used hybrid processes such as the combination of ultrashort laser irradiation and chemical etching or the liquid-assisted drilling by ultrashort laser scanning along an optical axis. However, single femtosecond laser pulse irradiation using high laser pulse energy and high numerical aperture of objective lens can also produce the reasonable long channels. Figure 4.2 shows the axial cross section (xz-plane) of features and channels created inside fused silica sample using laser pulse energy of 10 μJ, 20 μJ, and 30 μJ, respectively at the same focusing depth of 1500 μm below the top surface of 3 mm thick fused silica with standard flatness of 3-5 waves/inch from transmission DIC optical microscopy. The features defined by the distinctive color change around irradiated regions due to material alteration in optical and mechanical properties, have high aspect ratios (length/width). The feature is strongly dependent on laser pulse energy as shown in Fig. 4.2, and the formation of larger features is corresponded to the higher the laser pulse energies. Inside the features, there are dark core regions, and these regions could be the consequence of the high level of interaction which subsequently generates high temperature and high pressure, and eventually causes the material explosion inside laser focal volume. The dark color regions are

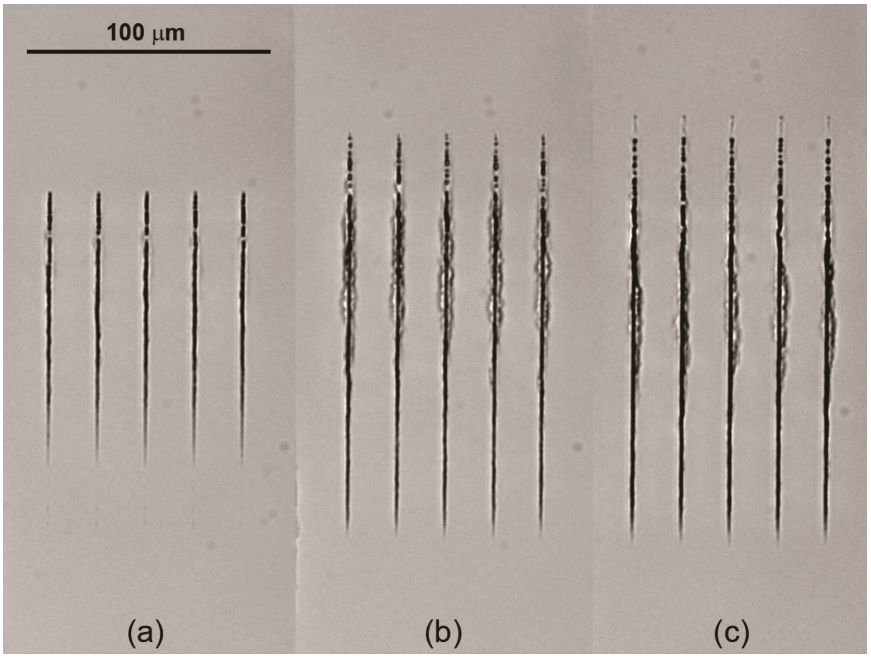

Figure 4.2: Transmission DIC optical microscopy of axial cross section (xz-plane) of features and channels at same focusing depth of 1500 μm using pulse energy of (a) 10 μJ, (b) 20 μJ, and (c) 30 μJ. The above three figures have been adjusted to the same scale.

believed to be cavities, and the longest uniform dark color area inside the feature is identified as a channel from single laser pulse irradiation. The features and channels have a long and narrow tear drop shape corresponding to the shape of absorption volume.

To verify whether the identified channel is really a cavity, the fused silica sample was ground and polished from the top surface until the new polished surface was located at a line across channels. Figure 4.3 shows the radial cross section (xy-plane) of the polished sample irradiated by a series of single pulse with pulse energy of 30 μJ from reflection DIC optical microscopy. From the reflective optical image in Fig. 4.3, the cross section of channels looks dark as well as the optical transmitted image, and the radial cross section shape of features and channels is irregular, roughly circular shape. The size of features and channels in this x-y view image is about a few micrometers corresponding well with the x-z view image. The cavity on the surface of transparent material normally looks dark when observed with the reflective optical microscope;

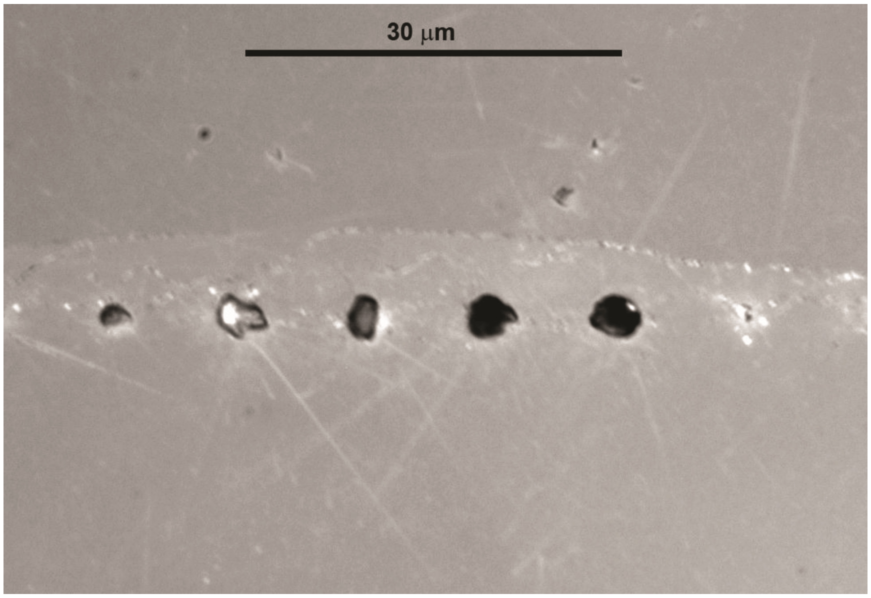

Figure 4.3: Reflection DIC optical microscopy of radial cross section (xy-plane) of the new polished surface across the channels irradiated by a series of single pulse energy of 30 μJ.

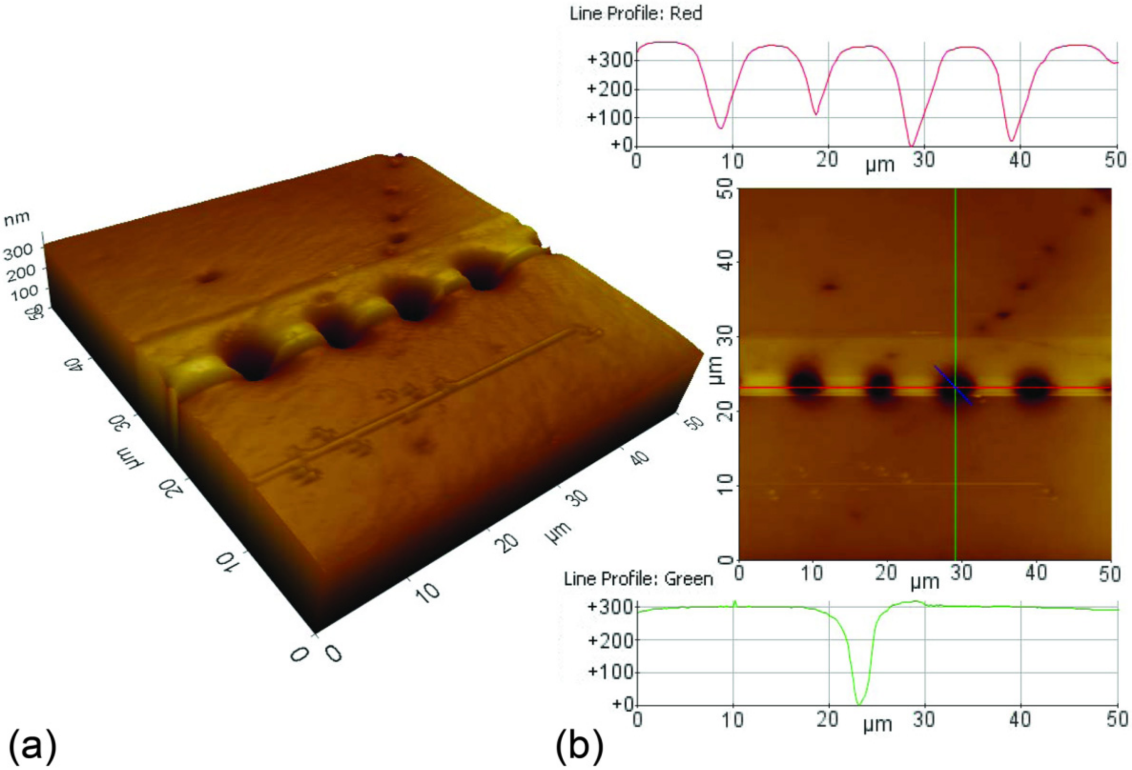

Figure 4.4: (a) 3D AFM topography and (b) the AFM top view image and line profiles across the channels on the new polished surface (xy-plane) across the channels irradiated by a series of single pulse energy of 30 μJ.

therefore, these identified channels could be assumed as cavities as well. However, the Atomic Force Microscopy (AFM) measurements of topography of channels in radial cross section were also performed to assure that the channels are cavities. The 3D topographic image of four distinctive channels with 10 μm spacing is illustrated in Fig. 4.4 (a). The AFM top view image and line profiles across channels can also be seen in Fig. 4.4 (b), and from the vertical line profile it can be concluded that the channel size in the direction perpendicular to the laser beam is about a few micrometers for laser pulse energy of 30 μJ. In addition to the optical microscopy and AFM topography images, the Raman spectroscopy was also used to measure structural changes at and around the feature and channel inside the fused silica sample. Raman signal measurements were performed in a series of fifteen points along the line cross the representative channel in x-z view as illustrated in Fig. 4.5 (a). Raman spectral analysis of fused silica reveals that there are three-, four-, and five- and six-fold rings structure in the material, and these rings structure correspond to the 606 cm^{-1}, 495 cm^{-1}, and 440 cm^{-1} peak in Raman spectra, respectively. The lowest peak intensity of all ring structures at point 10 which locates at center of the representative channel, and lower peak intensity at its adjacent points compared to other points in the reference region as plotted in Fig. 4.5 (b) reply that there are low detected volumes of material in the vicinity of those points. This Raman results could be indirectly verified that the identified channels are cavities as well. Therefore, the optical microscopy, AFM topography, and Raman spectroscopy support each other that the defined channels are cavities. Sidewall surface roughness is an important parameter in fluid flow through microchannels for optofluidic applications. Although it is not focused in this study, and the spatial resolution of the measurement with respect to the size of microchannels may not be high, inspection on the cross section of microchannels using optical profilometer suggested a sidewall surface roughness of ~ 1 nm.

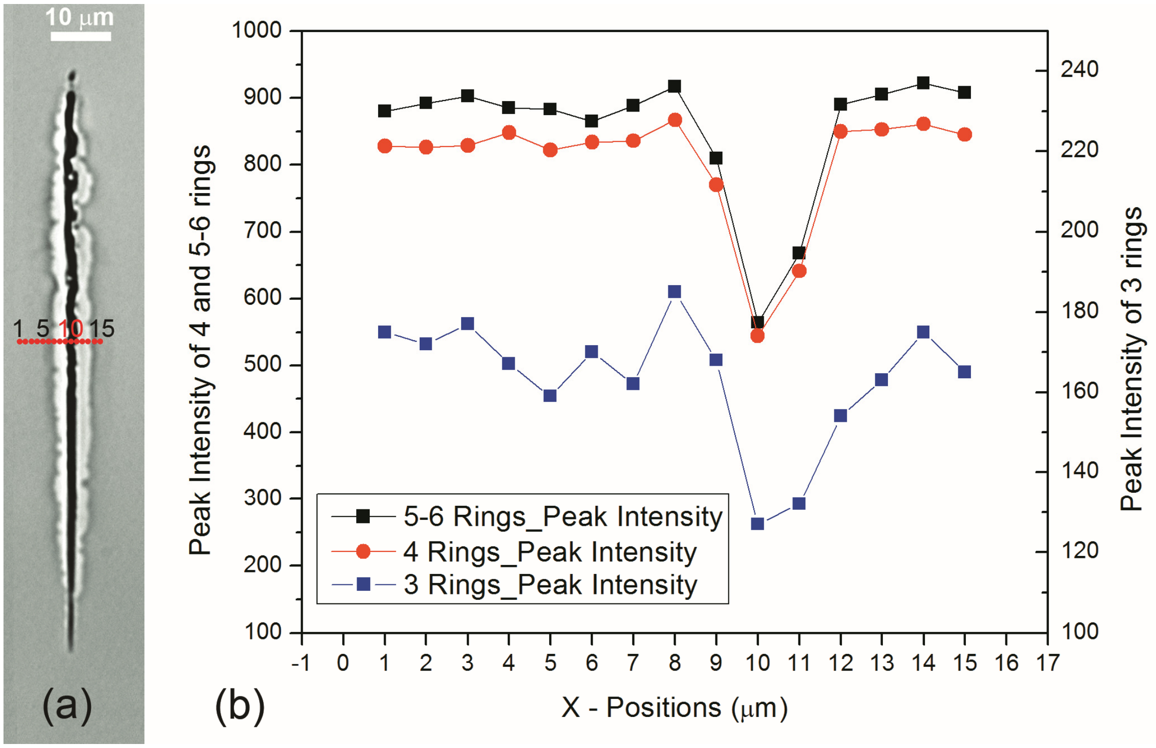

Figure 4.5: (a) Raman signal measurements points across the axial cross section (xz-plane) of a feature and channel, and (b) the peak intensity of the 3 rings, 4 rings, and 5-6 rings structure of fifteen points across the channel.

Figure 4.6 shows the shape and size of features and channels created inside fused silica sample using same laser pulse energy of 30 μJ at different focusing depth in the range of 500 – 2500 μm below the top surface within 3 mm thick of the material from the x-z view. It can be seen that the size especially in the optical direction (z-axis) is strongly dependent on the focusing depth. The greater the focusing depths correspond to the generation of longer features and channels. The variation in size in the optical direction is caused by spherical aberration due to the focusing of laser beam through the refractive index mismatched air-glass interface. On one hand, as illustrated in Fig. 4.1 the plane of focal volume will move to the lower location than the Gaussian focus plane (if there is no interface) due to the refraction of laser beam. On the other hand due to the presence of the air-glass interface, the focused rays inside laser beam cone, which initially converge to the single focal plane at different angle, will diversely propagate to different focal

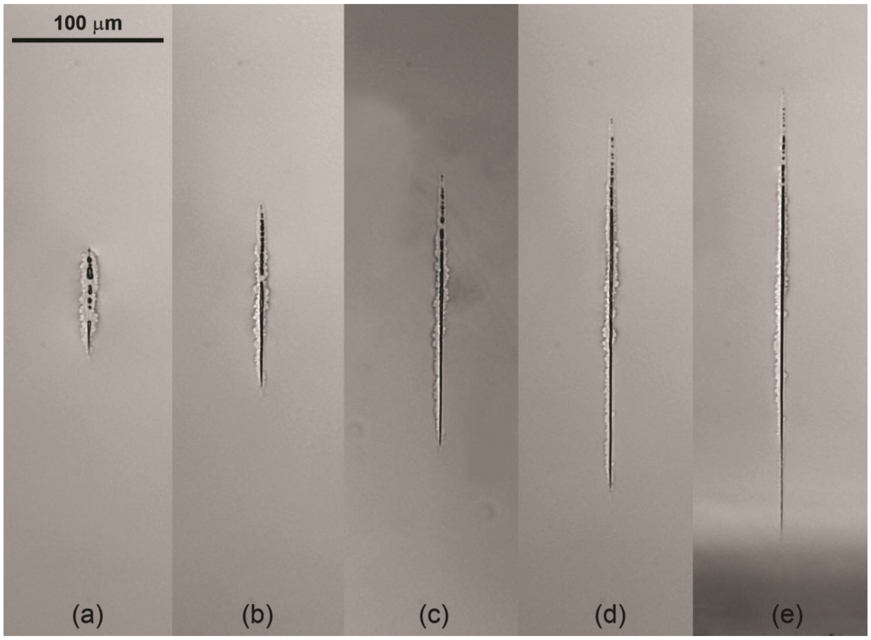

Figure 4.6: Transmission DIC optical microscopy of axial cross section (xz-plane) of features and channels using same pulse energy of 30 μJ at different focusing depths of (a) 500 μm, (b) 1000 μm, (c) 1500 μm, (d) 2000 μm, and (e) 3000 μm. The above five figures have been adjusted to the same scale.

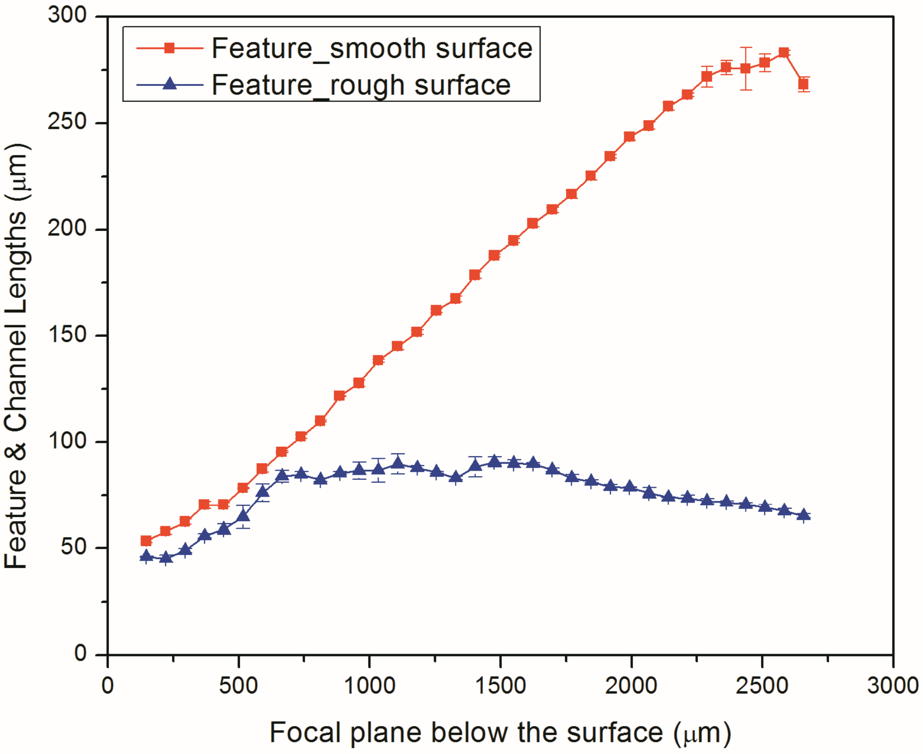

Figure 4.7: The effect of material surface roughness on the feature lengths using same laser pulse energy of 30 μJ at different focusing depths. Error bars denote standard deviation.

planes in glass, and this phenomenon results in a longitudinal aberration range. The deeper the focusing depths will correspond to the occurrence of longer aberration ranges. Figure 4.7 shows the effect of material surface roughness on the feature lengths using same laser pulse energy of 30 μJ at different focusing depths. The size of features generated by focusing the laser beam through the optical finishing smooth surface with standard flatness of 3-5 waves/inch is significantly enhanced from the case that generated by focusing through the rough cutting surface using speed saw. With optical finishing smooth surface, low fraction of laser beam reflection and scattering on the surface is occurred, and higher energy can be deposited inside the transparent material. Therefore, to generate quite reasonable long features and channels inside fused silica by single femtosecond laser pulse, one should seriously consider using the optical finishing smooth top surface of the material.

Figure 4.8 shows the feature lengths at different focusing depths of pulse energies of 10 μJ, 20 μJ, and 30 μJ, respectively, compared to longitudinal aberration ranges in Eq. (4.1) defined as Paraxial aberration ranges in section 4.2.1. The feature lengths have increasing trends with the focusing depths with respect to the top surface of samples, and range from 23 to 283 microns in length and 4 to 46 in aspect ratio. As seen in Fig. 4.8, the feature lengths depend on both focusing depths and laser pulse energies. The greater the focusing depth, the longer the feature length; the length of the feature also increases with laser pulse energy. The features lengths of all pulse energies in this study fall within the paraxial aberration ranges. This could be due to the deposited laser pulse energy will be absorbed and broadly distributed in this paraxial aberration ranges, and the absorbed energy density of points only within this ranges will probably be greater than the material damage threshold. It results in feature lengths shorter than the paraxial aberration ranges. The feature lengths show leveling trends at deep focusing depths, and due to

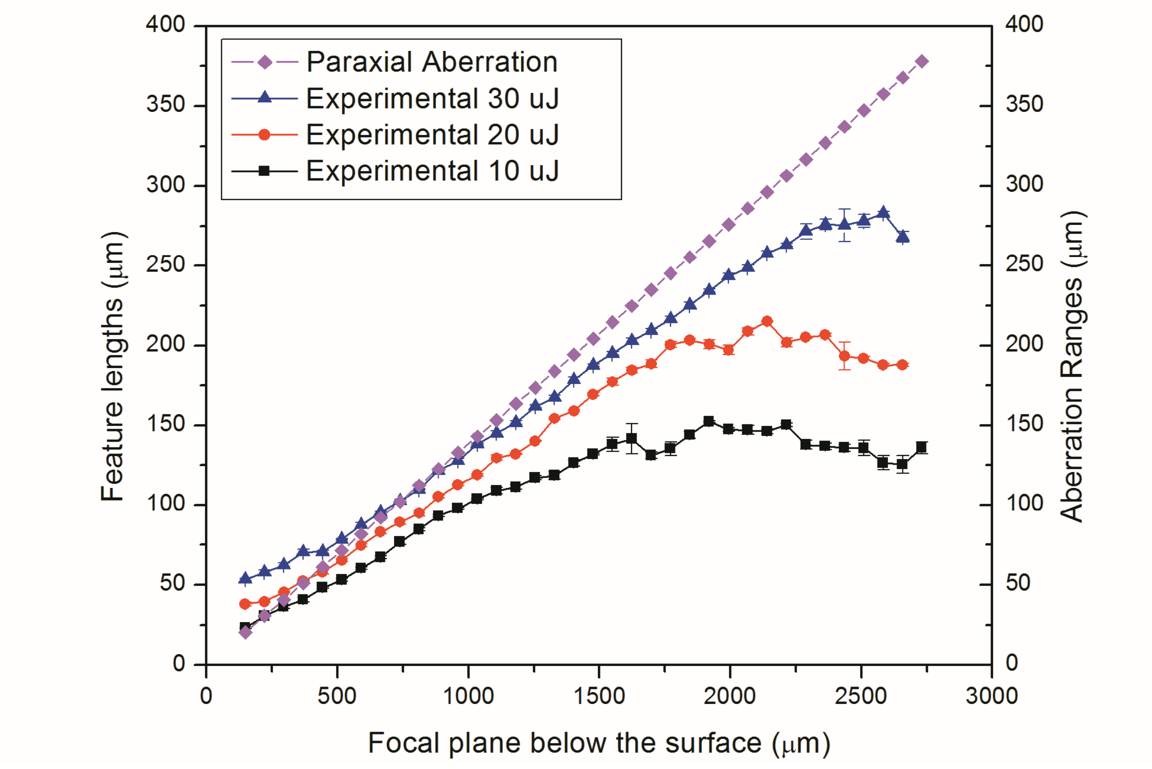

Figure 4.8: Comparison of experimental feature lengths at 10 μJ, 20 μJ, and 30 μJ, and the paraxial aberration range at different focusing depths. Error bars denote standard deviation.

the spreading of lower energy within the same aberration ranges caused by the lower absorbed energy density, the lower pulse energies level off at shallower focusing depths compared to the higher ones as observed in Fig. 4.8. Although the paraxial aberration ranges are not perfectly matched the feature lengths, a guideline that the feature lengths will be approximately equal or less than the paraxial aberration ranges could be used.

Figure 4.9 shows the channel lengths at different focusing depths of pulse energies of 10 μJ, 20 μJ, and 30 μJ, respectively, compared to longitudinal aberration ranges in Eq. (4.2) defined as diffraction limited aberration ranges in section 4.2.1. In the range of this study with respect to focusing depths, the channel lengths have only an increasing trend for the case of 30 μJ pulse energy, but also show leveling and decreasing trends for the case of 10 μJ pulse energy. It replies that at further depth locations the pulse energy will be over spreading such that the absorbed energy

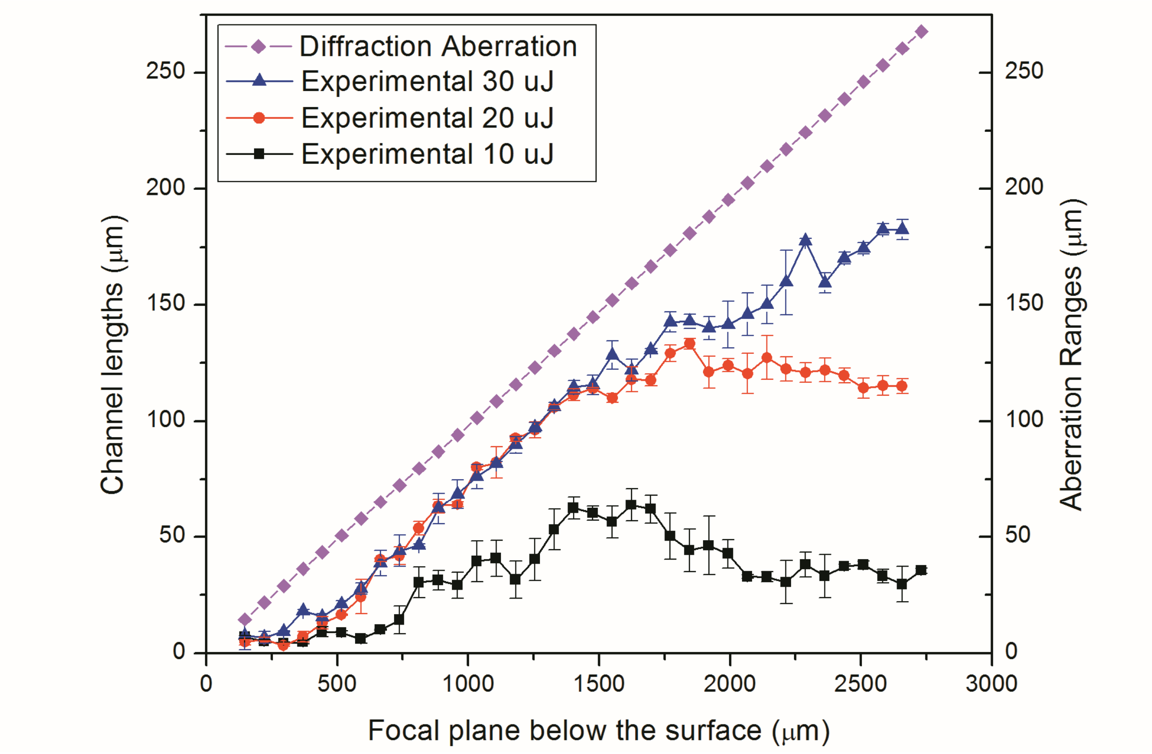

Figure 4.9: Comparison of experimental channel lengths at 10 μJ, 20 μJ, and 30 μJ, and the diffraction limited aberration range at different focusing depths. Error bars denote standard deviation.

density that is greater than the material damage threshold occurs in shorter and shorter ranges, and the material explosion will happen in shorter ranges as well resulting in shorter channel lengths as clearly seen in case of 10 μJ in Fig. 4.9. The diffraction limited aberration ranges are sometimes shorter or longer than the feature lengths at different laser pulse energies in this study, however, they are quite close to and always greater than the channel lengths of all pulse energies and focusing depths. Therefore, a quick guideline could also be used to estimate that the resulting channel lengths will be less than the diffraction limited aberration ranges.

By cascading a single pulse channel along the optical axis within the thickness of fused silica sample using a long working distance objective lens, the connection of channels can be performed to produce a long channel which has adequate length for most microfluidic and lab-on-a-chip applications. However, the appropriate overlapping distance of single channel has to be considered. Figure 4.10 (a) and 4.10 (b) show the transmission DIC optical image in xz-plane of cascading channels using different overlapping distance for two single pulses. The left and the middle one are the locations of the bottom and the top channels that will be cascading, respectively. The right channels are the results of cascaded channels. As seen in Fig. 4.10 (a), the two channels are not completely connected due to an inadequate overlapping distance. When the overlapping distance is increased, the cascaded channel has uniform dark color in the overlapping region, which implies that the channel cascading can be succeeded if an appropriate overlapping distance has been used. Figure 4.10 (c) shows the representative cascaded channels of multiple single pulses. From observation by optical microscope, the channel cascading is

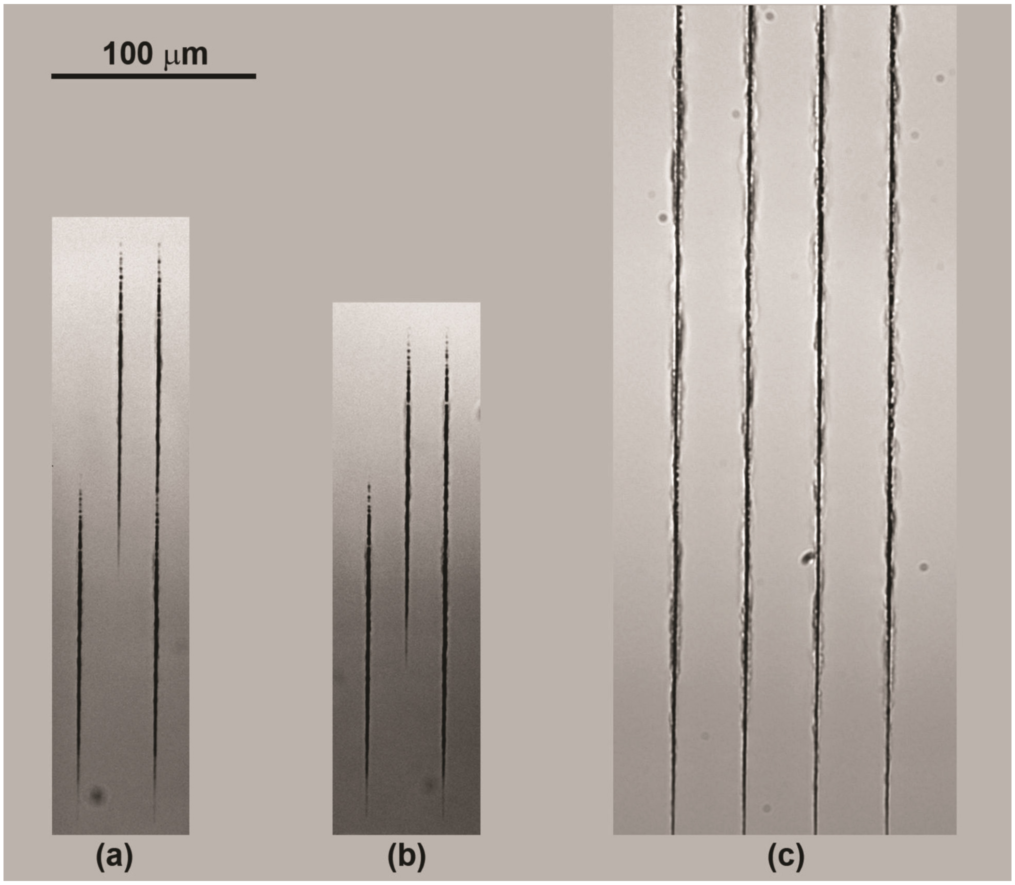

Figure 4.10: Cascading of two single pulses with (a) an inadequate overlapping distance, and (b) an appropriate overlapping distance. (c) Cascading of multiple single pulses using pulse energy of 30 μJ. The above three figures have been adjusted to the same scale.

usually succeeded if the overlapping distance of the features is equal to or greater than 68%. Although the microchannels by single-step channeling process can be performed only in the direction that is paralleled to the incident laser beam and the shape of microchannels has to be simple and straight rather than contour or complex, this novel process could still be a potential alternative to produce micro-scale channels inside transparent materials for microfluidic and lab-on-a-chip applications. In addition to long 1D channel, which is easily fabricated by this technique, the 2D and 3D structures with the changes in directions of microchannels could be fabricated by changing the setups during processing or by using a robot arm with six degrees of freedom to handle the workpiece. However, the effects of non-perpendicular surface with respect to the incident laser beam on shape and size of microchannels need to be further explored

4.4.2 Numerical Modeling

From experimental results, the shape and size of features and channels varies as a function of focusing depth. In order to predict the shape and size of those features and channels at different focusing depths below the specimen surface, the two numerical models of laser absorption volume and electric energy density field inside a transparent material were constructed. The first numerical model considers the temporal profile and spatial intensity of Gaussian laser beam which propagates through a focusing lens and an air-glass interface to points in the vicinity of a focal plane, and determines breakdown points which have intensity greater than the material intensity damage threshold. The second numerical model considers the electric field inside the second medium after focusing electromagnetic wave through a focusing lens and an interface between two different mediums, then determines the electric energy density field in the vicinity of a focal plane, and compares it with the energy density damage threshold of the material. Both numerical models will take effect of the longitudinal aberration ranges into account.

4.4.2.1 Absorption Volume Modeling

From temporal and spatial distribution characteristics of femtosecond laser pulses, the intensity of an unfocused laser beam in each time slice was determined. When the unfocused laser beam has been converged to the smaller area in the vicinity of a focal plane, the magnified intensity will be compared to the material intensity damage threshold, and the breakdown points which have intensity greater than the threshold will be determined [25]. Consequently, the corresponding locations in the optical axis of these breakdown points will be calculated considering focusing parameters, optical properties of two materials, and aberration effects from air-glass interface. Eventually, all breakdown points will combine and generate the absorption volume. Figure 4.11 shows the representative simulated axial cross section (rz-plane) of the absorption volume by 30 μJ pulse energy at the focusing depth (a paraxial focal plane) of 1000 μm below the top surface of fused silica material. The cross section shape of the absorption volume

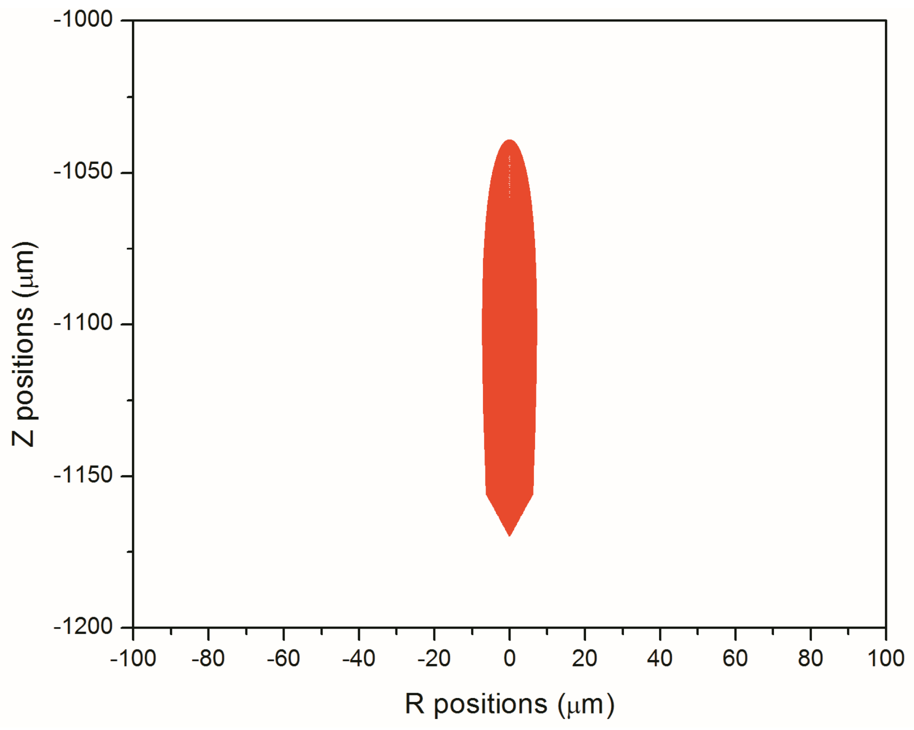

Figure 4.11: The representative simulated cross section (rz-plane) of the absorption volume by 30 μJ pulse energy at the focusing depth of 1000 μm from the absorption volume model.

looks like the teardrop shape and has high aspect ratios (length/width). It is interesting that the top breakdown point in optical axis of this representative absorption volume is occurred closely to the diffraction limited focal plane at -1040.4 μm rather than the paraxial focal plane at -1000 μm. The size of the absorption volume is indeed dependent on the focusing depths and laser pulse energies, and the longest distance along the optical axis of the absorption volume is defined as the numerical feature lengths simulated by the absorption volume modeling. More details of the results from this numerical model will be shown and verified with the other numerical model and the experimental results in section 4.4.2.3.

4.4.2.2 Electromagnetic Diffraction Modeling

A superposition of plane waves inside mediums can represent electromagnetic fields. Taking into account the optical properties of two different mediums, the focusing parameters, and Fresnel's refraction law at the interface between two different mediums, a superposition of refracted plane waves can construct the time-independent or time-averaged electric and magnetic fields. The area in the vicinity of the focal plane which has high enough electric energy density especially greater than the damage threshold of the material can be counted as a material structural alteration area which represents the feature and channel generated by a single femtosecond laser pulse. Figure 4.12 illustrates the 3D surface map of representative electric energy density field on the xz-plane along an optical axis in the vicinity of the focal plane for laser pulse energy of 30 μJ at the focusing depth of 1000 μm below the top surface of fused silica material. The region of interest is located between the focal plane of axial and peripheral rays within the angular semi-aperture of the objective lens with numerical aperture (NA) equal to 0.6. As seen in Fig. 4.12, the electric energy density is extremely high only near the optical axis between the paraxial focal plane at -1000 μm and the peripheral focal plane at -1138.4 μm below the top surface of the material.

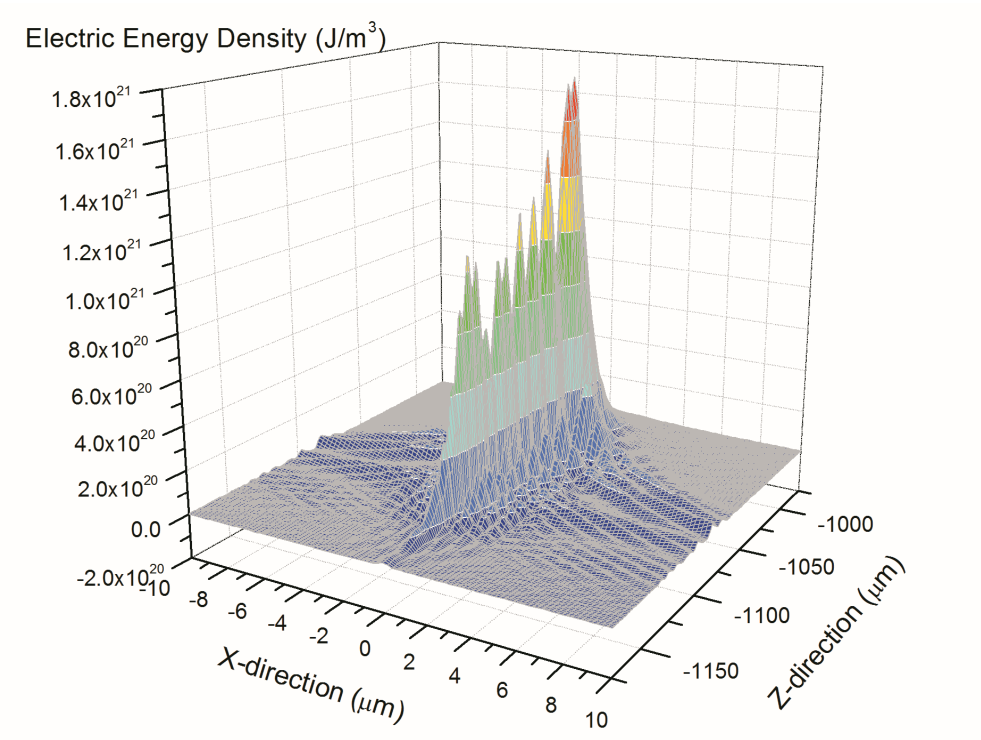

Figure 4.12: The 3D surface map of representative electric energy density field on the xz-plane along an optical axis in the vicinity of the focal plane for laser pulse energy of 30 μJ at the focusing depth of 1000 μm.

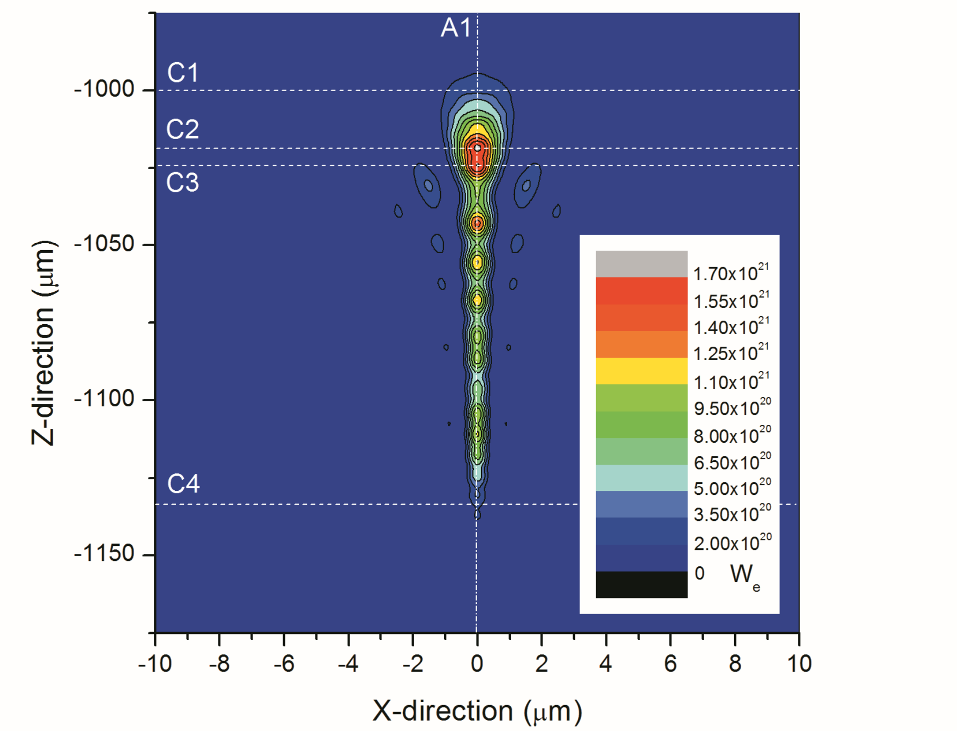

Figure 4.13: The contour map of representative electric energy density field on the xz-plane along an optical axis in the vicinity of the focal plane for laser pulse energy of 30 μJ at the focusing depth of 1000 μm. Lines C1, C2, C3, C4, and A1 represent section lines across this field.

The contour map of electric energy density in this region of interest by 30 μJ pulse energy at 1000 μm focusing depth is shown in Fig. 4.13. This Contour looks like tear drop shape and similar to the appearance of features and channels, and the total length and width of this contour are also about the same size as the experimental features in Fig. 4.6 (b). In the Fig. 4.13, lines C1, C2, C3, C4, and A1 represent section lines across this representative high electric energy density field. Lines C1 and C4 are located along the paraxial- and peripheral-ray focal planes, respectively. Lines C2 and C3 are located along the top two peaks of electric energy density, and line A1 is located along the optical axis. The contour and 3D surface maps on xy-planes along lines C1, C2, C3, and C4 are illustrated in Fig. 4.14 (a), (b), (c), and (d), respectively. From these

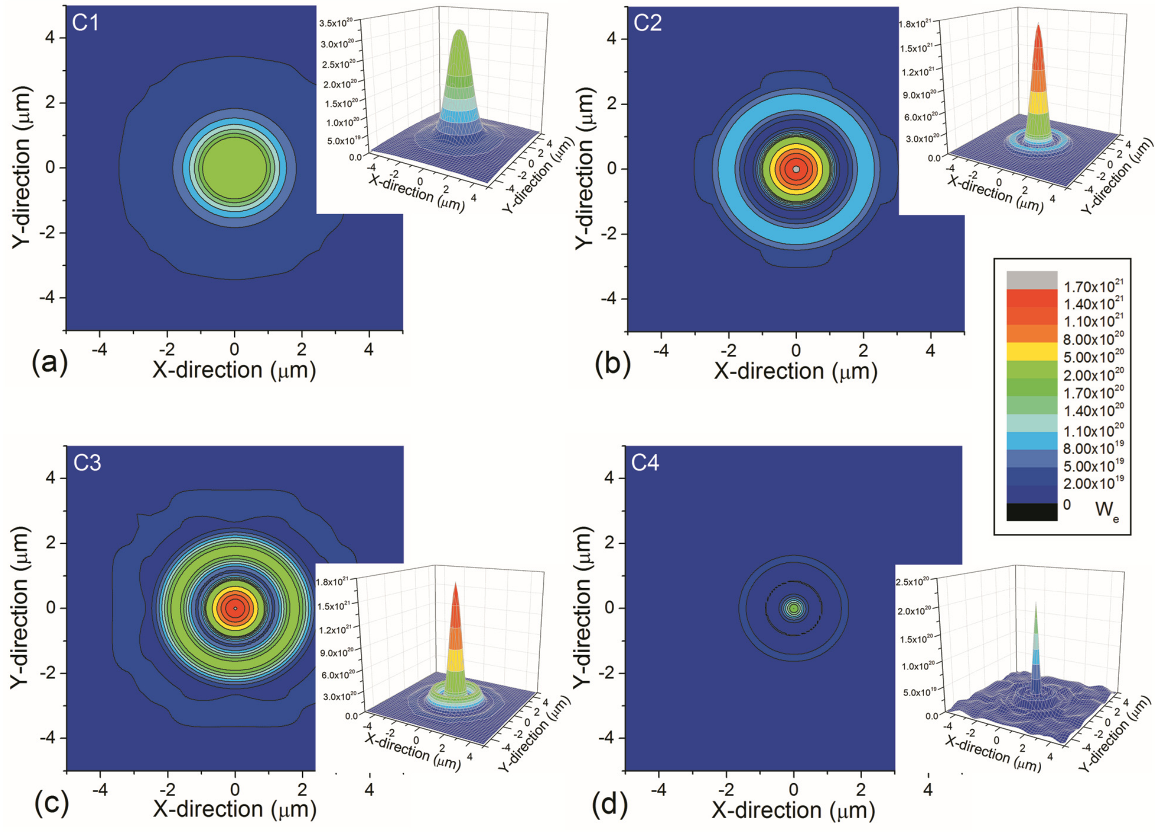

Figure 4.14: The contour and 3D surface maps in xy-planes along (a) line C1 located along the paraxial-ray focal plane, (b) line C2 located along the highest peak of electric energy density, (c) line C3 located along the second highest peak of electric energy density, and (d) line C4 located along the peripheral-ray focal plane.

contour and 3D surface maps, the distribution of electric energy density along axes perpendicular to the laser propagation direction has a Gaussian profile. The peak energy density of electric field on both paraxial- and peripheral-ray focal planes in Fig. 4.14 (a) and (d) are slightly less than the material damage threshold, and this could give the answer why the experimental feature lengths in section 4.4.1 are usually shorter than the defined paraxial aberration. The contour maps in Fig. 4.14 (b) and (c) along the xy-planes which have top two peaks of electric energy density show multiple rings which have energy density greater than the material damage threshold. The size of outbound rings with such high electric energy density is approximately 2 μm, and it can be seen that this size is corresponded to the width of experimental features and channels in section 4.4.1.

Figure 4.15 shows the electric energy density on the optical axis along line A1 in Fig. 4.13. The oscillation of the electric energy density along this optical axis could be due to the constructive

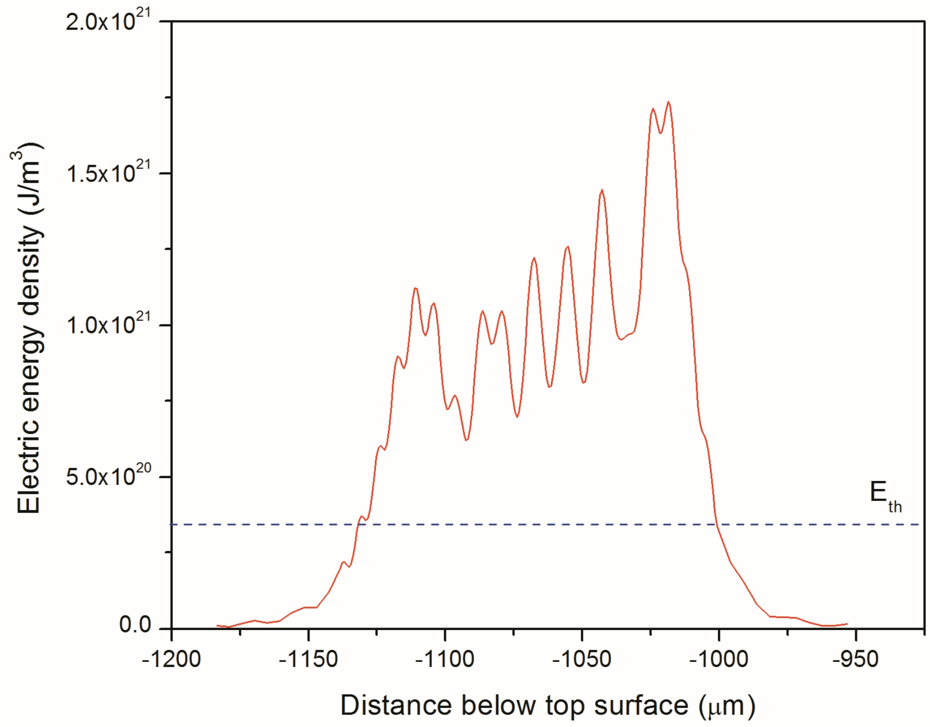

Figure 4.15: The electric energy density on the optical axis along line A1 in Fig. 4.13 compared to the damage threshold of fused silica sample.

and destructive interference of phase factor resulting from a superposition of refracted plane waves. From the line profile of electric energy density along the optical axis, the numerical feature length simulated by the electromagnetic diffraction model is defined as the distance whereas the electric energy density is greater than the material damage threshold (E_{th}) as illustrated in Fig. 4.15. The numerical feature lengths from this model are strongly dependent on both the focusing depths and the laser pulse energies. More details of the results from this numerical model will be shown and verified with the previous numerical model and the experimental results in next section.

4.4.2.3 Validation of Numerical Models with Experimental Results

From the simulated absorption volumes similar to the representative cross section map in Fig. 4.11, and the simulated electric energy density line profiles along the optical axis similar to the representative profile in Fig. 4.15, the numerical feature lengths calculated by absorption volume and electromagnetic diffraction models at different focusing depths below the top surface of fused silica sample using the single femtosecond laser pulse energy of 30 μJ as well as the experimental feature lengths are plotted in Fig. 4.16. The feature lengths from both numerical models have increasing trends with the focusing depths, and line up pretty well with the experimental feature length results. Especially for this particular laser pulse energy of 30 μJ, the results from the electromagnetic diffraction model almost perfectly match the experimental results and better predict the feature lengths than the absorption volume modeling. By taking the aberration effect from air-glass interface into consideration, the locations of breakdown points in the optical axis of the absorption volume model are approximated by using the law of tangents; therefore, the longer the focusing depth, the greater the discrepancy predicted by the absorption volume model. The electromagnetic diffraction model thus gives the better fit for the focusing

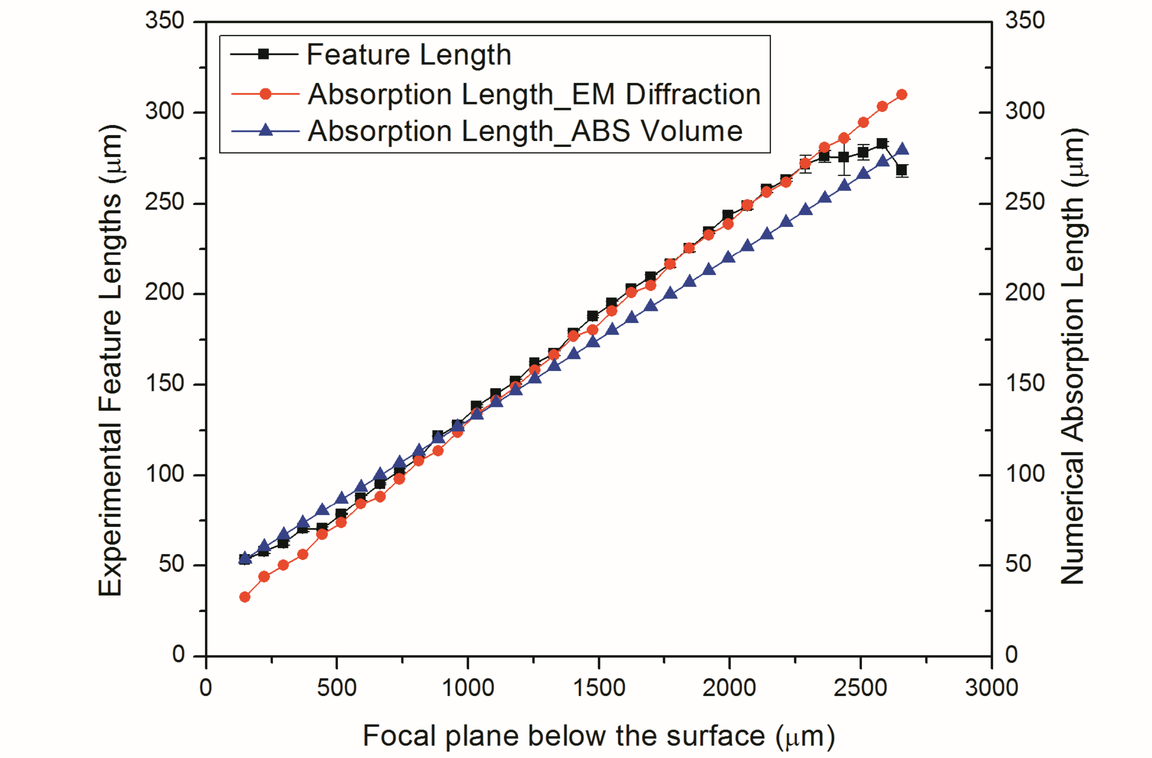

Figure 4.16: Comparison of feature lengths from two numerical models and experimental results at different focusing depths using laser pulse energy of 30 μJ.

depth longer than 500 μm. For the focusing depth shorter than 500 μm, there is less spreading of the electric energy density near focal plane, and energy density could be so intensified that it would conduct to an adjacent area resulting in longer experimental feature length; therefore, the absorption volume model apparently gives better results. Figure 4.17 shows the numerical and experimental feature length as a function of laser pulse energy at two different focusing depths of 1000 μm and 1500 μm below the top surface of fused silica sample, respectively. As seen in Fig. 4.17, the electromagnetic diffraction model has some difficulties in determining the feature length when the laser pulse energy is less than 20 μJ due to the electric energy density become lower than the material damage threshold at low pulse energies, and the level of laser pulse energy at which feature lengths could not be defined is also dependent on the focusing depths. The deeper the focusing depths, the greater the spreading of electric energy density resulting in the higher levels of pulse energy at which the feature lengths could not be determined. This problem could be due to the time-independent or time-averaged based approximation of the model whereas the absorption volume model which considers the temporal profile of laser pulse as well as the spatial profile still be able to predict the feature lengths at low pulse energy, however, the discrepancy between the numerical and experimental results will increase correspond to the lower pulse energies. Therefore, depending on the working parameters, the electromagnetic diffraction model better predicts the feature lengths with some restrictions at low pulse energies.

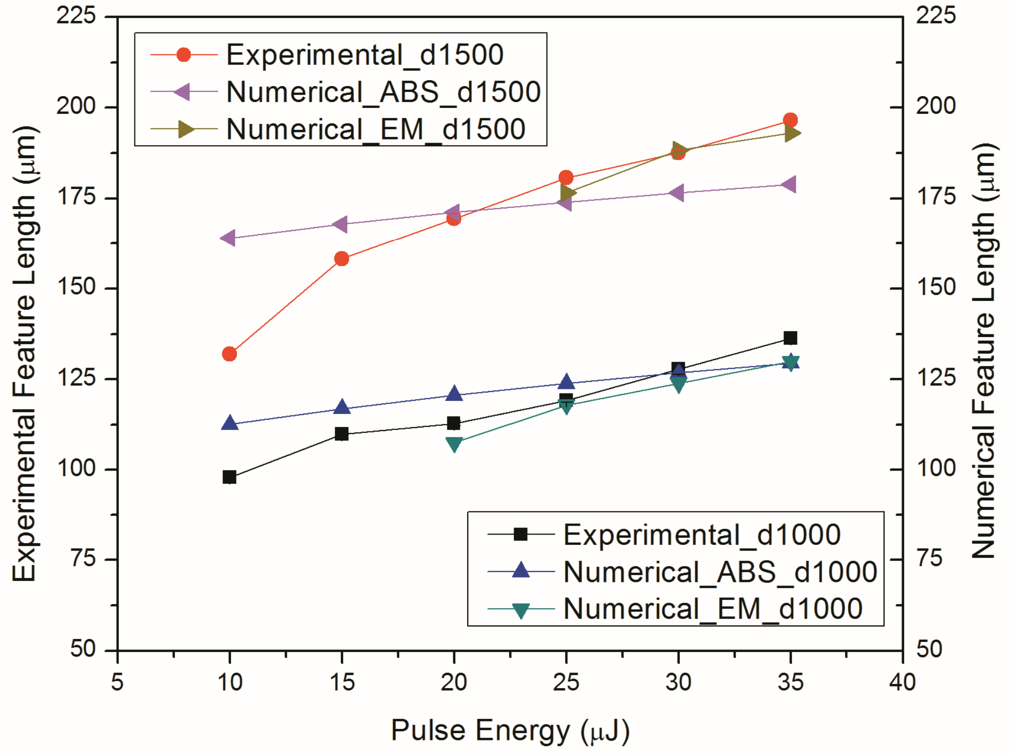

Figure 4.17: Comparison of feature lengths from two numerical models and experimental results at different pulse energies for focusing depth of 1000 μm and 1500 μm below the top surface of fused silica sample, respectively.

4.5 Conclusion

Single step channeling inside fused silica glass was performed by a series of single femtosecond laser pulses. The axial cross section of the generated features by the transmission DIC optical microscopy revealed that they range from 23 to 283 microns in length and 4 to 46 in aspect ratio. Those features also have a long uniform dark colored region, which is identified as a microchannel. The radial cross sectioning of this channel in conjunction with the surface topography confirmed that the channels are cavities. The reflection DIC optical microscopy and Raman spectroscopy also support this fact. The size of the features and channels is strongly dependent on the laser pulse energies and focusing depths. The variation in size of features and channels with focusing depths is due to aberration caused by the refractive index mismatch at air-glass interface. With overlapping distance of the feature equal or greater than 68%, channel cascading could be successfully performed to produce a longer channel in millimeter scale. Two numerical models were developed to investigate the shape and size of features and channels generated by single femtosecond laser pulses at different laser pulse energies and focusing depths. The numerical results were validated using the experimental ones, and both absorption volume and electromagnetic diffraction models could be used to estimate the feature lengths.

Chapter 5: Laser Induced Porosity and Crystallinity Modification of a Bioactive Glass Coating on Titanium Substrates

5.1 Introduction

Biomaterials are a class of materials used in biomedical applications for the repair and reconstruction of diseased or damaged parts of the human body. Their compositions can be categorized into four major classes: metals, ceramics, polymers and composites. Based on their interaction with the human body, they can be classified into three additional groups: bioinert, bioactive and bioresorbable [1]. Ti and its alloys, both bioinert metals, are most widely used in orthopedic implants due to their excellent bulk properties of high strength, ductility, corrosion resistance and biocompatibility [2]. However, they do not provide strong enough bonding to bone due to interfacial stability problems with the host tissues [1,3,4]. Bioactive glasses, on the other hand, have the ability to form a hydroxycarbonate apatite (HCA) layer on their surface and in consequence naturally bond with bone. The rate of development of the interfacial bond between bioactive glasses and bone can be referred to as the level of bioactivity. Among the widely known bioactive materials hydroxyapatite (HA), 45S5 Bioglass, and A/W glass-ceramics, 45S5 Bioglass has the highest rate of bioactivity [5]. This leads to the rapid surface reactions that form a bone-bonding HCA layer [6].

The bonding between bioactive glasses and bone is biochemical bonding (i.e., ionic, hydrogen, etc.) [7]. However, the limited mechanical strength and low toughness of bioactive glasses prevented their use for load-bearing applications such as orthopedic implants [1,8]. In order to solve this issue, coating bioactive glasses onto biocompatible metal substrates has been developed. Among investigated coating methods such as enameling, plasma spraying, rapid immersion, pulsed laser deposition (PLD), electrophoretic deposition (EPD), ion beam sputtering, sol-gel technique and laser coating, enameling and plasma spraying are the most commonly used coating methods. However, they presented cracks and porosity in the coating, caused relatively poor adhesion at the metal-glass interface, and high temperature treatments of the whole implant could damage the metal substrates [1]. On the other hand, laser coating is a localized heating process and has potential to both fusion bond and sinter the bioactive glasses on the metal substrates. Moritz et al. [9] explored the possibility of applying CO_2 laser irradiation for coating bioactive glass 1-98 on titanium medical implants. Mirhosseini et al. [10] used a combined laser/sol-gel technique to produce calcium silicate coatings and determined its effect on osteoblast response. Cheng et al. [11] investigated transmission laser coating of HA on Ti substrates. Comesana et al. [12] investigated the potential of the laser cladding technique to produce S520 bioactive glass coatings on Ti6Al4V alloy substrates. Chen et al. [13] made a functionally graded composite material coatings of different HA and pure Ti mixture on Ti6Al4V alloy substrates by laser cladding . O'Flynn et al. [14] examined the effect of laser sintering on a G250 bioactive glass-ceramic, but their attempts to coat G520 on Ti6Al4V by laser enameling were unsuccessful. Studies referenced above reported laser coatings of different bioactive glass compositions. However, the laser coating of 45S5 Bioglass, which has the highest rate of bioactivity, has not been investigated yet. Furthermore, plasma spraying and enameling coatings are unsuccessfully performed for this material [15,16].

Among the factors that determine the effectiveness of a material as a bioactive agent are the textural and morphological properties. Three main factors that affect the bioactivity of bioactive materials are porosity, surface roughness, and crystallinity. Porosity of the implants greatly enhances their bone bonding ability. Microroughening the bioactive glass surface significantly accelerated the early formation of surface reactions [17], and an increase in the surface area of the initial glass accelerates chemical reactivity in bioactive glasses. The crystallization rate of the apatite layer is affected by the texture of the silica substrate, increasing as pore size and pore volume increase [18–20]. Formation of silica rich and calcium phosphate-rich layers, indicating bioactivity, was slower on surfaces of samples that included sodium calcium silicate crystals than on the amorphous parent glass. The apatite formation increased from 10 hours for amorphous parent glass to 22-25 hours for 60-100% crystallized glass-ceramic [21]. Therefore, crystallization did not prevent the development of a crystalline HCA layer, but rather it increased the onset time of generating this layer.

In this study, a Nd:YAG laser and a Fiber laser both at 1064 nm wavelength are used to produce double layer coatings of 45S5 Bioglass on titanium substrates to achieve a functionally graded bioactive glass coating. This coating has a strong adhesion to the titanium substrates and high bioactivity on the top surface of the coating material. The sintering mechanisms, morphology and microstructure of sintered bioactive glass, as well as the effects of laser processing parameters on the porosity and crystallinity of the coating material have been investigated. A numerical model is also developed to yield greater insight into the temperature dependent laser sintering behavior of the bioactive glass and to predict its porosity and crystallinity.

5.2 Background

5.2.1 Implants and Bioactive Glasses

Most implants, such as hip and knee replacements, that use only bioinert metal substrates, often suffer from problems of interfacial stability with host tissues. Bioactive glasses are a group of surface reactive biomaterials that have been used to repair and replace diseased or damaged bone in the human body. However, bioactive glasses alone are not strong enough to be used for these load-bearing applications. Therefore, applying a glass coating onto a mechanically tough substrate is an alternative to reduce the risk of early implant failure. Coating a substrate with a bioactive glass serves three purposes: the substrate is protected from corrosion, tissues are protected from corrosion products which may induce systemic effects, and the bioactive glass bond easily with bone. Bioactive glass coating of bioinert metal implants has increased bone-implant contact in the early growth period. Early bone ongrowth is known to increase primary implant fixation and reduce the risk of early implant failure. A common characteristic of bioactive glasses is a time-dependent, kinetic surface modification that occurs upon implantation. When a bioactive glass is immersed in a physiological environment, such as a human body or simulated body fluid (SBF), reactions on the surface of this material are as following [8] :

1) Ion exchange between modifier cations in the glass with ions in the solution leads to formation of silanols (Si-OH):

$$\mathrm{Si - O - Na^+ + H^+ + OH^- \rightarrow Si\text{-}OH + Na^+_{(solution)} + OH^-}$$

2) Hydrolysis, in which Si-O-Si bonds are broken and the glass network is disrupted, leads to further formation of silanols:

$$\mathrm{2(Si\text{-}O\text{-}Si) + 2(OH) \rightarrow Si\text{-}OH + OH\text{-}Si}$$

3) Polycondensation of silanols in which the disrupted glass network changes its morphology to form a hydrated silica gel-like surface layer:

$$\mathrm{2(Si\text{-}OH) + 2(OH\text{-}Si) \rightarrow \text{-}Si\text{-}O\text{-}Si\text{-}O\text{-}Si\text{-}O\text{-}Si\text{-}O\text{-}}$$

4) Precipitation, in which an amorphous calcium phosphate layer is deposited on the gel.

5) Mineralization, in which the calcium phosphate layer gradually transforms into a crystalline hydroxyapatite layer (HCA).

When a layer of biologically active HCA forms, bonding of the implant with tissue can occur. The rate of HCA formation and the time for onset of crystallization varies greatly depending on the composition, morphology, and microstructure of the bioactive glass.

5.2.2 Kinetics of Sintering

Sintering is a processing technique used to produce density-controlled materials. Powdered particles join together by the application of thermal energy. Three categories of sintering processes are solid-state, liquid-phase, and viscous sintering. Densification of glass occurs by viscous flow, and viscous sintering is the dominant sintering mechanism for glasses. At temperatures above the glass transition temperature, glasses behave as ordinary Newtonian liquids. Due to surface tension, viscous flow takes place resulting in neck growth and shrinkage during sintering of glass particles. The work done by surface tension in decreasing the total surface area is equal to the total energy produced by dissipation of the flow of the viscous glass. Based on an energy balance concept, Frenkel [22] first proposed a viscous sintering model for the initial stage sintering. For viscous flow sintering, the neck growth and shrinkage are expressed as the following:

$$x^2 = \frac{4\gamma_s a}{\eta} t \tag{5.1}$$

$$\frac{\Delta l}{l} = \frac{3\gamma_s}{8\eta a} t \tag{5.2}$$

where x is the neck radius, a is the particle radius, γ_s is the surface energy, η is the viscosity, t is the sintering time, and $\Delta l/l$ is the shrinkage. The viscosity of glasses varies significantly from an average value of $10^{11.3}$ Pa·s at the glass transition temperature to a viscosity of ≤ 10 Pa·s at the practical melting temperature. The temperature dependence of the viscosity of glass is commonly expressed by the Vogel-Fulcher-Tamman (VFT) equation as following:

$$\eta = \eta_0 exp(\frac{B}{T - T_0}) \tag{5.3}$$

where η_0 is a constant, B is a variable related to the activation energy for viscous flow, T_0 is a fitting temperature ranging from zero to glass transition temperature, and T is the absolute temperature. When the glass powders are heat-treated over their transition temperature, a remarkable shrinkage of the material from viscous sintering occurs, and the powder structure starts consolidating and porosity is significantly reduced.

5.2.3 Kinetics of Crystallization

Both glass formation and crystallization are kinetic phenomena. The manufacture of glass is based on rapidly cooling the melt so that it will not form a crystalline, low-energy state[23]. Most glass-forming melts show some sign of crystallization if held just below the liquidus temperature long enough for structural arrangements to occur. Crystallization can occur either on cooling slowly from the melts or reheating to the temperatures below the practical melting point. The overall crystallization results from nucleation and crystal growth, and it could be analyzed using the Johnson-Mehl-Avrami-Kolmogorov (JMAK) theory [24–26]. The primary crystalline phase in crystallization correlates strongly with the oxide content of the glass and its thermal history. In bioactive glasses, different crystal types can form depending on the composition. Bioactive glass 45S5 has been reported to crystallize to $Na_2Ca_2Si_3O_9$ ($2Na_2O \cdot CaO \cdot 3SiO_2$) during heating [27,28].

The compositions of 45S5 bioactive glasses are in the $N_1C_2S_3$-$N_1C_1S_2$ composition region as shown in phase diagram of $CaO \cdot SiO_2$ - $Na_2O \cdot SiO_2$ in Fig. 5.1 [29]. The crystals grown in this glass are solid solutions ($Na_2Ca_2Si_3O_9$ ss) having the chemical formula Na_{4+2x}-$Ca_{4-x}[Si_6O_{18}]$ ($0 \leq x \leq 1$). These solid solutions are formed by replacement of one Ca atom by two Na atoms. Ohsato [30] explained that the structure of $Na_4Ca_4[Si_6O_{18}]$ in high temperature form, made up of

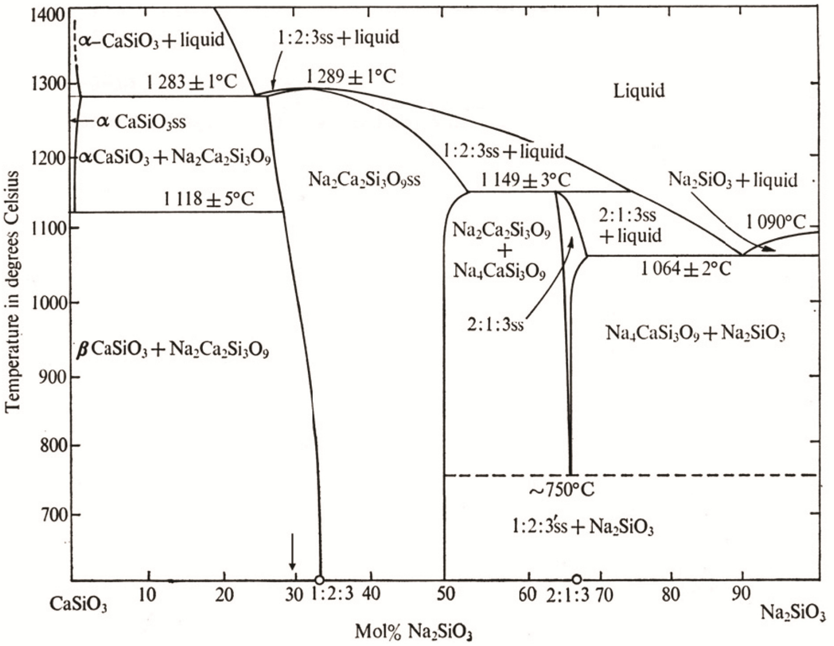

Figure 5.1: CaO·SiO2-Na2O·SiO2 pseudo-binary phase diagram of the sodium/calcium silicate system [29].

puckered six-membered $[Si_6O_{18}]^{12-}$ rings, is isostructural with $Na_6Ca_3[Si_6O_{18}]$. The structures consist of puckered six-membered rings of silicate tetrahedral, which are stacked in a cubic close-packing arrangement and held together by alkali and alkaline-earth ions. In the initial stage of phase transformation in both stoichiometric and non-stoichiometric glasses, the compositions of the crystals deviate considerably from those of the parent glasses [31]. The variation in the crystal composition is accounted for by the replacement of one Ca atom by two Na atoms. In the final stages of phase transformation, the average composition of crystals equals that of the parent glass. The crystals are solid solutions, and their composition changes during growth, approaching the parent glass composition with increasing crystallized volume fraction [32].

5.3 Numerical Simulation

Coupled modeling of the heat transfer, sintering potential, pore growth, and crystallization is performed to simulate the laser sintering behavior of bioactive glass. The laser radiation is considered as a heat source, and laser energy is assumed to be absorbed in a volume of a green body defined by a Gaussian distribution in the radial direction and exponential decay in the depth direction.

$$Q(r,z) = Q_0 exp\left(\frac{-2r^2}{R_0^2}\right) exp(-\alpha z) \tag{5.4}$$

where Q is the flux at point (r,z), Q_0 is the peak flux, R_0 is $1/e^2$ radius of the laser beam on the top surface, and α is the absorption coefficient of the green body.

In laser sintering, nucleation and crystal growth occur simultaneously, with rates that change continuously as the temperature changes during heating and cooling. According to the JMAK crystallization kinetics, the crystallized volume fraction for a non-isothermal condition can be expressed as [33]:

$$X(T(t)) = 1 - exp\left\{-\left(\int_{t_0}^{t} K\big(T(t')\big)dt'\right)^d\right\} \tag{5.5}$$

where X is the volume fraction transformed (crystallized), d is the dimensionality of growth (which is equal to 3 for homogeneous bulk crystallization), t is the time the sample experienced laser sintering, T is the temperature, and K is a temperature dependent crystallization rate that includes both nucleation and growth. Its function can be assumed by the Arrhenius equation:

$$K(T) = K_0 exp\left(-\frac{E_c}{RT}\right) \tag{5.6}$$

where E_c is the activation free energy of crystallization, R is the gas constant, K_0 is the pre-exponentials of crystallization rate, and T is the absolute temperature.

Based on the continuous media theory for selective laser sintering developed by Kolossov et al. [34], the porosity of the coating layer is defined by a sintering potential ϕ given by:

$$\phi(T(t)) = 1 - exp\left(-\int_0^t \zeta(T(\tau)d\tau\right) \tag{5.7}$$

where the range of ϕ is [0,1) corresponding to either the relative density of an original green body at $\phi = 0$ or fully dense glass $\phi = 1$. The rate of densification $\zeta(T)$ is first derived by Frenkel [22] and later expanded to be a temperature dependent function given by:

$$\zeta(T) = \frac{\gamma(T)}{\eta(T)d_0} \tag{5.8}$$

where γ is the surface tension or surface energy, η is the viscosity of heat-treated material, and d_0 is a characteristic length scale of the initial material. The thermal conductivity of partially dense glass depends on the temperature and sintering potential, and is given by:

$$k(\phi, T) = [a + (1 - a)\phi]k_{bulk}(T) \tag{5.9}$$

where k_{bulk} is the thermal conductivity of the bulk, and a is the ratio between the conductivity of loose powder and the bulk conductivity. The temperature dependent viscosity of amorphous glass can be expressed using the Vogel-Fucher-Tamman (VFT) equation as mentioned in section 2.2. When glass is partially crystallized, the effective viscosity, η_{eff}, will depend on the degree of crystallization and the viscosity of the amorphous glass. The effective viscosity can be approximated by the Einstein-Roscoe equation:

$$\eta_{eff}(X(T(t))) = \eta(T)\left(1 - \frac{X(T(t))}{X_{max}}\right)^{-n} \tag{5.10}$$

where X_{max} and n are adjustable parameters, and the values of 0.75 and 2.5 are widely used, respectively [35]. When densification and crystallization take place simultaneously, the increase of effective viscosity may reduce the sintering rate and inhibit the densification. Only glass-glass contacts develop necks by viscous flow [36,37]; therefore, the modified sintering rate with concurrent crystallization could be expressed as:

$$\zeta(T) = \frac{\gamma(T)}{d_0\eta(T)\left(1 - \frac{X(T(t))}{0.75}\right)^{-2.5}}[1 - X(T(t)] \tag{5.11}$$

During the later stage of sintering, it is possible that an isolated pore containing gas may diffuse and coalesce with its neighboring pore. The rate of pore growth caused by pore diffusion and coalescence could be expressed as [38]:

$$\frac{dr_p}{dt} = \frac{mD_p\gamma(T)v_p}{r_p^2 k_B T} \tag{5.12}$$

where r_p is a pore radius, v_p is the pore molar volume, k_B is the Boltzmann constant, and D_p is the pore diffusion coefficient, which is temperature dependent and can also be determined by the Arrhenius equation. The pore growth factor, P_g, can be calculated as a function of final pore radius, r_f, and initial pore radius, r_i:

$$P_g = \frac{r_f^3 - r_i^3}{r_i^3} \tag{5.13}$$

The overall porosity results from the competing mechanisms of viscous flow densification and pore coalescence. The overall porosity, P, can be determined as a function of initial density, ρ_i, sintering potential, and pore growth factor by the expression below:

$$P = 1 - \{\rho_i + (1 - \rho_i)\phi - P_g[1 - \rho_i - (1 - \rho_i)\phi]\} \tag{5.14}$$

To systematically predict temperature, sintering potential, pore growth, and crystallization, the mathematical model of each module described above needs to be rationally arranged. The flow chart of the integration of these modules is shown in Fig. 5.2. This setup is solved using COMSOL Multiphysics. Simulation results offer a useful insight into the temperature dependent behavior of laser sintering, capturing the combined effects of laser heating, densification, pore coalescence, and crystallization on the resulting porosity and crystallinity.

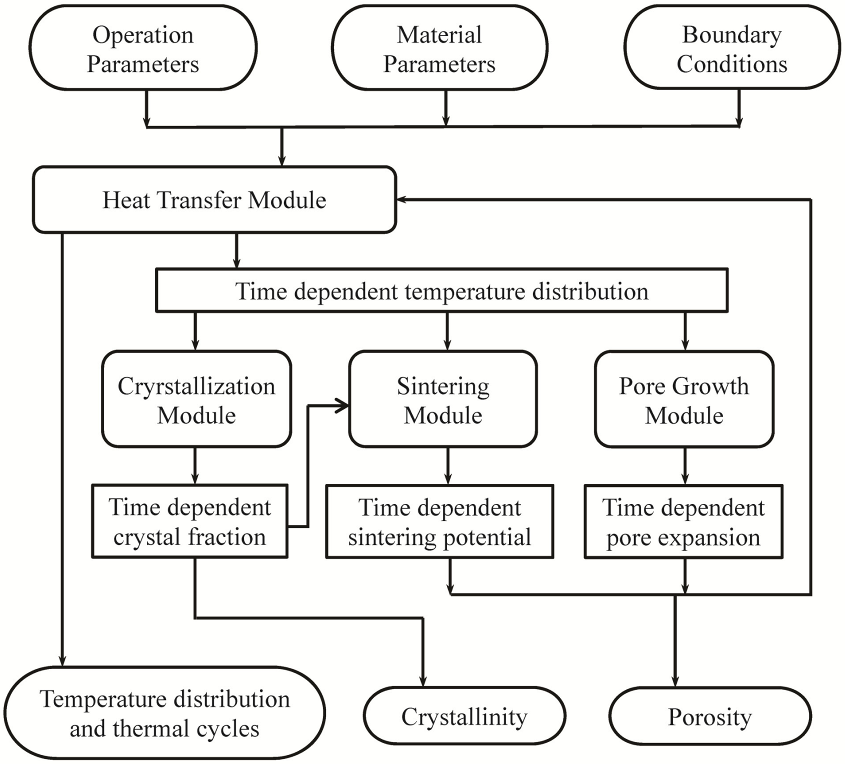

Figure 5.2: Flow chart of the numerical model. It captures the combined effects of laser heating, densification, pore coalescence, and crystallization to predict degree of porosity and crystallinity.

5.4 Experimental Setup and Characterization

45S5 bioactive glass powder was pre-coated on Titanium grade 2 substrates using a sedimentation method by mixing the glass powder with ethanol before depositing the glass slurry on the substrates. Before sedimentation, the substrate was ground using a 120 grit silicon carbide paper to roughen its surface, allowing for increased mechanical interlocking between the substrate and the coating layer. The sample is subsequently heated in a furnace at 120 °C for 12 hours to assure that the ethanol is completely evaporated. A GSI Lomonics JK-2000 Nd:YAG laser and a SPI redEnergy G4 Fiber laser both operating in continuous wave (CW) mode at a wavelength of 1064 nm were used for double layer coating of the bioactive glass on a titanium substrate. The Nd:YAG laser at fixed intensity of 40 W/mm^2 and scanning speed of 1.25 mm/s was used for coating the dense bond coat layer onto Ti substrates. A second layer of glass slurry was subsequently deposited on top of this densified bond coat. Finally, the Fiber laser with spot size of 700 μm was used for sintering the porous top coat layer onto the dense bond coat layer of the bioactive glass. Laser powers of 10 to 12 W (intensities of 26 to 31 W/mm^2) and scanning speeds of 1.0 to 2.0 mm/s were adjusted for sintering of the top coat. Laser coatings were performed with shielding by ultra-high purity argon gas which was flowed on the surface at a flow rate of 12scfh. A schematic diagram of the experimental setup is illustrated in Fig. 5.3.

The glass powder is highly transmitting at the 1064 nm wavelength; however, due to multiple surface scattering [39] the overall absorptivity of deposited glass powder is as high as the case of a nonlinear absorption mechanism [40] after measuring a time-averaged laser power that passes

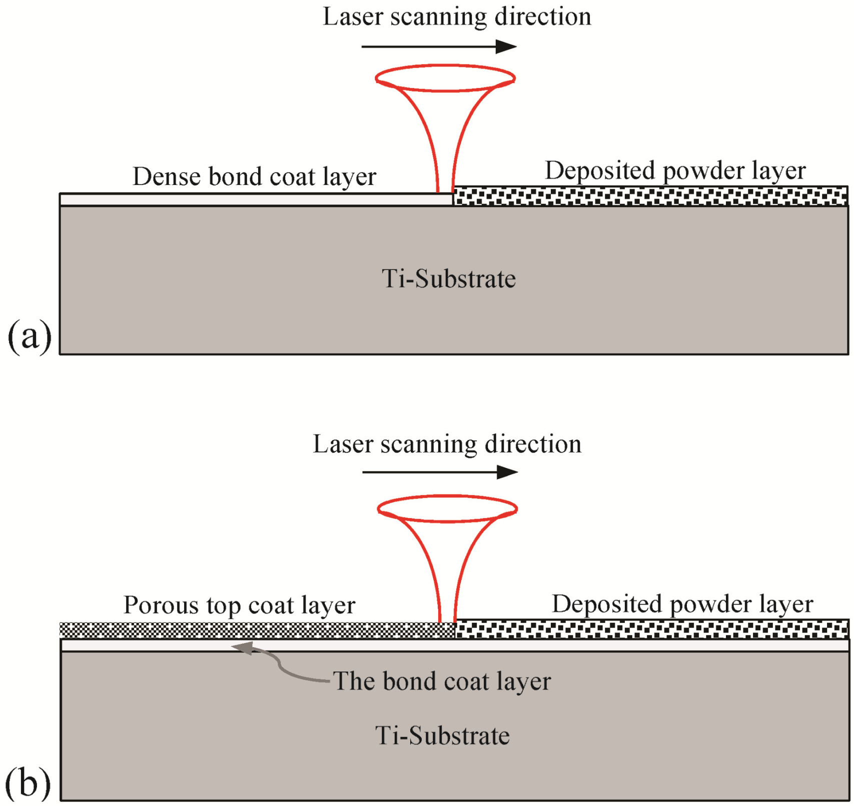

Figure 5.3: Schematic representation of 45S5 Bioglass laser coating on a titanium substrate. Laser sintering of (a) the dense bond coat layer and (b) the porous top coat layer. The bond coat layer is necessary to achieve strong adhesion on the substrate. The top coat layer with a highly bioactive porous structure is beneficial for early formation of a bone-bonding HCA layer.

through the deposited glass powder layer on fused silica. After laser coating, the samples were embedded in epoxy molds, and then ground with silicon carbide papers and polished with alumina and leather polishing pads to examine the cross section views using a Hitachi S-4700 scanning electron microscope (SEM). Compositional analysis was also performed using energy dispersive x-ray spectroscopy (EDX) on the Hitachi S-4700. Morphology and microstructure of the bioactive glass were also observed using an Olympus BX-60 optical microscope. An Inel XRG-3000 X-ray diffractometer (XRD) with CuKα radiation was used to determine the crystallization phase and percent crystallinity.

5.5 Results and Discussion

5.5.1 Morphology and Porosity of Pre-treated Glass Powder

For 45S5 Bioglass, which has the highest rate of bioactivity, coatings by plasma spraying or enameling usually fail due to the lack of adhesion to the substrate [15,16]. By properly controlling the parameters of laser irradiation on the glass powder layer, a functionally graded 45S5 Bioglass coating with dense structure having strong adhesion on a titanium substrate, and with a highly bioactive porous structure on the top surface was achieved. Figure 5.4 (a) and (b) show the representative top-view optical micrograph and cross-sectional SEM image of this deposited powder layer before laser irradiation. The crushed 45S5 Bioglass powder has no specific shape, with particle size < 50 μm. These glass particles temporarily stay together to form a thin layer on the titanium substrate. The deposited powder layer has high porosity as shown in Fig. 5.4 (b). The porosity was characterized using image-analysis by direct observation of the cross-sections of the deposited powder layer. Areas of the glass particles and the pores were separately specified as shown in Fig. 5.4 (c). The yellow lines indicate boundaries of glass particles. Area fraction calculation of porosity was done by using ImageJ software. The average porosity is 39.2%, or the relative density of the deposited glass powder layer is 60.8%.

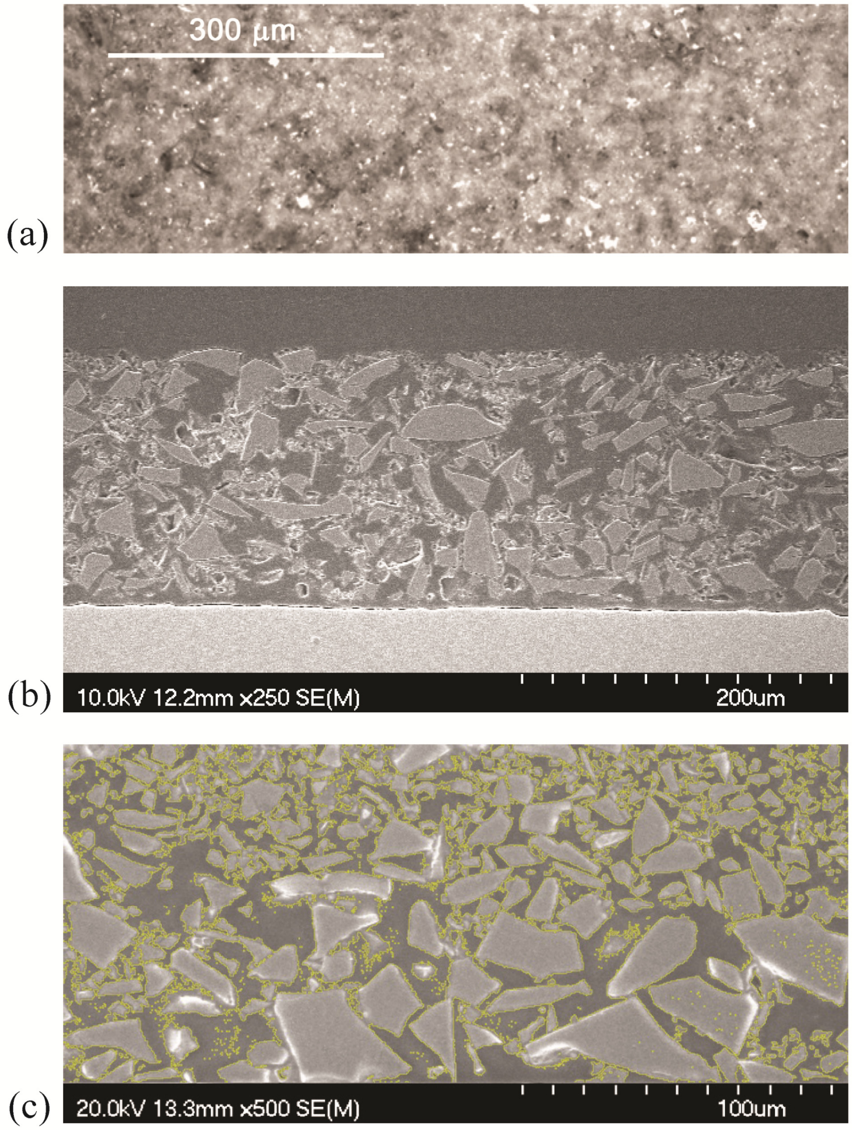

Figure 5.4: (a) Top-view optical micrograph and (b) cross-sectional SEM image of deposited glass powder layer by sedimentation; (c) Image analysis to characterize porosity. The yellow lines indicate boundaries of glass particles, and the average porosity of deposited glass powder layer is 39.2%.

5.5.2 Bond Coat Layer on the Ti Substrate

The coating of a bioactive material on a bioinert metal for orthopedic implants is considered to be successful if the coated material is strongly adhered onto the substrate. Laser irradiation of the glass particles increases their temperature such that the viscosity of 45S5 Bioglass is decreased from the softening point ($10^{6.65}$ Pa·s) to the practical melting point (10 Pa·s). For the required dense structure of the bond coat layer, higher laser power for increasing the temperature of 45S5 Bioglass above its practical melting point is required. Figure 5.5 shows the morphology of this desired bond coat layer in both top and cross-section views. Due to the Gaussian distribution of the laser beam, there are two distinctive regions of laser affected zone as shown in the top-view optical micrograph in Fig. 5.5 (a). The dark center region apparently has a dense structure, and the glass powder is believed to reach the practical melting temperature in this area. With lower laser intensity in the peripheral area of the beam, the resulting gray region has a porous structure. The glass powder experiences temperatures above the softening point and sintering takes place in this area. There is a transition between these two regions, and the microstructure in the transition

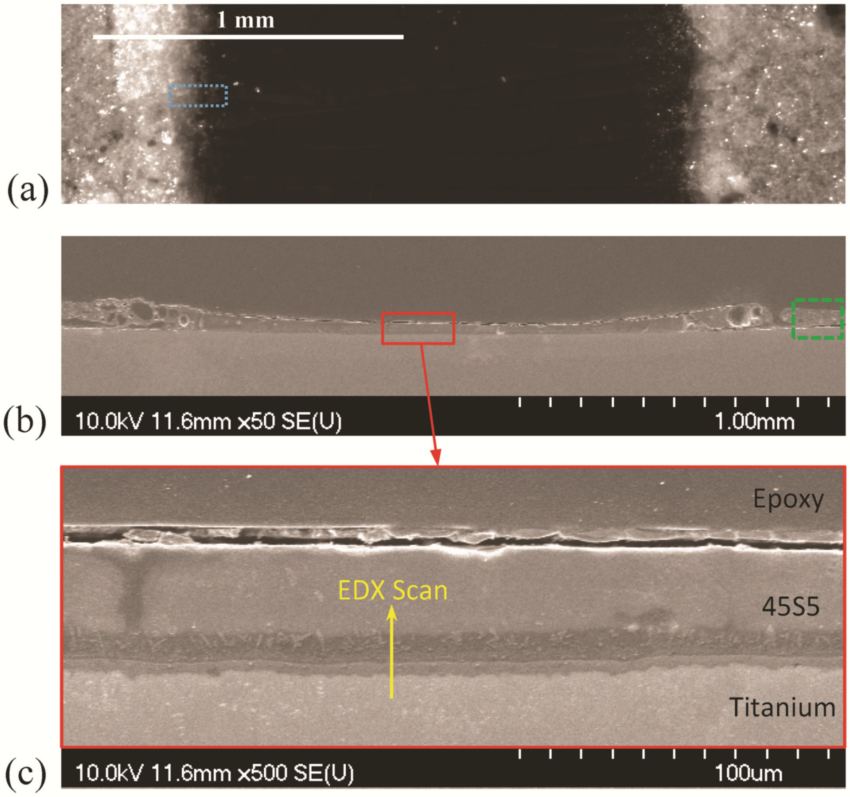

Figure 5.5: (a) Top-view optical micrograph and (b) cross-sectional SEM image of the bond coat layer; (c) Expanded view at the interface between Ti-substrate and the bond coat. Region at the center has a dense structure.

area will be discussed in Section 5.3.2. From the cross-sectional view in Fig. 5.5 (b), and (c), it indeed shows that the center region has a dense structure, and there is continuity without any lateral cracks on the coating interface between the 45S5 Bioglass and the titanium substrate. On the other hand, there is a distinctive gap between the deposited powder layer and the substrate as shown in Fig. 5.4 (b). Figure 5.6 shows an EDX composition map and line scan composition profiles across the interface as depicted in Fig. 5.5 (c). The existence of a 10 μm wide mixed interfacial layer is clearly shown in Fig. 5.6 (a) and (c). In a thermally activated process, there is diffusion of titanium into silicate glass melts [41,42]. When the thermal energy of a titanium atom

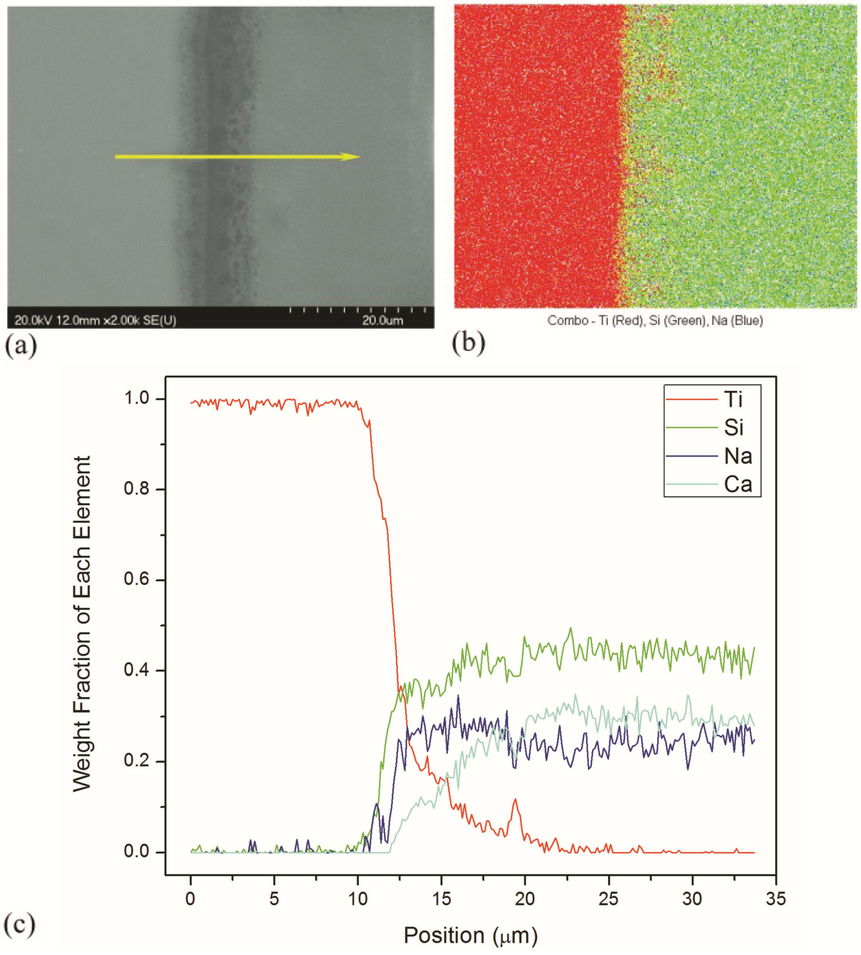

Figure 5.6: (a) Cross-sectional SEM image of the interface region in Fig. 5.5(c) denoting a scanning area for (b) EDX composition map and a scanning line for (c) EDX composition profiles across the interface. It indicates titanium diffusion into the glass with a ten microns wide mixed interfacial layer.

is greater than its activation energy, it could break inter-atomic bonds to move into melted glass causing interfacial reactions to form titanium silicides and titanium oxide [43,44]. The EDX composition map in Fig. 5.6 (b) shows that Ti from the titanium substrate diffuses towards the glass, resulting in relatively strong chemical bonding between the bond coat layer and the titanium substrate.

5.5.3 Top Coat Layer on the Bond Coat

5.5.3.1 Morphology and Porosity

The porous structure on the top surface of the coated implants is desirable for high bioactivity. It can be achieved by applying lower laser powers to not reach the melting regime of the 45S5 Bioglass, but high enough to induce sintering of the material. If the processing parameters are used for coating the porous top coat layer directly onto the titanium substrate, there will be a gap between the bioactive glass and the substrate as shown in Fig. 5.7 (a), and the coating layer would be easily detached from substrate by applying a relatively small force. Therefore, the bond coat layer of bioactive glass as discussed in the previous section is essential. The deposition of the 45S5 Bioglass powder on the bond coat layer is shown in Fig. 5.7 (b). This deposited glass powder layer was laser irradiated under sintering conditions resulting in the top coat layer as shown in Fig. 5.7 (c). The glass powder was successfully sintered together and also bonded with the bond coat layer. It is clear that the top coat layer has a porous structure with mostly closed pores, but some open pores are found near the top surface. The fluorescence micrograph in Fig. 5.7 (d) shows the existence of the open pores as a fluorescent dye mixed with epoxy flows into those pores from the top surface. Since the 45S5 Bioglass is originally an amorphous material, the dominant material transport mechanism is the viscous flow. The densification by viscous flow proceeds more rapidly than that by other solid-state diffusion mechanisms [45,46]. During

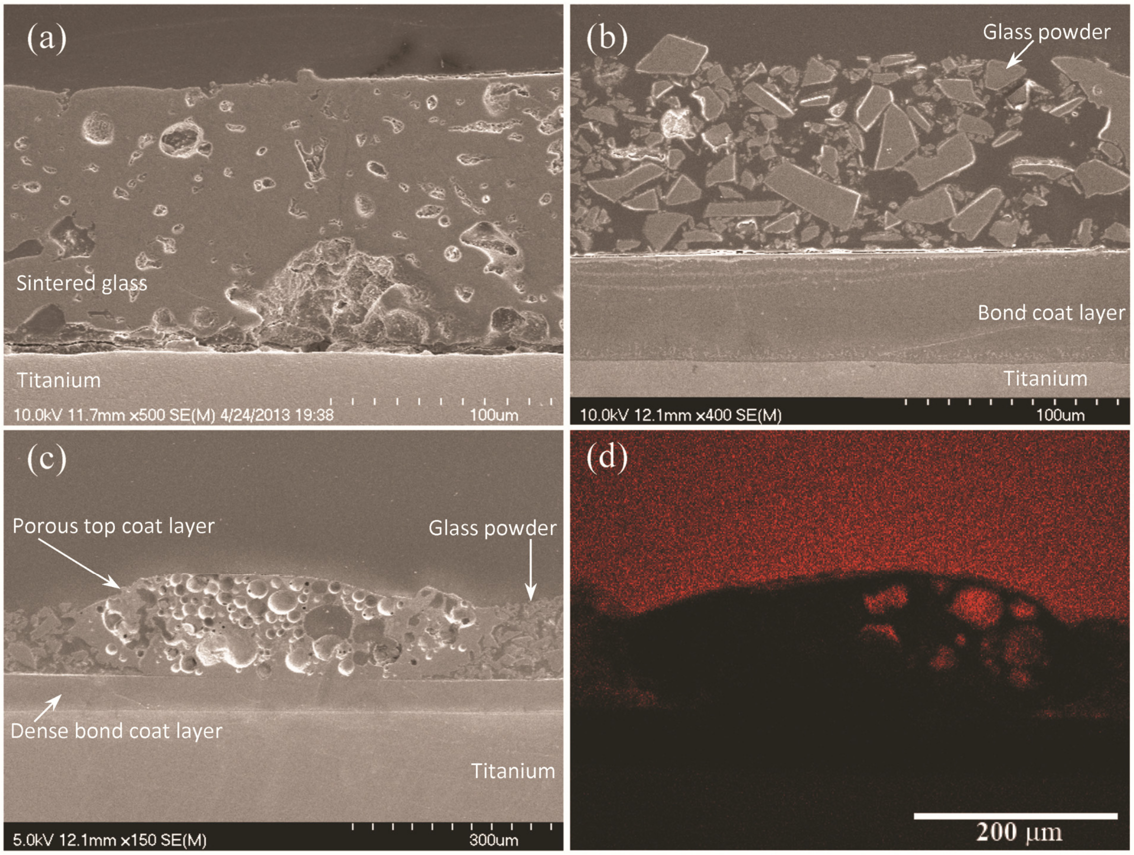

Figure 5.7: Cross-sectional SEM images of (a) direct laser sintering (from the denoted rectangular area in Fig. 5.5(b)) of a porous glass layer onto a Ti-substrate, (b) a second layer of glass powder deposited on the dense bond coat before another laser irradiation, (c) morphology of resulting dense bond and porous top coat layers by laser coating; (d) The fluorescence micrograph of pores opened to the top surface. Figure 5.7 (a) shows weak attachment of porous glass coating directly on a titanium substrate as compared to the double layer coating with a dense structure having strong adhesion on the substrate and with a highly bioactive porous structure on the top surface in Fig. 5.7 (c).

laser sintering, the decrease in temperature-dependent viscosity causes the orientation of glass particles to be changed, and glass particles will develop more points of contact. Neck formation at the contact points and neck growth subsequently occur together with the formation of an array of interconnected pores. Finally, the shape and size of particles and pores gradually change until the pores become isolated. Figure 5.8 shows the SEM cross-section micrographs with expanded views of isolated pores and pre-existing interface area between the two glass layers. There is no distinctive gap between the layers as shown in Fig. 5.8 (c). With the open pore structure of the deposited glass powder layer as seen in Fig. 5.7 (b), the sintering atmosphere has important effects

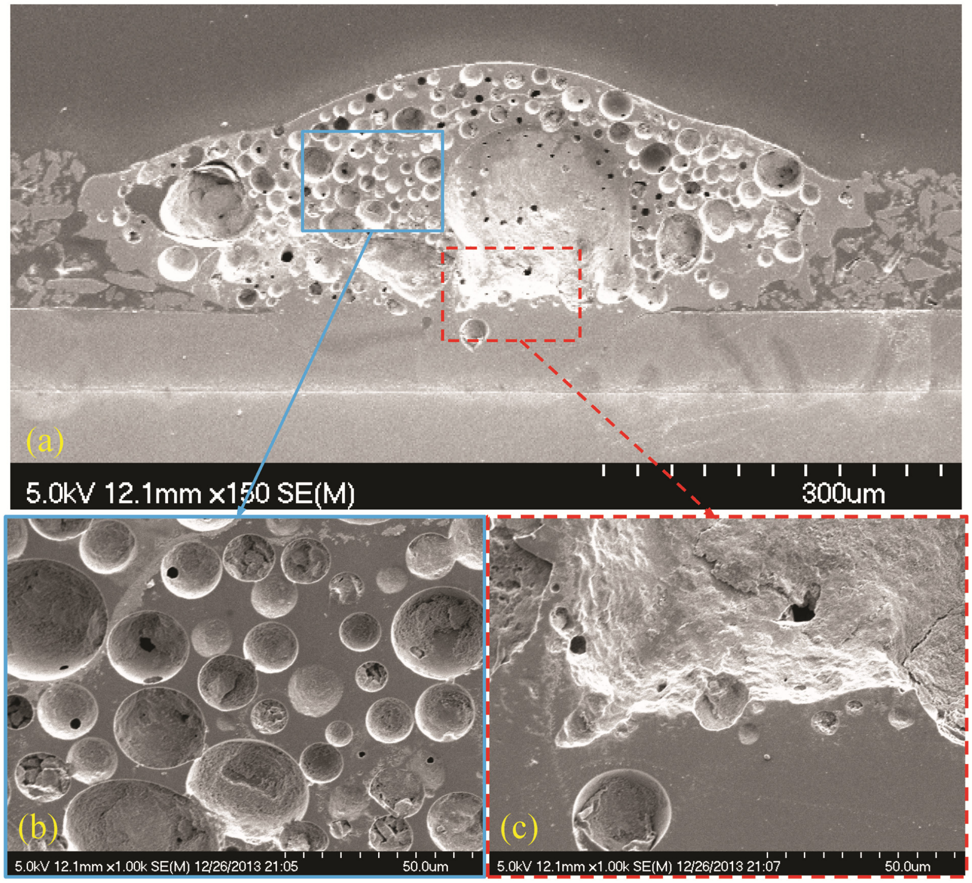

Figure 5.8: Cross-sectional SEM images of (a) double layer laser coating; (b) Expanded view at the porous top coat layer and (c) the pre-existing interface between two layers. Swelling of the porous top coat layer results from pore coalescence dominating over viscous flow densification. There is no gap between the bond and top coat layers.

on densification and microstructural development during sintering. Atmospheric gas will get trapped inside when the pores pinch off and become isolated. For an insoluble gas like air, the gas is compressed and its pressure increases as the shrinkage of the isolated pores takes place. When the gas pressure becomes equal to the driving force for sintering, the shrinkage stops. At the same time it is possible that diffusion of the gas between neighboring pores can occur [47]. Temperature gradients and gas pressure differences in various sizes of pores are the driving force for the diffusion. Volume shrinkage due to densification by viscous flow and volume expansion due to pore growth (or pore coalescence) by gas diffusion will compete with each other. When the pore coalescence is more dominant than viscous flow densification, swelling of the laser-sintering region occurs as shown in Fig. 5.8 (a). Since laser sintering is a considerably fast heating and cooling process, most of the pores do not have enough time to rise to the surface based on their buoyancy. Different spherical-like shapes of various pores, resulting from the competition between viscous flow densification and pore coalescence is shown in Fig. 5.8 (b). They range from six to tens of microns. The overall porosity of laser sintering of 45S5 Bioglass depends on not only viscous flow densification and pore coalescence, but also crystallization which will be discussed in the next section.

5.5.3.2 Microstructure and Crystallinity

Thermal treatments of 45S5 Bioglass above the glass transition temperature lead to crystallization. Crystallized or devitrified glass occurs by nucleation of the crystal phase and subsequent growth. A bulk 45S5 Bioglass sample can be fully crystallized, and the microstructure of heat-treated bulk 45S5 Bioglass is shown in Fig. 5.9 (a). From this optical micrograph, the grain structure and boundaries are clearly observed, and the average grain size is roughly ten microns. For 45S5 Bioglass powder, during heat treatment, sintering and crystallization occur at the same time. In the sintering temperature range, a material experiences necking and becomes denser due to viscous flow. At the same time, it also starts nucleation and growth of the $Na_2Ca_2Si_3O_9$ crystal phase, and the material will be partially crystallized. With laser irradiation, the heating and cooling times are so fast that the result of treated glass powder will be either fully dense glass without a crystal phase or porous glass with a partially crystallized phase. This depends on whether or not the treatment temperature is above the practical melting point. In this study, a higher laser power condition was selected to induce melting of the glass powder so that it would fusion bond with the titanium substrate, resulting in a strong adhesion to the substrate as shown in Fig. 5.5 (a). However, in the peripheral area of the

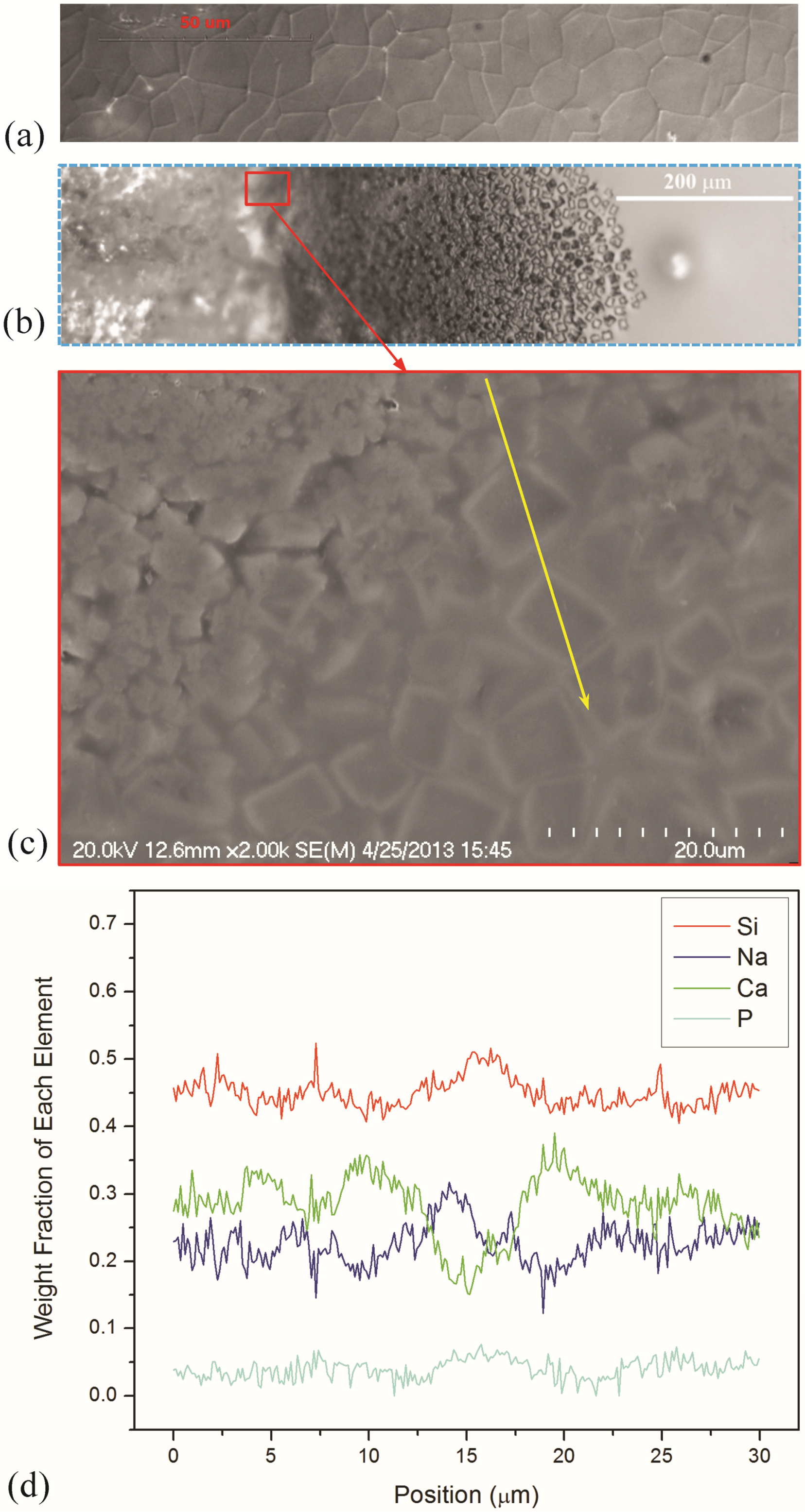

Figure 5.9: (a) Optical micrograph of crystallized 45S5 bulk glass heat-treated in the furnace; (b) Top-view optical micrograph (expanded view from the denoted rectangular area in Fig. 5.5(a)) and (c) top-view SEM image of the partially crystallized dense area by laser sintering; (d) EDX composition profiles show that crystals are calcium-rich compared to the amorphous glass.

Gaussian laser beam, there is a sintering region. From the left to the right of the indicated area in Fig. 5.5 (a), there are sintering, transition, and melting regions, respectively as shown in Fig. 5.9 (b). Among these regions, glass powder experiences different temperature regimes. On the left hand side, the temperature is within sintering temperature but lower than the practical melting point; therefore, it becomes partially crystallized and porous glass. On the right hand side, the temperature is above the practical melting point; therefore, it becomes densely amorphous glass. However, in the transition region, there is partially crystallized dense glass with cubic like isolated grain approximately five microns in size. In this region the temperature is supposedly high enough to fully densify the residual glass and the $Na_2Ca_2Si_3O_9$ crystal phase together, but lower than the liquidus temperature of the crystal phase. Figure 5.9 (d) shows line scan EDX composition profiles across the two isolated crystals in Fig. 5.9 (c). Based on the phase diagram of the $CaO \cdot SiO_2$ - $Na_2O \cdot SiO_2$ in Fig. 5.1, even though there is a continuous variation in glass and crystal compositions during crystallization by the replacement of one Ca atom by two Na atoms in the crystals [30,32], the crystals should be calcium-rich and sodium-depleted when compared to the parent glass as shown in Fig. 5.9 (d). Figure 5.10 shows the XRD spectra from the deposited glass powder layer by sedimentation, the laser coating sample, and the coating sample by enameling. The deposited glass powder shows a typical amorphous spectrum with single broad peak. In both partially crystalline samples, the diffraction pattern and all distinctive peaks agreed with those of the $Na_2Ca_2Si_3O_9$ crystal phase reported on PDF card No.04-011-6167. The spectrum of the enameled sample by firing in the furnace at 750 °C for 15 min shows higher peak intensity than the laser coating sample, and it shows that the crystallinity of the laser coating sample is lower than the enameling coating sample. The lower degree of crystallinity is more desirable for achieving the high bioactivity of the implants. The quantification of crystallinity and porosity of laser coating samples at different processing parameters were performed and discussed in the next section.

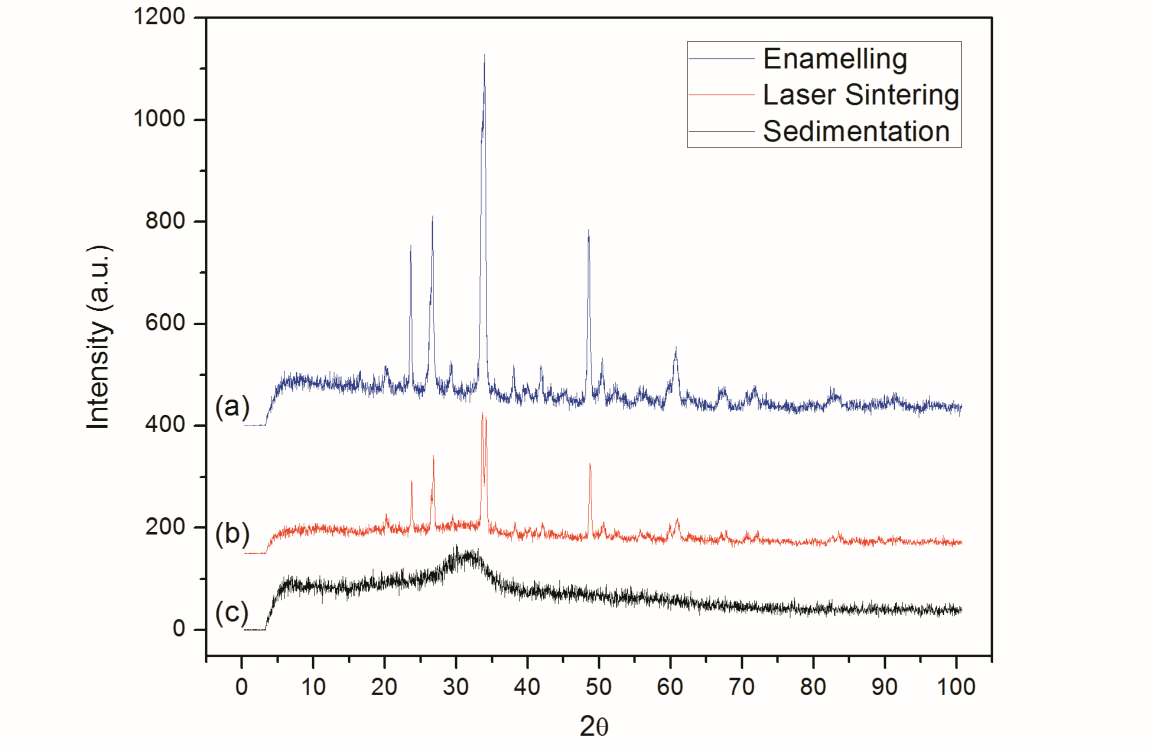

Figure 5.10: XRD Spectra of (a) the enameling process sample fired at 750 °C for 15 min in the furnace, (b) laser sintering of the porous top coat layer at 12W and 2.0 mm/s, and (c) amorphous 45S5 bioactive glass powder deposited by sedimentation. Laser sintering causes less crystallinity than enameling, which is beneficial for bioactivity of implants.

5.5.3.3 Effect of Laser Processing Parameters

The overall porosity of a laser coating sample was characterized by using image-analysis to directly observe a sintering cross-section area of the porous top coat layer of bioactive glass. The boundary line of the sintering area was traced, and its area was calculated and compared with the powder-deposited area before laser sintering to determine the overall porosity. The degree of crystallinity of a laser sintering sample was quantified by comparing its integrated peaks intensity in XRD spectrum to that of the fully crystallized sample [48]. A heat-treated sample at 750 °C in the furnace for ten hours is assumed to be fully crystallized and its spectrum was used

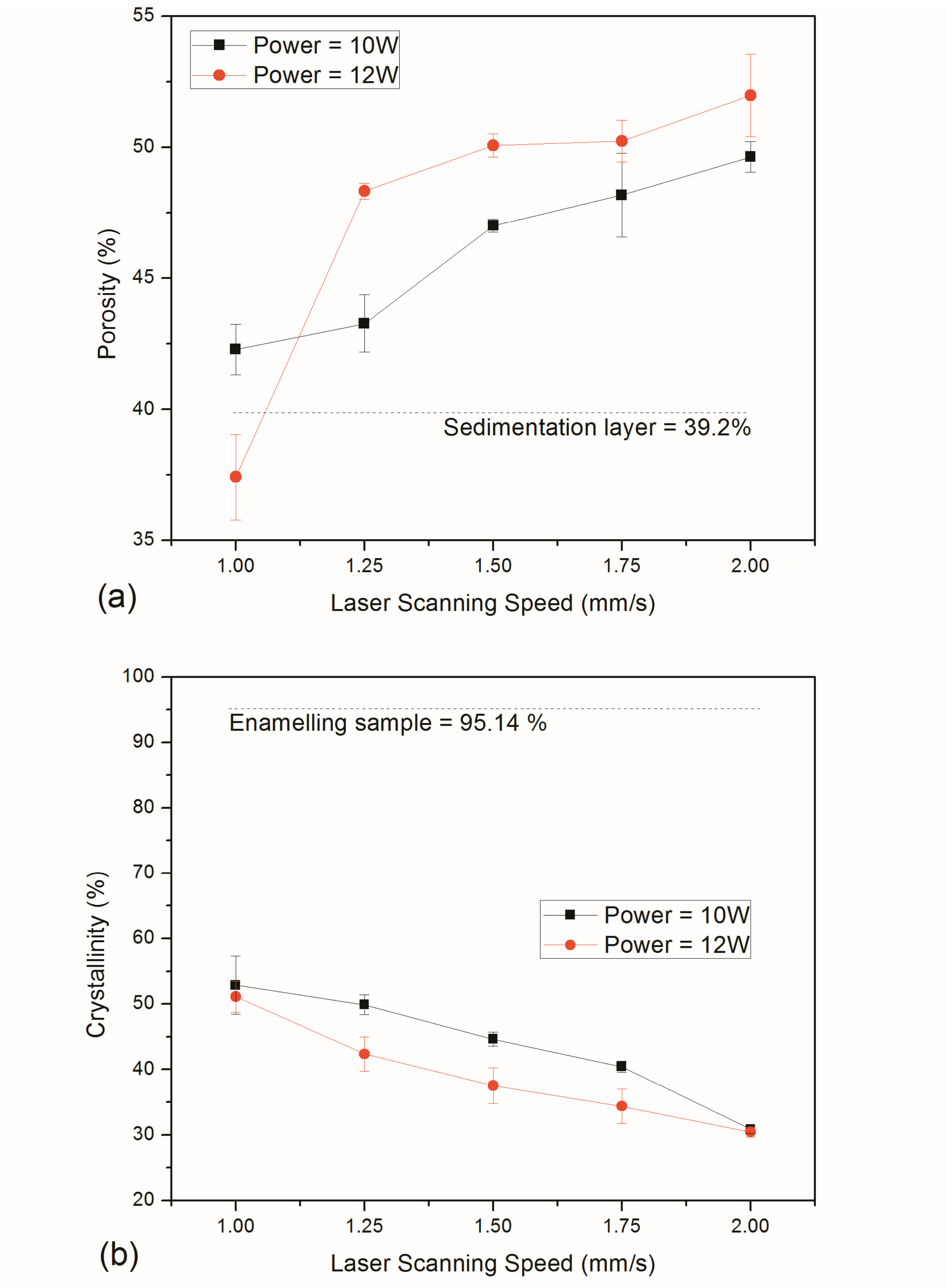

Figure 5.11: (a) Porosity and (b) crystallinity of laser sintering samples vs. laser scanning speed. Error bars denote standard deviation. Faster scanning speeds correspond to the formation of higher porosity and lower crystallinity.

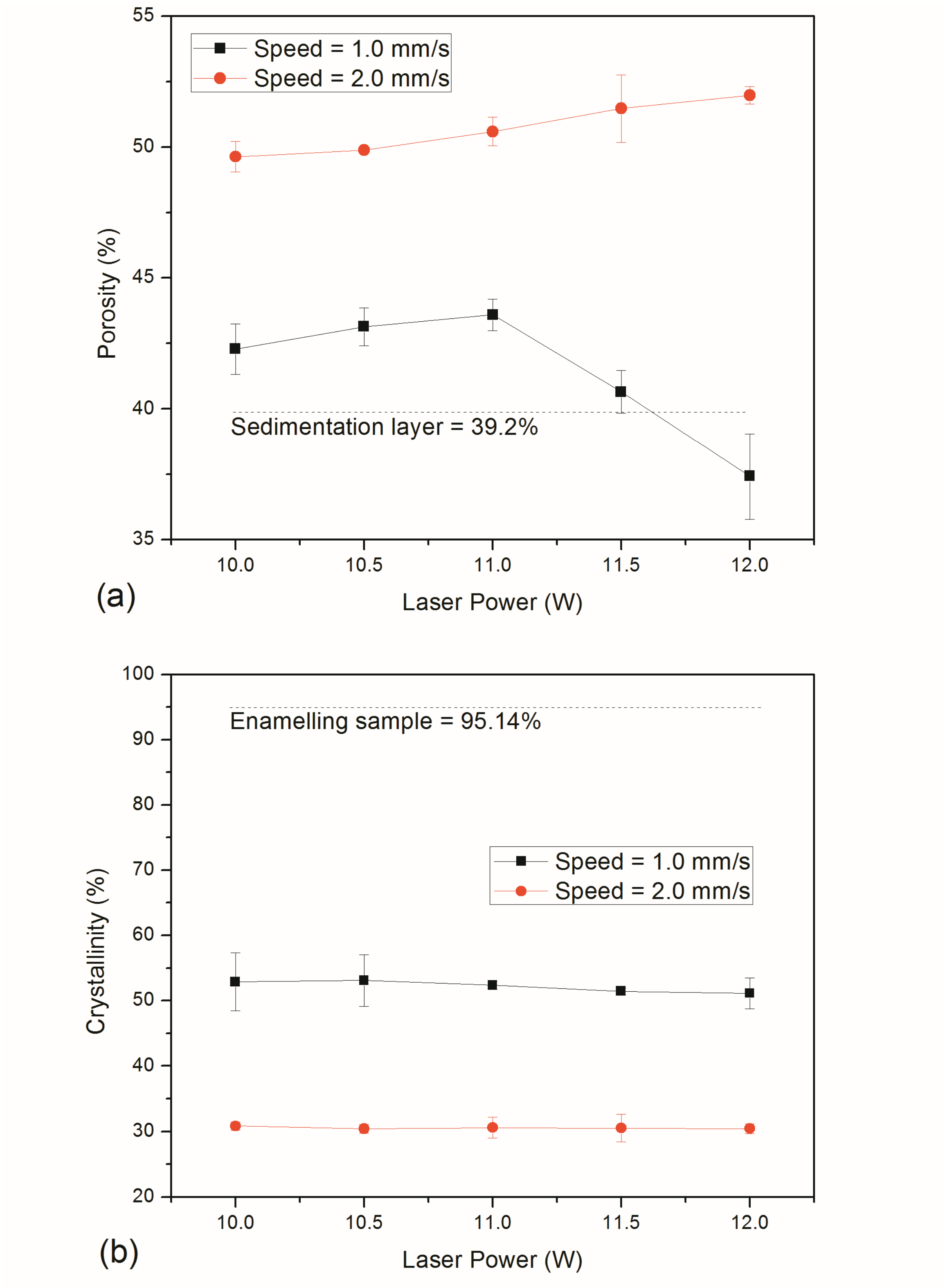

Figure 5.12: (a) Porosity and (b) crystallinity of laser sintering samples vs. laser power. Error bars denote standard deviation. Crystallinity is more-or-less constant with laser powers.

as a reference. Figure 5.11 (a) and (b) show the porosity and crystallinity of laser sintering samples as a function of laser scanning speed. Both of these quantities are strongly dependent on the scanning speed. Faster scanning speeds correspond to the formation of higher porosity where pore growth becomes more dominant as compared to densification. This implies that sintering time has more influence on the viscous flow densification than the pore growth. However, at the highest power of 12 W and the lowest scanning speed of 1.0 mm/s, the overall porosity is less than the deposited glass powder layer as shown in Fig. 5.11 (a). The higher sintering temperature (close to the practical melting point) and the longer sintering time made the viscous flow densification dominant. Figure 5.11 (b) shows that sintering time significantly influences the crystallization kinetics. Longer sintering times result in larger crystal fraction of the laser sintering sample. The porosity and crystallinity of laser sintering samples as a function of laser power are shown in Fig. 5.12 (a) and (b). For higher laser powers, the pore growth further dominates the densification at the scanning speed of 2.0 mm/s. This implies that the sintering temperature has more influence on the pore growth than the sintering time does. However, at the scanning speed of 1.0 mm/s, the higher laser powers induced higher sintering temperature (close to the practical melting point) resulting in the transition for the dominant mechanism from the pore growth to viscous flow densification, as show in Fig. 5.12 (a). At the same scanning speeds, the crystallinity is more-or-less constant with the laser power as shown in Fig. 5.12 (b). Since the crystallization temperature of 45S5 Bioglass is below 750 °C [49], the increase in sintering temperature far beyond this temperature by higher laser power has little effect on the crystallinity. All processing conditions result in a porous structure with low crystallinity; therefore, the laser coating is a viable process for bioactive glass coating of biomedical implants.

5.5.4 Numerical Modeling

A 2D axisymmetric FEM laser sintering model with the set of coupled heat transfer, crystallization, sintering, and pore coalescence equations are solved concurrently within a spatially resolved finite element domain. The 3D model is more realistic to simulate the temperature rise ahead of a laser beam, however, for computation simplicity 2D axisymmetric model using the laser irradiation times equal to the laser spot size divided by the scanning speeds could be reasonable to achieve the equivalent thermal time history and to imitate different scanning speeds of experiments. Only small fraction of glass would be partially crystallized due to high heating and cooling rates by laser irradiation, the latent heat of crystallization is assumed to be negligible. The numerical models are validated using experimental results and can be used to predict the porosity and crystallinity of the laser sintering

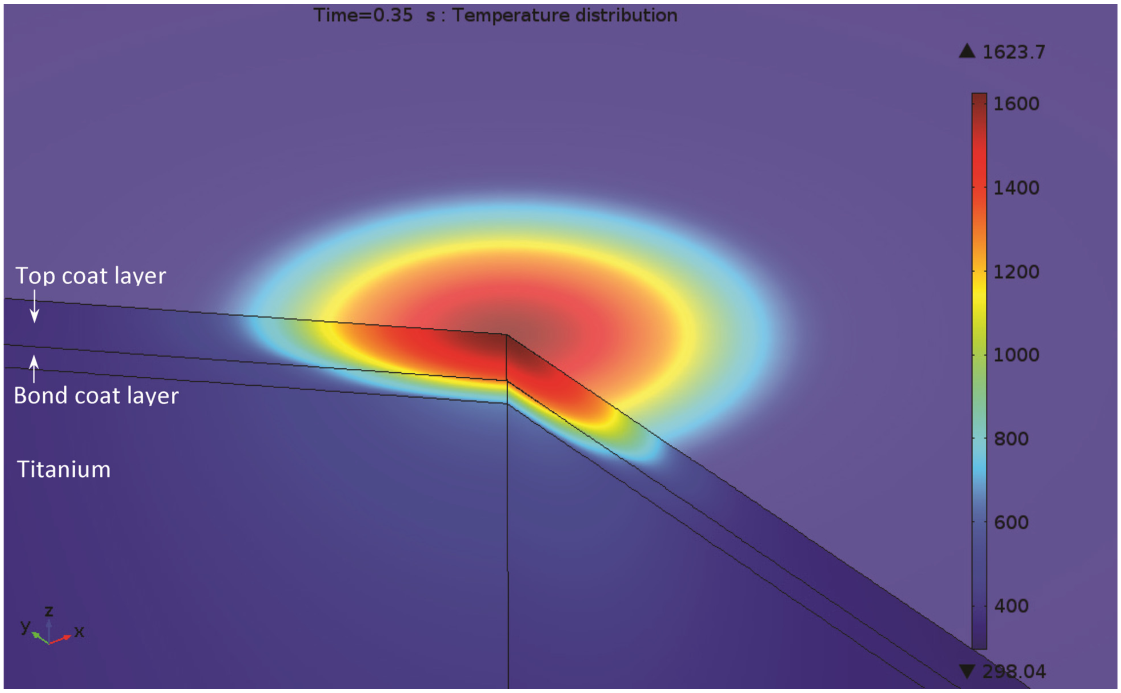

Figure 5.13: Representative revolution (225 degree) of 2D temperature distribution of a coupled laser-source heat transfer, sintering potential, pore growth, and crystallization model (laser power of 11 W, at 0.35s of laser irradiation).

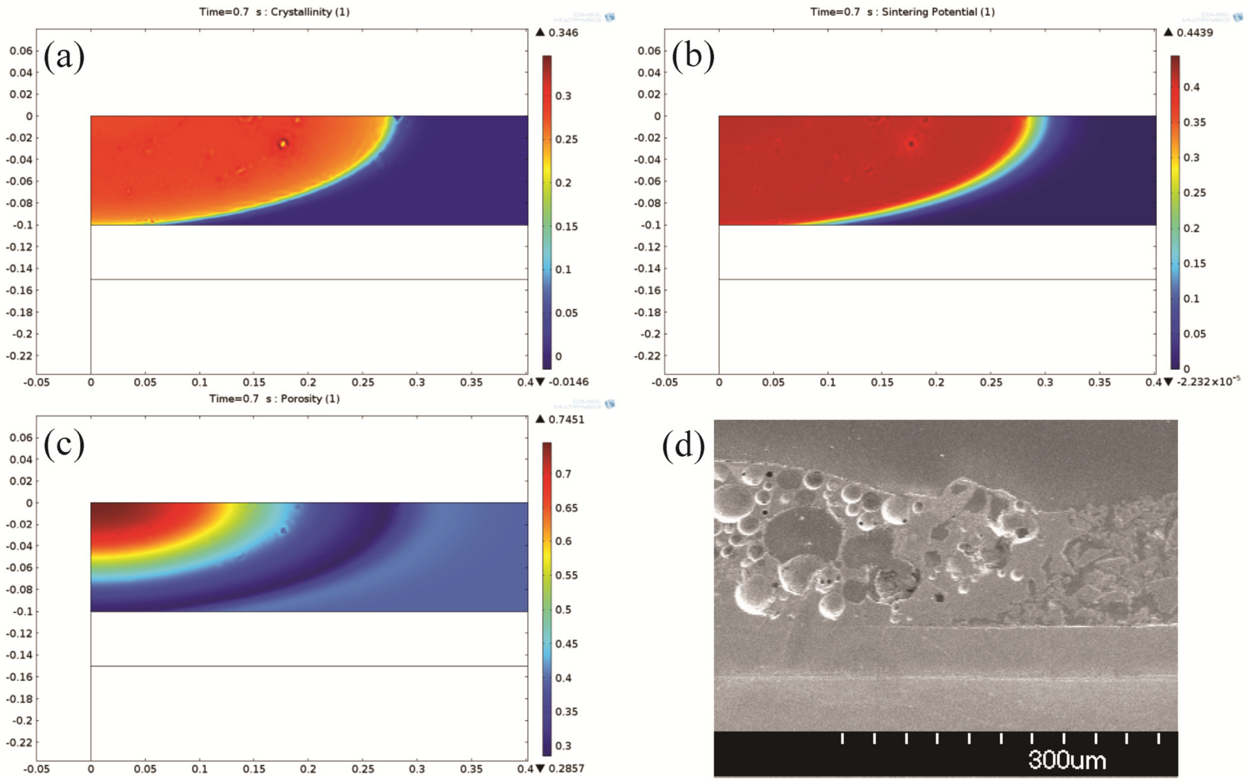

Figure 5.14: 2D cross-sectional images for (a) crystallinity, (b) sintering potential, and (c) porosity; (d) The morphology of sintered glass whose shape corresponds well with the numerical one.

layer. Figure 5.13 shows a representative 2D revolution (225 degree) of temperature distribution of the laser sintering from the numerical simulation. Peak temperature is below the practical or apparent melting point of 45S5 Bioglass. However, it high enough to sinter the glass powder onto the bond coat layer, resulting in the porous top coat layer. Figure 5.14 shows cross-sectional views of the crystallinity, sintering potential, and porosity from the numerical simulation, as well as an experimental feature for comparison. The size of the sintered and crystallized area of bioactive glass in the model as shown in Fig. 5.14 (a) and (b) is essentially comparable to the experimental sintered area in Fig. 5.14 (d). The resulting porosity in the model as shown in Fig. 5.14 (c) is calculated from the combined effect of densification and pore growth using Eq. (5.14). The porosity contour map in Fig. 5.14 (c) corresponds well with the morphology of the sintered glass in Fig. 5.14 (d). Compared to the initial porosity of deposited glass powder, the porosity of the sintered glass is higher at the center of the laser-irradiated area while lower at the peripheral area, because pore growth is dominant compared to densification at higher temperatures. To validate the numerical models with the experimental results, the overall porosity of sintered glass in the models for each processing condition is determined from the average of spatial porosity within the sintering region. Additionally, the crystallinity is determined from the average of spatial crystallinity within sintered radius in the r-direction and the X-ray penetration depth in z-direction. For the XRD equipment used in this study with 25° incident angle, the X-ray penetration depth is 57.98 μm. Since the numerical model is a 2D axisymmetric model, it is more reasonable to validate the results only at different laser powers. Figure 5.15 shows the numerical and experimental results of porosity and crystallinity as a function of laser power. The numerical results correspond well with the experimental results by predicting an increasing trend of the porosity and a more-or-less constant trend of the crystallinity with the laser power. At the same scanning speed, the increasing porosity shows that the higher temperature distribution from the higher power condition results in more driving force for gas entrapped in the pores to diffuse and coalesce with the surrounding ones, and the pore growth mechanism further dominates the densification. On the other hand, temperatures much higher than the onset temperature of crystallization mentioned in the previous section has less effect on the crystallization kinetics compared to crystallization time. Therefore, the crystallinity of sintered glass is nearly constant with the laser power. The porosity predicted from numerical models may have a small discrepancy compared with that from the experimental results, however, the numerical model is proved to predict the right trends and yield greater insight into the temperature dependent behavior of laser sintering of glass.

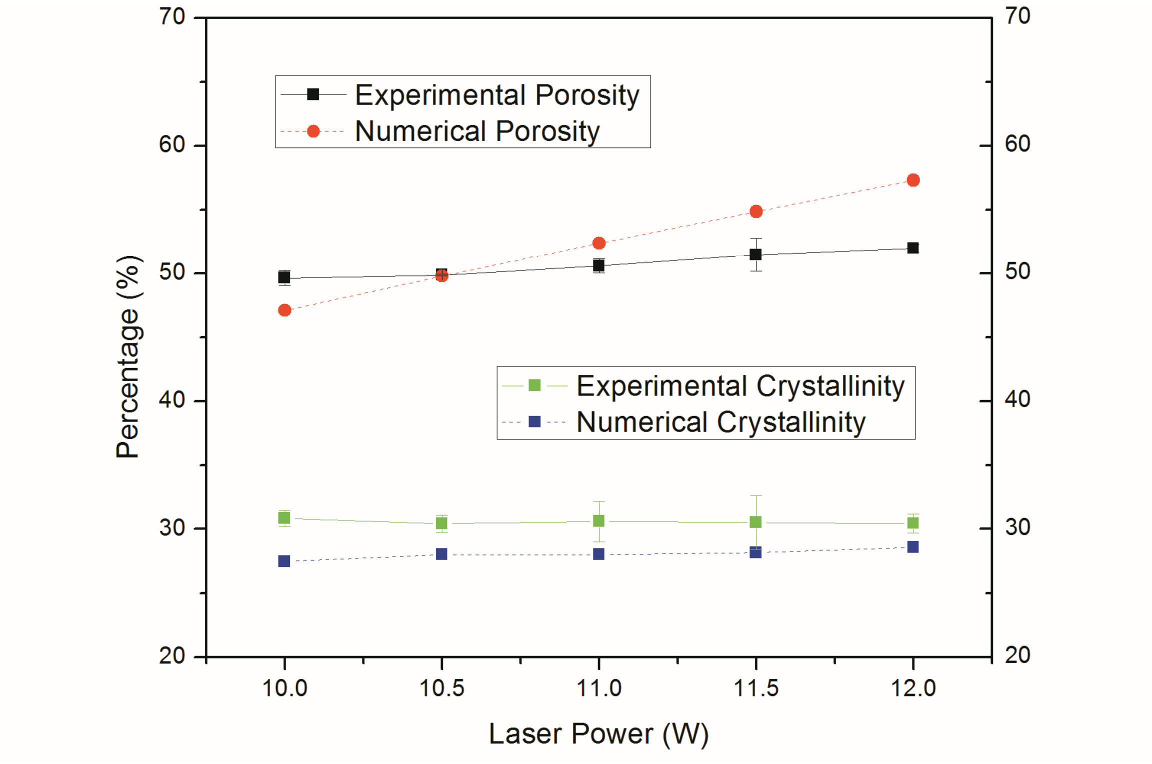

Figure 5.15: Numerical (dashed lines) and experimental (solid lines) percentages of porosity and crystallinity at different laser powers. Numerical models predict an increasing trend of porosity and more-or-less constant trend of crystallinity with the laser powers.

5.6 Conclusion

Laser coating of 45S5 bioactive glass on titanium substrates has been investigated for biomedical implants. Line scan EDX composition profiles show that there is mixed interfacial layer between a dense bond coat layer and the titanium substrate indicating a relatively strong chemical bonding. A porous top coat layer is successfully sintered onto the bond coat layer with no interface. All processing parameters investigated here for the top coat layer result in a porous structure with low crystallinity. The overall porosity of laser coating results from competing mechanisms between viscous flow densification and pore coalescence. Swelling of the porous top coat layer is due to pore coalescence dominating over viscous flow densification. Higher porosity and lower crystallinity correspond to faster scanning speeds while crystallinity is more-or-less constant with laser powers. The numerical models developed in this work aid in understanding the laser sintering mechanisms and allow for prediction of the overall porosity and crystallinity in top coat layers. The numerical results correspond well with the experimental ones. The work described above shows that double layer laser coating of the 45S5 bioactive glass with high level of bioactivity is successfully done.

Chapter 6: Conclusion

In this thesis, a number of laser processes aimed to investigate the modification and integration of glasses. Glasses are highly transmitting at wavelengths in a wide range of spectrum from near ultraviolet (NUV) to near infrared (NIR). However, most of the laser energy can be coupled into glasses by either nonlinear absorption or multiple surface scattering. The nonlinear absorption takes place in high intensity regime by femtosecond laser irradiation. The multiple surface scattering can occur in low intensity regime by continuous wave (CW) laser irradiation of a glass powder layer. In the case of femtosecond laser irradiation, the changes in morphology, structure, and mechanical properties of glasses upon laser irradiation have been extensively investigated, and the state of knowledge of these changes has been advanced. New processes for the modification and integration of these materials into devices are developed. In the case of CW laser irradiation, coatings of bioactive glass powder on a titanium substrate have been investigated. The sintering mechanisms, as well as the porosity and crystallinity of coated bioactive glass are analyzed through both experimental and numerical investigations. The major findings and contributions of each study are summarized as follows.

6.1 Femtosecond Laser Irradiation

6.1.1 Feature Formation and Property Changes

When ultrashort laser pulses are focused in the interior of glass, features are generated within a volume confined by surrounding material due to a nonlinear absorption mechanism. Feature generation strongly depends on the laser processing parameters. The link between these parameters, the knowledge of absorption volume, and resulting morphology are the main factors to explain their formation mechanisms. The morphology of the features is investigated through the use of transmission differential interference contrast (DIC) optical microscopy. The shape and size of an absorption volume is performed through the development of 2D axisymmetric absorption volume model which includes considerations of the temporal and spatial distribution of laser, beam propagation after a focusing lens, and the intensity breakdown threshold of a material. The absorption volumes constructed from numerical models show an inverse teardrop shape similar to experimental features. Feature formation was understood to be based on micro-explosions with the side effect from thermal accumulation. Temperature increase by thermal accumulation has a tendency to lower the intensity breakdown threshold. It causes the material to breakdown further upward in case of laser irradiation on the high overlapping area such as the use of a low scanning speed condition.

Changes in mechanical and structural properties of glass induced by femtosecond laser irradiation are experimentally characterized through spatially resolved nanoindentation and Raman spectroscopy. Reconfiguration of the three-, four-, and combination of five- and six-fold rings within the treated area has been quantified through identification of the volume fraction of those particular ring structures. The strength of fluorescence signal in Raman spectra, which represents the non-bridging oxygen hole center (NBOHC), has also been quantified to show the presence of small cavities in the laser-irradiated area. The reduction in Young’s modulus and hardness from nanoindentation measurements in combination with the increase of densely packed structure and small cavities from Raman spectroscopy show that the features are generated by micro-explosion mechanism resulting in more densified glass mixed with small cavities. Young’s modulus and hardness decrease; however, the E/H ratio and ductility index increase. This indicates that more energy is required to fracture the laser-irradiated region compared to the reference region, or it implies that the fracture toughness of the treated material is higher which may be beneficial to transmission welding applications.

6.1.2 Transmission Welding (TW) and Single Step Channeling (SSC)

Joining of two glass substrates in flat panel display, OLED lighting, and lab-on-a-chip applications based on adhesives have poor reliability, moreover they are susceptible to moisture permeability. Some adhesives and other bonding processes such as thermal bonding and anodic bonding require high curing temperature of entire parts for a long period of time. Since femtosecond laser represents a non-contact, flexible tool, which enables the localized processing even in the interior of glasses with minimal heat affected zone (HAZ), a new joining process (TW) has been developed by utilizing a nonlinear absorption mechanism to form a highly localized joint at the interface between two glass substrates. The morphology of the joints formed using the TW by femtosecond laser is investigated, and it indicates that the joining is successful with no gap at the pre-existing interface. The welding affected region assembles the teardrop shape similar to features in the interior of glass. The joint width is found to be corresponded to the predicting absorption width from an absorption volume model. The numerical model suggests high numerical aperture and higher laser pulse energy to achieve bigger joint width and lesser affected region distanced from the interface. High-load nanoindentation to induce cracks has been performed on the weld seams. It shows a shorter crack line at the joint compared to that at the glass base material. The shorter crack length and the greater E/H ratio confirm the hypothesis from the previous study that the fracture toughness of femtosecond laser-irradiated region is increased compared to the reference region. Through indentation analysis at different high-loads, it also indicates that the fracture strength of the joint is increased. Therefore, TW has the potential to achieve a reliable, highly localized sealing process for the flat panel display and biomedical industry.

Microchannels are the essential features in micro-fluidic devices, lab-on-a-chip (LOC) devices, and micro-total analysis systems (μ-TAS) for biomedical applications. Currently, fabrication of these devices heavily relies on photolithographic techniques, which require multilayer and multistep processing procedures to form microchannel structures. These techniques can introduce alignment errors in joining process, and liquid adhesive would also run into etched channels. Since high energy single femtosecond laser pulse can generate a reasonably long microchannel when appropriately control the laser and focusing parameters, a new process (SSC) has been developed by utilizing an aberration effect and a micro-explosion mechanism to form a high aspect ratio, long microchannel in the interior of glass. The elongation of the absorption volume, resulting from spherical aberration of a laser beam which focuses through the air-glass interface, has been investigated by numerical models. Models can be used to predict the length of microchannels with respect to the laser and focusing parameters. The microchannel geometry by single femtosecond laser pulse is investigated through the use of transmission DIC optical microscopy. Because of the micro-explosions inside the elongated absorption volume, the generated features represent a long narrow dark color area. Experimental characterizations at cross sections of microchannels through the use of AFM topography and Raman spectroscopy indicated that the narrow dark color area observed from the side view of the optical micrograph is a cavity. With the utilization of a simulation to predict a channel length as a function of laser pulse energy and focusing depth for single laser pulse, a long microchannel can be achieved by cascading a series of single pulse channels along the optical axis within the thickness of glass. SSC could be a potential alternative to produce microscale channels inside transparent materials for microfluidic and lab-on-a-chip applications.

6.2 Continuous Wave (CW) Laser Irradiation

Bioactive glass can be transformed into bone like phase and naturally bond with bone. The best use of bioactive glass in load bearing implant applications is as a coating on one of common implant metals and alloys. High bioactivity of bioactive glass accelerates the bonding time so that the risk of early implant failure is reduced in orthopedic implant (hip and knee replacement) and dentistry implant applications. 45S5 Bioglass has the highest rate of bioactivity, however, its coatings by plasma spray and enameling techniques usually fail due to its significant crystallization leading to lack of adhesion to the substrate. To address this limitation, double layer coating of bioactive glass by CW laser irradiation has been developed by utilizing fast localized heating to form a dense structure fusion bonded with metal substrate, and a porous structure sinter bonded to the dense glass. The resultant joint between 45S5 Bioglass and titanium substrate is analyzed by EDX composition map and profiles across the interface. It indicates a diffusion-based joining mechanism with a ten microns wide mixed interfacial layer.

It is shown that there is swelling of the laser sintering region with its overall porosity higher than the initial porosity of a deposited powder layer. The microporosity in the sintered area is not detrimental due to it enhances bioactivity of the bioactive material. The evidence of swelling shape gives insight into sintering mechanisms. There are not only crystallization and viscous flow densification but also pore coalescence by diffusion of entrapped gas in pores. A numerical model has been developed to yield valuable insight into the temperature dependent behavior of laser sintering process. It neatly captures the combined effects of laser heating, densification, crystallization, and pore growth on the resulting morphology and microstructure of the sintered glass. The numerical model predicts consistent trends of porosity and crystallinity by the effects of laser processing parameters and corresponds well with those measured experimentally. The top bond coat layer formed through the couple layer laser coating process is found to have a porous structure with low crystallinity. The degree of crystallinity delays the bioactivity of the bioactive material; however, the crystallinity of laser coating sample is significantly lower than that of the enameling sample. Hence, the CW laser coating could be a viable process for bioactive glass coating (including the 45S5 Bioglass) of biomedical implants.

6.3 Future Work

The major findings and contributions outlined above, in both modification and integration by a femtosecond laser and coating by a CW laser at 1024 nm wavelength form a foundation on which further developments can be based. In terms of transmission welding process, the results have shown the ability of femtosecond laser to join the two glass substrates. While the mechanical properties have been extensively investigated, the permeability of the moisture and oxygen has yet to be tested. Since most devices in flat panel display and OLED lighting applications are encapsulated between glass plates that both act as a hermetic barrier and form the substrate for the device, the seal between these substrates should be hermetic as well in order to provide a barrier for oxygen and water. Investigation of hermetic sealing of transmission welding by femtosecond laser should provide an insight into a possible process improvement. In addition to the transmission welding by laser irradiation from the top surface of the glass substrates, the different orientation of the glass substrate may be examined such as laser irradiation from the side onto the interface of two glass substrates. The wider welding width may be possible to be achieved in such a case. Taking into account the dielectric properties of air gap and reflections at glass-air interfaces, the absorption volume model would be further improved to investigate their effects on the shape and size of the absorption volume. Transmission welding of dissimilar glasses may also be conducted to investigate effects of different dielectric properties on the weld seams. In terms of single step channeling process, it may be possible to study the channel that is generated by couple of femtosecond laser pulses at different delay times of the second pulse with respect to the first one in the range of picoseconds to microseconds. The micro-explosions caused by the second pulse may help refresh the channel and may improve its surface roughness. The use of aberration correction optics such as deformable mirrors or spherical aberration compensation plates would also be considered to control and modify a size of the resulting channel.

In terms of double layer laser coating, the work described above focuses primarily on the sintering mechanisms, the effect of processing parameters on the degree of porosity and crystallinity of the sintered glass. While the high porosity and low crystallinity is desirable for acceleration the bonding time, the bioactivity test has yet to be conducted to investigate the competing effects of these two factors. This test may be useful to verify which factor would have more influence on the bioactivity of bioactive coating implants. In addition, it may be of interest to investigate double layer laser coating of different glass compositions. In order to provide a greater deal of scope for further work, glass compositions with different crystalline phases would give considerable insight into the kinetics of sintering with concurrent crystallization during laser coating.

References

Chapter 1:

[1] Poulain M., 1983, “Halide glasses,” J. Non. Cryst. Solids, **56**(1-3), pp. 1–14.

[2] Varshneya A. K., 1994, Fundamentals of Inorganic Glasses, Academic Press, Inc., San Diego, CA.

[3] Zarzycki J., 1991, Glasses and the Vitreous State, Cambridge University Press, Cambridge, UK.

[4] Kingery W. D., Bowen H. K., and Uhlmann D. R., 1976, Introduction to Ceramics, Wiley, New York.

[5] Shelby J. E., 1997, Introduction to Glass Science and Technology, The Royal Society of Chemistry, Cambridge, UK.

[6] Bach H., and Neuroth N., eds., 1995, The Properties of Optical Glass, Springer, Mainz, Germany.

[7] Hartmann P., Jedamzik R., Reichel S., and Schreder B., 2010, “Optical glass and glass ceramic historical aspects and recent developments: a Schott view,” Appl. Opt., **49**(16), p. D157.

[8] Hench L. L., 2006, “The story of Bioglass.,” J. Mater. Sci. Mater. Med., **17**(11), pp. 967–78.

[9] Hench L. L., Splinter R. J., Allen W. C., and Greenlee T. K., 1971, “Bonding mechanisms at the interface of ceramic prosthetic materials,” J. Biomed. Mater. Res., **5**(6), pp. 117–141.

[10] Rahaman M. N., Day D. E., Bal B. S., Fu Q., Jung S. B., Bonewald L. F., and Tomsia A. P., 2011, “Bioactive glass in tissue engineering.,” Acta Biomater., **7**(6), pp. 2355–73.

[11] El-Meliegy E., and Noort R., 2012, “Glasses and Glass Ceramics for Medical Applications,” pp. 221–227.

[12] Jones J. R., 2013, “Review of bioactive glass: from Hench to hybrids.,” Acta Biomater., **9**(1), pp. 4457–86.

[13] Pantano C. G., 2003, “Looking Clearly to the Future Through Glass,” Am. Ceram. Soc. Bull., **82**(10), pp. 19–20.

[14] Lee J.-H., Liu D. N., and Wu S.-T., 2008, Introduction to Flat Panel Displays, John Wiley & Sons, Chichester.

[15] Nathan A., Ahnood A., Lai J., and Guo X., 2013, "Large Area Electronics," Guide to State-of-the-Art Electron Devices, J.N. Burghartz, ed., John Wiley & Sons, Chichester, pp. 249–262.

[16] Fujitsu Microelectronics America I., 2006, "Fundamentals of Liquid Crystal Displays – How They Work and What They Do."

[17] Figueiredo D. A., and Patil H. R., 2010, "TFT-LCD Panel Fundamentals," Electron. You, (March), pp. 113–116.

[18] Ellison A., and Cornejo I. a., 2010, "Glass Substrates for Liquid Crystal Displays," Int. J. Appl. Glas. Sci., **1**(1), pp. 87–103.

[19] Bocko P. L., and Lee H. S., 2008, "Highly Engineered Glass Substrates for LCD Television: Why Reducing Value Is Incompatible with Consumer Expectations," Inf. Disp. (1975)., **24**(5), pp. 26–30.

[20] Bocko P. L., 2012, Handbook of Visual Display Technology, Springer Berlin Heidelberg, Berlin, Heidelberg.

[21] Bond T., and News T., 1994, "Materials for Sealing Liquid Crystal," ThreeBond Tech. News, pp. 1–8.

[22] Wong W. S., and Alberto S., eds., 2009, Flexible Electronics, Springer.

[23] Lee S. J., and Lee S. Y., 2004, "Micro total analysis system (micro-TAS) in biotechnology.," Appl. Microbiol. Biotechnol., **64**(3), pp. 289–99.

[24] Ahn C. H., and Choi J.-W., 2004, "Microfluidic Devices and Their Applications to Lab-on-a-Chip," Springer Handbook of Nanotechnology, B. Bhushan, ed., Springer-Verlag, New York, pp. 523–548.

[25] Li P., 2006, Microfluidic Lab-on-a-Chip for Chemical and Biological Analysis and Discovery, Taylor & Francis Group, LLC, Boca Raton, FL.

[26] Abgrall P., and Gué a-M., 2007, "Lab-on-chip technologies: making a microfluidic network and coupling it into a complete microsystem—a review," J. Micromechanics Microengineering, **17**(5), pp. R15–R49.

[27] Hwang D. J., Choi T. Y., and Grigoropoulos C. P., 2004, "Liquid-assisted femtosecond laser drilling of straight and three-dimensional microchannels in glass," Appl. Phys. A Mater. Sci. Process., **79**(3), pp. 605–612.

[28] Sun Q., Saliminia A., Théberge F., Vallée R., and Chin S. L., 2008, "Microchannel fabrication in silica glass by femtosecond laser pulses with different central wavelengths," J. Micromechanics Microengineering, **18**(3), p. 035039.

[29] Juodkazis S., Misawa H., Hashimoto T., Gamaly E. G., and Luther-Davies B., 2006, "Laser-induced microexplosion confined in a bulk of silica: Formation of nanovoids," Appl. Phys. Lett., **88**(20), p. 201909.

[30] Oshida Y., 2007, Bioscience and Bioengineering of Titanium Materials, Elsevier Ltd.

[31] Liu X., Chu P., and Ding C., 2004, "Surface modification of titanium, titanium alloys, and related materials for biomedical applications," Mater. Sci. Eng. R Reports, **47**(3-4), pp. 49–121.

[32] Davis J. R., ed., 2003, Handbook of Materials for Medical Devices, ASM International, Materials Park.

[33] Hench L. L., and Wilson J., 1993, An Introduction to Bioceramics, World Scientific Publishing.

[34] Von der Linde D., Sokolowski-Tinten K., and Bialkowski J., 1997, "Laser–solid interaction in the femtosecond time regime," Appl. Surf. Sci., **109-110**, pp. 1–10.

[35] "http://www.edmundoptics.com/technical-resources-center/optics/optical-glass/."

[36] Trager F., ed., 2007, Springer Handbook of Lasers and Optics, New York.

[37] Jiang L., and Tsai H. L., 2003, "Femtosecond Lasers Ablation : Challenges and Opportunities," NSF Workshop on Unsolved Problems and Research Needs in Thermal Aspects of Material Removal Processes, Stillwater, OK, pp. 1–15.

[38] Schaffer C. B., Brodeur A., and Mazur E., 2001, "Laser-induced breakdown and damage in bulk transparent materials induced by tightly focused femtosecond laser pulses," Meas. Sci. Technol., **12**(11), pp. 1784–1794.

[39] Vukelić S., Kongsuwan P., and Yao Y. L., 2010, "Ultrafast Laser Induced Structural Modification of Fused Silica—Part I: Feature Formation Mechanisms," J. Manuf. Sci. Eng., **132**(6), p. 061012.

[40] Keldish L. V., 1965, "Ionization in the Field of a Strong Electromagnetic Wave," Sov. Phys. JETP, **20**(5), pp. 1307–1314.

[41] Duley W. W., 1996, UV Lasers: Effects and Applications in Materials Science, Cambridge University Press, New York.

[42] Stuart B., Feit M., Rubenchik A., Shore B., and Perry M., 1995, "Laser-Induced Damage in Dielectrics with Nanosecond to Subpicosecond Pulses," Phys. Rev. Lett., **74**(12), pp. 2248–2251.

[43] Schaaf P., ed., 2010, Laser Processing of Materials, Springer Berlin Heidelberg, Berlin, Heidelberg.

[44] Bäuerle D., 2011, Laser Processing and Chemistry, Springer Berlin Heidelberg, Berlin, Heidelberg.

[45] Perry M. D., Stuart B. C., Banks P. S., Feit M. D., Yanovsky V., and Rubenchik a. M., 1999, "Ultrashort-pulse laser machining of dielectric materials," J. Appl. Phys., **85**(9), p. 6803.

[46] Gattass R. R., and Mazur E., 2008, "Femtosecond laser micromachining in transparent materials," Nat. Photonics, **2**(4), pp. 219–225.

[47] Born M., and Wolf E., 1999, Principles of Optics: Electromagnetic Theory of Propagation, Interference and Diffraction of Light, Cambridge University Press, New York.

[48] Richards B., and Wolf E., 1959, "Electromagnetic Diffraction in Optical Systems. II. Structure of the Image Field in an Aplanatic System," Proc. R. Soc. A Math. Phys. Eng. Sci., **253**(1274), pp. 358–379.

[49] Zipfel W. R., Williams R. M., and Webb W. W., 2003, "Nonlinear magic: multiphoton microscopy in the biosciences.," Nat. Biotechnol., **21**(11), pp. 1369–1377.

[50] Vukelic S., 2009, "Laser Induced Deformation and Structural Modification of Crystalline and Amorphous Materials," Columbia University.

[51] Schaffer C. B., Jamison A. O., and Mazur E., 2004, "Morphology of femtosecond laser-induced structural changes in bulk transparent materials," Appl. Phys. Lett., **84**(9), pp. 1441–1443.

[52] Török P., Varga P., Laczik Z., and Booker G. R., 1995, "Electromagnetic diffraction of light focused through a planar interface between materials of mismatched refractive indices: an integral representation," J. Opt. Soc. Am. A, **12**(2), p. 325.

[53] Genman R. M., 1996, Sintering Theory and Practice, John Wiley & Sons, New York, NY.

[54] Fang Z. Z., ed., 2010, Sintering of Advance Materials, Woodhead Publishing Limited.

[55] Kang S.-J. L., 2005, Sintering: Densification, Grain Growth, and Microstructure, Elsevier Butterworth-Heinemann, Burlington, MA.

[56] Scherer G. W., 1997, "Sintering of sol-gel films," J. Sol-Gel Sci. Technol., **8**(1-3), pp. 353–363.

[57] Doremus R. H., 2002, "Viscosity of silica," J. Appl. Phys., **92**(12), p. 7619.

[58] Frenkel J., 1945, “Viscous Flow of Crystalline Bodies Under the Action of Surface Tension,” J. Phys. USSR, **9**(5), pp. 385–391.

[59] Mackenzie J. K., and Shuttleworth R., 1949, “A Phenomenological Theory of Sintering,” Proc. Phys. Soc. Sect. B, **62**(12), pp. 833–852.

[60] Scherer G. W., 1977, “Sintering of Low-Density Glasses: I, Theory,” J. Am. Ceram. Soc., **60**(5-6), pp. 236–239.

[61] Fokin V. M., Yuritsyn N. S., and Zanotto E. D., 2005, “Nucleation and Crystallization Kinetics in Silicate Glasses: Theory and Experiment,” Nucleation Theory and Applications, J.W.P. Schmelzer, ed., Wiley-VCH Verlag GmbH & Co., pp. 74–125.

[62] Karpukhina N., Hill R. G., and Law R. V, 2014, “Crystallisation in oxide glasses - a tutorial review.,” Chem. Soc. Rev.

[63] Schneider J., Mastelaro V. R., Zanotto E. D., Shakhmatkin B. a., Vedishcheva N. M., Wright A. C., and Panepucci H., 2003, “Qn distribution in stoichiometric silicate glasses: thermodynamic calculations and 29Si high resolution NMR measurements,” J. Non. Cryst. Solids, **325**(1-3), pp. 164–178.

[64] Fischer-Cripps A. C., 2011, Nanoindentation, Springer, New York.

[65] Oliver W. C., and Pharr G. M., 1992, “An Improved Technique for Determining Hardness and Elastic Modulus,” J. Mater. Res., **7**(6), pp. 1564–1580.

Chapter 2:

[1] Miyamoto, I., Horn, A., Gottmann, J., Wortmann, D., and Yoshino, F., 2007, “Fusion Welding of Glass Using Femtosecond Laser Pulses with High-repetition Rates,” Journal of Laser Micro/Nanoengineering, **2**(1), pp. 57-63.

[2] Kutchoukov, V.G., Laugere, F., van der Vlist, W., Pakula, L., Garini, Y., and Bossche, A., 2004, “Fabrication of Nanofluidic Devices Using Glass-to-glass Anodic Bonding,” Sensors and Actuators A, **114**(2-3), pp. 521-527.

[3] Davis, K.M., Miura, K., Sugimoto, N., Hirao, K. (1996) “Writing Waveguides in Glass with a Femtosecond Laser,” Optics Letters, **21**(21), pp. 1729-1731.

[4] Glezer, E.N., Milosavljevic, M., Huang, L., Finlay, R.J., Her, T.-H, Callan, J.P., and Mazur, E., 1996, “Three-Dimensional Optical Storage Inside Transparent Materials,” Optics Letters, **21**(24), pp. 2023-2025.

[5] Schaffer, C.B., Jamison, A.O., and Mazur, E., 2004, “Morphology of Femtosecond Laser-Induced Structural Changes in Bulk Transparent Materials,” Applied Physics Letters, **84**(9),

pp. 1441-1443.

[6] Schaffer, C.B., Brodeur, A. Garcia, J.F., and Mazur, E., 2001, "Micromachining Bulk Glass by Use of Femtosecond Laser Pulses with Nanojoule Energy," Optics Letters, **26**(2), pp. 93-95.

[7] Glezer, E.N., and Mazur, E., 1997, "Ultrafast-Laser Driven Micro-Explosions in Transparent Materials," Applied Physics Letters, **71** (7), pp. 882-884.

[8] Tamaki, T., Watanabe, W., Nishii, J., and Itoh, K., 2005, "Welding of Transparent Materials Using Femtosecond Laser Pulses," Japanese Journal of Applied Physics, **44**(22), pp. L687-L689.

[9] Tamaki, T., Watanabe, W., and Itoh, K., 2006, "Laser Micro-welding of Transparent Materials by a Localized Heat Accumulation Effect Using a Femtosecond Fiber Laser at 1558 nm," Optics Express, **14**(22), pp. 10468-10476.

[10] Miyamoto, I., Horn, A., Gottmann, J., Wortmann, D., Mingareev, I., Yoshino, F., Schmidt, M., Bechtold, P., Okamoto, Y., Uno, Y., and Herrmann, T., 2008, "Novel Fusion Welding Technology of Glass Using Ultrashort Pulse Lasers," M304, Proc. 27th International Congress on Applications on Lasers & Electro-Optics, Temecula, CA, pp. 112-121.

[11] Borrelli, N., Helfinstine, J., Price, J., Schroeder, J., Streltsov, A., and Westbrook, J., 2008 "Glass Strengthening with an Ultrafast Laser," M404, Proc. 27th International Congress on Applications on Lasers & Electro-Optics, Temecula, CA, pp. 185-189.

[12] Bellouard, Y., Colomb, T., Depeursinge, C., Dugan, M., Said, A.A., and Bado, P., 2006, "Nanoindentation and Birefringence Measurements on Fused Silica Specimen Exposed to Low-energy Femtosecond Pulses," Optics Express, **14**(18), pp. 8360-8366.

[13] Schaffer, C.B., Garcia, J.F., and Mazur, E., 2003, "Bulk Heating of Transparent Materials Using a High-repetition-rate Femtosecond Laser," Applied Physics A, **76**, pp. 351-354.

[14] Krol, D.M., 2008, "Femtosecond laser modification of glass," Journal of Non-Crystalline Solids, **354**, pp. 416-424.

[15] Gamaly, E.G., Rode, A.V., Luther-Davies, B., and Tikhonchuk, T.V., 2002, "Ablation of Solids by Femtosecond Lasers: Ablation Mechanism and Ablation Thresholds for Metals and Dielectrics," Physics of Plasmas, **9**(3), pp. 949-957.

[16] Gamaly, E.G., Juodkazis, S., Nishimura, K., Misawa, H., Luther-Davies, B., Hallo, L., Nicolai, P., and Tikhonchuk, V.T., 2006, "Laser-matter Interaction in the Bulk of a Transparent Solid: Confined Microexplosion and Void Formation," Physical Review B, **73**, pp. 214101-1-15.

[17] Vukelic, S., 2009, "Laser Induced Deformation and Structural Modification of Crystalline

and Amorphous Materials," Ph.D. thesis, Columbia University, New York, NY.

[18] Juodkazis, S., Masawa, H., Hashimoto, T., Gamaly, E.G., and Luther-Davies, B. 2006 "Laser-induced Microexplosion Confined in a Bulk of Silica: Formation of Nanovoids," Applied Physics Letters, **88**(20), pp. 201909-1-3.

[19] Fischer-Cripps, A.C., 2004, Nanoindentation, Springer, New York, USA, Chap. 2.

[20] Lawn, B.R., and Howes, V.R., 1981, "Elastic Recovery at Hardness Indentations," Journal of Materials Science, **16**, pp. 2745-2752.

[21] Lawn, B.R., Evans, A.G., and Marshall, D.B., 1980, "Elastic/Plastic Indentation Damage in Ceramics: The Median/Radial Crack System," Journal of the American Ceramic Society, **63**(9-10), pp. 574-581.

[22] Sih, G.C., 1973, "Handbook of Stress Intensity Factors," Lehigh University Press, Pennsylvania, USA.

[23] Pharr, G.M., Harding, D.S., and Oliver, W.C., 1993, "Measurement of Fracture Toughness in Thin Films and Small Volume Using Nanoindentation Methods," in Mechanical Properties and Deformation Behavior of Materials Having Ultra-Fine Microstructures, Nastasi, M., eds., Kluwer Academic Publishers, Netherlands, pp. 449-461.

[24] Lawn, B.R., and Marshall, D.B., 1979, "Hardness, Toughness, and Brittleness: An Indentation Analysis," Journal of the American Ceramic Society, **62**(7-8), pp. 347-351.

[25] Suzuki, K., Benino, Y., Fujiwara, T., and Komatsu, T., 2002, "Densification Energy During Nanoindentation of Silica Glass," Journal of the American Ceramic Society, **85**(12), pp. 3102-3104.

[26] Sakai, M., 1999, "The Meyer Hardness: A Measure for Plasticity?," Journal of Materials Research, **14**(9), pp. 3630-3639.

[27] Zipfel, W.R., Williams, R.M., and Webb, W.W., 2003, "Nonlinear Magic: Multiphoton Microscopy in the Biosciences," Nature Biotechnology, **21**(11), pp. 1369-1377.

[28] Jiang, L., and Tsai, H-L., 2005, "Improved Two-Temperature Model and Its Application in Ultrashort Laser Heating of Metal Films," Journal of Heat Transfer, **127**, pp. 1167-1173.

[29] Johnson, K.L., 1985, Contact Mechanics, Cambridge University Press, Cambridge, pp. 171-175, Chap. 6.

[30] Shelby, J.E., 1997, Introduction to Glass Science and Technology, The Royal Society of Chemistry, Cambridge, UK.

[31] Charles, R.J., 1961, "A Review of Glass Strength," Progress in Ceramic Science, **Vol.1**,

Burke, J.E., eds., Pergamon Press, New York, pp. 1-38.

[32] Varshneya, A.K., 1994, Fundamentals of Inorganic Glasses, Academic Press, California, USA.

[33] Hagan, J.T., 1979, "Cone Cracks Around Vickers Indentations in Fused Silica Glass," Journal of Materials Science, **14**, pp. 462-466.

Chapter 3:

[1] Watanabe W., Onda S., Tamaki T., and Itoh K., 2007, "Joining of transparent materials by femtosecond laser pulses," Proceedings of SPIE Vol.6460, SPIE, pp. 646017–1–6.

[2] Tamaki T., Watanabe W., Nishii J., and Itoh K., 2005, "Welding of Transparent Materials Using Femtosecond Laser Pulses," Jpn. J. Appl. Phys., **44**(No. 22), pp. L687–L689.

[3] Watanabe W., Onda S., Tamaki T., Itoh K., and Nishii J., 2006, "Space-selective laser joining of dissimilar transparent materials using femtosecond laser pulses," Appl. Phys. Lett., **89**(2), pp. 021106–1–3.

[4] Tamaki T., Watanabe W., and Itoh K., 2006, "Laser micro-welding of transparent materials by a localized heat accumulation effect using a femtosecond fiber laser at 1558 nm," Opt. Express, **14**(22), p. 10460.

[5] Bovatsek J., Arai A., and Schaffer C. B., 2006, "Three-Dimensional Micromachining Inside Transparent Materials Using Femtosecond Laser Pulses : New Applications," CLEO/QELS and PhAST 2006, CA, pp. 8–9.

[6] Miyamoto I., 2007, "Local Melting of Glass Material and Its Application to Direct Fusion Welding by Ps-laser Pulses," J. Laser Micro/Nanoengineering, **2**(1), pp. 7–14.

[7] Horn A., Mingareev I., Werth A., Kachel M., and Brenk U., 2008, "Investigations on ultrafast welding of glass–glass and glass–silicon," Appl. Phys. A, **93**(1), pp. 171–175.

[8] Miyamoto I., Horn A., Gottmann J., Wortmann D., Mingareev I., Yoshino F., Schmidt M., and Bechtold P., 2008, "Novel Fusion Welding Technology of Glass Using Ultrashort Pulse Lasers," Proc. 27th International Congress on Applications on Lasers & Electro-Optics, Temecula, CA, pp. 112–121.

[9] Borrelli N., Helfinstine J., Price J., and Schroeder J., 2008, "Glass Strengthening with an Ultrafast Laser," Proc. 27th International Congress on Applications on Lasers & Electro-Optics, Temecula, CA, pp. 185–189.

[10] Bellouard Y., Colomb T., Depeursinge C., Dugan M., Said A. A., and Bado P., 2006, "Nanoindentation and birefringence measurements on fused silica specimen exposed to low-energy femtosecond pulses.," Opt. Express, **14**(18), pp. 8360–8366.

[11] Kongsuwan P., Wang H., Vukelic S., and Yao Y. L., 2010, "Characterization of Morphology and Mechanical Properties of Glass Interior Irradiated by Femtosecond Laser," J. Manuf. Sci. Eng., **132**(4), pp. 041009–1–10.

[12] Schaffer C. B., Jamison A. O., and Mazur E., 2004, "Morphology of femtosecond laser-induced structural changes in bulk transparent materials," Appl. Phys. Lett., **84**(9), pp. 1441–1443.

[13] Miyamoto I., 2007, "Fusion Welding of Glass Using Femtosecond Laser Pulses with High-repetition Rates," J. Laser Micro/Nanoengineering, **2**(1), pp. 57–63.

[14] Hallo L., Mézel C., Bourgeade A., Hébert D., Gamaly E. G., and Juodkazis S., 2010, "Laser-Matter Interaction in Transparent Materials : Confined Micro-explosion and Jet Formation," Extreme Photonics & Applications, T.J. Hall, S. V. Gaponenko, and S.A. Paredes, eds., Springer Netherlands, pp. 121–146.

[15] Gamaly E. G., Luther-Davies B., Hallo L., Nicolai P., and Tikhonchuk V. T., 2006, "Laser-matter interaction in the bulk of a transparent solid: Confined microexplosion and void formation," Phys. Rev. B, **73**(21), pp. 214101–1–15.

[16] Kitchener J. A., and Prosser A. P., 1957, "Direct Measurement of the Long-Range van der Waals Forces," Proc. R. Soc. A Math. Phys. Eng. Sci., **242**(1230), pp. 403–409.

[17] Gere J. M., and Timoshenko S. P., 1997, Mechanics of Materials, PWS Pub. Co., Boston.

[18] Sokolowski-Tinten K., Bialkowski J., Cavalleri A., von der Linde D., Oparin A., Meyer-ter-Vehn J., and Anisimov S., 1998, "Transient States of Matter during Short Pulse Laser Ablation," Phys. Rev. Lett., **81**(1), pp. 224–227.

[19] Rethfeld B., Sokolowski-Tinten K., von der Linde D., and Anisimov S. I., 2004, "Timescales in the response of materials to femtosecond laser excitation," Appl. Phys. A, **79**(4-6), pp. 767–769.

[20] Zhigilei L. V., and Garrison B. J., 2000, "Microscopic mechanisms of laser ablation of organic solids in the thermal and stress confinement irradiation regimes," J. Appl. Phys., **88**(3), pp. 1281–1298.

[21] Miotello a., and Kelly R., 1999, "Laser-induced phase explosion: new physical problems when a condensed phase approaches the thermodynamic critical temperature," Appl. Phys. A Mater. Sci. Process., **69**(7), pp. S67–S73.

[22] Gu M., 2000, Advanced Optical Imaging Theory, Springer Berlin Heidelberg, Berlin, Heidelberg.

[23] Hallo L., Bourgeade A., Tikhonchuk V. T., Mezel C., and Breil J., 2007, "Model and numerical simulations of the propagation and absorption of a short laser pulse in a transparent dielectric material: Blast-wave launch and cavity formation," Phys. Rev. B, **76**(2), pp. 024101–1–12.

[24] Lawn B. R., 1993, Fracture of Brittle Solids, Cambridge University Press, Cambridge, UK.

[25] Kese K., and Rowcliffe D. J., 2003, "Nanoindentation Method for Measuring Residual Stress in Brittle Materials," J. Am. Ceram. Soc., **86**(5), pp. 811–816.

[26] Irwin G. R., 1962, "Crack-Extension Force for a Part-Through Crack in a Plate," J. Appl. Mech., **29**(4), pp. 651–654.

[27] Tada H., Paris P. C., and Irwin G. R., 2000, The Stress Analysis of Cracks Handbook, ASME Press, New York.

[28] Kern W., 1990, "The Evolution of Silicon Wafer Cleaning Technology," J. Electrochem. Soc., **137**(6), pp. 1887–1892.

[29] Zipfel W. R., Williams R. M., and Webb W. W., 2003, "Nonlinear magic: multiphoton microscopy in the biosciences.," Nat. Biotechnol., **21**(11), pp. 1369–1377.

[30] Bhardwaj V. R., Corkum P. B., Rayner D. M., Hnatovsky C., Simova E., and Taylor R. S., 2004, "Stress in femtosecond-laser-written waveguides in fused silica.," Opt. Lett., **29**(12), pp. 1312–1314.

[31] Ye D., Bing-Kun Y., Bo L., Jian-Rong Q., Xiao-Na Y., Xiong-Wei J., and Cong-Shan Z., 2005, "Thermal Stress-Induced Birefringence in Borate Glass Irradiated by Femtosecond Laser Pulses," Chinese Phys. Lett., **22**(10), pp. 2626–2629.

[32] Mecholsky J. J., 1983, "Toughening in Glass Ceramics," Fracture Mechanics of Ceramics, Volume 6: Measurements, Transformations, and High-Temperature Fracture, R.C. Bradt, A.G. Evans, D.P.H. Hasselman, and F.F. Lange, eds., Plenum Press, New York.

[33] Krol D., 2008, "Femtosecond laser modification of glass," J. Non. Cryst. Solids, **354**(2-9), pp. 416–424.

[34] Broek D., 1986, Elementary Engineering Fracture Mechanics, Martinus Nijhoff Publishers, Dordrecht, The Netherlands.

[35] Soga N., 1985, "Elastic Moduli and Fracture Toughness of Glass," J. Non. Cryst. Solids, **73**(1-3), pp. 305–313.

[36] Varshneya A. K., 1994, Fundamentals of Inorganic Glasses, Academic Press, Inc., San Diego, CA.

[37] West J., 1999, “The application of fractal and quantum geometry to brittle fracture,” J. Non. Cryst. Solids, **260**(1-2), pp. 99–108.

Chapter 4:

[1] Osellame R., Hoekstra H. J. W. M., Cerullo G., and Pollnau M., 2011, “Femtosecond laser microstructuring: an enabling tool for optofluidic lab-on-chips,” Laser Photon. Rev., **5**(3), pp. 442–463.

[2] Liao Y., Ju Y., Zhang L., He F., Zhang Q., Shen Y., Chen D., Cheng Y., Xu Z., Sugioka K., and Midorikawa K., 2010, “Three-dimensional microfluidic channel with arbitrary length and configuration fabricated inside glass by femtosecond laser direct writing.,” Opt. Lett., **35**(19), pp. 3225–7.

[3] Glezer E. N., and Mazur E., 1997, “Ultrafast-laser driven micro-explosions in transparent materials,” Appl. Phys. Lett., **71**(7), p. 882.

[4] Juodkazis S., Misawa H., Hashimoto T., Gamaly E. G., and Luther-Davies B., 2006, “Laser-induced microexplosion confined in a bulk of silica: Formation of nanovoids,” Appl. Phys. Lett., **88**(20), p. 201909.

[5] Gamaly E., Juodkazis S., Misawa H., Lutherdavies B., Rode A., Hallo L., Nicolai P., and Tikhonchuk V., 2008, “Formation of nano-voids in transparent dielectrics by femtosecond lasers,” Curr. Appl. Phys., **8**(3-4), pp. 412–415.

[6] Marcinkevičius A., Juodkazis S., Watanabe M., Miwa M., Matsuo S., Misawa H., and Nishii J., 2001, “Femtosecond laser-assisted three-dimensional microfabrication in silica,” Opt. Lett., **26**(5), p. 277.

[7] Hnatovsky C., Taylor R. S., Simova E., Rajeev P. P., Rayner D. M., Bhardwaj V. R., and Corkum P. B., 2006, “Fabrication of microchannels in glass using focused femtosecond laser radiation and selective chemical etching,” Appl. Phys. A, **84**(1-2), pp. 47–61.

[8] Sun Q., Saliminia A., Théberge F., Vallée R., and Chin S. L., 2008, “Microchannel fabrication in silica glass by femtosecond laser pulses with different central wavelengths,” J. Micromechanics Microengineering, **18**(3), p. 035039.

[9] Kiyama S., Matsuo S., Hashimoto S., and Morihira Y., 2009, “Examination of Etching Agent and Etching Mechanism on Femotosecond Laser Microfabrication of Channels Inside Vitreous Silica Substrates †,” J. Phys. Chem. C, **113**(27), pp. 11560–11566.

[10] Sugioka K., Cheng Y., and Midorikawa K., 2005, "Three-dimensional micromachining of glass using femtosecond laser for lab-on-a-chip device manufacture," Appl. Phys. A, **81**(1), pp. 1–10.

[11] Wang Z., and Zheng H., 2009, "Ultrashort laser subsurface micromachining of three – dimensional microfluidic structures inside photosensitive glass," Laser Part. Beams, **27**, pp. 521–528.

[12] Li Y., Itoh K., Watanabe W., Yamada K., Kuroda D., Nishii J., and Jiang Y., 2001, "Three-dimensional hole drilling of silica glass from the rear surface with femtosecond laser pulses," Opt. Lett., **26**(23), p. 1912.

[13] Hwang D. J., Choi T. Y., and Grigoropoulos C. P., 2004, "Liquid-assisted femtosecond laser drilling of straight and three-dimensional microchannels in glass," Appl. Phys. A Mater. Sci. Process., **79**(3), pp. 605–612.

[14] Iga Y., Ishizuka T., Watanabe W., Itoh K., Li Y., and Nishii J., 2004, "Characterization of Micro-Channels Fabricated by In-Water Ablation of Femtosecond Laser Pulses," Jpn. J. Appl. Phys., **43**(No. 7A), pp. 4207–4211.

[15] An R., Li Y., Dou Y., Liu D., Yang H., and Gong Q., 2006, "Water-assisted drilling of microfluidic chambers inside silica glass with femtosecond laser pulses," Appl. Phys. A, **83**(1), pp. 27–29.

[16] Liao Y., Song J., Li E., Luo Y., Shen Y., Chen D., Cheng Y., Xu Z., Sugioka K., and Midorikawa K., 2012, "Rapid prototyping of three-dimensional microfluidic mixers in glass by femtosecond laser direct writing.," Lab Chip, **12**(4), pp. 746–9.

[17] Gamaly E. G., Luther-Davies B., Hallo L., Nicolai P., and Tikhonchuk V. T., 2006, "Laser-matter interaction in the bulk of a transparent solid: Confined microexplosion and void formation," Phys. Rev. B, **73**(21), pp. 214101–1–15.

[18] Hallo L., Mézel C., Bourgeade A., Hébert D., Gamaly E. G., and Juodkazis S., 2010, "Laser-Matter Interaction in Transparent Materials : Confined Micro-explosion and Jet Formation," Extreme Photonics & Applications, T.J. Hall, S. V. Gaponenko, and S.A. Paredes, eds., Springer Netherlands, pp. 121–146.

[19] Hnatovsky C., Taylor R. S., Simova E., Bhardwaj V. R., Rayner D. M., and Corkum P. B., 2005, "High-resolution study of photoinduced modification in fused silica produced by a tightly focused femtosecond laser beam in the presence of aberrations," J. Appl. Phys., **98**(1), p. 013517.

[20] Marcinkevičius A., Mizeikis V., Juodkazis S., Matsuo S., and Misawa H., 2003, "Effect of refractive index-mismatch on laser microfabrication in silica glass," Appl. Phys. A Mater. Sci. Process., **76**(2), pp. 257–260.

[21] Liu D., Li Y., An R., Dou Y., Yang H., and Gong Q., 2006, “Influence of focusing depth on the microfabrication of waveguides inside silica glass by femtosecond laser direct writing,” Appl. Phys. A, **84**(3), pp. 257–260.

[22] Sun Q., Jiang H., Liu Y., Zhou Y., Yang H., and Gong Q., 2005, “Effect of spherical aberration on the propagation of a tightly focused femtosecond laser pulse inside fused silica,” J. Opt. A Pure Appl. Opt., **7**(11), pp. 655–659.

[23] Török P., Varga P., Laczik Z., and Booker G. R., 1995, “Electromagnetic diffraction of light focused through a planar interface between materials of mismatched refractive indices: an integral representation,” J. Opt. Soc. Am. A, **12**(2), p. 325.

[24] Richards B., and Wolf E., 1959, “Electromagnetic Diffraction in Optical Systems. II. Structure of the Image Field in an Aplanatic System,” Proc. R. Soc. A Math. Phys. Eng. Sci., **253**(1274), pp. 358–379.

[25] Kongsuwan P., Satoh G., and Yao Y. L., 2012, “Transmission Welding of Glass by Femtosecond Laser: Mechanism and Fracture Strength,” J. Manuf. Sci. Eng., **134**(1), p. 011004.

Chapter 5:

[1] Sola A., Bellucci D., Cannillo V., and Cattini A., 2011, “Bioactive glass coatings: a review,” Surf. Eng., **27**(8), pp. 560–572.

[2] Liu X., Chu P., and Ding C., 2004, “Surface modification of titanium, titanium alloys, and related materials for biomedical applications,” Mater. Sci. Eng. R Reports, **47**(3-4), pp. 49–121.

[3] Shi J. Z., Chen C. Z., Zhang S., and Wu Y., 2007, “Application of surface modification in biomedical materials research,” Surf. Rev. Lett., **14**(3), pp. 361–369.

[4] Ramaswamy Y., Wu C., and Zreiqat H., 2009, “Orthopedic coating materials: considerations and applications.,” Expert Rev. Med. Devices, **6**(4), pp. 423–30.

[5] Hench L. L., 1998, “Biomaterials: a forecast for the future.,” Biomaterials, **19**(16), pp. 1419–23.

[6] Hench L. L., 2013, “Chronology of Bioactive Glass Development and Clinical Applications,” New J. Glas. Ceram., **03**(02), pp. 67–73.

[7] Hench L. L., Splinter R. J., Allen W. C., and Greenlee T. K., 1971, “Bonding mechanisms at the interface of ceramic prosthetic materials,” J. Biomed. Mater. Res., **5**(6), pp. 117–141.

[8] Hench L. L., and Wilson J., 1993, An Introduction to Bioceramics, World Scientific Publishing.

[9] Moritz N., Rossi S., Vedel E., Tirri T., Ylänen H., Aro H., and Närhi T., 2004, “Implants coated with bioactive glass by CO2-laser, an in vivo study.,” J. Mater. Sci. Mater. Med., **15**(7), pp. 795–802.

[10] Mirhosseini N., Crouse P. L., Li L., and Garrod D., 2007, “Combined laser/sol–gel synthesis of calcium silicate coating on Ti–6Al–4V substrates for improved cell integration,” Appl. Surf. Sci., **253**(19), pp. 7998–8002.

[11] Cheng G. J., and Ye C., 2010, “Experiment, thermal simulation, and characterizations on transmission laser coating of hydroxyapatite on metal implant.,” J. Biomed. Mater. Res. A, **92**(1), pp. 70–9.

[12] Comesaña R., Quintero F., Lusquiños F., Pascual M. J., Boutinguiza M., Durán A., and Pou J., 2010, “Laser cladding of bioactive glass coatings.,” Acta Biomater., **6**(3), pp. 953–61.

[13] Chen K., and Jia Y., 2010, “Laser coating of multi layer Hydroxyapatite on titanium alloy,” 2010 3rd International Conference on Biomedical Engineering and Informatics, IEEE, pp. 1704–1706.

[14] O’Flynn K. P., and Stanton K. T., 2013, “Laser sintering and crystallization of a bioactive glass-ceramic,” J. Non. Cryst. Solids, **360**, pp. 49–56.

[15] Pazo a., Saiz E., and Tomsia A. P., 1998, “Silicate glass coatings on Ti-based implants,” Acta Mater., **46**(7), pp. 2551–2558.

[16] Gomez-Vega J. M., Saiz E., Tomsia a P., Marshall G. W., and Marshall S. J., 2000, “Bioactive glass coatings with hydroxyapatite and Bioglass particles on Ti-based implants. 1. Processing.,” Biomaterials, **21**(2), pp. 105–11.

[17] Itälä A., Ylänen H. O., Yrjans J., Heino T., Hentunen T., Hupa M., and Aro H. T., 2002, “Characterization of microrough bioactive glass surface: surface reactions and osteoblast responses in vitro.,” J. Biomed. Mater. Res., **62**(3), pp. 404–11.

[18] Pereira M. M., and Hench L. L., 1996, “Mechanisms of hydroxyapatite formation on porous gel-silica substrates,” J. Sol-Gel Sci. Technol., **7**(1-2), pp. 59–68.

[19] Pereira M. M., Clark A. E., and Hench L. L., 1995, “Effect of Texture on the Rate of Hydroxyapatite Formation on Gel-Silica Surface,” J. Am. Ceram. Soc., **78**(9), pp. 2463–2468.

[20] Vellet-Regi M., Salinas A. J., Martinez I., Izquierdo-Barba I., and Perez-Pariente J., 2004, “Textural properties of CaO-SiO2 glasses for use in implants,” Solid State Ionics, **172**(1-4), pp. 441–444.

[21] Filho O. P., Latorre G. P., and Hench L. L., 1996, “Effect of crystallization on apatite-layer formation of bioactive glass 45S5,” J. Biomed. Mater. Res., **30**, pp. 509–514.

[22] Frenkel J., 1945, “Viscous Flow of Crystalline Bodies Under the Action of Surface Tension,” J. Phys. USSR, **9**(5), pp. 385–391.

[23] Vogel W., 1994, “Crystallization of Glasses,” Glass Chemistry, Springer Berlin Heidelberg, pp. 280–362.

[24] Avrami M., 1939, “Kinetics of Phase Change. I General Theory,” J. Chem. Phys., **7**(12), p. 1103.

[25] Johnson W. A., and Mehl R., 1939, “Reaction Kinetics in Processes of Nucleation and Growth,” Trans. AIME, **135**, pp. 416–442.

[26] Kolmogorov A. N., 1937, “On the Statistical Theory of Metal Crystallisation,” Izv. Akad. Nauk SSSR, **3**, p. 355.

[27] Peitl O., Zanotto E. D., Serbena F. C., and Hench L. L., 2012, “Compositional and microstructural design of highly bioactive P2O5-Na2O-CaO-SiO2 glass-ceramics.,” Acta Biomater., **8**(1), pp. 321–32.

[28] Chen Q. Z., Xu J. L., Yu L. G., Fang X. Y., and Khor K. a., 2012, “Spark plasma sintering of sol–gel derived 45S5 Bioglass®-ceramics: Mechanical properties and biocompatibility evaluation,” Mater. Sci. Eng. C, **32**(3), pp. 494–502.

[29] Moir G. K., and Glasser F. P., 1974, “Phase Equilibria in the System Na2SiO3-CaSiO3,” Phys. Chem. Glas., **15**(1), pp. 6–11.

[30] Ohsato H., Takéuchi Y., and Maki I., 1990, “Structural study of the phase transition of Na4Ca4[Si6O18],” Acta Crystallogr. Sect. B Struct. Sci., **46**(2), pp. 125–131.

[31] Fokin V. M., Potapov O. V., Zanotto E. D., Spiandorello F. M., Ugolkov V. L., and Pevzner B. Z., 2003, “Mutant crystals in Na2O·2CaO·3SiO2 glasses,” J. Non. Cryst. Solids, **331**(1-3), pp. 240–253.

[32] Fokin V. M., and Zanotto E. D., 2007, “Continuous compositional changes of crystal and liquid during crystallization of a sodium calcium silicate glass,” J. Non. Cryst. Solids, **353**(24-25), pp. 2459–2468.

[33] Krüger P., 1993, “On the relation between non-isothermal and isothermal Kolmogorov-Johnson-Mehl-Avrami crystallization kinetics,” J. Phys. Chem. Solids, **54**(11), pp. 1549–1555.

[34] Kolossov S., Boillat E., Glardon R., Fischer P., and Locher M., 2004, “3D FE simulation for temperature evolution in the selective laser sintering process,” Int. J. Mach. Tools Manuf., **44**(2-3), pp. 117–123.

[35] Bouhifd M. A., Richet P., Besson P., Roskosz M., and Ingrin J., 2004, “Redox state, microstructure and viscosity of a partially crystallized basalt melt,” Earth Planet. Sci. Lett., **218**(1-2), pp. 31–44.

[36] Prado M. O., and Zanotto E. D., 2002, “Glass sintering with concurrent crystallization,” Comptes Rendus Chim., **5**(11), pp. 773–786.

[37] Gutzow I., Pascova R., and Karamanov A., 1998, “The kinetics of surface induced sinter crystallization and the formation of glass-ceramic materials,” J. Mater. Sci., **33**(21), pp. 5265–5273.

[38] Gupta T. K., and Coble R. L., 1968, “Sintering of ZnO: II, Density Decrease and Pore Growth During the Final Stage of the Process*,” J. Am. Ceram. Soc., **51**(9), pp. 525–528.

[39] Tan H., and Lawrence Yao Y., 2013, “Laser Joining of Continuous Glass Fiber Composite Preforms,” J. Manuf. Sci. Eng., **135**(1), p. 011010.

[40] Kongsuwan P., Satoh G., and Yao Y. L., 2012, “Transmission Welding of Glass by Femtosecond Laser: Mechanism and Fracture Strength,” J. Manuf. Sci. Eng., **134**(1), p. 011004.

[41] Kirchhof J., Unger S., Dellith J., and Scheffel A., 2014, “Diffusion in binary TiO_2-SiO_2 glasses,” Opt. Mater. Express, **4**(4), p. 672.

[42] Zhang Y., Ni H., and Chen Y., 2010, “Diffusion Data in Silicate Melts,” Rev. Mineral. Geochemistry, **72**(1), pp. 311–408.

[43] Tomsia a P., and Pask J. a, 1986, “Chemical reactions and adherence at glass/metal interfaces: an analysis.,” Dent. Mater., **2**(1), pp. 10–6.

[44] Stanton K. T., O’Flynn K. P., Nakahara S., Vanhumbeeck J.-F., Delucca J. M., and Hooghan B., 2009, “Study of the interfacial reactions between a bioactive apatite-mullite glass-ceramic coating and titanium substrates using high angle annular dark field transmission electron microscopy.,” J. Mater. Sci. Mater. Med., **20**(4), pp. 851–7.

[45] Scherer G. W., 1997, “Sintering of sol-gel films,” J. Sol-Gel Sci. Technol., **8**(1-3), pp. 353–363.

[46] Kang S.-J. L., 2005, Sintering: Densification, Grain Growth, and Microstructure, Elsevier Butterworth-Heinemann, Burlington, MA.

[47] Rahaman M. N., 2003, Ceramic Processing and Sintering, Marcel Dekker, New York.

[48] Kim B. H., and Lee K. H., 1994, "Crystallization and sinterability of cordierite-based glass powders containing CeO2," J. Mater. Sci., **29**(24), pp. 6592–6598.

[49] Arstila H., Vedel E., Hupa L., and Hupa M., 2007, "Factors affecting crystallization of bioactive glasses," J. Eur. Ceram. Soc., **27**(2-3), pp. 1543–1546.

Appendix

This appendix provides a detailed account of numerical models developed during this thesis, their use, and many software scripts used to analyze data. This appendix has been organized into sections, each associated with a specific chapter of the thesis. Processing data, software scripts, and numerical simulations associated with internal feature generation and modification are located in (*\\Appendix\Chapter2*), transmission welding in (*\\Appendix\Chapter3*), single step channeling in (*\\Appendix\Chapter4*), and double layer coating in (*\\Appendix\Chapter5*).

A1: Internal Feature Generation and Modification

Numerical models with different laser processing parameters were developed to predict feature size inside glass irradiated by femtosecond laser pulses. They were implemented using Abaqus/standard, the commercial finite element (FEM) program. The relevant files of the representative numerical model are included in ('*\\Appendix\Chapter2*'). '*FS-Laser_Glass.cae*' is a model file which can be opened from within the Abaqus/CAE window. Model geometry, basic material parameters, analysis steps, boundary conditions, load conditions as well as mesh controls can be defined within this file. '*FS-Laser_Glass.inp*' is an input file (script) which was written from the CAE file. It includes all of the information contained within '*FS-Laser_Glass.cae*'. '*FS-Laser_Glass.for*' is the user-defined subroutine used in the model. It is body heat flux 'Dflux' of which the user can define the absorption and distribution of the thermal energy input by laser. The simulation should be run in Abaqus Command window using the command "*Abaqus job=FS-Laser_Glass.inp user=FS-Laser_Glass.for interactive*". When the simulation is completed, it will generate many files including '*FS-Laser_Glass.odb*' which is the visualization file. *FS-Laser_Glass*.odb can subsequently be opened in Abaqus CAE window through which the visualization of the thermal profile can be performed. Decomposition data of

Raman spectra is located in ('*\\Appendix\Chapter2\Raman Decomposition*'). The decomposition is processed using OriginPro software by specifying a user defined fitting function that consists of three Lorentz peaks (volume fraction of different ring structures) and stretched exponential (fluorescence). The experimental and numerical feature sizes, the raw load-displacement curves of spatially resolved nanoindentation, and the summary of nanoindentation measurements are provided in excel files. The schematic drawings of experimental setup and the compiled data of morphology, Raman spectroscopy, and nanoindentation for work associated with internal feature generation and modification are also included in ('*\\Appendix\Chapter2*').

A2: Transmission Welding

A 2D axisymmetric numerical model developed to offer greater insight into physical phenomena corresponding to nonlinear absorption of a femtosecond laser pulse by transparent dielectrics, and to predict the absorption volume inside glass and a welding width of transmission welding. It was implemented using MATLAB program. By specifying the laser parameters and number of points in time and space, the script '*AbsorptionVol1.m*' first calculates the power distribution in each time slice, and subsequently calculates the intensity distribution in space of an unfocused laser beam. The intensity increase as the laser beam is focused to the smaller area toward the focal plane. Once it reach the material intensity damage threshold, absorption assumed to occur (close to the focal plane), and the radial coordinates of breakdown points are determined followed by their corresponding axial coordinates from the beam propagation equation. Those breakdown points in each time slice will construct an absorption line, and all lines from every time slice will form the absorption volume. The user has to input the laser pulse energy (E [J]), the numerical aperture (NA), and the lens focal length (f [m]), and the simulation should be run in MATLAB command window using the command "*AbsorptionVol1 (E, NA, f)*". Another

MATLAB script '*AbsorptionVol2.m*' is similar to '*AbsorptionVol1.m*' but considering the change in converging angle of laser beam at air-glass interface due to the refractive index mismatch. The shape of this numerical absorption volume is assumed top-half ellipsoid and bottom half conical frustum. The absorption volume, its surface area, average pressure, van der Waals force and deflection are calculated by running the script '*Volume_AbsorptionVol1.m*'. The schematic drawings of experimental setup and the compiled data of Atomic Force Microscopy (AFM), nanoindentation, and indentation fracture analysis for work associated with transmission welding (TW) are also included in ('*\\Appendix\Chapter3*').

A3: Single Step Channeling

A number of different numerical models were developed to predict channel lengths inside glass by single step channeling (SSC) process. The 2D axisymmetric absorption volume model as described in Chapter 3 of this thesis is further improved by taking into account the aberration effects due to the refractive index mismatch at air-glass interface. Considering the different incident and refracted angles of focusing rays, the breakdown points occur upward in the optical direction. It generates the longer absorption length as a function of pulse energy and focusing depth. One additional input (the paraxial focusing depth: Depth [m]), is required to run the MATLAB script '*AbsorptionVol3.m*', and the command "*AbsorptionVol3 (E, NA, f, Depth)*" should be run in the MATLAB command window. '*AbsorptionVol3_DiffD.m*' and '*AbsorptionVol3_DiffE.m*' are MATLAB scripts that can be run automatically to generate numerical results at different paraxial focusing depths and different laser pulse energies, respectively. A three dimensional (3D) electromagnetic diffraction model, which captures the electric energy density field in the vicinity of focal plane of a single femtosecond laser pulse irradiation inside glass is also developed. Taking into account the optical properties of two different mediums (air and glass), the focusing parameters, and Fresnel's refraction laws at the interface between two different mediums, a superposition of refracted plane waves can construct the time-independent or time-averaged electric fields. The MATLAB script for the electromagnetic diffraction model is '*EM_Diffraction_XYZ.m*'. It calls the integrals I_0, I_1, and I_2 as given in Eq. (4.6) to Eq. (4.8) from other MATLAB scripts, which are '*Torox_I0_XYZ.m*', '*Torox_I1_XYZ.m*', and '*Torox_I2_XYZ.m*', respectively. The schematic drawings of experimental setup and the compiled data of experimental features and channels, Raman spectroscopy, and numerical results for work associated with SSC are also included in ('*\\Appendix\Chapter4*').

A4: Double Layer Coating

Simulation of double layer laser coating of bioactive glass is performed through COMSOL Multiphysics. A 2D axisymmetric FEM laser sintering model with the set of coupled heat transfer, crystallization, sintering, and pore coalescence equations are solved concurrently within a spatially resolved finite element domain in a fully coupled backward Euler time. It captures the combined effects of heat transfer by laser heat source, viscous flow densification, pore coalescence, and crystallization due to laser sintering. The relevant model file is included in ('*\\Appendix\Chapter5*'). '*TopCoat_2Da_Sintering.mph*' can be opened though COMSOL Multiphysics, within which all relevant model parameters such as geometry, laser parameters, material parameters, boundary conditions, meshing, etc. can be modified. The parameters in global definitions of the model are listed in '*Parameters_Global Definitions.txt*', whereas the variables in model definitions are listed in '*Variables_Model Definitions.txt*'. The *Heat Transfer (ht)* module determines the temperature distribution in time and space from a user defined heat source as given in Eq. (5.4) and thermal conductivity (as a function of sintering potential) as given in Eq. (5.9). Other three modules, which are *Sintering Potential_PDE (g)*, *Crystallization_PDE (g2)*, and *Pore Growth_PDE (g3)*, use temperature as a main input parameter to determine their temperature dependent properties such as Sintering Potential (ϕ) as given in Eq. (5.7), Crystallized volume fraction (X) as given in Eq. (5.5), and Pore radius (r_p) as given in Eq. (5.12), respectively. Meshing is performed with bias toward the top surface of top bond coat layer and the center of the laser beam. The MATLAB scripts are also included for analysis of data. '*Changecolor3_TiNaCa.m*' can be used to change the background color of the composition contour map from Energy dispersive X-ray spectroscopy (EDX). '*SingleLayer_Ab.m*' is used to determine the absorption coefficient of deposited glass powder layer. In addition, the compiled data of experimental porosity, X-ray diffraction (XRD), and EDX line profiles for work associated with double layer coating are also included in ('*\\Appendix\Chapter5*').

A5: Publications Under Candidature

Kongsuwan, P., Brandal, G., Yao, Y.L., 2014, "Laser Induced Porosity and Crystallinity Modification of a Bioactive Glass Coating on Titanium Substrates," *Journal of Manufacturing Science and Engineering*, submitted.

Kongsuwan, P., Wang, H., Yao, Y.L., 2012, "Single Step Channeling in Glass Interior by Femtosecond Laser," *Journal of Applied Physics,* **112**(2), pp. 023114-1 to 10.

Also, *Proceedings of the 40th North American Manufacturing Research Conference*, Notre Dame, IN, June, 2012.

Kongsuwan, P., Satoh, G., Yao, Y.L., 2012, "Transmission Welding of Glass by Femtosecond Laser: Mechanism and Fracture Strength," *Journal of Manufacturing Science and Engineering*, **134**(1), pp. 01104-1 to 11.

Also, *Proceedings of the 29th International Congress on Applications of Lasers & Electro-Optics*, Anaheim, CA, September 2010, pp. 1069-1078.

Kongsuwan, P., Wang, H., Vukelic, S., Yao, Y.L., 2010, "Characterization of Morphology and Mechanical Properties of Glass Irradiated by Femtosecond Laser," *Journal of Manufacturing Science and Engineering,* **132**(4), pp. 041009-1 to 10.

Also, *Proceedings of the 28th International Congress on Applications of Lasers & Electro-Optics*, Orlando, FL, November 2009, pp. 1214-1223.

Kongsuwan, P., Vukelic, S., Yao, Y.L., "Structuring and Joining Transparent Materials with Ultra Short Pulse Lasers," *Proceedings of the 32th International Congress on Applications of Lasers & Electro-Optics*, Miami, FL, October 2013. [Invited Paper]

Vukelic, S., **Kongsuwan, P.**, Yao, Y.L., "Investigation of the morphology of the features generated via femtosecond lasers in the interior of a bovine cornea sections," *SPIE BiOS: Optical Interactions with Tissue and Cells XXIV Conference*, San Francisco, CA, February 2013.

Wang, H., **Kongsuwan, P.**, Satoh, G., Yao, Y.L., 2012, "Femtosecond Laser-induced Simultaneous Surface Texturing and Crystallization of a-Si:H Thin Film: Absorption and Crystallinity," *Journal of Manufacturing Science and Engineering*, **134**(3), pp. 031006-1 to 10.

Also, *Proceedings of the 39th North American Manufacturing Research Conference*, Corvallis, OR, June 2011.

Wang, H., **Kongsuwan, P.**, Satoh, G., Yao, Y.L., 2013, "Femtosecond Laser-induced Simultaneous Surface Texturing and Crystallization of a-Si:H Thin Film: Morphology Study," *The International Journal of Advanced Manufacturing Technology,* **65**(9), pp. 1691-1703.

Also, *Proceedings of the 2010 International Manufacturing Science and Engineering Conference*, Erie, PA, October 2010.

Wang, H., **Kongsuwan, P.**, Satoh, G., Yao, Y.L., "Effect of Processing Medium and Condition on Absorption Enhancement of Femtosecond Laser Treated a-Si:H Thin Film," *Proceedings of the 39th North American Manufacturing Research Conference*, Corvallis, OR, June 2011, pp. 4751-1 to 10.

Vukelić, S., **Kongsuwan, P.**, Ryu, S., Yao, Y. L., 2010 "Ultra Fast Laser Induced Structural Modification of Fused Silica. Part II: Spatially Resolved and Decomposed Raman Spectral Analysis," *Journal of Manufacturing Science and Engineering*, **132**(6), pp. 061013-1 to 9.

Vukelić, S., **Kongsuwan, P.**, Yao, Y. L., 2010 "Ultra-Fast Laser Induced Structural Modification of Fused Silica. Part I: Feature Formation Mechanisms," *Journal of Manufacturing Science and Engineering*, **132**(6), pp. 061012-1 to 8.